

Ciocco

C-Holes Update Report: Reinterpretation of the Reactive Tracer Test in the Bullfrog Tuff and Results of Laboratory Testing

Paul W. Reimus
Marc J. Haga
Timothy Callahan
Ioana Anghel
H. J. Turin
Dale Counce

ABSTRACT

Predicting the future performance of a potential nuclear waste repository at Yucca Mountain requires understanding saturated-zone radionuclide transport processes. To test conceptual saturated zone transport models at the field scale, Los Alamos National Laboratory conducted a cross-hole forced-gradient tracer test over a distance of approximately 30 meters in fractured tuffs ranging from about 300 to 400 meters below the water table at the C-Holes (a cluster of 3 wells located about 1.5-km from the potential repository footprint). This test, conducted from October 1996 to September 1997, involved the simultaneous injection of pentafluorobenzoate (PFBA), lithium bromide, and polystyrene microspheres (~0.36- μ m diameter) into a packed-off interval that included both moderately-welded, nonzeolitized tuff and poorly-welded, partially zeolitized tuff in the Bullfrog member of the Crater Flat Tuff. The breakthrough curves of all tracers were bimodal in nature, indicating multiple flow pathways. Parameters describing dispersion and matrix diffusion in the system were estimated by comparing the responses of the PFBA and bromide, which served as nonsorbing tracers with free diffusion coefficients differing by about a factor of three. Field-scale sorption parameters for lithium were deduced by comparing the lithium response to that of the PFBA and bromide (lithium sorbs weakly to the tuffs by cation exchange and serves as an analog for ion-exchanging radionuclides). The polystyrene microspheres provided an indication of the potential for colloid contaminant transport in the system, and they also served as low diffusivity tracers that should have been excluded from the porous matrix.

PFBA
Li Br
P microspheres

*

of only 30m?

ϕ_{eff} ?

In a parallel effort, laboratory investigations of the transport behavior of the tracers used in the Bullfrog field test as well as in an upcoming field test in the Prow Pass member of the Crater Flat Tuff (at the C-Holes) have been conducted over the past few years. These laboratory tests have included batch sorption experiments to characterize lithium sorption to various tuffs below the water table at the C-Holes, column transport experiments (both crushed tuff and fractured cores), cation exchange capacity measurements, characterization of bulk mineralogy by x-ray diffraction (XRD), and experiments to measure diffusion coefficients in saturated tuff matrices. The laboratory experiments have provided a relatively comprehensive data base to support and constrain field tracer test interpretations, to allow comparisons of laboratory- and field-derived transport parameters, and ultimately to help reduce uncertainty in transport parameter estimates derived from the field experiments.

This report presents a reinterpretation of the reactive tracer test conducted in the Bullfrog Tuff in FY 1997 based on the new laboratory data that have been generated

since the test was completed in September 1997. (A previous interpretation was reported in YMP Milestone SP23APMD, Reimus and Turin, July 1997). This report also summarizes all of the laboratory data that have been generated to date to support the field testing efforts, and it offers predictions of transport behavior in the upcoming Prow Pass reactive tracer test.

Based on the reinterpretation of the field test and a comparison of the field-derived and laboratory-derived transport parameters, we conclude that (1) a dual-porosity conceptual transport model is valid for the saturated zone in the vicinity of Yucca Mountain, (2) the potential exists for colloid transport over significant distances in the saturated zone, and (3) field-derived lithium sorption parameters are in good agreement with laboratory measurements. The last conclusion lends validity to the practice of using laboratory-derived sorption parameters to predict field-scale transport of ion-exchanging solutes. However, this conclusion should be applied cautiously to sorbing radionuclides, for which there are no field data in the immediate vicinity of Yucca Mountain

How was this shown?
over what scale?

Hans ARLT

1.0 Introduction

Yucca Mountain, Nevada, located about 150 km northwest of Las Vegas, is the site of a potential high-level nuclear waste repository, and it is currently undergoing extensive characterization and assessment to determine its suitability for such a role. Current plans call for wastes emplaced within Yucca Mountain to be isolated from the accessible environment by a system of multiple barriers. These include "engineered barriers," consisting of components within the repository itself, and a two-part "geologic barrier," consisting of (1) the unsaturated tuff between the repository and the regional aquifer below, and (2) the saturated-zone aquifer system extending from directly below the repository to the down-gradient wells and springs that mark the final groundwater discharge zone. The characterization of radionuclide transport processes within the saturated zone is the subject of this study.

To support this characterization process, we conducted tracer tests at a three-well complex known as the C-wells (UE-25c#1, UE-25c#2, and UE-25c#3), which are located approximately 2 km southeast of the potential repository footprint. Fig. 1-1 shows the layout of the wells and their vertical deviations at depth, including the locations of the intervals in which the tracer tests described in this report were conducted. Each well penetrates approximately 900 m below surface, with the water table being about 400 m below surface. Regional groundwater flow is believed to be approximately north to south, although local flow at the C-wells has been postulated to be northwest to southeast, in the direction indicated in Fig. 1-1 (Geldon, 1995).

The hydrogeology below the water table at the C-wells is depicted in Fig. 1-2 (derived from Geldon, 1993, 1996). The stratigraphy, consisting of Miocene-age fractured tuff layers, is considered representative of the stratigraphy beneath Yucca Mountain, although the water table occurs in different units at different locations around the mountain because of faulting. Matrix porosities at the C-wells range from about 0.10 to 0.35. A consistent observation in all stratigraphic units below the water table is that bulk permeabilities (determined from hydraulic aquifer tests) exceed matrix permeabilities (determined by laboratory core measurements) by 2 to 6 orders of magnitude (Geldon, 1993). This high bulk-to-matrix permeability contrast is indicative of fracture flow, consistent with flow logs at the C-wells that indicate relatively discrete flow zones. The tracer tests described in this report were conducted in a packed-off, ~90-m interval of the central and lower portions of the Bullfrog member of the Crater Flat Formation (Fig. 1-2). These tuffs exhibit at least a 5 order-of-magnitude bulk-to-matrix permeability contrast (Geldon, 1993), and the test interval included the most transmissive zones in all three wells, accounting for over 60% of the flow in each well during open-hole flow surveys. The interval is not hydrologically isolated, as there are pressure responses both above and below the packed-off zone in c#1 and c#2 when c#3 is pumped. However, vertical conductivity is believed to be only a small fraction of horizontal conductivity, and Geldon (1996) has characterized the Bullfrog Tuff as being a confined, nonleaky "aquifer" based on hydraulic testing.

Although water flow in the Bullfrog Tuff and other stratigraphic units below the water table is expected to occur predominantly in fractures, most of the water volume in the system is contained in the porous tuff matrix, where it is essentially stagnant. Radionuclide and tracer transport is therefore expected to be attenuated by diffusive mass transfer between the flowing water in the fractures and the stagnant water in the matrix, a process known as matrix diffusion. Matrix diffusion in fractured systems has

been discussed and modeled at length by others (Neretnieks, 1980; Grisak and Pickens, 1980; Tang et al., 1981; Maloszewski and Zuber, 1983, 1985). A system exhibiting this behavior is frequently called a "dual-porosity" system because of the two distinct porosities corresponding to the fractures and the matrix. We distinguish such a system from a "dual-permeability" or a "dual-porosity, dual-permeability" system because it is assumed that the matrix permeability is negligible relative to fracture permeability and that all flow occurs in fractures. It has been suggested elsewhere that the saturated zone in the vicinity of Yucca Mountain should behave as a dual-porosity system (Robinson, 1994). This concept has important transport implications, particularly for sorbing radionuclides, because it suggests that solutes will have access to a very large surface area for sorption once they diffuse out of fracture flow pathways and into the matrix.

*matrix material is considered only for storage
→ only fracture system communicates globally / computationally less intensive than dual permeability*

The strategy, procedure, results, and interpretation of the reactive tracer test conducted in the Bullfrog Tuff at the C-Holes in FY 1997 are presented in Section 2.0 of this report. Much of this material is nearly identical to material presented in YMP Milestone SP23APMD (Reimus and Turin, July 1997), but it is included here for completeness. The most important differences between this report and the previous milestone are (1) this report contains nearly three more months worth of field data than the previous report (because the test was still in progress when the previous report was written), (2) the transport parameters derived from the test interpretation in this report are slightly different than in the previous report because of additional constraints imposed on the analysis as a result of laboratory data generated since July 1997, and (3) this report contains a preliminary interpretation of the microsphere response from the reactive tracer test (not included in the previous milestone). The interpretations in this report should supercede those in the previous report.

Lithium ion was used as a sorbing tracer in the field experiments. Lithium serves as a reasonable surrogate for ion-exchanging radionuclides (Fuentes et al., 1989), and it has the advantages of being environmentally benign, acceptable to regulators, readily detectable, and affordable. We have studied the sorption characteristics of lithium onto several tuff lithologies present below the water table at the C-Holes in laboratory tests under both static (batch) and dynamic (flowing) conditions. The methodology and results of the batch sorption experiments conducted to date are presented in Section 3.0. The dynamic transport experiments have been conducted by eluting tracer solutions through either crushed tuff columns or fractured tuff columns. The crushed tuff column experiments were conducted to (1) verify that the equilibrium sorption parameters determined in the batch sorption tests were also valid under flowing conditions, and (2) estimate rate constants for lithium sorption and desorption. The fractured column experiments were conducted to more closely simulate fracture flow conditions in the field and to study tracer transport under the combined influence of matrix diffusion (acting on all tracers) and sorption (acting on lithium). Results of the dynamic transport experiments conducted to date are presented in Section 4.0. All rocks used in the batch sorption and dynamic transport experiments were derived from core taken from the C-Holes.

In addition to the batch sorption and dynamic transport tests, "diffusion cell" experiments were conducted to measure the diffusion coefficients of tracers in intact blocks of tuff matrices taken from various intervals in the C-holes (the rocks used were again taken from C-Holes core). These experiments were conducted to help constrain interpretations of the field tracer tests. The methodology and results of the diffusion cell experiments are presented in Section 5.0.

Section 1.0 References

- Fuentes, H. R., Polzer, W. L., Essington, E. H. and Newman, B. D., Characterization of reactive tracers for C-wells field experiment I: Electrostatic sorption mechanism, lithium. *Los Alamos National Laboratory Report LA-11691-MS*, Los Alamos, NM, 1989.
- ✓ Geldon, A. L., Preliminary hydrogeologic assessment of boreholes UE-25c#1, UE-25c#2, and UE-25c#3, Yucca Mountain, Nye County, Nevada, *Water-Resources Investigations Report 92-4016*, United States Geological Survey, Denver, CO, 1993.
- Geldon, A. L., Average linear velocity and travel time at the C-hole complex, *Memo to the Record*, March 1, 1995.
- Geldon, A. L., Results and interpretation of preliminary aquifer tests in boreholes UE-25c#1, UE-25c#2, and UE-25c#3, Yucca Mountain, Nye County, Nevada, *Water-Resources Investigations Report 94-W-0412*, United States Geological Survey, Denver, CO, 1996.
- Grisak, G. E. and Pickens, J. F., Solute transport through fractured media, 1: The effect of matrix diffusion, *Water Resour. Res.*, 16(4), 719-730, 1980.
- Maloszewski, P. and Zuber, A., Interpretation of artificial and environmental tracers in fissured rocks with a porous matrix, in *Isotope Hydrology*, International Atomic Energy Agency (IAEA), Vienna, Austria, pp. 635-651, 1983.
- Maloszewski, P. and Zuber, A., On the theory of tracer experiments in fissured rocks with a porous matrix, *J. Hydrology*, 79, 333-358, 1985.
- Neretnieks, I., Diffusion in the rock matrix: An important factor in radionuclide migration?, *J. Geophys. Res.*, 85(B8), 4379-4397, 1980.
- Reimus P. W. and Turin, H. J., Draft report of results of hydraulic and tracer tests at the C-holes complex, *Yucca Mountain Site Characterization Project Milestone Report SP32APMD*, Los Alamos National Laboratory, Los Alamos, NM, 1997.
- Tang, D. H., Frind, E. O., and Sudicky, E. A., Contaminant transport in a fractured porous media: Analytical solution for a single fracture, *Water Resour. Res.*, 17(3), 555-564, 1981.
- Waddell, R., Printouts of C-holes borehole vertical deviation surveys dated 7/3/84 (c#1), 7/11/84 (c#2), and 7/12/84 (c#3), obtained from A. L. Geldon, USGS, 1995.

Section 1.0 Figures

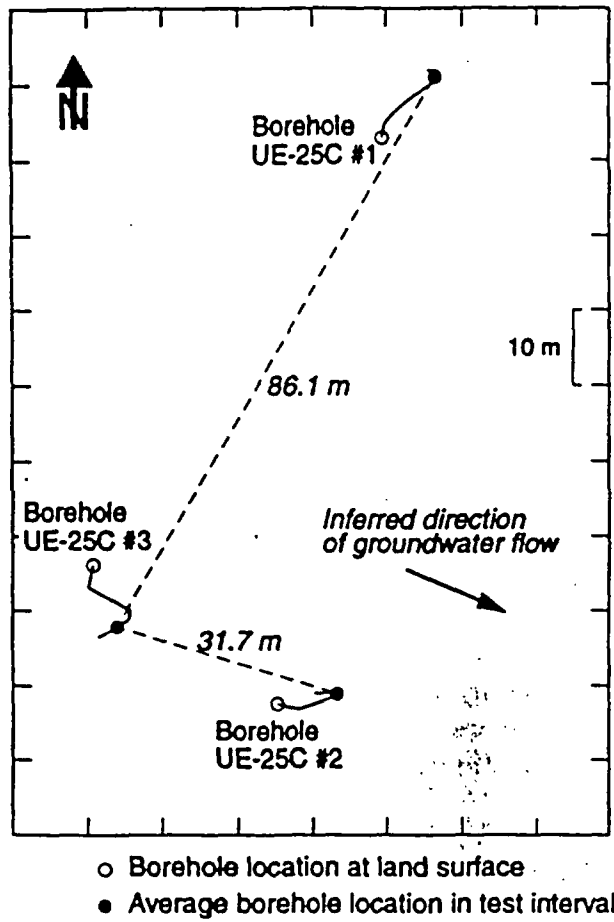


Figure 1-1. C-wells layout showing interwell distances between tracer test intervals (Geldon, 1993, personal communications, and Waddell 1984).

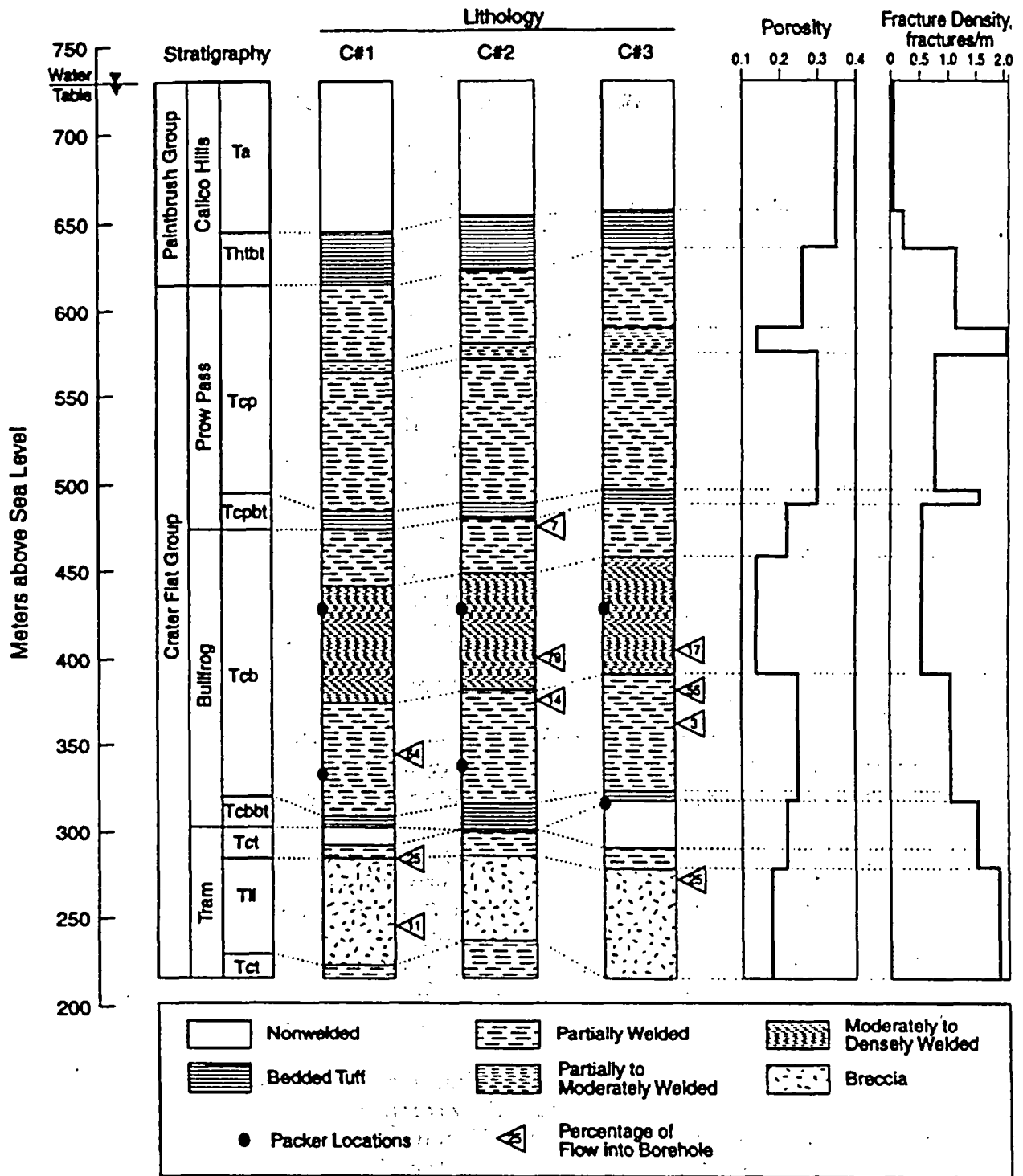


Figure 1-2. Stratigraphy, lithology, matrix porosity, fracture density, and inflow (from open-hole flow surveys) at the C-wells. Packer locations indicate intervals in which tracer tests were conducted. Information derived from Geldon (1993, 1996, and personal communications).

2.0 Reactive Tracer Test in Bullfrog Member of Crater Flat Tuff

2.1 Test Strategy

The C-wells tracer tests were conducted with the multiple objectives of (1) testing/validating conceptual models of radionuclide transport through a dual-porosity system, (2) obtaining estimates of key transport parameters in the Bullfrog Tuff, and (3) assessing the applicability of laboratory-derived sorption parameters to field-scale transport predictions. To accomplish all of the test objectives in a reasonable time, we chose to conduct a forced-gradient, cross-hole tracer test involving the simultaneous injection of four tracers having different physical and chemical properties. By simultaneously introducing the tracers (in a single solution), we ensured that they all experienced the same flow field and hence followed identical flow pathways through the system. The test interpretation could then be based on comparing the responses of the different tracers in addition to analyzing the individual responses of the tracers. The tracers used were (1) pentafluorobenzoate (PFBA), (2) bromide ion, (3) lithium ion, and (4) ~360-nm diameter carboxylate-modified-latex polystyrene microspheres (Interfacial Dynamics, Inc.). Lithium bromide salt was used as the source of lithium and bromide. PFBA and bromide were analyzed by high-pressure liquid chromatography with a UV absorbance detector, lithium was analyzed by inductively coupled plasma-atomic emission spectrometry (ICP-AES), and the microspheres were analyzed by flow cytometry (Steinkamp et al. 1991, Becker et al., submitted).

The bromide and PFBA served as nonsorbing solutes with matrix diffusion coefficients differing by about a factor of three (as determined from diffusion cell experiments discussed in Section 5.0). Batch sorption experiments have established the nonreactivity of both bromide and PFBA in with C-wells tuffs (Section 3.0). Both tracers are monovalent anions in C-wells groundwater, which has a pH of about 8. A comparison of the responses of these two tracers was expected to yield information about matrix diffusion, as the smaller bromide ion would be expected to diffuse more readily into the matrix than the larger PFBA. Robinson (1994) has shown that in a dual-porosity system, a higher diffusivity tracer is expected to have a breakthrough curve with a lower, slightly delayed peak and a longer tail relative to a lower diffusivity tracer. However, in a single-porosity system (i.e., a classic porous medium) two such tracers should behave identically. Thus, if bromide appeared attenuated relative to PFBA, it would indicate that a dual-porosity system conceptualization was valid. By simultaneously analyzing the breakthrough curves of the two tracers, we planned to obtain quantitative estimates of parameters describing both flow field dispersion and matrix diffusion in the system.

As described in the introduction, lithium ion served as a weakly-sorbing solute tracer. Its response was to be interpreted by comparing with the responses of the PFBA and bromide. The diffusion coefficient of lithium is expected to be intermediate between PFBA and bromide (about two-thirds of the bromide diffusion coefficient; Newman 1973), so in the absence of sorption, its response would be expected to fall between that of PFBA and bromide. Therefore, any attenuation of lithium relative to bromide, manifested as either a lower peak, a delayed peak, or both, could be attributed to sorption. In unpublished calculations, we have predicted lithium transport relative to nonsorbing solutes in a field test using the laboratory-derived Bullfrog tuff sorption parameters and assuming both a single- and a dual-porosity medium. These

Milestone SP32E2M4

Polystyrene - low diffusivity

bromide + PFBA

- nonsorbing solutes

- MD coeff differ by factor of 3

- non-reactive in Tuffs (batch sorption tests)

- Br smaller ion than PFBA + have higher diffusivity, delayed peak, etc.

Lithium - weakly sorbing solute tracer

DC < Li diffusion coeff < PFBA

2.1

- matrix diffusion coefficients

- dispersion

Draft, 9/3/98

trac?

?

calculations have shown that in a dual-porosity system with no sorption in fractures (i.e., open fractures), the lithium response should have a lower peak relative to nonsorbing solutes, but the peak will not be significantly delayed in time. However, in a single-porosity system or a dual-porosity system with sorption in fractures, the lithium response should have both a much lower peak and a significant time delay relative to the nonsorbing solutes. We planned to deduce lithium sorption parameters in the system using the models described in Appendix A to fit the lithium breakthrough curve under the constraint that the dispersion and matrix diffusion parameters deduced from the simultaneous analysis of the bromide and PFBA responses must apply to the lithium as well. Thus, the only adjustable parameters in the lithium fitting exercise would be sorption parameters.

The polystyrene microspheres were introduced into the test for two purposes: (1) they served as colloid tracers to provide insights into the potential for colloidal radionuclide transport in the saturated zone near Yucca Mountain, and (2) they served as large, low diffusivity tracers that should be excluded from the matrix and hence provide an indication of true fracture flow in the system without the effects of matrix diffusion. Carboxylate-modified-latex (CML) polystyrene microspheres with fluorescent dye tags were used because these microspheres had previously been shown to have less tendency for attenuation/filtration in fractured systems than other synthetic colloids that we considered (Reimus, 1995). The spheres have a density of 1.055 g/cm^3 , which minimizes their tendency to settle in groundwater. The fluorescent dye tags allowed the spheres to be discriminated from natural colloidal material and to be quantified at concentrations as low as $\sim 100/\text{mL}$ using flow cytometry (Steinkamp et al. 1991, Becker et al., in prep.). The CML spheres have carboxyl functional groups on their surfaces, which give them a negative surface charge at pHs greater than about 5; and unlike most other polystyrene microspheres, they also have hydrophilic surfaces (Wan and Wilson, 1994). Both of these features tend to minimize attractive interactions with rock surfaces, and they make the spheres very stable against flocculation, even at relatively high ionic strengths, which is important if the spheres are to be injected simultaneously with solutes in a relatively concentrated solution. However, despite these measures, we still expected significant attenuation of the spheres based on previous experience in both laboratory- and field-scale fractured systems (Becker et al., in prep.). We used 360-nm-diameter spheres because we found in previous work that larger spheres were more attenuated in fractured systems, possibly due to more rapid settling of the larger particles (Becker et al., in prep.). Also, the flow cytometer that we had access to had a lower size detection limit of about 250-nm diameter, although this does not represent a fundamental limitation of the technique.

2.2 Test Procedure

Because of the considerable investment associated with conducting a test involving multiple tracers, we first conducted two single-tracer pilot tests to determine nonsorbing tracer travel times and recoveries from wells c#1 and c#2 to well c#3. Well c#3 was used as the production well in all tests because it has the largest open-hole transmissivity of the three C-wells (Geldon, 1993). The pilot tests allowed us to (1) determine which hole, c#1 or c#2, offered a faster, higher peak concentration response and would therefore be the preferred injection hole for a test involving a reactive tracer, (2) estimate tracer masses required for the multiple tracer test, and (3) plan sampling frequencies for the multiple tracer test. Although c#2 is much closer to c#3 than c#1

Parameters calculated

dispersion
matrix diffusion
sorption
effective porosity(?)

(~30 m vs. ~80 m at depth), it was not taken for granted that c#2 would have a better tracer response because (1) local fracture strikes tend to be oriented more in the direction of c#1-to- c#2, (2) c#1 had approximately the same magnitude pressure response as c#2 when pumping c#3, and (3) the natural gradient is believed to be approximately in the direction from c#3 to c#2 (Geldon 1993). We were particularly concerned that if we didn't inject enough lithium bromide (which is only ~8% lithium by mass) into the system, we would not observe any lithium at the production well. This concern stemmed from the uncertainty in the expected lithium attenuation due to sorption and also because of the relatively high lithium background concentration, ~65 µg/L, in the groundwater. Additionally, environmental permitting dictated that we minimize, within reason, tracer masses injected.

The packed-off zone in c#3 (Fig. 1-2) was pumped continuously at about 575 L/min in each test. The first pilot tracer test involved the injection of approximately 10 kg of PFBA into well c#2 on May 15, 1996. The PFBA was dissolved in ~1000 L of groundwater. The test was conducted under partial recirculation conditions with about 20 L/min of the water produced from c#3 (~3.5% of production rate) being continuously reinjected into c#2. The recirculation was initiated approximately 24 hr before tracer injection to establish a steady flow field, and it was continued for 23 days after injection. The tracer solution was plumbed into the recirculation loop such that there were no flow interruptions during injection.

The second pilot test involved the injection of about 12.7 kg of iodide (~15 kg of sodium iodide dissolved in ~1000 L of groundwater) into c#1. It was conducted in a manner very similar to the PFBA pilot test and was initiated on June 18, 1996. The recirculation rate in this test was about 15 L/min (~2.6% of production rate), and recirculation continued for 16 days after injection.

The results of these two pilot tests clearly indicated that c#2 was the preferred injection hole for the multiple tracer test, as the PFBA recovery from the May injection was about 73% and the iodide recovery from the June injection was estimated between 6 and 10%. The May PFBA response from c#2 was previously reported by Reimus and Turin (1996) (also shown in Figs. 2-3 and 2-6 of this report), and the iodide response from c#1 is shown in Fig. 2-1. Based on these results, a tracer test involving the simultaneous injection of ~12 kg PFBA, ~180 kg of lithium bromide (14.5 kg lithium, 165.5 kg bromide), and ~7 g of microspheres (~ 3.5×10^{14} spheres) into c#2 was initiated on October 9, 1996. Because of the much greater tracer mass in this test than in the pilot tests, and the desire to minimize solute concentrations to prevent microsphere flocculation, the tracers were dissolved in ~12,000 L of groundwater instead of the ~1000 L used in the pilot tests. The greater volume kept the density contrast between tracer solution and the downhole groundwater about the same as in the pilot tests. The microspheres were actually introduced to the tracer mixture after about one-third of the solution had been injected, which corresponded to about one injection interval volume. The test was carried out under partial recirculation conditions with a recirculation rate of about 20 L/min that was continued for 40 days. Steady flow conditions were established by starting recirculation ~36 hr prior to tracer injection.

2.3 Test Results

The breakthrough curves (normalized to mass injected) of the four tracers in the multiple-tracer test are shown on a log-log plot in Fig. 2-2. This test was conducted for ~8200 hrs, and the tracer recoveries at the end of the test were estimated to be ~69% for

PFBA, ~69% for bromide, ~39% for lithium, and ~15% for the microspheres (at ~6900 hr into the test). Microsphere concentrations dropped below quantifiable levels (<50/ml) after 6900 hrs, so results were not reported after that time, although the spheres were still detectable in the production water. PFBA concentrations also dropped below quantifiable levels (<4 µg/L) after about 7500 hr into the test. This fact, coupled with the uncertainty in how much PFBA from the May 1996 pilot test was still contributing to the PFBA response in the multiple-tracer test, introduced considerable uncertainty into estimates of PFBA concentrations and recoveries from the October 1996 injection, particularly at late times. The PFBA response shown in Fig. 2-2 represents the lower bound case for PFBA concentrations from the October injection. This lower bound was obtained by subtracting 10 µg/L (the residual PFBA concentration in the system at the beginning of the reactive tracer test) from the measured concentrations. Although this assumption may seem unrealistic, it is supported by the fact that the PFBA concentrations from the May injection remained essentially constant at 10-14 µg/L for the last 6-7 weeks prior to the October injection. PFBA concentrations were also calculated by subtracting (from the measured concentrations) an exponentially-decaying function with a decay constant determined by a linear least-squares fit to the tail of the May breakthrough curve on a log-log plot. We found that the PFBA response up to 2000 hrs after injection was insensitive to which assumption was made about residual PFBA concentrations. However, because the measured concentrations after 2000 hrs declined to the point where assumed residual concentrations became a significant fraction of the measured values, the tail of the PFBA curve assuming an exponential decay became noticeably higher than the tail of the PFBA curve shown in Fig. 2-2.

This uncertainty in residual PFBA concentrations significantly affects calculated PFBA recoveries; the recoveries associated with the two cases described above were 63% for the first case and 74% for the exponential decay case. We give more weight to the exponential decay case at late times because if the assumptions associated with the first case are accepted, then the PFBA concentrations from the October injection actually become negative after about 6000 hrs because the measured PFBA concentration decreases to less than 10 µg/L at this time. Because negative concentrations are a physical impossibility, we conclude that concentrations from the May injection must have continued to decline after the October injection, although probably not as fast as the exponential decay assumed for the upper curve in Fig. 2-2. We therefore consider 69% to be reasonable estimate of the PFBA recovery from the October injection given the uncertainties and lines of reasoning discussed above.

* The most striking feature of the breakthrough curves in Fig. 2-2 is their bimodal (double-peaked) behavior, discussed below. The PFBA and bromide responses show clear qualitative evidence of matrix diffusion, as the normalized PFBA concentrations are higher than the normalized bromide concentrations at both peaks, and the second bromide peak is somewhat delayed relative to the PFBA with a tail that appears to cross over the PFBA at long times. As discussed above, these are all hallmarks of matrix diffusion in a dual-porosity system. The lithium response shows obvious attenuation relative to the nonsorbing tracers, providing clear evidence of lithium sorption. It is interesting that the attenuation of the first peak is almost exclusively a lowering of the peak with little or no time delay, while the attenuation of the second peak involves a clear time delay along with a dramatic lowering of concentration. Explanations for this behavior are offered in the test interpretation section.

The microsphere breakthrough curve, which is corrected for the ~3.5-hr delay in their injection time relative to the solutes, is clearly attenuated compared to the solutes. However, it is interesting that their first arrival preceded the solutes, although if the delay in their injection is not accounted for, the first arrival time is very close to the first solute arrival time. The early microsphere arrival behavior has been observed in other field and laboratory tests in fractured systems (Reimus, 1995; Becker et al., in prep.), and it may be attributed to a small fraction of the spheres moving rapidly through high-velocity streamlines in fractures without having the opportunity to diffuse into low-velocity or stagnant water. The majority of the microspheres may have been attenuated by filtration mechanisms, possibly gravitational settling, as proposed by Becker et al. (in prep.). It is also interesting that while the first microsphere peak occurs earlier than the solutes, the second peak occurs later than the solutes. A quantitative interpretation of the microsphere response is discussed in Section 2.5.

The response to the May PFBA injection into c#2 was significantly different than the response in October. The first 1800 hrs of the normalized PFBA breakthrough curves in the two tests are shown in Fig. 2-3 (with linear axes). The May breakthrough curve is a more conventional single mode response. PFBA concentrations from the May injection were monitored for just over 3000 hr with a total recovery of ~73%, and the total recovery at 3000 hr in the October test was ~58%; i.e., a higher recovery in the May test than in the October test at the same point in time.

We offer the following explanation for the different responses in May and October. Because of the lack of mixing in the injection interval, the tracer solutions, which were injected directly below the top packer and were ~2% more dense than the groundwater in each test, probably sank rapidly to the bottom of the interval in each test. The tests were conducted in an identical manner in every respect except that only ~1000 L of tracer solution was injected in May, while ~12,000 L was injected in October. (The duration of recirculation was also different, 23 vs. 40 days, but all significant differences occurred prior to 23 days.) The injection interval volume was ~4300 L, so in the May test, only one-quarter of an interval volume was injected, and it is very possible that only flow pathways in the lower part of the interval conducted tracers out of the borehole. In contrast, in the October test, approximately three interval volumes of tracer solution were injected, so the volume between the packers should have completely filled with tracer solution and tracers would have accessed flow pathways throughout the entire length of the interval. We suspect that the first peak in October was the result of a small percentage (~13%) of the injected tracer mass entering a flow pathway (or set of pathways) in the upper part of the borehole that was not accessed in May. The flow survey information depicted in Fig. 1-2 certainly suggests that the zone of highest flow in well c#2 occurs in the upper half of the interval, although one cannot necessarily conclude that there is a cross-hole connection originating from these pathways. Much of the remaining mass then presumably followed pathways that were also accessed in May and resulted in the second peak occurring at the same time as the May peak (Fig. 2-3). However, because the shapes of the May and second October peaks are different, and the total PFBA recovery was actually lower in October despite the early peak, we also suspect that a considerable fraction of the mass injected in October followed other pathways that were not accessed in May and were slower, in general, than those accessed in May.

Although we have no direct proof to support this hypothesis, we conducted some simple laboratory experiments involving the injection of dyed salt solutions into a ~2-m-long, ~1.5-cm ID, clear plastic tube with a tee about 1 m from the top of the tube

to serve as a "pathway" out of the "borehole." The dyed solution had approximately the same density as the solutions injected in the field experiments, and it was injected at the same rate, relative to the diameter of the tube, as in the field. We found that even though the tee was the only exit point for flow out of the tube, most of the dyed solution sank below the tee and remained in the lower part of the tube (unpublished data). However, it must be recognized that the Reynolds number (a measure of turbulence - Bird et al., 1960) was drastically different in the laboratory than in the field; more turbulence would have been expected in the field.

We view the bimodal response in October and the single-peak response in May as serendipitous good fortune. First, the two peaks allow us to objectively conclude that there are at least two separate sets of flow pathways that contributed to the October tracer responses. This allows us to estimate a different set of transport parameters for each set of pathways, meaning that we effectively conducted "two tests in one." It should be noted that if as much as 20% of the tracer mass had followed the faster pathways in October (instead of ~12%), the result probably would have been a single peak instead of two peaks.

2.4 Quantitative Interpretation of Solute Responses

The solute tracer responses were interpreted by simultaneously fitting the breakthrough curves using a semi-analytical, dual-porosity transport model, RELAP, which is described in detail in Appendix A and briefly summarized here (see also, Reimus and Dash, 1998). The physical, conceptual, and mathematical models assumed for the field transport system are depicted in Fig. 2-4. The equations shown at the bottom of Fig. 2-4 are Laplace-domain "transfer functions" that describe tracer residence time distributions within each of the system "components." The most important of these is the transfer function for the groundwater system, which is taken from Tang, et. al. (1981). This transfer function assumes 1-dimensional advective-dispersive transport in parallel-plate fractures with 1-dimensional diffusion (perpendicular to fracture flow) into a homogeneous, infinite matrix. It also assumes linear, equilibrium, reversible sorption of a reactive species and a constant flow velocity in the fractures. Model formulations assuming a finite matrix (Maloszewski and Zuber, 1983, 1985), radial flow (Moench, 1995; Becker and Charbenaev, submitted) and rate-limited sorption (Maloszewski and Zuber, 1991) are also embodied in RELAP. These were used to evaluate the sensitivity of the derived transport parameters to radial vs. linear flow, infinite vs. finite matrix, and equilibrium vs. rate-limited sorption. A detailed description of the mathematical development of the models embodied in RELAP is provided in Appendix A.

The transfer functions shown in Fig. 2-4 were multiplied together to describe transport throughout the system; a multiplication in the Laplace domain is equivalent to a convolution integral in the time domain (Churchill, 1958). Although not shown explicitly in Fig. 2-4, recirculation of the production water from well c#3 into c#2 was also accounted for (see Appendix A). However, the amount of recirculation was so small (~3.3%) that it made virtually no difference whether or not recirculation was accounted for at all. Wellbore storage was accounted for by assuming that the boreholes were well-mixed, with the tracers experiencing an exponential-decay residence time distribution with a time constant slightly greater than the volume of the interval divided by the volumetric flow rate into (injection well) or out of (production well) the interval. Note that an equation for wellbore mixing in the production well is

not shown in Fig. 2-4 because residence times in this well were very short (less than 10 minutes) due to the high flow rate out of the well (~575 L/m). The Laplace domain solutions were then inverted to the time domain using a Fourier-transform inversion technique (Appendix A). Because the Fourier-transform technique is very efficient (and stable), it could be performed thousands of times per minute on a computer workstation, making it practical to estimate model parameters by systematic, brute-force adjustments of their values to achieve a least-squares fit to the data. The fitting procedure used to quantitatively interpret the October tracer responses is summarized in Table 2-1 and discussed in detail in the following two subsections.

2.4.1 Nonsorbing Solutes

The first step in the interpretation procedure involved using the transfer function model depicted in Fig. 2-4 to simultaneously fit the PFBA and bromide data assuming that all transport parameters except for diffusion coefficients were identical for the two solutes. Bromide matrix diffusion was assumed to be triple that of PFBA based on diffusion cell results presented in Section 5.0. The matrix and fracture retardation factors for these two nonsorbing tracers were set equal to 1. The procedure involved simultaneously fitting the early tracer peak(s) with a single set of model parameters assuming that only a fraction of the tracer mass accounted for the peak. The parameters adjusted to achieve the fit were (1) the mass fraction, f , (2) the mean fluid residence time, τ , (3) the Peclet number, $Pe = L/\alpha$, where L is the distance between wells and α is the dispersivity, and (4) the lumped parameter, $\frac{\phi}{b} \sqrt{D_m}$, which is effectively a mass transfer coefficient for diffusion into stagnant water, assumed to be in the matrix (ϕ is the matrix porosity, b is the fracture half-aperture, and D_m is the matrix diffusion coefficient). The matrix porosities and matrix diffusion coefficients measured in laboratory diffusion cell experiments (see Section 5.0) were assumed to apply to the field test; these measurements made it possible to estimate fracture half-apertures in the field test (the only variable in the lumped parameter that could not be independently measured). All other parameters in the transfer function model were fixed according to the manner in which the test was conducted (e.g., the injection concentration, injection duration, and time constants for mixing in the injection and production wellbores).

Although the injection duration was about 10 hrs, we arbitrarily assumed an injection delay time of 4 hr followed by a 6-hr injection when fitting the early tracer response (the first peak). Our rationale for making this assumption was that there was no early response in the May PFBA test (which involved an injection duration of less than one hour), so it seemed logical to assume that the earliest injected tracer solution did not follow the earliest-arriving pathways. We chose a 4-hr delay time because the injected tracer solution volume exceeded the injection interval volume by this time, and we felt that this was a reasonable criteria for when at least a portion of the tracer solution should have begun moving through the earlier-arriving pathways. Subsequent sensitivity analyses indicated that the best-fitting model parameters were not very sensitive to assumed tracer injection durations ranging from 2 hr to 10 hr, although there was a definite trend toward smaller Peclet numbers (greater dispersion) as the injection duration was shortened. This result is undoubtedly due to the fact that shorter tracer pulses must "spread" more to match the observed breakthrough curve. The injection duration for the second peak was assumed to be the full 10 hrs of injection.

The best fit to the first peak was subtracted from the entire breakthrough curve of each tracer, leaving only a single second peak. The simultaneous fitting procedure was then repeated for the second peak. All of the parameters describing the second peak were adjusted independently of the parameters that offered the best fit to the first peak (except that the sum of the mass fractions in both fits could not exceed 1). This procedure assumed that each peak could be described by a single advection-dispersion equation to account for flow and dispersion in fractures with a single mass transfer coefficient accounting for matrix diffusion. We recognize that the tracer response in reality was probably the result of flow through many pathways in a fracture network, and that these pathways undoubtedly had a distribution of residence times, dispersivities, and matrix diffusion mass transfer coefficients. However, without specific data on the geometry and transport properties of individual pathways, it is difficult to justify assuming more pathways than the number of peaks in the tracer responses. Thus, we initially limited ourselves to two "pathways," one for each peak.

It is important to recognize that the simultaneous interpretation of the PFBA and bromide breakthrough curves offers a tremendous advantage over the interpretation of either tracer breakthrough curve individually. In fact, without this simultaneous interpretation, it is not possible to distinguish between the effects of hydrodynamic dispersion and matrix diffusion in a field tracer test. This dilemma is illustrated in Fig. 2-5, which shows arguably equally good fits to the May PFBA breakthrough curve obtained using the sets of model parameter values given in Table 2-2. It is apparent that, although there is an upper limit to the matrix diffusion mass transfer coefficient that can be assumed in the system (constrained by the fact that the mass fraction of tracer participating in the test cannot exceed 1), a reasonably good fit to the data can be obtained by assuming no matrix diffusion at all (i.e., a single-porosity system). Note that even though the curve with the largest amount of matrix diffusion appears to offer the best fit to the data in Fig. 2-5, an equally good fit can be obtained by assuming two overlapping single-porosity pathways with different dispersion parameters or by simply assuming a much longer mean residence time for the tracer solution in the injection borehole. Thus, while the analysis of a single breakthrough curve can offer an upper bound on matrix diffusion and a range of possible values for the dispersion coefficient and mean fluid residence time in the system, it cannot conclusively establish that matrix diffusion is occurring in the system.

We consider fractional mass participation in the tracer tests to be a definite possibility, as the natural gradient is believed to be almost opposite the direction of induced flow from c#2 to c#3 (Fig. 1-2), and some of the tracer mass could have "sunk" (due to density effects) out of the zone of influence of induced flow. Also, it is possible that at least some of the unaccounted-for tracer mass could have actually moved through the tuff matrix rather than through fractures because the matrix permeability is not zero (as assumed in the dual-porosity model formulation). It can be shown that even with very low matrix permeabilities relative to fracture permeabilities, a significant amount of tracer mass can still move through the matrix if the cross-sectional area available for matrix flow is much greater than that for fracture flow. Given the fracture densities and apertures observed in C-Holes logs, it is not unreasonable to expect a significant amount of total mass flow through the matrix.

Fig. 2-6 shows the best fits to the PFBA and bromide breakthrough curves in the reactive tracer test. The transport model parameters used to obtain the fits are given in Table 2-3. Note that different mean residence times (τ) and Peclet numbers (Pe) were obtained in each pathway depending on whether linear or radial flow was assumed. In

a heterogeneous, confined aquifer, the flow velocity to a single production well is expected to vary between linear and radial (National Research Council, 1996). Thus, if we assume that the Bullfrog Tuff is reasonably confined, as suggested by Geldon (1996), presenting the two sets of residence times and Peclet numbers in Table 2-3 is a way of bounding these parameter estimates as a result of flow field uncertainty. The radial mean residence time is always less than the linear residence time, and the radial Peclet number is always greater than the linear Peclet number. This somewhat confusing result can be qualitatively explained by recognizing that the models implicitly assume that the dispersion coefficient is the product of the dispersivity (α) and the fluid velocity. Under this assumption, for a given dispersivity, a solute will tend to experience more dispersion in radial flow than in linear flow because any time the solute disperses ahead of the mean position, it will be subjected to a greater flow rate, and any time it disperses behind the mean position, it will be subjected to a slower flow rate. Thus, leading solute particles will tend to be swept further ahead and lagging solute particles will tend to lag further behind in radial flow than they would be in linear flow. In effect, the radial flow field has an additive effect to the dispersion that would be experienced in a linear flow field. Any breakthrough curve can always be fitted equally well assuming either type of flow field; only the values of the parameters will differ. Fig. 2-7 shows the relationships between τ and Pe in radial and linear flow as a function of linear Peclet number. These relationships were derived using RELAP to fit a linear response with a radial model.

Table 2-3 also indicates that the assumption of a finite matrix with a fracture spacing of 4 cm in the second pathway offered a better fit to the end of the tracer breakthrough curves than an infinite matrix assumption (which resulted in underprediction of the tracer responses). This was the only instance where assuming a finite matrix improved a fit. However, we do not consider this result terribly significant because the data at the ends of the breakthrough curves have considerable scatter due to (1) lower analytical precision at the low concentrations, (2) approach to background concentrations, and (3) in the case of PFBA, uncertainty in the contribution from the May 1996 injection.

Another assumption that resulted in better fits to the PFBA and bromide breakthrough curves was that a portion of the reactive tracer test responses was due to tracers following exactly the same pathways as the PFBA in the May test (since the May peak and the second October peak occurred at the same time). In this case, the second peak can be accounted for almost entirely by the May pathways, and a third set of pathways is then required to fit the long tails of the October responses. This approach was discussed in considerable detail in YMP milestone SP23APMD (Reimus and Turin 1997), and it is therefore not discussed further here. Although the three-pathway approach can be readily justified because of the observed May PFBA response, we consider it to be a deviation from our self-imposed constraint of not introducing more "pathways" than the observed number of tracer peaks. Also, the introduction of additional pathways should always result in better fits to tracer responses, so it is not surprising that assuming three pathways results in a better fit than assuming two-pathways.

It is interesting that the lumped matrix diffusion parameters that offered the best fits to the PFBA and bromide data (see Table 2-3) suggest that the amount of matrix diffusion in the second set of pathways was significantly less than in the first set of pathways. This result appears to contradict our theory that the first peak was the result of a small amount of tracer mass following pathways that were higher in the injection

borehole (see Section 2.3). The upper half of the injection interval was in the more densely welded central Bullfrog Tuff lithology, which has about a factor of three lower matrix porosity than the tuff in the lower half of the injection interval (see Section 5.0). Also, laboratory measurements of matrix diffusion coefficients in the central and lower Bullfrog Tufts indicate that the diffusion coefficients in the poorly-welded lower unit are at least two times higher than those in the central unit (also in Section 5.0). Thus, if the early peak was due to tracers moving through the central Bullfrog Tuff and the later peak was due to tracers moving through the lower Bullfrog Tuff, the expectation would be that the first peak would have smaller matrix diffusion parameters, not larger ones, as determined in the fits. However, it must be kept in mind that (1) we do not know the exact locations of the flow pathways that resulted in the tracer responses (they could have all been in either the central or the lower units), (2) the lumped matrix diffusion parameter includes the average fracture half-aperture, which could have been significantly larger in the pathways that resulted in the later peak, thus resulting in a smaller lumped matrix diffusion parameter for these pathways, and (3) there is undoubtedly some variability in porosity and matrix diffusion coefficients within a given lithology (the samples analyzed for porosity and matrix diffusion coefficients were taken from only a few discrete locations). Given these uncertainties, we do not consider it terribly surprising that the amount of matrix diffusion appeared to be greater in the shorter residence time pathways.

2.4.2 Lithium

We proceeded to fit the lithium data using the same mean residence times and Peclet numbers that offered the best simultaneous fit(s) to the PFBA and bromide data.

The lumped matrix diffusion mass transfer coefficient, $\frac{\phi}{b}\sqrt{D_m}$, for lithium was

assumed to be two-thirds that of bromide and twice that of PFBA, based on the ratios of the diffusion coefficients of these ions (Newman 1973). Fits were obtained by adjusting the fracture and matrix retardation coefficients in the flow system equation of Fig. 2-8, which assumes equilibrium, linear, and reversible sorption in homogeneous pathways. Sorption in fractures could be the result of the presence of mineral alteration phases (mineral coatings) with a high cation exchange capacity or the presence of crushed tuff within the fractures, or a combination of both. The retardation coefficient, R , is related to the linear distribution coefficient through the well-known expression,

$$R = 1 + \frac{\rho_B}{\phi} K_D \quad (2.1)$$

where ρ_B = bulk density, g/cm³,

ϕ = porosity,

K_D = linear distribution coefficient, cm³/g.

Note that the assumption of a linear sorption isotherm is contrary to the nonlinear Langmuir isotherm behavior observed in the lithium laboratory experiments described in Section 3.0. However, the asymptotic, low concentration behavior of a Langmuir isotherm is the same as a linear isotherm with K_D equal to $K_L S_{max}$, so we felt that assuming linear sorption behavior was a reasonable starting point. Also, the

relatively fast sorption kinetics observed in the laboratory column experiments and in earlier batch sorption tests (Fuentes et al. 1989) suggested that the assumption of equilibrium sorption should be valid for the tracer arrival times in the October test.

Our initial attempts to fit the first lithium peak (up to about 120 hr into the test) using the physical model parameters deduced from the PFBA and bromide fits were unsatisfactory. We found that assuming linear, equilibrium sorption in the matrix resulted in a peak that occurred later than the actual data with a tail that was much higher than the data. We also found we had to assume no sorption in fractures (i.e., $R_f = 1$) because any fracture sorption resulted in a peak that occurred much too late to match the data. Note that the absence of fracture sorption does not necessarily mean that lithium wasn't sorbing to fracture surfaces; it simply means that the fractures had very little surface area available for sorption (i.e., without crushed fill or sorptive coatings). Because of the relatively poor fits obtained assuming equilibrium, linear sorption behavior, we proceeded to fit the lithium data assuming (1) rate-limited, linear sorption, (2) equilibrium, nonlinear (Langmuir) sorption, and (3) rate-limited, nonlinear sorption with a rate constant equal to the slowest rate constant measured in the crushed-tuff column experiments described in Section 4.1. RELAP offers the option of using a transfer function expression for rate-limited, linear sorption in a dual-porosity system; and a numerical model, RETRAN, was used to simulate nonlinear sorptive transport through a dual-porosity system (Appendix A; Reimus and Dash, 1998).

Fig. 2-8 shows fits to the first lithium peak obtained for the cases mentioned above, including the equilibrium, linear case. Sorption parameters corresponding to the fits in Fig. 2-8 are given in Table 2-4. These parameters were calculated assuming that the flow pathways resulting in the first peak were in the central Bullfrog Tuff ($\rho_s = 2.34 \text{ g/cm}^3$ and $\phi = 0.1$). The K_D and S_{max} values would be ~3.5 times higher if it were assumed that the flow pathways were in the lower Bullfrog Tuff ($\rho_s = 1.90 \text{ g/cm}^3$ and $\phi = 0.29$). The best fit to the data was obtained assuming rate-limited, linear sorption in both the fractures and matrix, although Table 2-4 shows that the best-fitting rate constants were over an order of magnitude lower than those observed in the laboratory column experiments. The assumption of equilibrium nonlinear (Langmuir) sorption provided a better fit to the tail of the data than the equilibrium linear fit, but the peak was predicted to occur too early. The assumption of rate-limited nonlinear (Langmuir) sorption using rate constants from the crushed-tuff column experiments (Section 4.1) also resulted in improved fits to the tail of the data, but the peak was again predicted to occur early. Fig. 2-9 shows a comparison of the Langmuir isotherms derived from the laboratory data and from the field data assuming both equilibrium and rate-limited sorption. Note that the rate-limited field-derived isotherm is in quite good agreement with the laboratory isotherm.

It should be emphasized that the fits in Fig. 2-8 and Table 2-4 are not unique; reasonable fits can be obtained for any isotherm ranging from the equilibrium, field-derived Langmuir isotherm shown in Fig. 2-9 to a linear isotherm, provided that the sorption rate constants are allowed to vary (slower rate constants result in more linear isotherms). The rate-limited nonlinear fit shown in Fig. 2-8 (with corresponding isotherm in Fig. 2-9) was selected for presentation because it corresponds to the slowest laboratory-observed sorption rate. It should also be noted that the lithium injection concentration in all RETRAN (nonlinear) simulations was assumed to be 1200 mg/L (the concentration of the injectate), which resulted in the maximum possible effect of isotherm nonlinearity on the resulting fits. The nonlinear "fits" obtained using RETRAN are not true least-squares fits because RETRAN does not currently offer

automated minimization of sums of squares of differences. However, after conducting many RETRAN simulations, we were confident that the nonlinear fits in Fig. 2-8 were relatively close to best fits. We found that better nonlinear fits could be obtained by assuming shorter injection pulse durations and correspondingly longer injection delays (we assumed a 6-hr pulse after a 4-hr delay), but we chose to maintain consistency with the assumptions made for the linear cases.

We also considered cases in which physical and chemical heterogeneity were assumed in the pathway(s) that resulted in the first set of tracer peaks. Lithium sorption in both of these cases was assumed to be linear and fast (equilibrium). In each case, the first "pathway" was split into two "pathways" which had either different matrix diffusion mass transfer coefficients (physical heterogeneity) or different lithium sorption parameters (chemical heterogeneity). An important constraint in this pathway-splitting approach was that the PFBA and bromide responses from the two pathways were required to sum to the total observed PFBA and bromide responses in the first 80-100 hrs of the test.

In the physical heterogeneity case, the first pathway was assumed to have a matrix diffusion mass transfer coefficient that was half that in the second pathway. The rationale for this assumption was that higher velocity pathways should tend to have larger average apertures. This has been shown to be the case in numerical simulations of flow and transport in single fractures, where flow is often predicted to be highly channelized in large aperture regions (Moreno et al. 1988, Thompson 1991, Reimus 1995). The larger average apertures of high-velocity channels give these channels smaller matrix diffusion mass transfer coefficients because the aperture appears in the denominator of the lumped mass transfer coefficient. The larger mass transfer coefficient assumed in the second set of pathways was expected to suppress the tail of the first lithium peak relative to the nonsorbing tracers, which is consistent with the behavior observed in the tracer test. Table 2-5 shows the model parameters used to obtain a reasonable fit to the early lithium response assuming physical heterogeneity.

In the chemical heterogeneity case, the mass transfer coefficients in the two pathways were constrained to be identical (equal to the single-pathway fit(s) to the PFBA and bromide data). However, lithium sorption was adjusted such that the first pathway accounted for almost the entire early lithium response, while the second pathway had only a minor contribution to the lithium response. This approach, while admittedly somewhat arbitrary, can be justified by recognizing that fractures often differ significantly in their degree of mineral alteration and fracture fill material as well as in the properties of the surrounding matrix, all of which can significantly affect sorption. It is also logical to assume that the fastest flow pathways may be the most open and least sorptive because of less fill material and possibly less mineral alteration to provide favorable sorption sites for lithium. Table 2-6 shows the model parameters used to obtain the best fit to the early lithium response assuming chemical heterogeneity.

An extreme variation of both the physical and chemical heterogeneity cases involved assuming that there was a pathway that had no sorption or matrix diffusion at all. This pathway was assumed to account for all of the first lithium peak and approximately half of the first PFBA and bromide peaks. The remainder of the early PFBA and bromide responses was then accounted for by a second pathway in which a large amount of matrix diffusion (and sorption) was assumed. This case was analyzed to demonstrate that it is possible, however unlikely, to postulate that matrix diffusion is not necessarily occurring in all flow pathways in the system. One would have to

$Q=VA$

speculate the existence of a very large aperture fracture pathway in this case that behaved essentially as a "pipe" to transport a small fraction of the tracers without any matrix diffusion or sorption. The microsphere data argue against this hypothesis because the microspheres would be expected to move very efficiently through such an open pathway, and this was not the case. Also, one would expect such an open pathway to respond even more quickly and with more tracer mass than was observed. Nevertheless, this case illustrates that it is possible to deduce that a small amount of tracer mass could have moved through the system without being affected by matrix diffusion and sorption. Table 2-7 shows the model parameters used to obtain the best fit to the early lithium response for this case. ?

The lithium fitting exercise was completed by assuming that an additional "pathway" accounted for the late lithium response. This pathway was assumed to have the same physical characteristics (mean residence time, Peclet number, and matrix diffusion mass transfer coefficient) that were deduced from the simultaneous fits to the late PFBA and bromide responses. Lithium sorption parameters were the only parameters adjusted to fit the data. We found that the assumption of equilibrium, linear sorption was adequate to provide good fits to the late lithium response, so rate-limited and nonlinear fits were not attempted. Table 2-8 provides lithium sorption parameters that yielded good fits to the late lithium data for the various cases discussed above. Note that the parameters resulting in good fits are all very similar regardless of which assumptions were made to explain the first lithium peak. Fig. 2-10 shows examples of a composite fits to the entire lithium response in the reactive tracer test. The fits in this figure assume (1) linear, rate-limited sorption of lithium during the early portion of the test (see Tables 2-3, 2-4, and 2-8 for parameters), and (2) linear, equilibrium sorption of lithium throughout the test, but with chemical heterogeneity in the first pathway (resulting in two sub-pathways, 1A and 1B - see Tables 2-3, 2-6 and 2-8 for parameters). The fits obtained by all other modeling approaches discussed in this section were nearly as good as the ones shown in Fig. 2-10.

It should be pointed out that, other than for the early lithium response (which required assuming no sorption in fracture flow pathways in order to obtain a reasonable fit), it was possible to explain the majority of the overall lithium response using a relatively wide range of combinations of fracture and matrix retardation factors. At one extreme, relatively large fracture retardation factors could be used with relatively small matrix retardation factors to obtain reasonable fits. At the other extreme, reasonable fits could also be obtained by assuming no fracture retardation at all, but with relatively large matrix retardation factors. Table 2-9 shows selected combinations of fracture and matrix retardation factors in pathways 1b and 2 that offered good fits to the lithium data for the cases discussed above.

While the lithium-fitting exercise points out considerable ambiguity in the interpretation of the lithium data, one must not lose sight of the overall goal of the exercise, which was to determine if laboratory measurements of lithium sorption could be used to predict lithium transport in the field. The field test interval included portions of two major lithologies, the moderately-welded central Bullfrog Tuff and the poorly-welded lower Bullfrog Tuff. Based on laboratory sorption measurements (Section 3.0) and measurements of matrix porosities (Section 5.0), the matrix retardation factors of these two tuffs were predicted to be 12.5 for the central Bullfrog Tuff and 12.0 for the lower Bullfrog Tuff. These retardation factors were calculated using equation (2.1) and assuming that K_D was equal to the asymptotic slopes of the Langmuir isotherms at low lithium concentrations (i.e., $K_D = K_L S_{max}$, which was 0.43 ml/g for the

central Bullfrog Tuff and 1.65 ml/g for the lower Bullfrog Tuff). Note that the lower Bullfrog Tuff has a lower predicted retardation factor than the central Bullfrog Tuff even though it sorbed lithium more strongly in the batch sorption tests. This result can be attributed to the higher porosity of the lower Bullfrog Tuff; in equation (2.1) the retardation factor is inversely proportional to the porosity, and furthermore, the bulk density is related to porosity by

$$\rho_b = \rho_s(1 - \phi) \quad (2.2)$$

where, ρ_s = density of pure rock material, g/cm³.

Thus, a lower porosity rock will always have a higher predicted retardation factor than a higher porosity rock if the sorption characteristics of the two rocks are similar. In this case, the lower Bullfrog Tuff sorbs lithium about 3 times more strongly than the central Bullfrog Tuff, but the porosity of the lower Bullfrog Tuff is also nearly 3 times higher than the porosity of the central Bullfrog Tuff. Thus, the higher porosity of the lower Bullfrog Tuff offsets its higher sorption capacity, and the end result is that the two rocks are predicted to have almost the same matrix retardation factor.

However, this analysis ignores the fact that retardation factors in reality should be dependent on the ratio of rock surface area to solution volume rather than rock mass to solution volume (as assumed in equation 2.1). One can readily verify that the blind application of equation (2.1) to very low porosity rocks will result in completely unrealistic retardation factors. In fact, these retardation factors will approach infinity as the matrix porosity approaches zero. If the higher porosity of the lower Bullfrog Tuff relative to the central Bullfrog Tuff were the result of 3 times as many pores per unit volume of rock, but the pores had the same size distribution in each rock, then the surface area to volume ratios in the two rocks would be about the same. In this case, the lower Bullfrog Tuff would be expected to have a factor of 3 greater retardation factor than the central Bullfrog Tuff because of its factor of ~3 greater lithium K_D value. Although we have no data on pore size distributions in the tuffs, we believe that this postulated situation is probably closer to reality than the implicit assumption that there is a significantly higher surface area to solution volume ratio in lower porosity rocks.

In light of this discussion, we can conclude that the lithium sorption parameters in Tables 2-4 through 2-9 are in quite good agreement with the laboratory sorption parameters measured for the central and lower Bullfrog Tuffs (see Section 3.0, and Table 3-5). The field-derived lithium retardation factors are consistently greater than or nearly equal to the retardation factors that would have been predicted from the laboratory measurements. Only in the case of the very early lithium response is the field-derived retardation factor lower than the laboratory-derived factor, and even here the difference (42%) could be readily explained if lithium concentrations in the fractures were high enough that sorption nonlinearity was important (recall that we assumed the asymptotic K_D at the lowest concentrations [= $K_L S_{max}$], which will always yield lower predicted concentrations). However, we also showed that it is possible to conclude that a small amount of lithium (as much as 5%) could have moved through the system unretarded. The general observation that there was greater lithium retardation in the second set of pathways compared to the first set of pathways is consistent with our deduction that the second set of pathways was more likely to have been in the more strongly sorbing lower Bullfrog Tuff. Given the physical and chemical heterogeneity

that was undoubtedly present over the ~30-meter long and ~100-meter thick section of tuff that the field test was conducted in, these results are very encouraging, and they lend validity to the practice of using laboratory-derived sorption data to predict field-scale transport of sorbing solutes. If anything, the use of the laboratory-derived lithium sorption parameters would have resulted in conservatively high predictions of total lithium transport through the field system. We conclude that predictions of sorbing solute transport through the saturated zone using laboratory-derived matrix sorption parameters should be conservative, especially if no sorption in fractures is assumed.

2.5 Interpretation of Microsphere Response

As with the solutes, the microsphere response in the multiple tracer test was interpreted using the RELAP code to fit the two peaks. We assumed that the mass fractions, mean residence times, and Peclet numbers of the two "pathways" that accounted for the nonsorbing solute responses (Sections 2.4.1) also applied to the spheres. However, the lumped matrix diffusion parameter was set equal to zero (i.e., no matrix diffusion) because of the large size and small diffusivity of the microspheres relative to the solutes. The only adjustable parameters in the analysis were a forward first-order filtration rate constant and a first-order reverse filtration rate constant (also called a resuspension or detachment rate constant).

The differential equations used to describe microsphere transport in the fractures were:

$$\frac{\partial C}{\partial t} + V \frac{\partial C}{\partial x} - D \frac{\partial^2 C}{\partial x^2} + k_{\text{fil}} C - k_{\text{res}} S = 0 \quad (2.3)$$

$$\frac{1}{b} \frac{\partial S}{\partial t} - k_{\text{fil}} C + k_{\text{res}} S = 0 \quad (2.4)$$

where, C = colloid concentration in solution, no./L
 S = colloid concentration on surfaces, no./cm²
 V = flow velocity in fractures, cm/sec
 D = dispersion coefficient, cm²/sec
 k_{fil} = filtration rate constant (1/sec) = λV, where λ = filtration coefficient (1/cm)
 k_{res} = resuspension rate constant, 1/cm-sec
 x, t = independent variables for distance and time, respectively.

Note that these equations are equivalent to equations (A1) and (A2) in Appendix A with $\left(\frac{\rho_f}{\eta}\right) = b^{-1}$, α_f , and $\beta_f = 1$, and $\phi = 0$. Thus, the RELAP semi-analytical model is capable of representing the simple colloid transport model given by equations (2.3) and (2.4).

We initially tried to fit the early microsphere response (the first peak) by assuming only irreversible filtration with no resuspension/detachment. We found that while this approach was capable of fitting the timing and normalized concentration of the first microsphere peak, it resulted in a much shorter tail than the data indicated. Therefore, to account for the tail, a small fraction of the filtered microspheres was assumed to detach. A fit to the tail was obtained by adjusting both the fraction of

spheres detaching and the detachment rate constant (while keeping the forward filtration rate constant the same as in the fit to the peak).

A fit to the second microsphere peak was obtained in the same manner. However, in this case, we found that the forward filtration rate constant had to be adjusted large enough so that essentially all of the microspheres were filtered as they moved through the system. This was necessary because any microspheres moving through the system without being filtered were predicted to arrive too early to match the observed response (note that the second microsphere peak occurred after the second nonsorbing solute peaks; see Fig. 2-2). Unfiltered spheres moving through the second set of pathways were predicted to arrive at about the same time as the low point in concentration between the two peaks.

Therefore, to account for the second microsphere peak, it was necessary to assume that a substantial fraction of the spheres in the second set of pathways were reversibly filtered. Unlike the first peak, however, we found that it was not possible to fit the entire second peak using a single detachment rate constant. The peak itself was fit by assuming a fraction of the microspheres experienced one detachment rate, and the tail was fit by assuming a separate fraction experienced another detachment rate. The remaining microspheres were assumed to not detach at all. The forward rate constant associated with each of these mass fractions was set equal to the minimum rate constant necessary to ensure that nearly all of the microspheres were filtered before making it through the system.

The resulting fit(s) to the microsphere data are illustrated in Fig. 2-11. The "pathways" labelled 1A and 1B represent the non-detaching and detaching fractions, respectively, of the microspheres following the pathway(s) that resulted in the first solute peak. Pathways 2A, 2B, and 2C in Fig. 2-11 represent the nondetaching and the two detaching fractions of the microspheres following the pathway(s) that resulted in the second solute peak. The fitted mass fractions and filtration parameters associated with the "subpathways" in Fig. 2-11 are given in Table 2-10.

Note that the predicted first arrival of microspheres precedes their actual first arrival by 2 to 3 hrs. This result can be attributed to the fact that we did not assume a 4-hr delay in the injection of microspheres into the pathways that resulted in the first tracer peaks (as we did for the solutes). We assumed no delay for the microspheres because the microsphere injection began about 3.5 hrs after the solutes were injected. We reasoned that if the solutes did not begin entering the pathways resulting in the first tracer peaks until after the microspheres were injected, then it was reasonable to assume that the microspheres should have entered those pathways at the same time as the solutes. However, if the microspheres experienced a delay similar to the solutes, then their predicted first arrival would actually be slightly later than the observed first arrival. In fact, in this case, the first arrival would coincide almost exactly with the first arrival of solutes. Thus, the uncertainty associated with when the microspheres actually began entering the flow system causes considerable uncertainty in the predicted first arrival of the microspheres.

It should be pointed out that the interpretation of the microsphere response presented in the preceding paragraphs is by no means unique. First, it is quite likely that there exists a continuous distribution of filtration and detachment rate constants rather than a few discrete ones, as assumed in the above analysis. Such a distribution could arise from a distribution of colloid surface properties and/or physical and chemical heterogeneities in fracture surfaces. It is also possible that colloid filtration and detachment are not linear first-order processes as assumed in equations (2.3) and

(2.4). Rather, they might be better described as nonlinear and/or stochastic processes (Dabros and Van de Ven, 1982, 1983). Finally, as mentioned above, the interpretation of the microsphere response relative to the solutes is complicated by the fact that the microsphere injection was started later than the solute injection. In addition to causing uncertainty in when the microspheres actually began moving into flow pathways, the differences in injection times may have resulted in the microspheres not being distributed into flow pathways in exactly the same proportion as the solutes (i.e., a different source term). If different assumptions were made about the distribution of spheres between the two major sets of pathways, different filtration parameters would be obtained.

Although these uncertainties exist, we believe that the interpretation of the microsphere response presented in Fig. 2-11 and Table 2-10 is one of the simplest that is consistent with the data. Even if the quantitative aspects of the interpretation are not entirely correct, it is difficult to refute the qualitative conclusions that (1) the microspheres were significantly attenuated relative to the solutes and (2) the microsphere response (specifically the long tailing behavior) can only be explained by assuming that at least a portion of the spheres were reversibly filtered. The latter conclusion implies that colloid detachment, or perhaps some other process that behaves like detachment, is important in predicting microsphere transport through saturated, fractured tuffs near Yucca Mountain.

2.6 Uncertainties in Test Interpretations

There are several sources of uncertainty associated with the tracer tests and their interpretation. First, there are data uncertainties, which are related to the accuracy and precision of the tracer chemical analyses, including both random and systematic errors. We believe that random errors were small because the breakthrough curve data are not widely scattered and show well-defined trends. The most significant sources of systematic errors would have been day-to-day differences in analytical instrument operation and in analytical standard preparation. However, careful checks with control samples and cross-checking with another analytical laboratory (University of Nevada at Las Vegas, unpublished data) indicated that systematic errors were minimal. Incomplete knowledge of the residual concentration of PFBA in the October test due to the May PFBA injection is an additional source of uncertainty in the October PFBA data (see Section 2.3), but this uncertainty can be bounded and shown to have minimal impact on the interpretative analysis.

Uncertainties in the model parameter estimates are related to uncertainties in the data, discussed above, and uncertainties in the uniqueness of the curve fits. Parameter uncertainty due to data scatter can generally be quantified by statistical measures such as "95% confidence intervals" (Draper and Smith, 1981). For a given set of modeling assumptions, we expect this uncertainty to be relatively small given the smoothness of the breakthrough curve data, but we have left its quantification for future work. It is clear that uniqueness-of-fit uncertainties are lower when several tracer responses are analyzed simultaneously than when only a single response is analyzed (Table 2-2) because more constraints are placed on the interpretation. However, a detailed analysis of this uncertainty is also reserved for future work.

We believe that the most important source of uncertainty in the tracer test interpretation is associated with the modeling assumptions made in the curve-fitting procedure. These uncertainties include: (1) not knowing whether the flow field was

linear or radial, (2) not knowing the exact duration and timing of the tracer injection that resulted in the first tracer peak, and (3) the possibility that the wellbore source functions could have been significantly different than an exponential decay with a time constant approximately equal to the borehole volume divided by the injection flow rate. The effects of uncertainties (1) and (2) were addressed in Section 2.5. The effect of radial vs. linear flow is reflected in Tables 2-3 and 2-5 through 2-7, and the effect of varying the tracer injection duration was found to have only a minor effect on the first peak response and virtually no effect on the second peak response.

The source term uncertainty was investigated by varying the exponential decay time constant by about an order of magnitude, from 0.13 to 1 hr⁻¹. For perspective, the value corresponding to the injection borehole volume divided by the injection rate was ~0.26 hr⁻¹. Interestingly enough, both the mean residence times and Peclet numbers decreased as the time constant was decreased (i.e., a slower exponential decay). This result suggested that the model was trying to compensate for a slow release from the injection wellbore by speeding up the movement of tracer through the formation and increasing the amount of mass arriving early as a result of dispersion. Because the fits tended to be better with faster decay constants, we used a decay constant of 1 hr⁻¹ to obtain all of the parameter estimates in Tables 2-3 through 2-10. It should be noted that the value of the decay constant (within the range stated above) had virtually no effect on the interpretation of the latter portion of the breakthrough curves.

2.7 Discussion

We now consider the implications of the test interpretations associated with these fits. First, it is apparent that regardless of which uncertainties or alternative test interpretations are considered for the solutes (particularly for lithium), it must be concluded that matrix diffusion and sorption are occurring in most, if not all, flow pathways. Second, the lithium sorption parameters deduced from the interpretative fits are in reasonably good agreement with the laboratory sorption data. The agreement between field and laboratory data is especially encouraging given all of the chemical and physical heterogeneity present in the field and the lack thereof in the interpretive models and the laboratory experiments. Furthermore, a comparison of the laboratory- and field-derived sorption parameters suggests that the use of the laboratory data to predict field-scale lithium transport will tend to slightly overestimate field transport rates over long distances and times. (See Section 2.4.2 for additional discussion of the implications of the lithium response). We conclude that a dual-porosity conceptualization of the saturated zone near Yucca Mountain is valid, and that the reasonable agreement between field and laboratory lithium sorption parameters lends validity to the practice of using laboratory-derived sorption data to predict field-scale transport behavior. However, this latter conclusion should be applied cautiously to sorbing radionuclides, for which there are no field data in the immediate vicinity of Yucca Mountain.

The microsphere response compared to the solutes indicates that while the majority of the spheres were irreversibly attenuated in the system (filtered or deposited), a significant fraction of them moved through the system quite efficiently (some without any apparent filtration). The response also indicates that a significant fraction of the spheres arriving at the production well experienced both filtration and resuspension/detachment, suggesting that not all filtration is irreversible. The implication is that a nontrivial fraction of groundwater colloids can be expected to

travel significant distances over significant times in the saturated zone at rates comparable to or exceeding those of nonsorbing solutes.

Table 2-11 provides ranges of physical parameter values derived from the field test interpretations. These ranges are intended to provide performance assessment modelers with lower and upper bounds for use in large-scale, abstracted transport models, although it must be recognized that the values apply strictly to only the central and lower Bullfrog Tuffs at the C-wells. Lithium sorption parameters are not included in Table 2-11 because they are not directly relevant to any radionuclides of importance to performance assessment. Although some of the parameter ranges in Table 2-11 seem large, the use of simultaneously-injected multiple tracers significantly reduced the range that would have been reported in a single tracer test.

The longitudinal dispersivity values in Table 2-11 were calculated using $\alpha = L/Pe$, where the travel distance, L , was assumed to take on minimum and maximum values of 30 and 100 m, corresponding to interborehole distance and the approximate distance between the bottom of one borehole and the top of the other (the maximum possible linear transport distance), respectively. The lower bound was calculated assuming a distance of 30 m and a Peclet number corresponding to the first set of pathways. The upper bound was calculated assuming a distance of 100 m and assuming a Peclet number corresponding to the second set of pathways. To put these dispersivities in perspective, Fig. 2-12 shows a box encompassing the entire range of calculated dispersivities superimposed on a plot of dispersivity vs. scale taken from Neuman (1990). It is apparent that the C-wells longitudinal dispersivity is reasonably consistent with other data sets and with existing theories on the scale dependence of dispersion.

The values in Table 2-11 for fracture apertures, fracture spacing, effective flow porosity, and effective fracture porosity are all very uncertain and should be used with caution. Fracture aperture values were calculated from the best-fitting lumped matrix diffusion parameters, $\frac{\phi}{b} \sqrt{D_m}$, assuming that the matrix diffusion coefficients and matrix porosities measured in diffusion cell experiments (see Section 5.0) applied in the field. The lower bound was calculated using the lumped parameter from the first set of pathways and assuming the matrix porosity and diffusion coefficients measured in the central Bullfrog Tuff. The upper bound was calculated using the lumped parameter from the second set of pathways and assuming the matrix porosity and diffusion coefficients measured in the lower Bullfrog Tuff. The lower bound for fracture spacing was based on fitting the extreme tail of the PFBA and bromide breakthrough curves where there is considerable scatter and uncertainty in the data. The upper bound is infinite because good fits to the early tracer data were obtained assuming an infinite matrix. Flow porosities were calculated using the following equation, which assumes homogeneous, isotropic, radial convergent flow of the entire production flow rate over the entire thickness of the test interval.

L - twice as large

$$\eta = \frac{Q\tau}{\pi R^2 L} \tag{2.5}$$

where, η = flow porosity
 Q = production rate (~34.1 m³/hr)
 τ = mean residence time, hr

R = distance between wells (~30 m)
L = formation thickness (~100 m).

Assuming radial convergent flow in a homogeneous, isotropic medium frequently results in high estimates of flow porosity when the medium is actually quite heterogeneous (unpublished results). Also, the upper bound flow porosity values are derived from the longest residence time pathways, which very likely received much less than 100% of the total production flow rate. The upper bound fracture porosity reported in Table 2-11 is distinguished from the upper bound flow porosity in that it is estimated by dividing the maximum fracture half-aperture (0.63 cm) by the half the minimum fracture spacing (4 cm). This upper bound is unrealistically high because it actually exceeds the highest matrix porosities measured in the laboratory. The lower bound for fracture porosity is zero because reasonable fits to the tracer data were obtained assuming an infinite matrix.

only talks abt upper-bound then why is it in table?

While we considered the tracer tests to be highly successful, we recognize that much work remains to be done. We tested only one formation at one location near Yucca Mountain, and it would not be prudent to base performance assessments of the entire saturated zone on such a limited data set. Thus, we plan to conduct additional tracer tests, possibly in other test configurations such as single-well injection-withdrawal mode, in other hydrogeologic formations, and at other locations near Yucca Mountain. Issues to be addressed in these tests include, but are not necessarily limited to, (1) the time- and distance-scale dependence of the processes of dispersion, matrix diffusion, and sorption, (2) the spatial variation of transport properties in the vicinity of Yucca Mountain, (3) the variation of transport properties in different stratigraphic zones and in different hydrogeologic settings (e.g., faulted vs. unfaulted rock, high conductivity vs. low conductivity rock, high matrix porosity vs. low matrix porosity rock, fractured rock vs. porous medium [e.g., alluvium]), (4) field sorption behavior in different rock types (e.g., mineralogically altered vs. unaltered, high in clays vs. low in clays, welded vs. unwelded, fractured vs. porous medium), and (5) the diameter, water chemistry, and geologic media dependence of microsphere/colloid transport in the saturated zone. We also plan to conduct additional laboratory experiments to (1) characterize the sorption of lithium and other potential reactive tracers onto other rocks likely to be encountered in the saturated zone near Yucca Mountain and (2) measure free-water diffusion coefficients of nonsorbing solutes so that quantitative estimates of tortuosity factors can be obtained from diffusion cell data.

We consider our modeling of the tracer tests to be a relatively simple approach to interpreting the data. This approach involves a minimum number of adjustable parameters, which is consistent with our limited knowledge of flow system geometry and heterogeneity. Although we believe that our conclusions are sound, we recognize that there is much room for revisiting the analyses using more sophisticated modeling tools and introducing more system complexity, particularly as more site-specific information becomes available. In the future, we plan to incorporate this information into numerical models that can better account for both physical and chemical heterogeneity in two- and three-dimensions. We also plan to examine other semi-analytical modeling approaches, such as the multi-rate diffusion model of Haggerty and Gorelick (1995), which has been used to interpret tracer tests conducted in a fractured dolomite near Carlsbad, NM for the Waste Isolation Pilot Plant project (Meigs et al., 1998). The fact that the matrix diffusion mass transfer coefficients in our analyses decreased as pathway residence times increased (Table 2-3) and that a finite fracture

they may have listened at Appendix 7.



spacing offered a better fit to the end of the conservative tracer breakthrough curves suggests that multiple diffusion rates and/or finite fracture spacings may be important at long time scales in the groundwater system. It might also suggest that interconnected porosity, and hence diffusion coefficients in the matrix, decrease with distance into the matrix (away from fractures). It is also possible that some of the apparent matrix diffusion in the field experiments was actually diffusion into stagnant water along the rough fracture walls or within the fractures themselves (occurring as a result of tracers diffusing out of high flow rate channels and into low flow zones), rather than into the matrix proper. These possibilities have important implications for saturated zone performance assessments and merit further study because, if valid, they would suggest that matrix diffusion might be overestimated in short-duration tracer experiments.

Section 2.0 References

Becker, M. W. and Charbeneau, R. J., A first passage time solution for radially convergent tracer tests, submitted to *Water Resour. Res.*, 1996.

Becker, M. W., Reimus, P. W., and Vilks, P., Microspheres detected by flow cytometry and their application as groundwater tracers in fractured rock, submitted to *Groundwater*, 1998.

Bird, R. B., Stewart, W. E., and Lightfoot, E. N., *Transport Phenomena*, John Wiley and Sons, New York, 1960.

Churchill, R. V., *Operational Mathematics*, 2nd ed. McGraw-Hill, New York, 1958.

Dabros, T. and Van de Ven, T. G. M., Kinetics of coating by colloidal particles, *J. Colloid Interface Sci.*, 89(1), 232-244, 1982.

Dabros, T. and Van de Ven, T. G. M., On the effects of blocking and detachment on coating kinetics, *J. Colloid Interface Sci.*, 93(2), 576-579, 1983.

Draper, N. R. and Smith, H., *Applied Regression Analysis*, 2nd ed. John Wiley and Sons, New York, 1981.

Fuentes, H. R., Polzer, W. L., Essington, E. H. and Newman, B. D., Characterization of reactive tracers for C-wells field experiment I: Electrostatic sorption mechanism, lithium. *Los Alamos National Laboratory Report LA-11691-MS*, Los Alamos, NM, 1989.

Geldon, A. L., Preliminary hydrogeologic assessment of boreholes UE-25c#1, UE-25c#2, and UE-25c#3, Yucca Mountain, Nye County, Nevada, *Water-Resources Investigations Report 92-4016*, United States Geological Survey, Denver, CO, 1993.

Geldon, A. L., Results and interpretation of preliminary aquifer tests in boreholes UE-25c#1, UE-25c#2, and UE-25c#3, Yucca Mountain, Nye County, Nevada, *Water-*

Resources Investigations Report 94-W-0412, United States Geological Survey, Denver, CO, 1996.

Haggerty, R. and Gorelick, S. M., Multiple-rate mass transfer for modeling diffusion and surface reactions in a media with pore-scale heterogeneity, *Water Resour. Res.*, 31(10), 2383-2400, 1995.

Maloszewski, P. and Zuber, A., Interpretation of artificial and environmental tracers in fissured rocks with a porous matrix, in *Isotope Hydrology*, International Atomic Energy Agency (IAEA), Vienna, Austria, pp. 635-651, 1983.

Maloszewski, P. and Zuber, A., On the theory of tracer experiments in fissured rocks with a porous matrix, *J. Hydrology*, 79, 333-358, 1985.

Maloszewski, P. and Zuber, A., Influence of matrix diffusion and exchange reactions on radiocarbon ages in fissured carbonate aquifers, *Water Resour. Res.*, 27(8), 1937-1945, 1991.

Meigs, L. C., Beuheim, R. L., McCord, J. T., Tsang, Y. W., and Haggerty, R., Design, modelling, and current interpretations of the H-19 and H-11 tracer tests at the WIPP Site, in *Field Tracer Transport Experiments*, proceedings of the first GEOTRAP Workshop, Cologne, Germany, August 28-30, 1996 (1998).

Moench, A. F., Convergent radial dispersion in a double-porosity aquifer with fracture skin: Analytical solution and application to a field experiment in fractured chalk, *Water Resour. Res.*, 31(8), 1823-1835, 1995.

National Research Council, *Rock Fractures and Fluid Flow: Contemporary Understanding and Applications*, National Academy Press, Washington, D.C., 1996.

Neuman, S. P., Universal scaling of hydraulic conductivities and dispersivities in geologic media, *Water Resour. Res.*, 26(8), 1749-1758, 1990.

Newman, J. S., *Electrochemical Systems*, Prentice-Hall, Englewood Cliffs, NJ, 1973.

Reimus, P. W. and Dash, Z. V., Models and methods summary for the reactive transport application, *Yucca Mountain Site Characterization Project Milestone Report SP32E1M4*, Los Alamos National Laboratory, Los Alamos, NM, 1997.

Reimus, P. W., The use of synthetic colloids in tracer transport experiments in saturated rock fractures, *Los Alamos National Laboratory Report LA-13004-T (also PhD Dissertation, University of New Mexico)*, Los Alamos National Laboratory, Los Alamos, NM, 1995.

Reimus P. W. and Turin, H. J., Draft report of results of hydraulic and tracer tests at the C-holes complex, *Yucca Mountain Site Characterization Project Milestone Report SP32APMD*, Los Alamos National Laboratory, Los Alamos, NM, 1997.

Reimus, P. W. and Turin, H. J., Results of reactive tracer testing at the C-holes, *Yucca Mountain Site Characterization Project Milestone Report 4270M*, Los Alamos National Laboratory, Los Alamos, NM, 1996.

Robinson, B. A., A strategy for validating a conceptual model for radionuclide migration in the saturated zone beneath Yucca Mountain, *Rad. Waste Mgmt. & Env. Restor.*, 19, 73-96, 1994

Steinkamp, J. A., Habbersett, R. C., and Hiebert, R. D., Improved multilaser/multiparameter flow cytometer for analysis and sorting of cells and particles, *Rev. Sci. Instrum.*, 62(11), 2751-2764, 1991.

Tang, D. H., Frind, E. O., and Sudicky, E. A., Contaminant transport in a fractured porous media: Analytical solution for a single fracture, *Water Resour. Res.*, 17(3), 555-564, 1981.

Thompson, M. E., Numerical Simulation of Solute Transport in Rough Fractures, *J. Geophys. Res.*, 96(B3), 4157-4166, 1991.

USGS (United States Geological Survey), Postings at the C-wells of packer placements in c#1, c#2, and c#3 (records maintained in USGS files), May, 1996.

Wan, J. and Wilson, J. L., Colloid transport in unsaturated porous media, *Water Resour. Res.*, 30(4), 857-864, 1994.

Section 2.0 Tables

Table 2-1. Summary of quantitative interpretation procedure for reactive tracer test.

1. Find the values of τ , Pe , ϕ/b , and f (with R_m and R_r equal to 1) that provide the best simultaneous fit to the first PFBA and bromide peaks.
2. Subtract the fits obtained in step 1 from the PFBA and bromide data sets, and repeat step 1 to fit the resulting second peaks (i.e, second set of pathways).
3. Fit the lithium data sequentially as in steps 1 and 2 by adjusting R_m and R_r while using the values of τ , Pe , ϕ/b , and f that gave best fits to PFBA and bromide data.
4. If step 3 results in poor fit(s) to the lithium data for any given peak, attempt to obtain a better fit by allowing rate-limited and/or nonlinear sorption or by assuming multiple pathways that have different physical or chemical characteristics.

Table 2-2. Parameter values resulting in best fits to the May 1996 PFBA data as a function of assumed matrix diffusion mass transfer coefficient, $\frac{\phi}{b}\sqrt{D_m}$.

$\frac{\phi}{b}\sqrt{D_m}, \text{sec}^{-1/2}$	τ, hr	Pe	Dispersivity, m^*	f
0.00346	150	29	1.1	0.99
0.00173	220	16	1.9	0.8
0.000866	310	9	3.4	0.72
0.000346	410	6	5.2	0.65
0 (single-porosity)	470	5	6.2	0.55

*Assumes a 30-m travel distance (borehole separation).

Table 2-3. Parameters obtained from fits to the PFBA and bromide responses in the reactive tracer test (R_r and $R_m = 1$).

Parameter	Pathway 1	Pathway 2
f , fraction mass	0.12	0.59
τ , linear flow, hr	37	995
Pe , linear flow	6.0	1.7
τ , radial flow, hr	31	640
Pe , radial flow	9.0	3.0
Bromide $\frac{\phi}{b}\sqrt{D_m}, \text{sec}^{-1/2}$	0.00158	0.000458
fracture spacing, cm	∞	4

Note: $\frac{\phi}{b}\sqrt{D_m}$ for PFBA is 0.577 times that for bromide.

Table 2-4. Sorption parameters derived from fits to the first lithium peak (Fig. 2-10) assuming that the flow pathways resulting in this peak were in the central Bullfrog Tuff. Other parameters used to obtain the fits were the same as for Pathway 1 in

Table 2-3 (with $\frac{\phi}{b}\sqrt{D_m}$ equal to two-thirds that for bromide). Laboratory Langmuir isotherm parameters for the central Bullfrog Tuff were $K_L = 0.014$ ml/g and $S_{max} = 31.4$ μ g/g (see Section 3.0). The laboratory forward sorption rate constant ranged from 2.2 to 18 hr⁻¹ (see Section 4.1).

Parameter	Linear, Equilibrium	Linear, Kinetic	Langmuir, Equilibrium	Langmuir, Kinetic
R_f	1 (no sorption)	1.3	1 (no sorption)	(see footnote 5)
R_m	7	30	-	-
$k_f^{(1)}$, hr ⁻¹	∞	0.14	∞	2.2
$k_m^{(2)}$, hr ⁻¹	∞	0.16	∞	2.2
$K_D^{(3)}$, ml/g	0.256	1.24	-	-
$K_L^{(4)}$, ml/ μ g	-	-	0.1	0.025
$S_{max}^{(4)}$, μ g/g	-	-	21	35.2

⁽¹⁾ Forward rate constant in fractures.

⁽²⁾ Forward rate constant in matrix.

⁽³⁾ Matrix value, calculated from equation (2) using fitted R_m and assuming $\rho_B = 2.34$ g/cm³ and $\phi = 0.1$ (laboratory values for central Bullfrog Tuff). K_D would be ~3.5 times larger if transport were assumed to be in the lower Bullfrog Tuff. K_D not calculated for fractures because of ambiguity in defining ρ_B and ϕ in fractures.

⁽⁴⁾ Matrix value, obtained from RETRAN assuming $\rho_B = 2.34$ g/cm³ and $\phi = 0.1$. K_L would be ~3.5 times larger if transport were assumed to be in the lower Bullfrog Tuff.

⁽⁵⁾ Sorption in fractures was assumed to be Langmuirian with same K_L as for matrix but with $S_{max} = 125$ μ g/g (to simulate slightly greater sorption capacity to fracture surfaces) and $\rho_B/\phi = 0.1$ (to simulate a lower surface area to volume ratio in fractures). These assumed values result in an R_f approximately equal to 1.3, which is the R_f value obtained for the linear, kinetic fit. RETRAN simulations were not very sensitive to fracture sorption parameters.

Table 2-5. Transport parameters resulting in a good fit to the early lithium response assuming two separate "pathways" that have different matrix diffusion mass transfer coefficients (physical heterogeneity) but nearly identical lithium sorption parameters.

Parameter	Pathway 1A	Pathway 1B
f, fraction mass	0.04	0.07
τ , linear flow, hr	22	41
Pe, linear flow	16	18
τ , radial flow, hr	20	38
Pe, radial flow	21	24
Bromide $\frac{\phi}{b} \sqrt{D_m}$, sec ^{-1/2}	0.00079	0.00158
Rf for lithium	1	1
Rm for lithium	13	18

Table 2-6. Transport parameters resulting in a good fit to the early lithium response assuming two separate "pathways" that have the same matrix diffusion mass transfer coefficients but different lithium sorption parameters (chemical heterogeneity).

Parameter	Pathway 1A	Pathway 1B
f, fraction mass	0.075	0.037
τ , linear flow, hr	27	46
Pe, linear flow	11	19
τ , radial flow, hr	24	43
Pe, radial flow	15	25
Bromide $\frac{\phi}{b} \sqrt{D_m}$, sec ^{-1/2}	0.00158	0.00158
Rf for lithium	1	5
Rm for lithium	6	40

Table 2-7. Transport parameters resulting in a good fit to the early lithium response assuming two separate "pathways", one of which has no matrix diffusion or sorption and the other of which has only matrix sorption.

Parameter	Pathway 1A	Pathway 1B
f, fraction mass	0.049	0.065
τ , linear flow, hr	42	30
Pe, linear flow	6	7
τ , radial flow, hr	35	25
Pe, radial flow	8.5	10
Bromide $\frac{\phi}{b} \sqrt{D_m}$, sec ^{-1/2}	-0-	0.00354
Rf for lithium	1	1
Rm for lithium	1	80

Table 2-8. Transport parameters resulting in good fits to the second lithium peak for the various cases presented in Tables 2-4 through 2-7 (see text also). Other parameters used to obtain the fits were the same as for Pathway 2 in Table 2-3 (with $\frac{\phi}{b} \sqrt{D_m}$ for lithium equal to two-thirds that for bromide).

Case	R _f	R _m
Rate-limited (see Table 4)	4	26
Physical heterogeneity (see Table 5)	5.5	16
Chemical heterogeneity (see Table 6)	5.5	16
No matrix diffusion or matrix sorption (Table 7)	5.5	20

Table 2-9. Combinations of fracture and matrix retardation coefficients resulting in good fits to the late lithium response. Other parameters used to obtain the fits are given in Tables 5-8 for Pathway 1B and Table 2-3 for Pathway 2 (with $\frac{\phi}{b}\sqrt{D_m}$ for lithium equal to two-thirds that for bromide in each case).

Case	Pathway 1B	Pathway 2
	R_f, R_m	R_f, R_m
Rate-limited (see Table 2-4)	N/A	1, 78 4, 26
Physical heterogeneity (see Table 2-5)	1, 18	1, 120 5.5, 16
Chemical heterogeneity (see Table 2-6)	1, 100	1, 120
	3, 70	5.5, 16
	5, 40	
No matrix diffusion or matrix sorption (Table 2-7)	1, 80	1, 130
	4, 60	5.5, 20
	7, 40	

Table 2-10. Microsphere filtration and resuspension parameters associated with the fit shown in Fig. 2-11. Other transport parameters used to obtain the fits are given in Table 2-3. Note that subpathways 1A and 1B represent a mass fraction split of Pathway 1 from Table 3, and subpathways 2A, 2B, and 2C represent a mass fraction split of Pathway 2 from Table 2-3.

Parameter	Path 1A	Path 1B	Path 2A	Path 2B	Path 2C
f, mass fraction	0.115	0.005	0.423	0.067	0.1
k_{fit} , 1/hr	0.2	0.2	0.04	0.04	0.04
$\lambda^{(1)}$, 1/cm	0.00247	0.00247	0.0133	0.0133	0.0133
k_{res} , 1/cm-hr	0	3.33	0	0.4	0.008

⁽¹⁾ λ calculated as k_{fit}/V , where V = average linear velocity determined from mean fluid residence time.

Table 2-11. Ranges of physical parameters derived from the interpretation(s) of the reactive tracer test. See text for assumptions and discussions of how lower and upper bounds were calculated.

Parameter	lower bound	upper bound
longitudinal dispersivity, m	3.3	59
b, cm	0.042	0.63
effective fracture spacing, cm	4	∞
effective flow porosity	0.0037	0.12
effective fracture porosity	-0-	0.32

very uncertain & should be used w/ caution:

*

all support by report

→ approaching matrix porosity.

Section 2.0 Figures

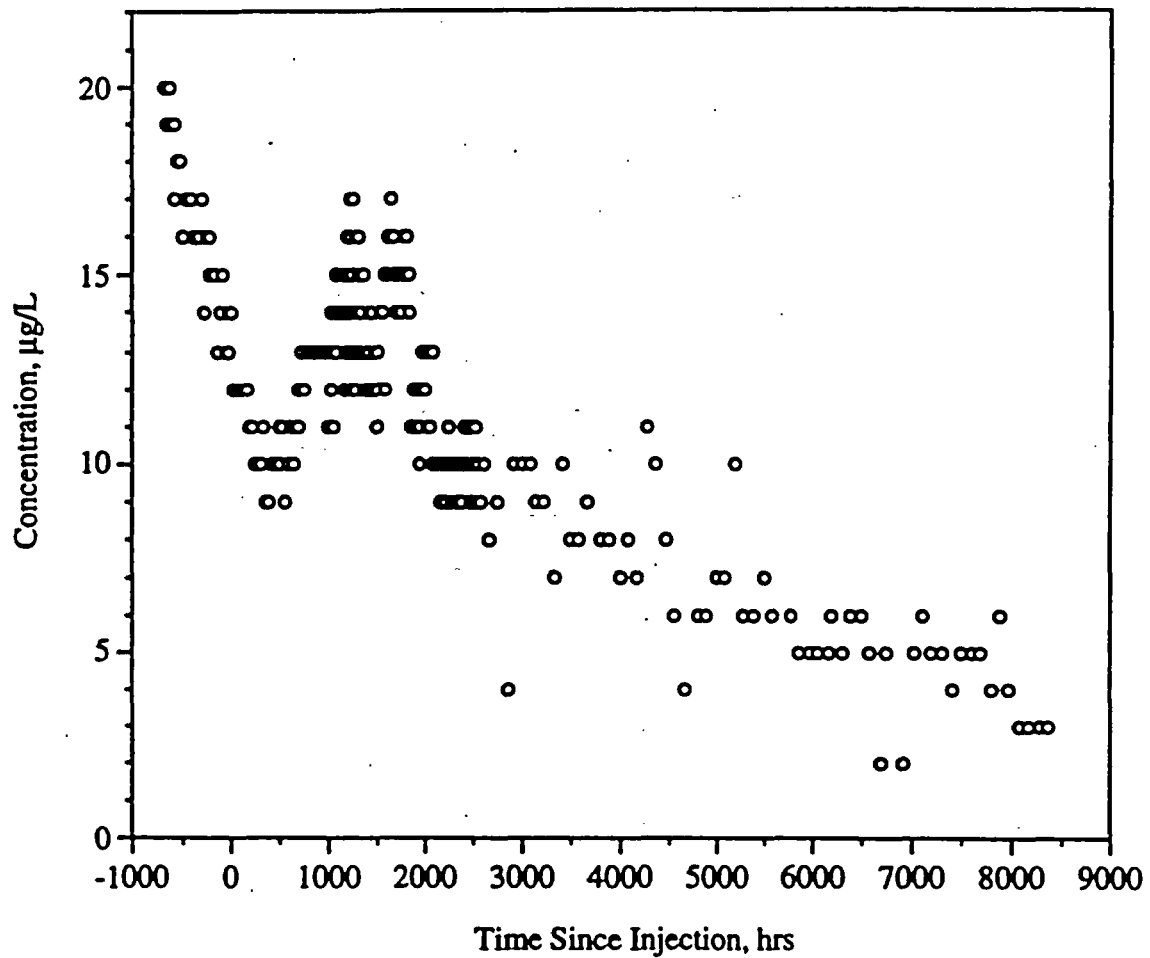


Figure 2-1. Breakthrough curve of iodide resulting from injection of ~12.7 kg of iodide into c#1 on June 18, 1996. Declining background prior to and immediately after injection is due to recovery of iodide from a February 1996 iodide injection into c#2. Estimated recovery from c#1 accounting for c#2 background was between 6 and 10% through June 1, 1997.

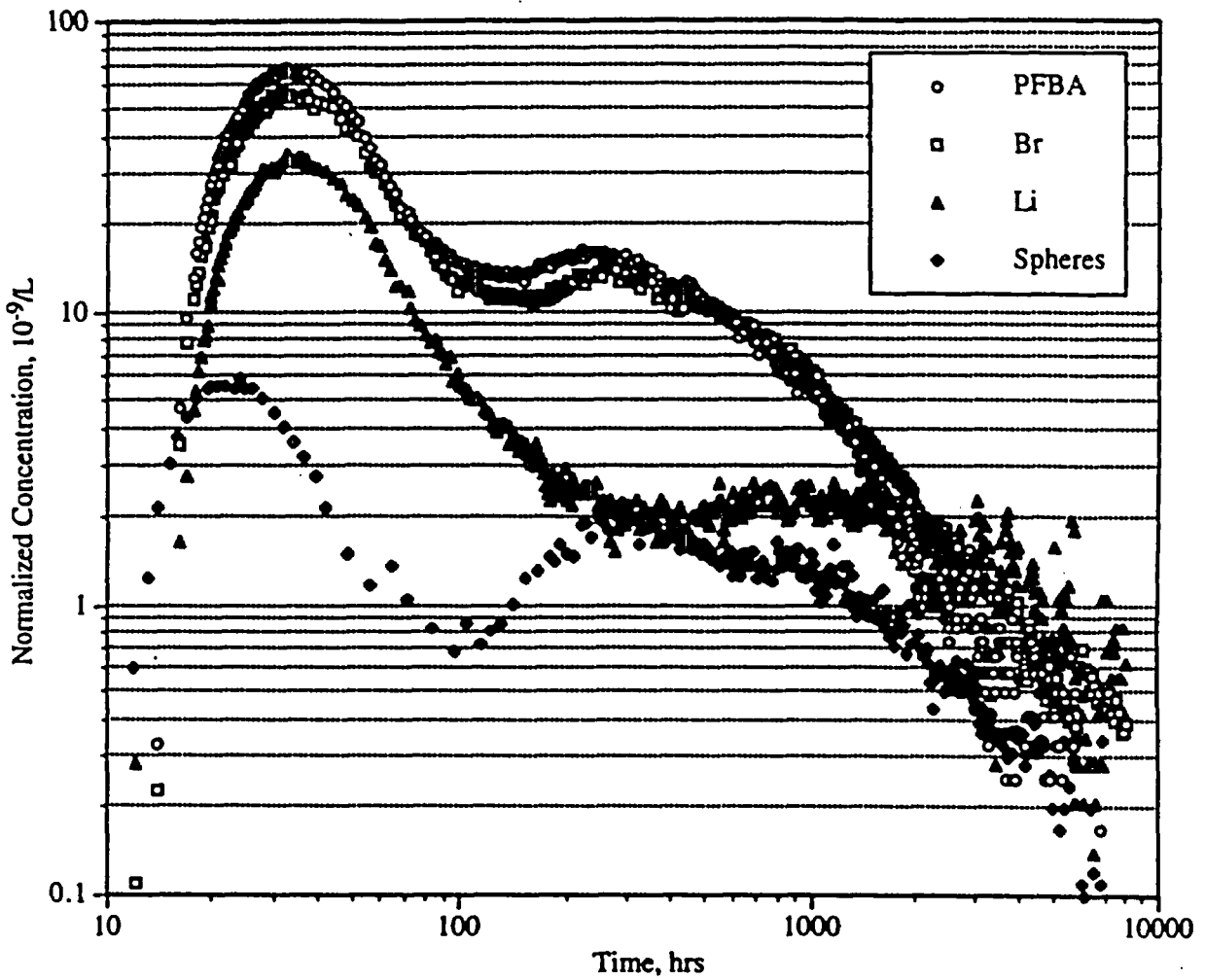


Figure 2-2. Normalized tracer breakthrough curves from the reactive tracer test conducted in the lower Bullfrog Tuff between wells c#2 and c#3. Tracer recoveries were ~69% for PFBA, ~69% for bromide, ~39% for lithium, and ~15% for microspheres.

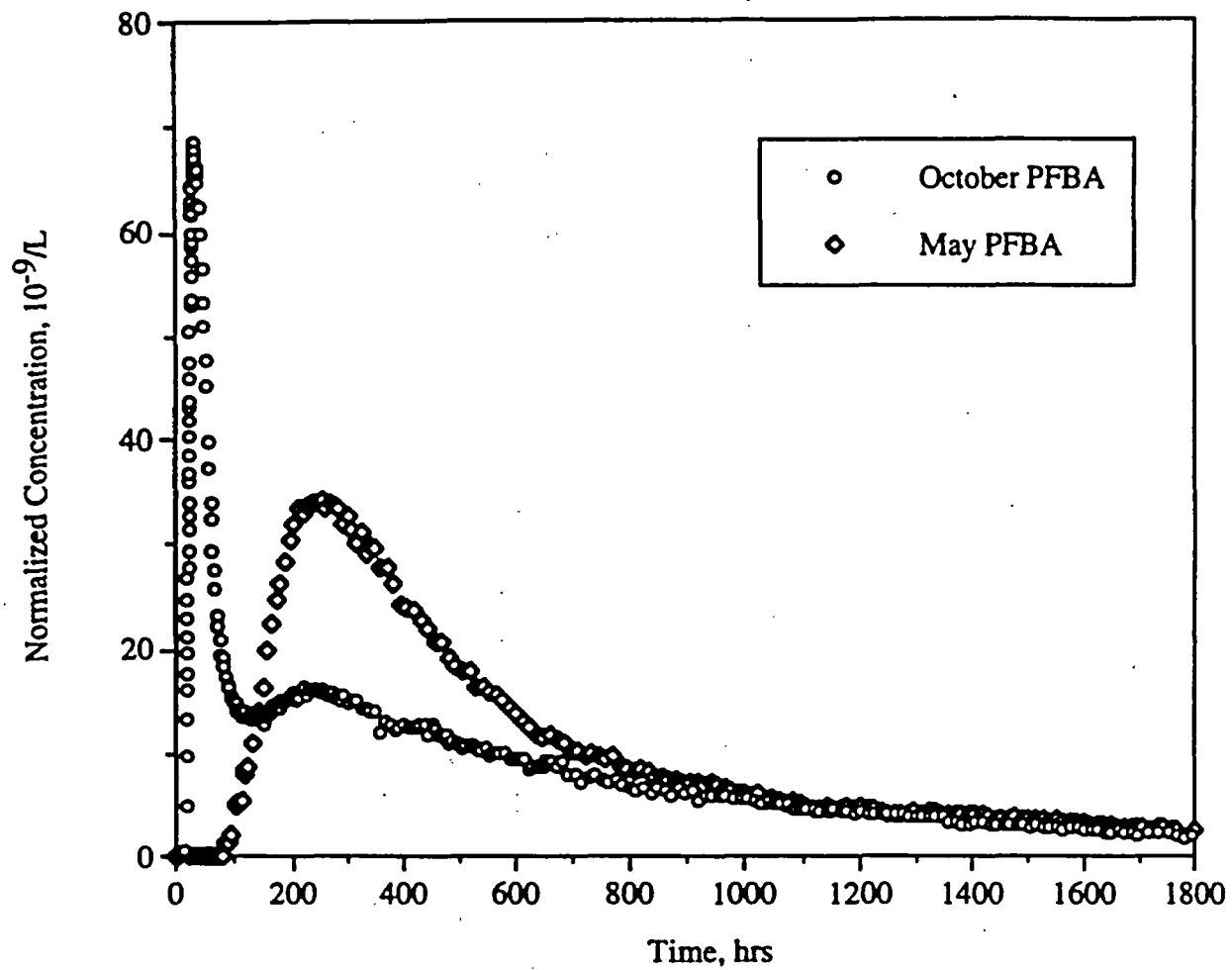
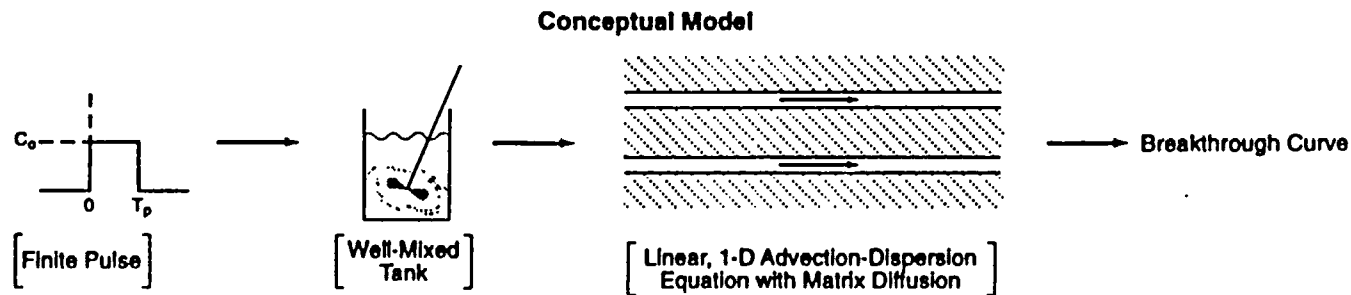
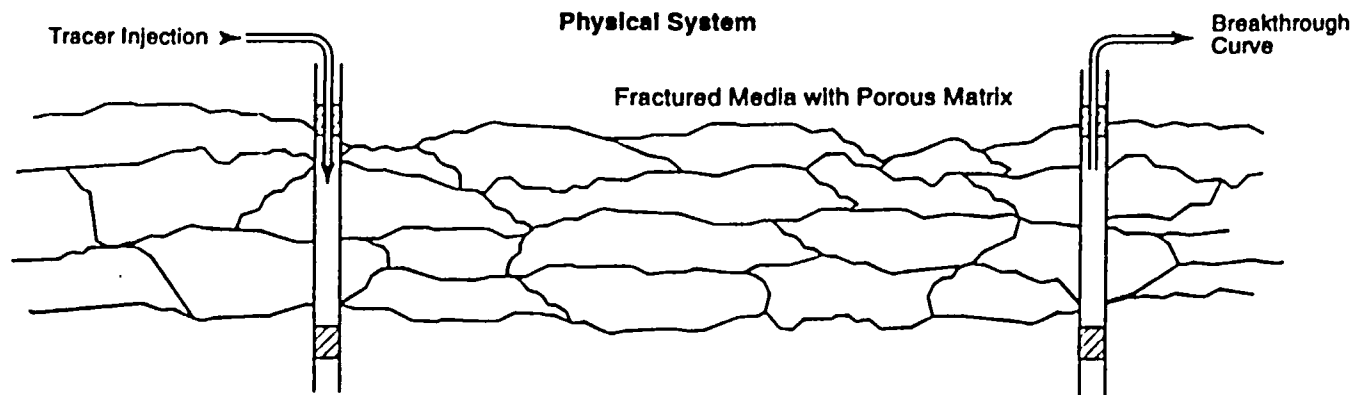


Figure 2-3. Normalized breakthrough curves of PFBA at C#3 (through 1800 hrs) from the October and May injections into c#2.



Laplace Transform Transfer Functions

$C_0 \left(\frac{1 - e^{-Ts}}{s} \right)$ <p>C_0 = injection concentration T_p = duration of pulse, sec</p>	$\frac{a_1}{s + a_1}$ <p>a_1 = decay time⁻¹, sec⁻¹</p>	$\exp \left[\frac{Pe}{2} \left(1 - \sqrt{1 + \frac{4\tau R_f s}{Pe} \left(1 + \frac{\phi}{bR_f} \sqrt{\frac{R_m D_m}{s}} \right)} \right) \right]$ <p>ϕ = matrix porosity b = fracture half aperture, cm R_f = fracture retardation factor R_m = matrix retardation factor D_m = diffusion coefficient in matrix, cm²/sec τ = mean fluid residence time, sec Pe = Peclet number = $\frac{L}{\alpha}$ (see text)</p>
s = Laplace transform variable		

Figure 2-4. Physical system, conceptual model, and Laplace transform transfer functions used to interpret tracer tests.

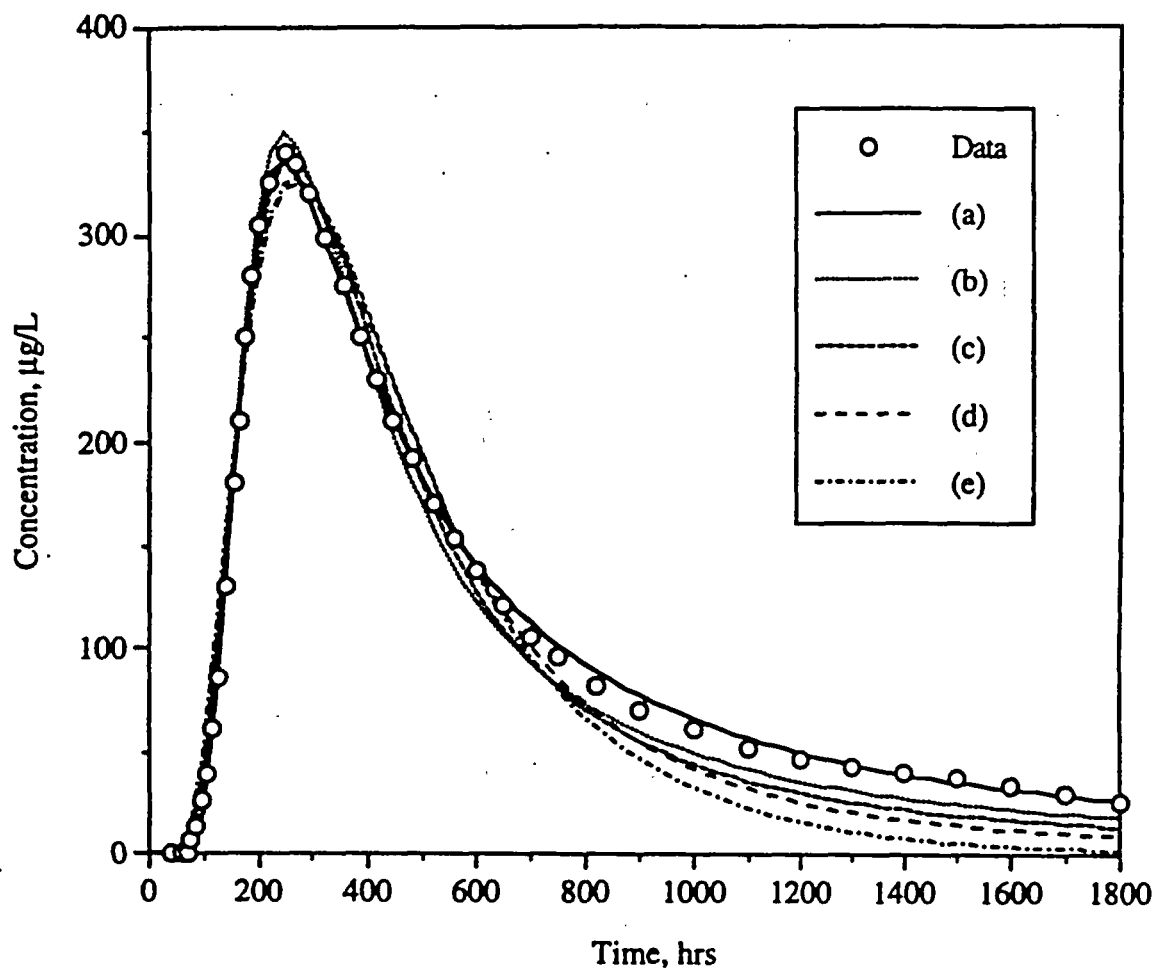


Figure 2-5. Fits to the May 1996 PFBA data assuming different values of the lumped matrix diffusion parameter, $\frac{\phi}{b}\sqrt{D_m}$: (a) 0.00346 cm^{-1} , (b) 0.00173 cm^{-1} , (c) 0.000865 cm^{-1} , (d) 0.000346 cm^{-1} , and (e) 0 cm^{-1} (single-porosity system). Parameter values yielding the fits are given in Table 2-2. Data points are a subset of the actual data (used for curve-fitting).

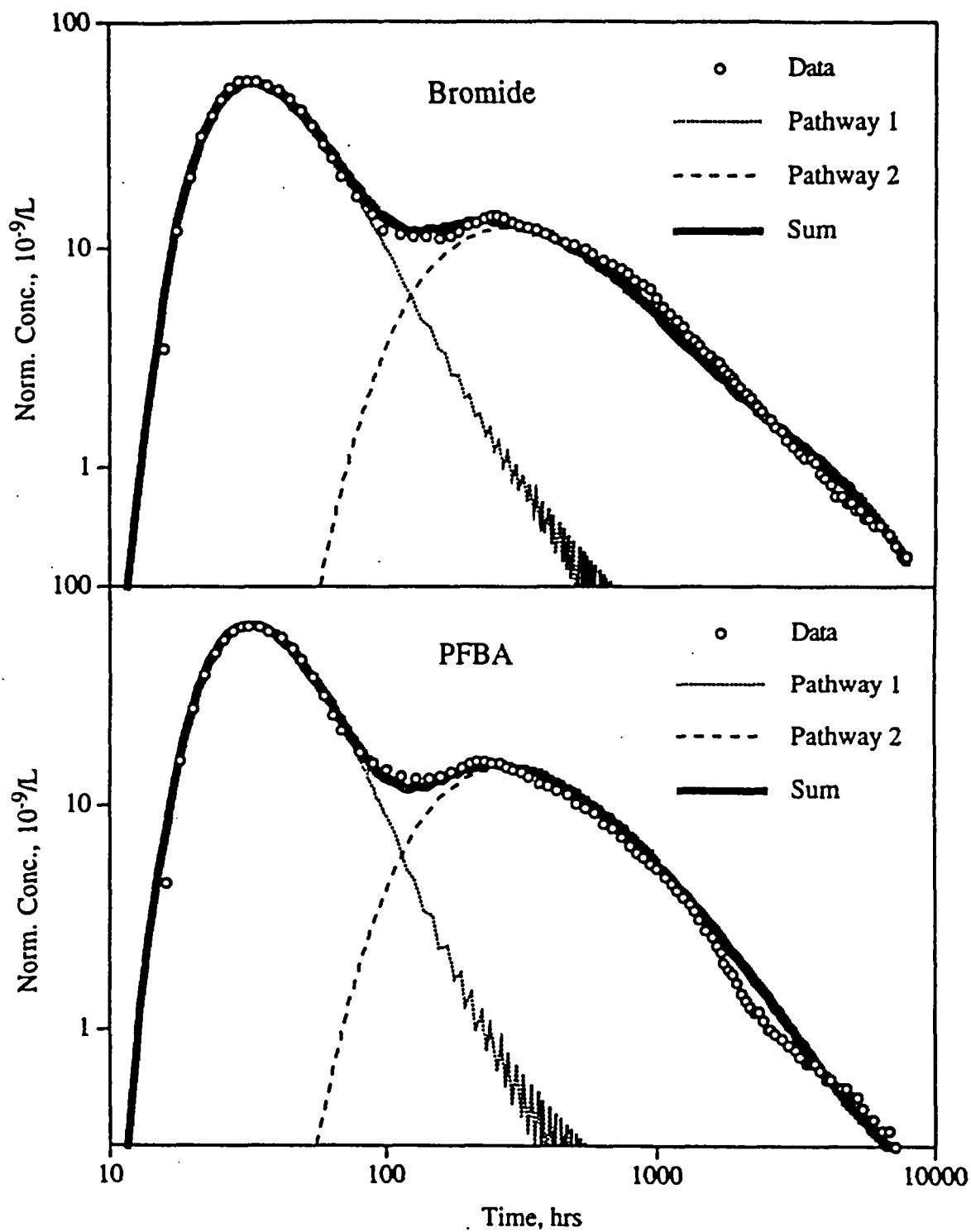


Figure 2-6. Fits to the PFBA and bromide data from the reactive tracer test assuming two "pathways." Model parameters corresponding to the fits are given in Table 2-3. The data points are a subset of the actual data (used for curve-fitting).

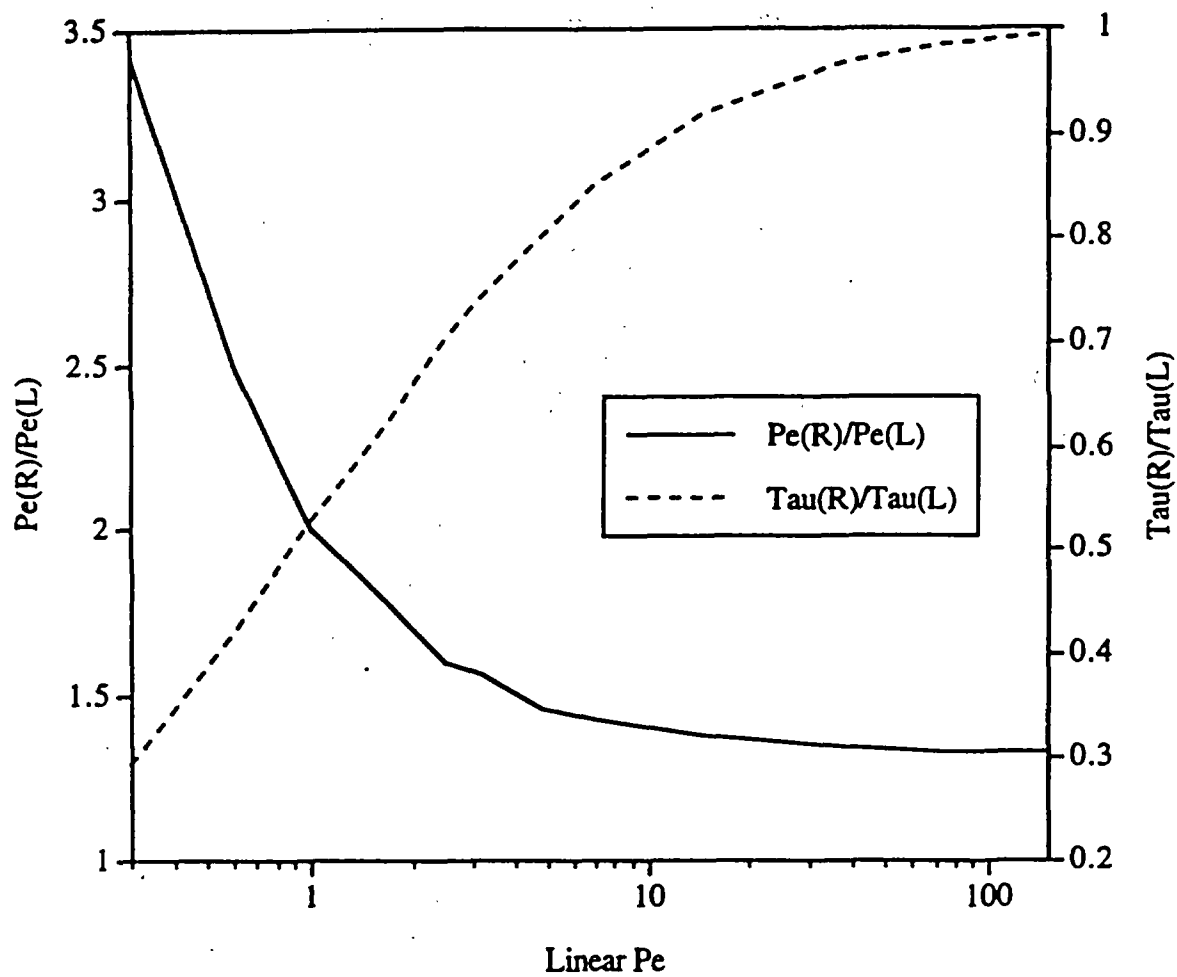


Figure 2-7. Ratios of radial and linear mean residence times (τ) and Peclet numbers (Pe) as a function of linear Peclet number. Curves were obtained by fitting a linear flow breakthrough curve of known τ and Pe using a radial model in RELAP.

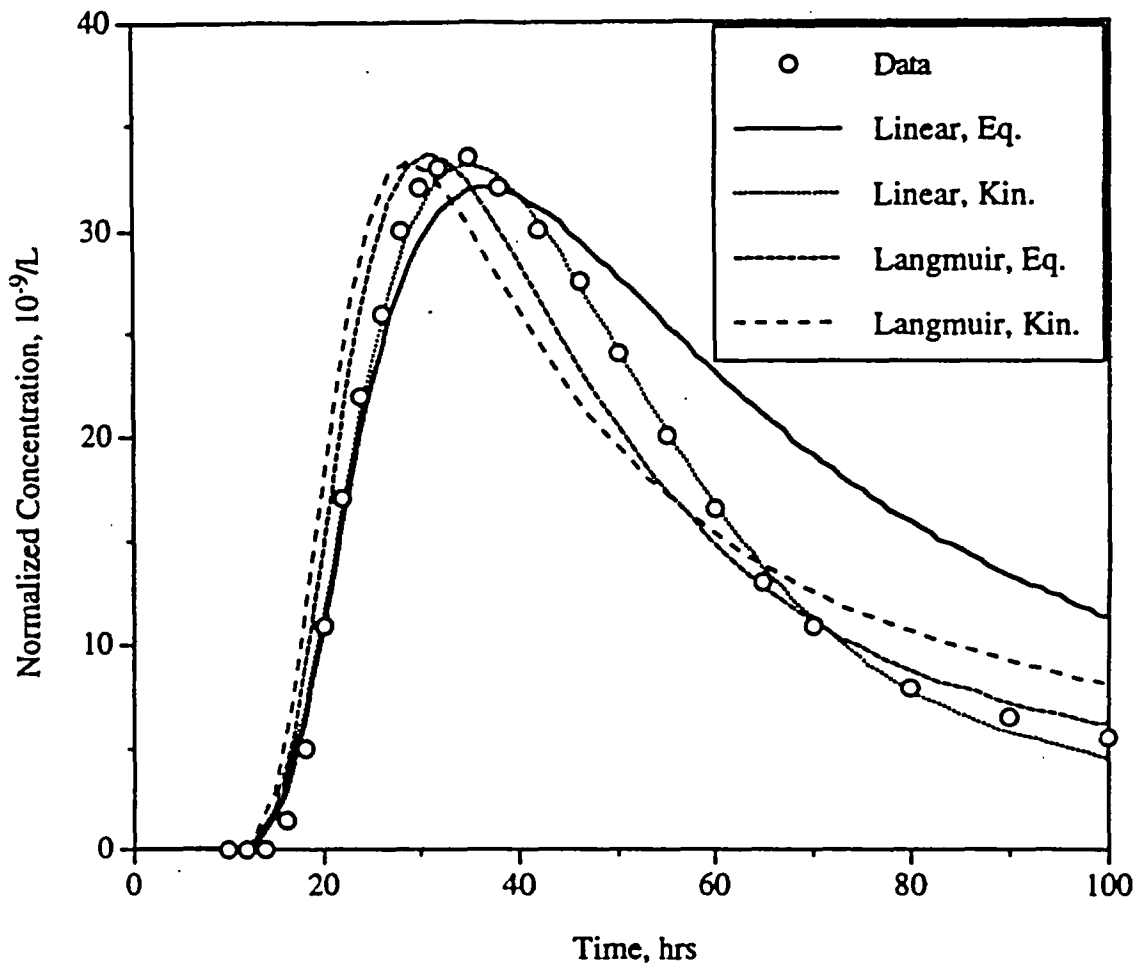


Figure 2-8. Fits to the first lithium peak in the reactive tracer test using different isotherms and assuming only a single pathway with the same hydrologic parameters that provided good fits to the PFBA and bromide data. The "Linear" curves were generated using the semi-analytical model, RELAP, while the "Langmuir" curves were generated using the numerical model, RETRAN. Model parameters corresponding to the fits are given in Table 2-4. The data points are a subset of the actual data (used for curve-fitting).

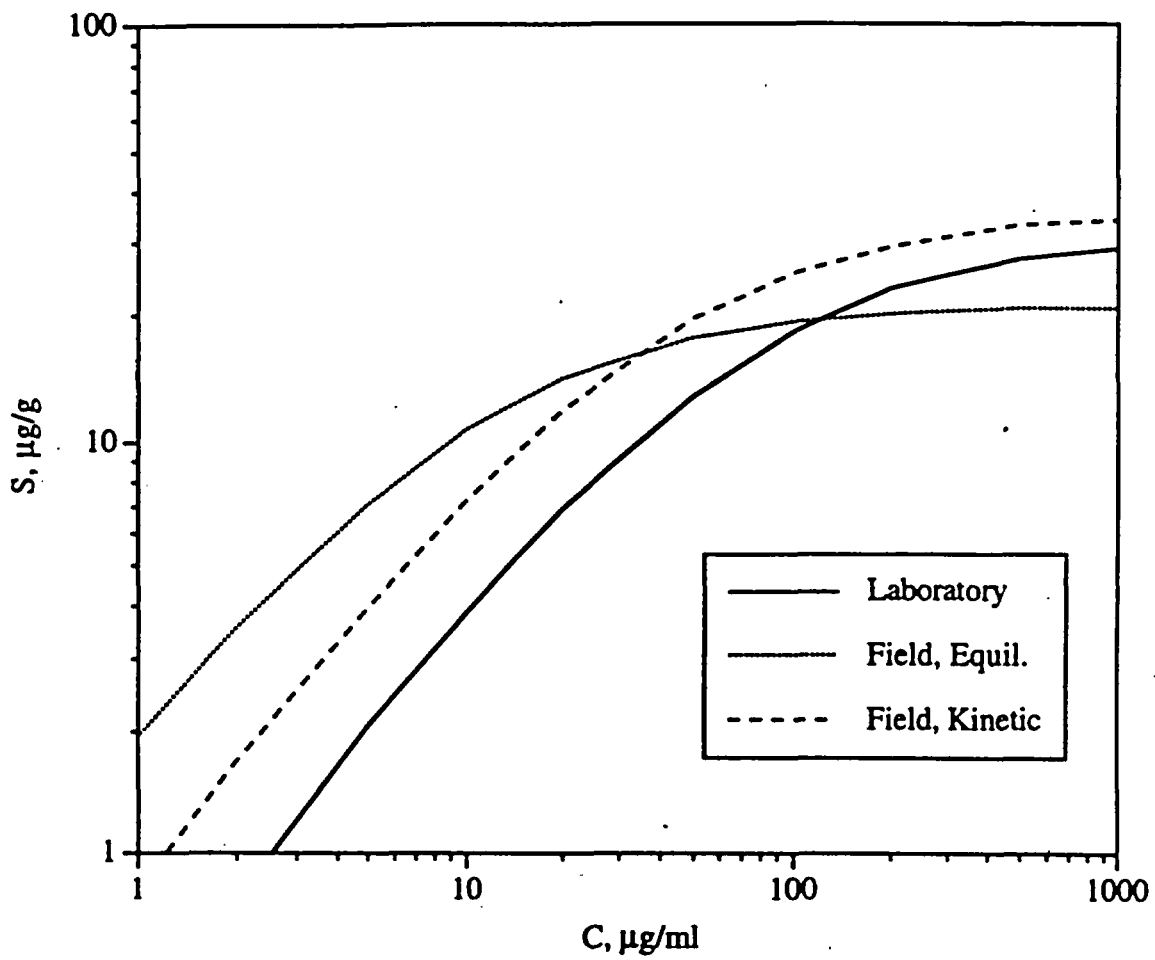


Figure 2-9. Langmuir isotherms derived for lithium ion from laboratory testing and from interpretations of the first lithium peak in the reactive tracer test. Table 2-4 gives Langmuir isotherm parameters used to generate the curves.

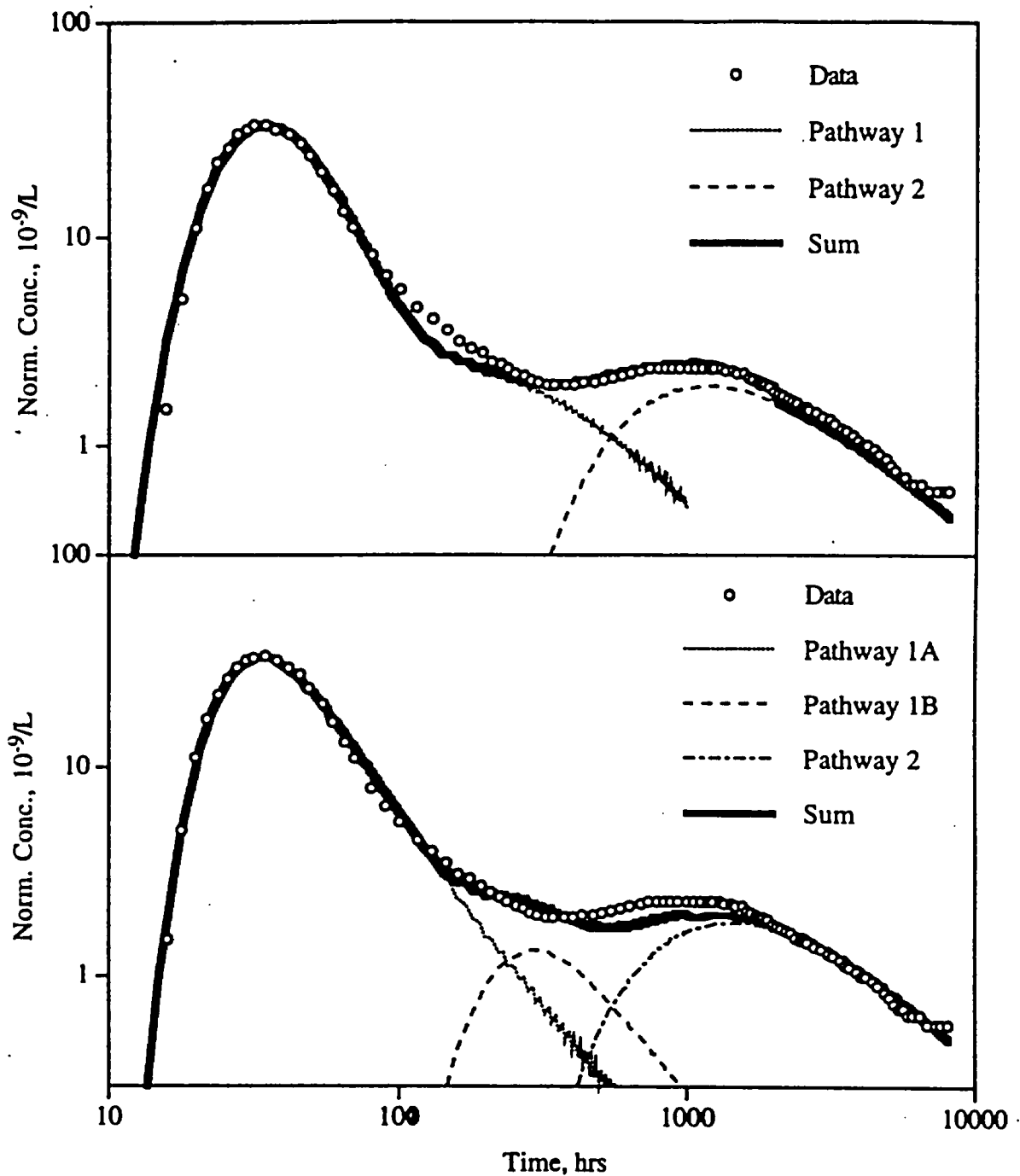


Figure 2-10. Fits to the lithium data in the reactive tracer test obtained by assuming linear, rate-limited sorption in the first pathway that results in the first peak (top) and by assuming chemical heterogeneity in the first pathway, resulting in two subpathways (1A and 1B) that each have linear, equilibrium sorption (bottom). Pathway 2 in both cases has linear, equilibrium sorption. Model parameters corresponding to the fits are given in Tables 2-3, 2-4, 2-6, and 2-8. The data points are a subset of the actual data (used for curve-fitting).

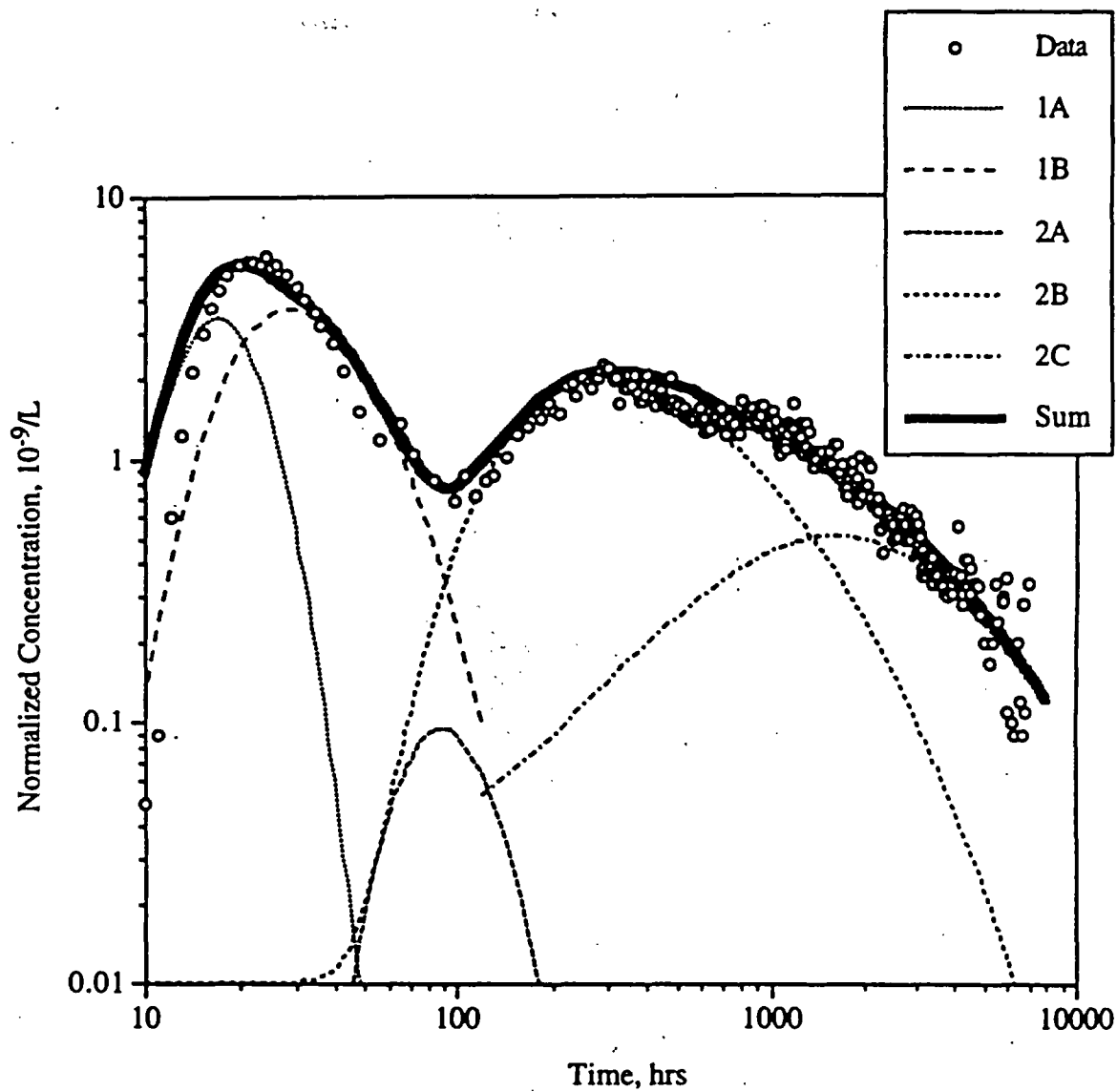


Figure 2-11. Split-pathway fits to the microsphere data from the reactive tracer test. Pathways 1A and 1B represent nondetaching and detaching fractions, respectively, of spheres moving through pathway 1. Pathways 2A, 2B, and 2C represent nondetaching and two detaching fractions, respectively, of spheres moving through pathway 2. Filtration and resuspension/detachment rate constants obtained from the fits are given in Table 2-10.

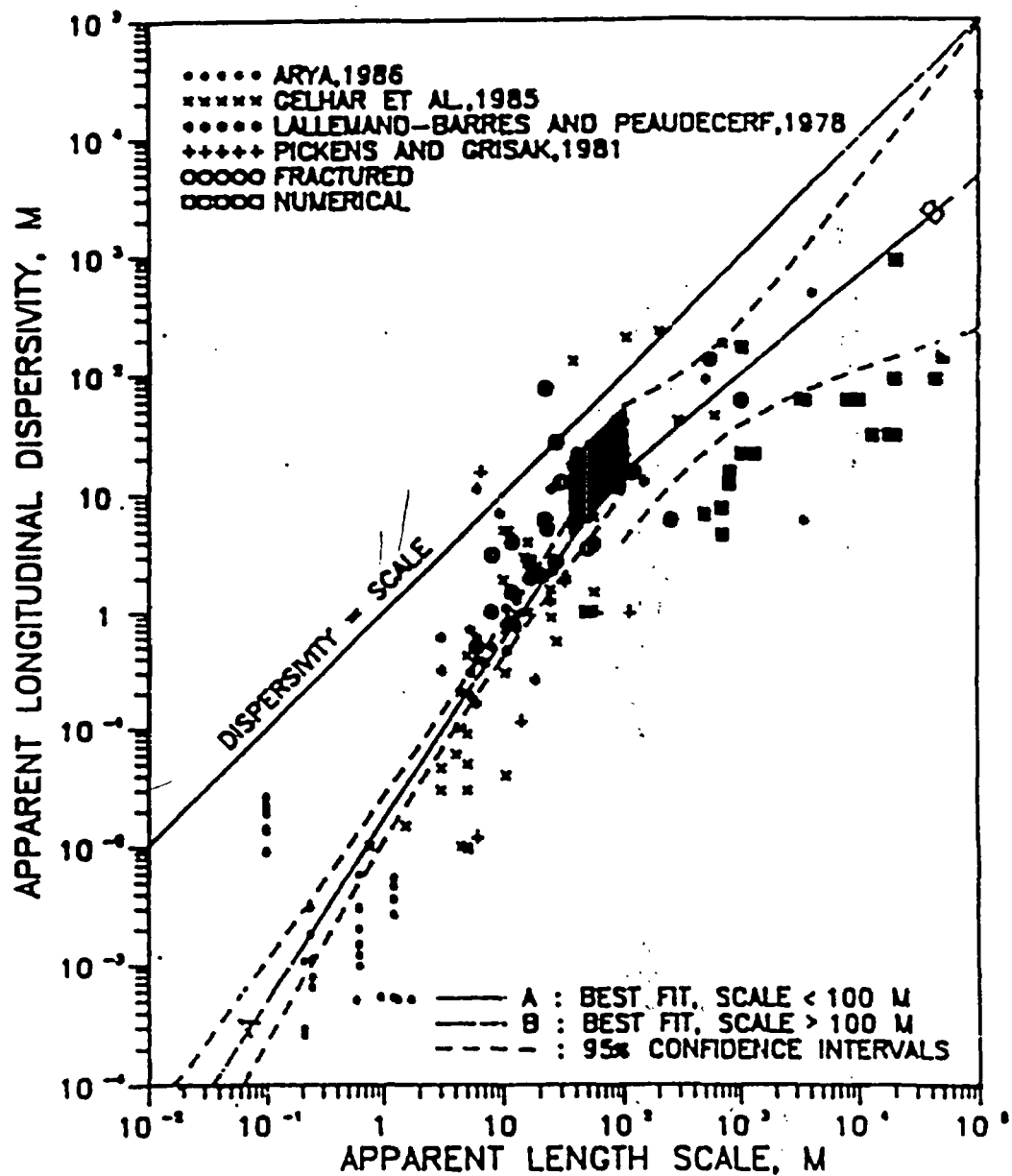


Figure 2-12. Plot of dispersivity vs. length scale showing range of C-holes values derived from interpretations of the reactive tracer test (darkened box). Plot taken from Neuman (1990).

3.0 Batch Sorption Experiments

Materials and Methods

Batch sorption experiments were conducted in a manner similar to that described by Reimus and Turin (1997, Appendix A), who reported results of batch sorption experiments of lithium ion onto central Bullfrog tuff. The following steps were common features of all experiments:

- C-holes core from a stratigraphic unit of interest was crushed, pulverized, and passed through a 500- μm sieve but retained on a 75- μm sieve.
- A specified amount of crushed tuff was added to polycarbonate (polyallomer) Oak Ridge centrifuge tubes. In some experiments, the tuff and centrifuge tubes were autoclaved prior to contacting the tuff with the lithium solution.
- The tuff was preconditioned with filter-sterilized (0.2- μm filter) J-13 water.
- A specified amount of tracer-bearing water (either from well J-13 or well C#3) was added to the preconditioned tuff, and the mixture was continuously shaken for 24 to 72 hrs at either 25°C or 38°C to achieve equilibration between solid and solution.
- After equilibration, the tubes were centrifuged and a portion of the supernate was filtered (0.2- or 0.4- μm filter) for tracer analysis to determine the tracer concentration remaining in solution. Lithium was analyzed by inductively-coupled plasma-atomic emission spectrometry (ICP-AES).
- The mass of tracer sorbed to the tuff was determined by mass balance, with corrections, if necessary, to account for sorption to the container walls, which was measured in control experiments in which tuff was omitted.
- All measurements were made in duplicate.

Isotherms were determined under several different experimental conditions: 1:1 solution:solid ratio in J-13 water at 25°C, 1:1 solution:solid ratio in J-13 water at 38°C, 2:1 solution:solid ratio in J-13 water at 25°C, 4:1 solution:solid ratio in C-3 water at 38°C, 4:1 solution:solid ratio in J-13 water at 25°C, and 4:1 solution:solid ratio in J-13 water at 38°C. The two temperatures were intended to span the range of conditions under which sorption would occur in either the laboratory or the field (the average groundwater temperature in the Bullfrog Tuff at the C-Holes is about 38°C).

At the time of these studies, groundwater from the C-Wells complex was not consistently available, so groundwater from well J-13, located 4 km southeast of the C-Wells complex, was used as a surrogate in most tests. J-13 water is well-characterized and has become the *de facto* standard groundwater for use in Yucca Mountain sorption studies (Harrar et al., 1990; Triay et al., 1993; Triay et al., 1996). A comparison of J-13 and C-Wells groundwater chemistry shows that the two waters are both sodium bicarbonate dominated and in all regards quite similar (Table 3-1). Lithium solutions for sorption tests were prepared by dissolving reagent grade lithium bromide in either C#3 or J-13 water. All solutions were filter-sterilized before use.

A few tests were conducted in a sodium bicarbonate solution having the same ionic strength as J-13 water but without the calcium and other cations present in J-13 water (Reimus et al., 1997). Lithium sorption in this solution was noticeably greater than in J-13 water, presumably because of the absence of cations that compete with

lithium for sorption sites (primarily calcium). The results of these experiments are not reported here.

Ion-exchange theory suggests that the actual ion exchange process is rapid and will reach equilibrium quickly; in natural systems apparent equilibration rates are limited by diffusion of ions through the solution to the mineral surface (Bolt et al., 1978). In a well-mixed system such as a shaken centrifuge tube, diffusion is not limiting, and equilibration should be achieved quickly. A previous study of lithium sorption to the Prow Pass Member of the Crater Flat Tuff found that sorption equilibrium was reached within 1 h, confirming this hypothesis (Newman et al., 1991). For consistency with other sorption studies and for scheduling convenience, a minimum equilibration period of 24 h was adopted for these studies.

Tuffs from seven different lithologies were tested, including two samples of the same unit (the central Bullfrog Tuff) from two different holes (C#1 and C#2) to allow an assessment of spatial heterogeneity in lithium sorption parameters. The experimental matrix of tuffs, groundwaters, temperatures, and solid-solution ratios is summarized in Table 3-2. Fig. 3-1 shows the sampling locations of the C-holes core used in the experiments. Core from these same locations were also used in the experiments described in Sections 4.0 and 5.0 of this report.

The mineralogy of the tuffs used in the batch sorption experiments is listed in Table 3-3. The mineralogy was determined from x-ray diffraction (XRD) analyses. The tuffs differ primarily in their smectite and zeolite (clinoptilolite and mordenite) content, both of which have high cation exchange capacities and would be expected to sorb lithium quite strongly compared to other minerals present in the rocks. Fig. 3-2 provides a graphical depiction of the smectite and zeolite content of the tuffs used in the batch sorption experiments.

The cation exchange capacities of most of the tuffs used in batch sorption experiments were measured according to the following procedure:

- The tuff samples were crushed and wet-sieved with J-13 water to a particle size range between 75-500 μm .
- 5g of each tuff was weighed into a 50 mL centrifuge Teflon tube.
- Samples were saturated three times with 30 mL of 1N LiBr-LiOAc solution to ensure replacement of cations present on mineral surface sites with Li. The pH of the solution was maintained at ~ 8.2 to prevent dissolution of calcite. After each LiBr addition, the tubes were sonified to disperse the centrifuged sediment, and then the samples were shaken for 30 min.
- Samples were centrifuged at 10000 rpm for 15 min and aliquots were pipetted out and analyzed for major cations such as Na, K, Ca, and Mg. The remaining solution in the tubes was dispensed into the same volumetric flask to determine the cation sorption after all three combined steps of Li sorption.
- After the Li sorption steps, the tuff present in the centrifuge tube was washed three times with 30mL 1N CsCl to remove the sorbed Li. The aliquots extracted after centrifuging were analyzed for Li, Na, Ca, K, and Mg. Cs has more affinity for zeolites, and it should therefore displace more cations than Li. In many cases, Cs sorption gives a measure of the total cation exchange capacity (Li measurements of the aliquots give the CEC for Cs exchange).
- It should be noted that analcime (a Na-exchangeable zeolite) is discussed in the literature as having more affinity for Na and less for Li or Cs (Sherry, 1969). Ming and Mumpton (1989) have stated that the relatively large ionic radius of Cs

may prevent it from penetrating the small pores/channels in analcime. It is possible that the ionic radius of hydrated Li is large enough that it will also not sorb internally.

The experimental cation exchange capacities are listed in Table 3-4. By comparing this table and Fig. 3-2, it is apparent that the cation exchange capacities are highly correlated with the smectite and zeolite content of the rocks.

Results and Discussion

During the course of the experiments, it became apparent that lithium sorption was essentially independent of solution:solid ratio, temperature, and water composition (J-13 or C#3) over the range of conditions studied. Therefore, the data sets for a given tuff lithology were combined to estimate sorption parameters. Three common isotherm models, defined as follows, were fitted to the data for each tuff:

Linear Isotherm:

$$S = K_D C \quad (3.1)$$

where S = equilibrium sorbed concentration ($\mu\text{g/g}$); C = equilibrium solution concentration ($\mu\text{g/mL}$); and K_D = linear distribution coefficient (mL/g).

Freundlich Isotherm:

$$S = K_f C^n \quad (3.2)$$

where K_f = Freundlich coefficient ($\text{mL}/\mu\text{g})^n(\mu\text{g/g})$ and n = Freundlich exponent (dimensionless).

Langmuir Isotherm:

$$S = K_L S_{\max} C / (1 + K_L C) \quad (3.3)$$

where K_L = Langmuir coefficient ($\text{mL}/\mu\text{g}$) and S_{\max} = Maximum solid sorption capacity ($\mu\text{g/g}$).

Figs. 3-3 to 3-9 show the experimental data for each tuff plotted as log equilibrium sorbed concentration ($\mu\text{g/g}$) vs. log solution concentration ($\mu\text{g/ml}$). A Langmuir isotherm consistently yielded better visual fits to the data than the other isotherms, so a fitted Langmuir isotherm is also shown in each figure. The Langmuir isotherm is the only isotherm that captures the curvature of the data when graphed on log-log axes. Furthermore, only the Langmuir isotherm recognizes the finite sorptive capacity of the solid matrix; the other models imply potential infinite sorption. A previous study of lithium sorption to the overlying Prow Pass Member of the Crater Flat Tuff also revealed Langmuir behavior (Newman et al., 1991). The Langmuir, Freundlich, and linear isotherm parameters associated with the data in Figs. 3-3 to 3-9 are given in Table 3-5. We conclude that a Langmuir isotherm provides the best representation of lithium sorption onto C-holes Tuffs. However, a detailed statistical

analysis to quantify how much better this representation is relative to the other isotherms (or whether it is statistically better) was not conducted. We also did not conduct statistical analyses to determine whether there were significant isotherm differences as a function of temperature, solid-solution ratio, or core taken from different locations in the same lithological unit (i.e., the central Bullfrog Tuff from C#1 or C#2). However, it appears from Figs. 3-3 to 3-9 that any of these differences should have been minimal. These analyses will be the subject of future studies.

The error bounds shown in Figs. 3-3 to 3-9 reflect uncertainty due to analytical errors in determining lithium concentrations in solution. The error bounds were calculated assuming a 5% relative standard deviation in the lithium concentration measurements (typical for ICP-AES analyses). Errors increase as concentrations increase because there is a lower percentage of lithium sorbing at higher concentrations and hence a smaller relative difference between measured initial and final solution concentrations. It is apparent that the scatter in the data sets often exceeds the analytical error bounds, suggesting other sources of error besides analytical errors. These other potential sources of error have not been systematically identified.

The fitted Langmuir isotherms corresponding to all seven C-Holes tuff lithologies are plotted together in Fig. 3-10. By comparing Fig. 3-10 to Fig. 3-2 and Tables 3-2 and 3-4, it is apparent that the two tuffs demonstrating the greatest affinity for lithium (Bedded Prow Pass and Lower Bullfrog) are also the tuffs that have the greatest smectite and/or zeolite content as well as the highest cation exchange capacities. Thus, as expected, the lithium sorption capacity is highly correlated to the smectite/zeolite content and the cation exchange capacity of the tuffs.

Batch sorption experiments were also conducted to determine whether PFBA and bromide sorbed to C-holes tuffs. The bromide experiments were actually conducted simultaneously with the lithium experiments, as lithium was added to the solutions as lithium bromide. The starting bromide concentrations ranged from ~10 ppm to ~1000 ppm. The PFBA experiments were conducted at a single concentration (1 ppm). These experiments were conducted on each rock type at 25°C. There was no measureable sorption of PFBA or bromide on any of the tuffs.

Section 3.0 References

- Fuentes, H. R., W. L. Polzer, E. H. Essington and B. D. Newman (1989). Characterization of Reactive Tracers for C-Wells Field Experiment I: Electrostatic Sorption Mechanism, Lithium, Los Alamos National Laboratory.
- Harrar, J. E., J. F. Carley, W. F. Isherwood and E. Raber (1990). Report of the Committee to Review the Use of J-13 Well Water in Nevada Nuclear Waste Storage Investigations, Lawrence Livermore National Laboratory.
- Ming, D.W., Mumpton, F.A., (1989) *Zeolites in Soils, Minerals in Soil Environments*, Soil Science Society of America Book Series No. 1, pp. 873-911.
- Newman, B. D., H. R. Fuentes and W. L. Polzer (1991). "An Evaluation of Lithium Sorption Isotherms and Their Application to Ground-Water Transport." *Ground Water* 29(6): 818-824.
- Reimus P. W. and Turin, H. J., Draft report of results of hydraulic and tracer tests at the C-holes complex, *Yucca Mountain Site Characterization Project Milestone Report SP32APMD*, Los Alamos National Laboratory, Los Alamos, NM, 1997.
- Sherry, H.S., (1969) The ion-exchange properties of zeolites. In *Ion Exchange*, 2, J.A. Marinsky, Ed. Marcel Dekker, Inc., N.Y., pp.89-133.
- Triay, I. R., A. Meijer, J. L. Conca, K. S. Kung, R. S. Rundberg and E. A. Strietelmeier (1996). Summary and Synthesis Report on Radionuclide Retardation for the Yucca Mountain Site Characterization Project, Los Alamos National Laboratory.
- Triay, I. R., B. A. Robinson, R. M. Lopez, A. J. Mitchell and C. M. Overly (1993). Neptunium Retardation with Tuffs and Groundwaters from Yucca Mountain. *Fourth Annual International Conference on High Level Radioactive Waste Management*, Las Vegas, NV, American Nuclear Society / American Society of Civil Engineers.

Section 3.0 Tables

Table 3-1. Comparison of J-13 and C-Wells groundwater chemistry. All analyses (except pH) in $\mu\text{g}/\text{mL}$ (Fuentes et al., 1989).

	J-13	C-Wells
Al	<0.03	
B	0.13	
Ba	<0.001	
Ca	11.3	11
Cl	7	7
Fe	0.02	
K	5	2
Li	0.040	0.11
Mg	<0.010	0.38
Mn	0.01	
Na	44	55
Si	30	25
Sr	0.040	0.044
PO ₄	<2.5	
SO ₄	19	22
HCO ₃	124	142
pH	7.2	7.8

Table 3-2. Summary of experimental test matrix.

Tuff ⁽¹⁾	Water	Solution:Solid (ml:g)	Temp. (°C)
Central Bullfrog, C#1, 715 m (1)	J-13	2:1	25
	J-13	2:1	38
Central Bullfrog, C#2, 734 m (2)	J-13	1:1	25
	J-13	1:1	38
	C#3	4:1	38
Lower Bullfrog, C#1, 795 m (3)	J-13	4:1	25
	J-13	4:1	38
	J-13	2:1	25
Upper Prow Pass, C#2, 533 m (4)	J-13	4:1	25
	J-13	4:1	38
Central Prow Pass, C#2, 553 m (5)	J-13	2:1	25
	J-13	4:1	38
	J-13	4:1	25
Lower Prow Pass, C#1, 573 m (6)	J-13	4:1	25
	J-13	4:1	38
	J-13	2:1	25
Bedded Prow Pass, C#2, 643 m (7)	J-13	4:1	25
	J-13	4:1	38
	J-13	2:1	25
Upper Tram, C#2, 839 m (8)	J-13	4:1	25
	J-13	4:1	38
	J-13	2:1	25

⁽¹⁾Lithology, borehole, and depth from land surface in meters. Numbers in parentheses correspond to numbers in Fig. 3-1 (which show locations where core was collected from the C-holes).

Table 3-2. X-ray Diffraction results* for tuffs from Prow Pass, Bullfrog and Tram units. Only the main sorptive fractions are listed; the balance of the tuffs was mostly quartz and feldspar with small amounts of hematite, mica/illite, and/or kaolinite.

Tuff	Depth, m	Smectite	Clinoptilolite	Mordenite	Analcime	Calcite
Central Bullfrog, C#1	715	2 ± 1	-	-	-	2 ± 1
Central Bullfrog, C#2	734	5 ± 2	NR	NR	NR	NR
Lower Bullfrog	795	9 ± 3	4 ± 1	3 ± 1	12 ± 1	4 ± 1
Upper Prow Pass	533	-	-	-	-	Trc.
Central Prow Pass	553	2 ± 1	-	-	-	2 ± 1
Lower Prow Pass	573	2 ± 1	-	-	-	-
Bedded Prow Pass	643	-	-	20 ± 4	39 ± 2	-
Upper Tram	839	1 ± 1	-	-	-	-

* = weight %

Trc. = trace abundance of < 0.5 wt%

Table 3-4. Cation exchange capacities of C-holes tuffs

Tuff Unit	Estimated Average CEC, (meq/100g)	Std. Dev.
Central Bullfrog, C-1	3.65	0.12
Lower Bullfrog	17.97	0.19
Upper Prow Pass	1.99	0.49
Central Prow Pass	4.32	0.14
Lower Prow Pass	3.19	0.38
Bedded Prow Pass	21.25	0.13
Upper Tram	1.93	0.12

Note: CEC of "Central Bullfrog, C#2" was not measured.

Table 3-5. Lithium sorption isotherm parameters associated with the different C-holes tuffs.

Unit	Langmuir Params.		Freundlich Params.		Linear Params.
	$K_L, L/mg$	$S_{max}, \mu g/g$	K_F	N	$K_d, ml/g$
Central Bullfrog	0.014	31.4	0.69	0.79	0.186
Lower Bullfrog	0.0070	233.9	2.26	0.75	0.321
Upper Prow Pass	0.00094	53.1	0.075	1.03	0.068
Central Prow Pass	0.0031	83.3	0.48	0.80	0.131
Lower Prow Pass	0.011	39.8	0.48	0.78	0.084
Bedded Prow Pass	0.012	254.9	4.17	0.69	0.383
Upper Tram	0.0026	59.8	0.27	0.78	0.072

Section 3.0 Figures

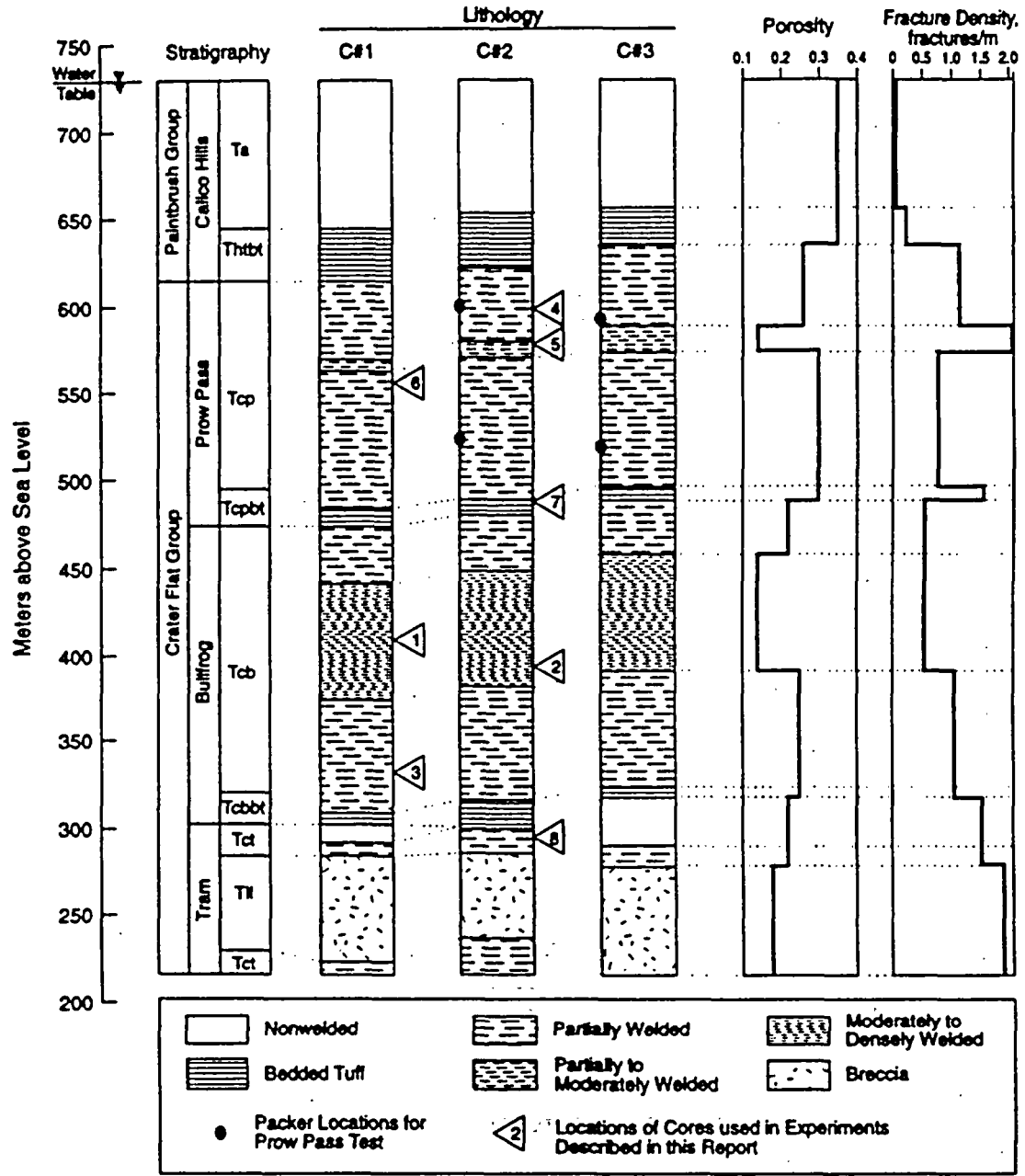


Figure 3-1. C-holes hydrogeology showing sampling locations of all core used in the laboratory experiments described in Sections 3.0, 4.0, and 5.0 of this report. Numbers correspond to numbers in Table 3-2. Also shown are approximate locations of packers for upcoming FY 1998 reactive tracer test in the Prow Pass Tuff are also shown.

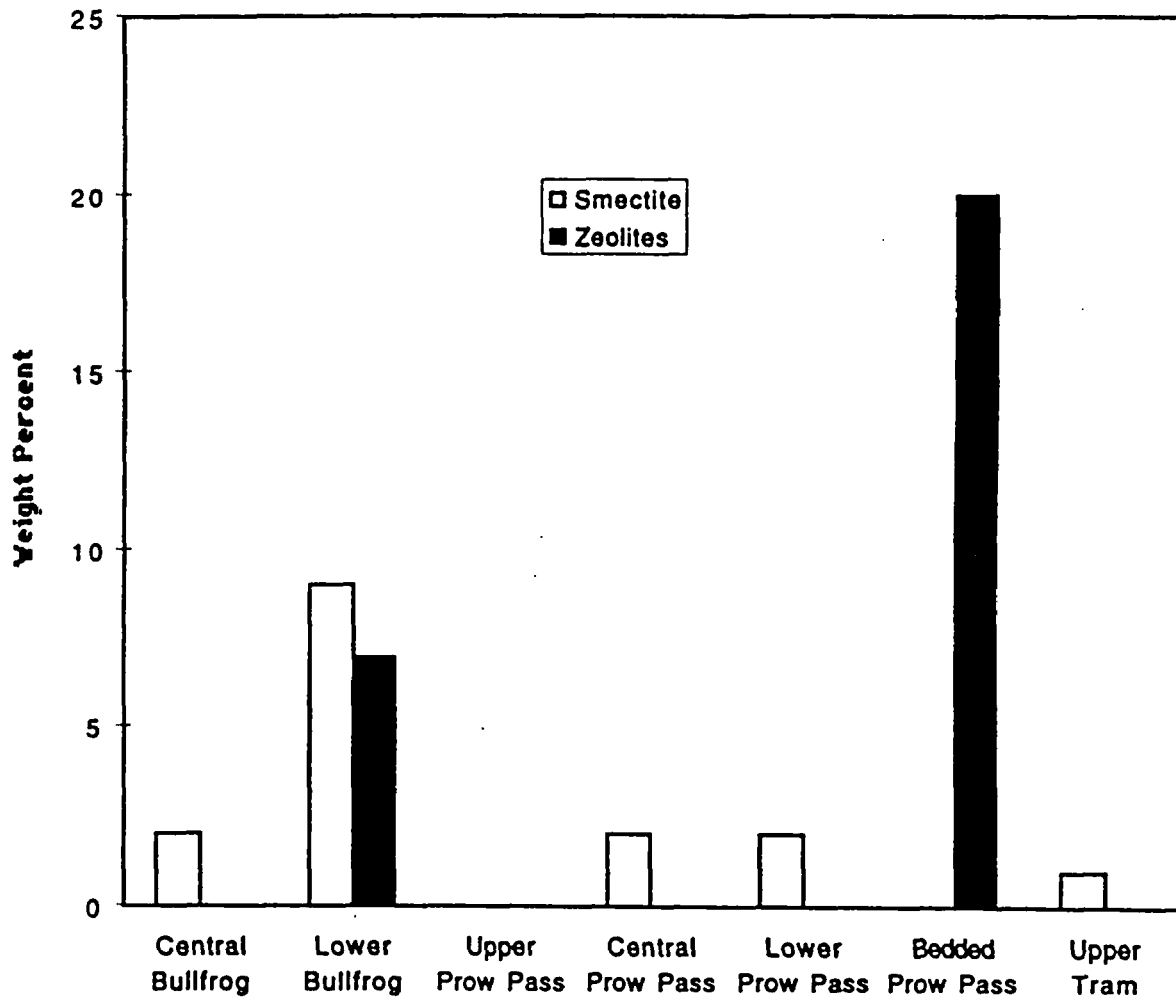


Figure 3-2. Smectite and zeolite weight percentages of the C-holes tuffs used in the batch sorption experiments.

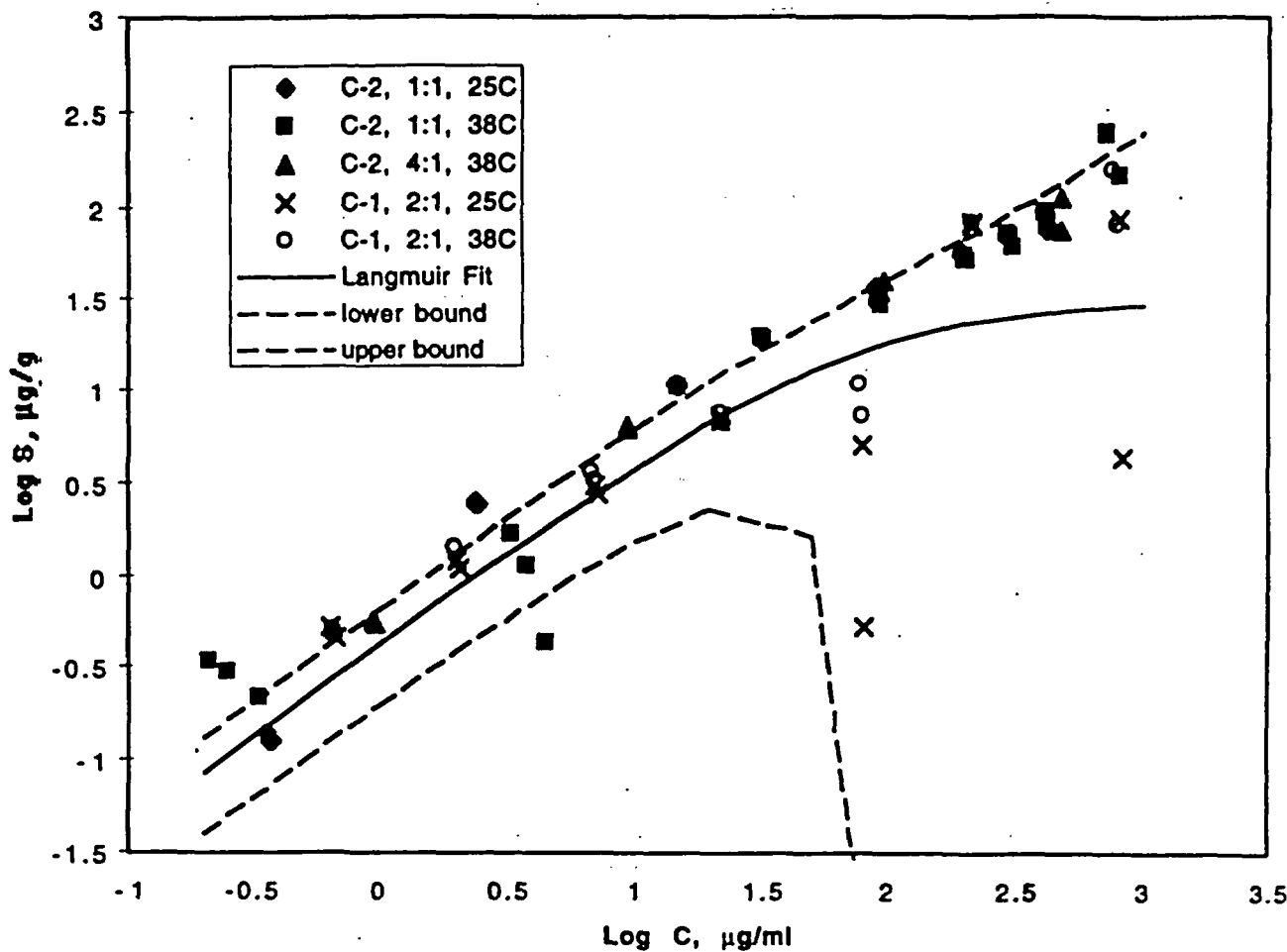


Figure 3-3. Lithium sorption data and fitted Langmuir isotherm for the central Bullfrog Tuff. The legend indicates the borehole (C#1 or C#2) from which the tuff came, the solution:solid ratio (ml:g), and the temperature of the experiments. The dashed lines are error bars associated with 5% analytical measurement error. J-13 water was used in all experiments except for "C-2, 4:1, 38C." Water from C#3 was used for "C-2, 4:1, 38C."

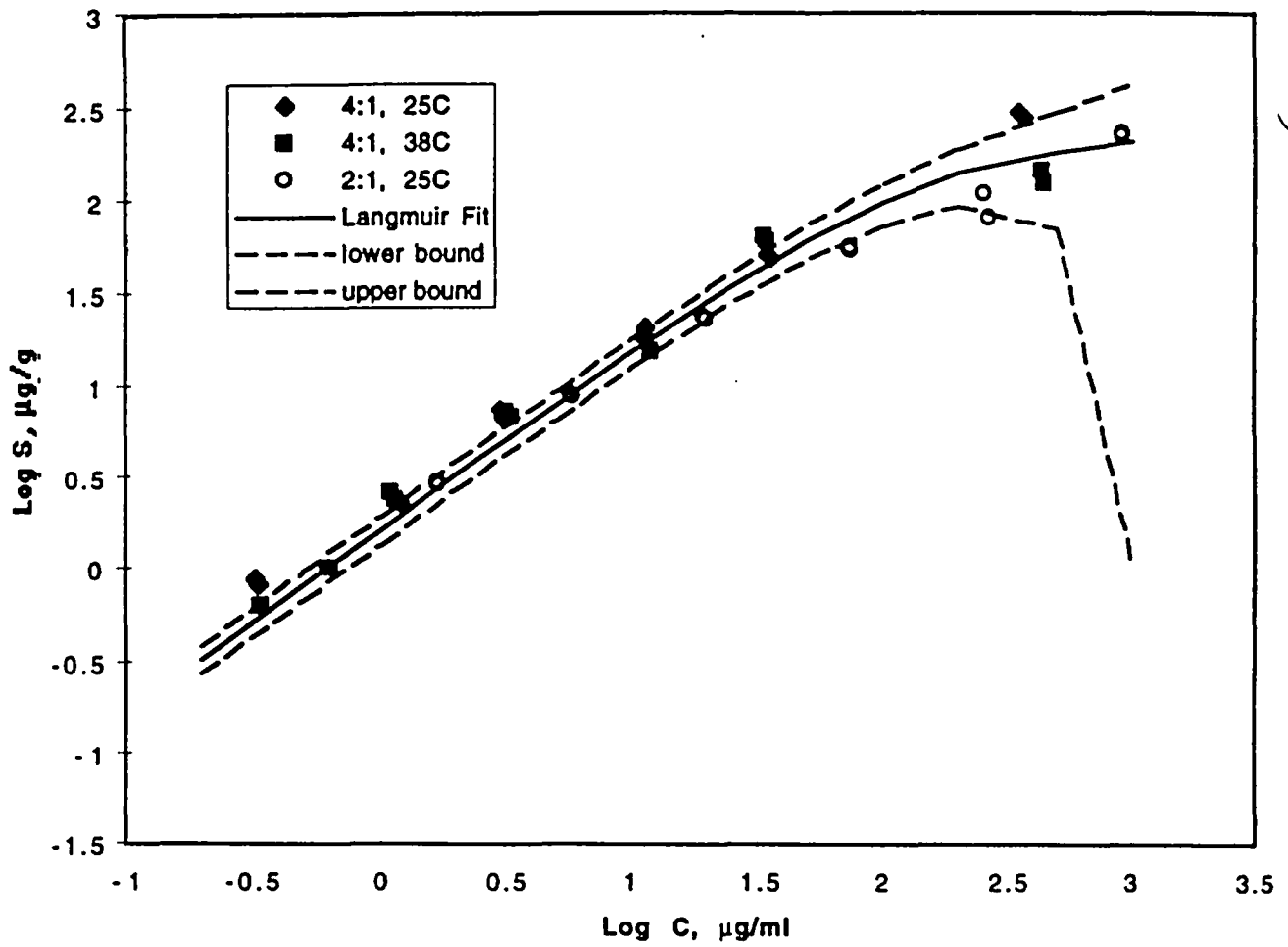


Figure 3-4. Lithium sorption data and fitted Langmuir isotherm for the lower Bullfrog Tuff. The legend indicates the solution:solid ratio (ml:g) and the temperature of the experiments. The dashed lines are error bars associated with 5% analytical measurement error. J-13 water was used in all experiments.

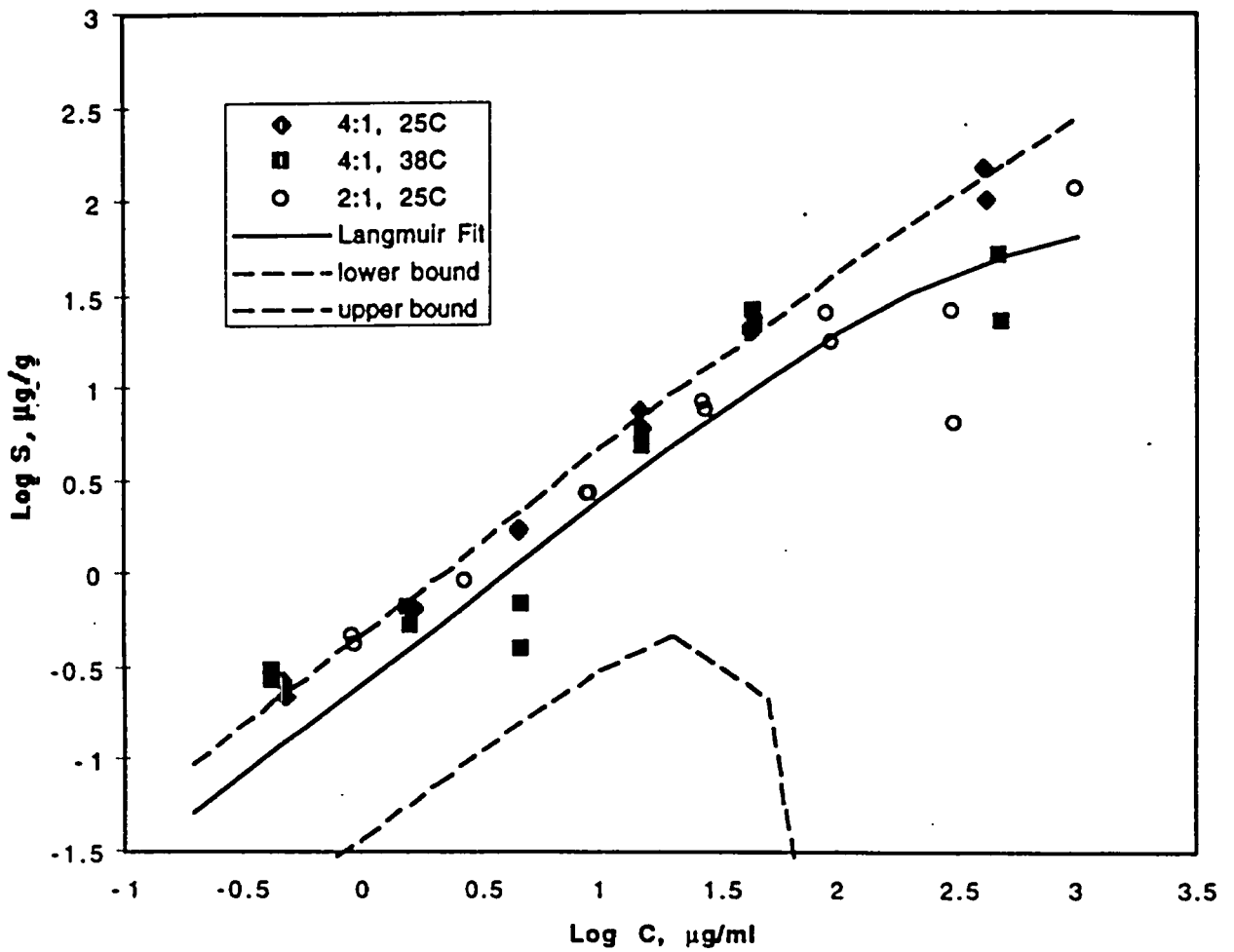


Figure 3-6. Lithium sorption data and fitted Langmuir isotherm for the central Prow Pass Tuff. The legend indicates the solution:solid ratio (ml:g) and the temperature of the experiments. The dashed lines are error bars associated with 5% analytical measurement error. J-13 water was used in all experiments.

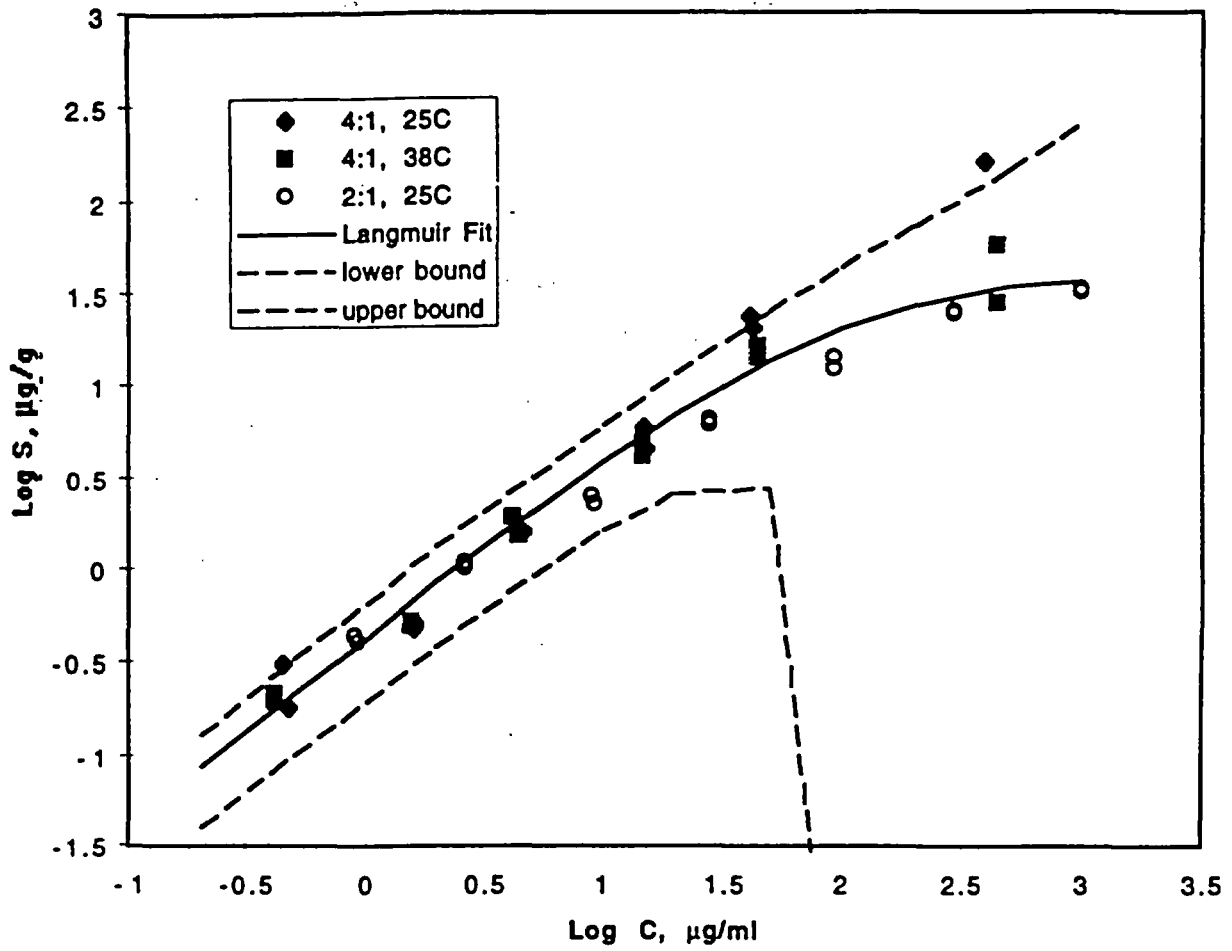


Figure 3-7. Lithium sorption data and fitted Langmuir isotherm for the lower Prow Pass Tuff. The legend indicates the solution:solid ratio (ml:g) and the temperature of the experiments. The dashed lines are error bars associated with 5% analytical measurement error. J-13 water was used in all experiments.

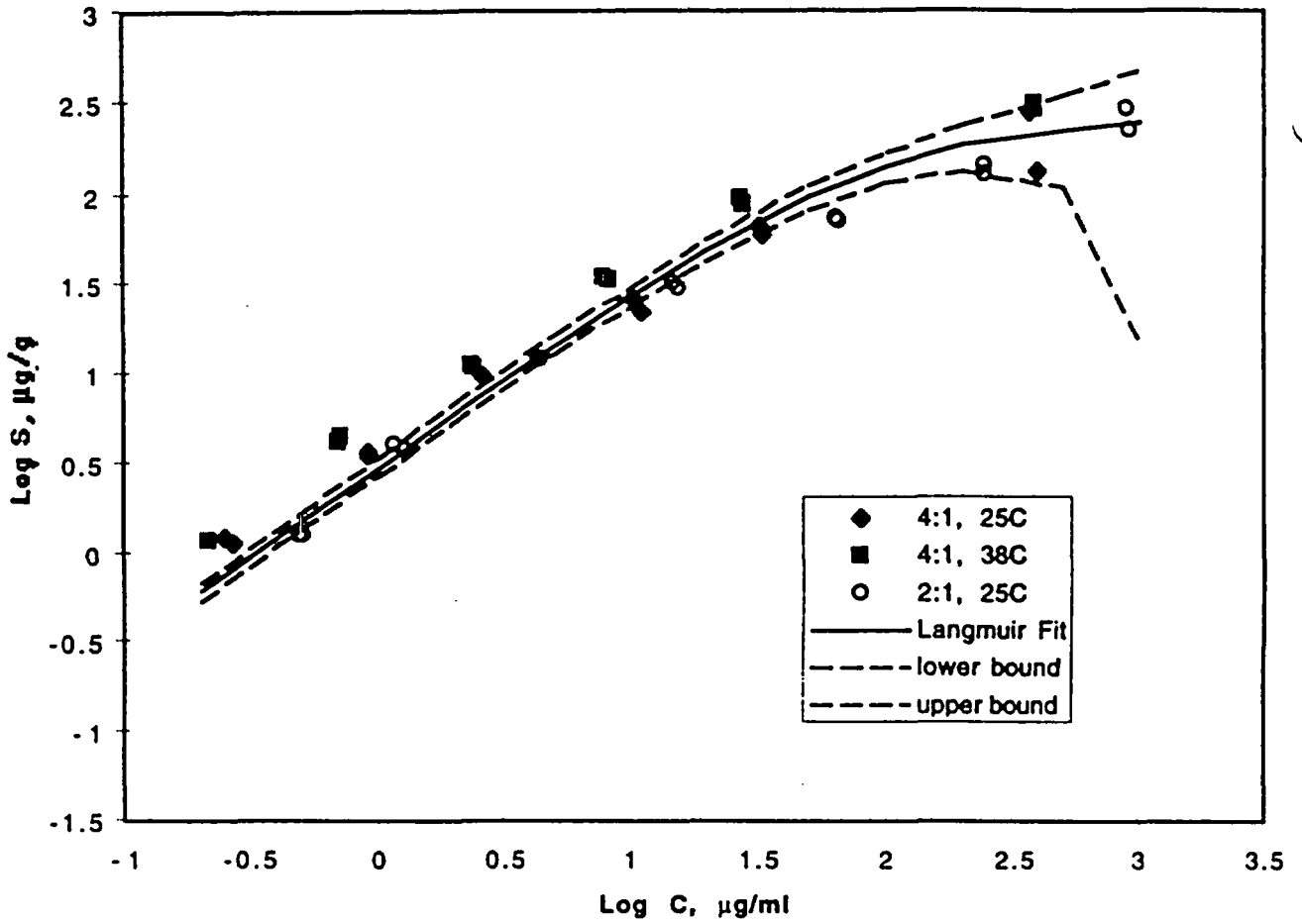


Figure 3-8. Lithium sorption data and fitted Langmuir isotherm for the bedded Prow Pass Tuff. The legend indicates the solution:solid ratio (ml:g) and the temperature of the experiments. The dashed lines are error bars associated with 5% analytical measurement error. J-13 water was used in all experiments.

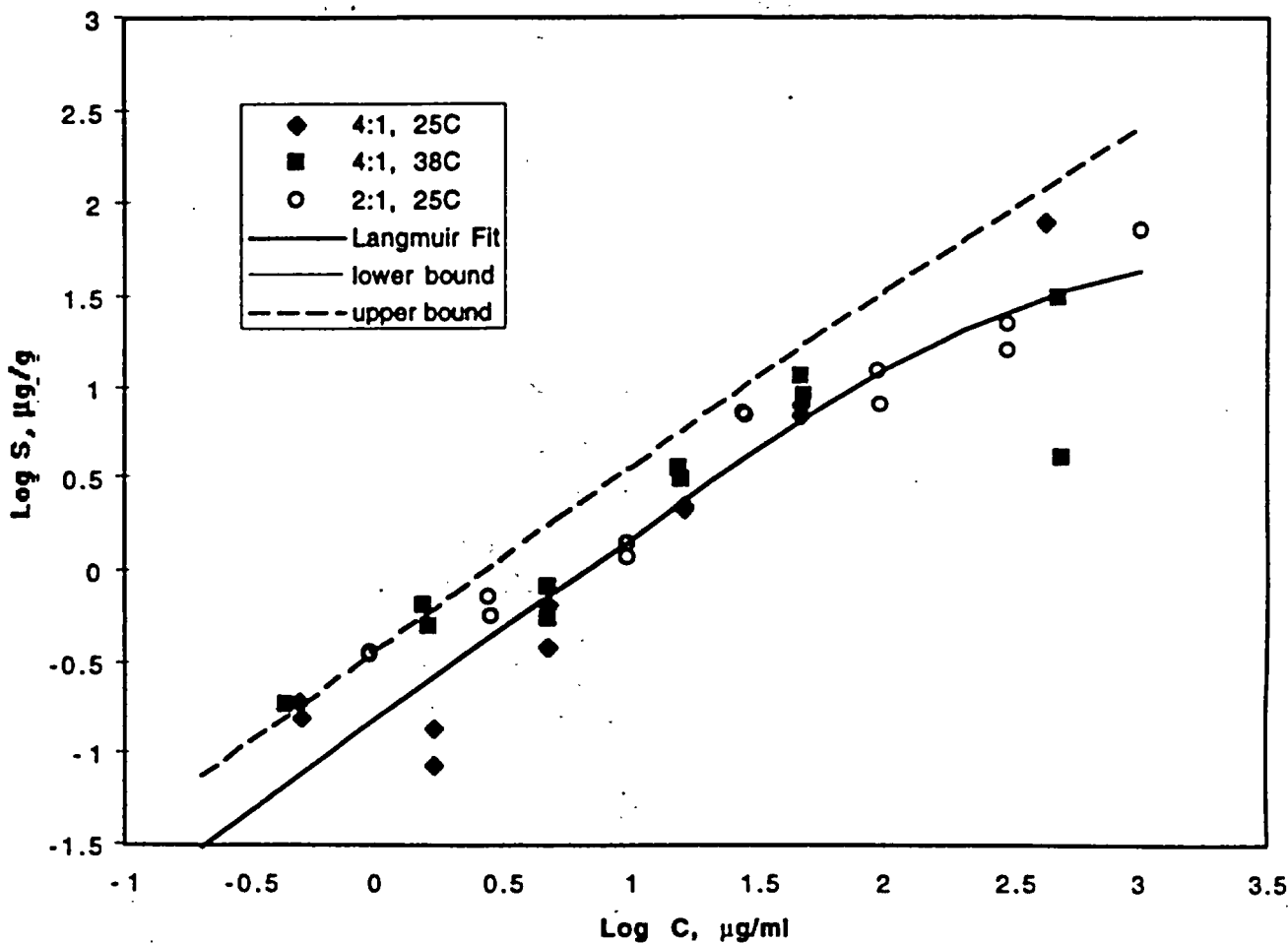


Figure 3-9. Lithium sorption data and fitted Langmuir isotherm for the upper Tram Tuff. The legend indicates the solution:solid ratio (ml:g) and the temperature of the experiments. The dashed lines are error bars associated with 5% analytical measurement error (lower error bound is off-scale over entire range of data). J-13 water was used in all experiments.

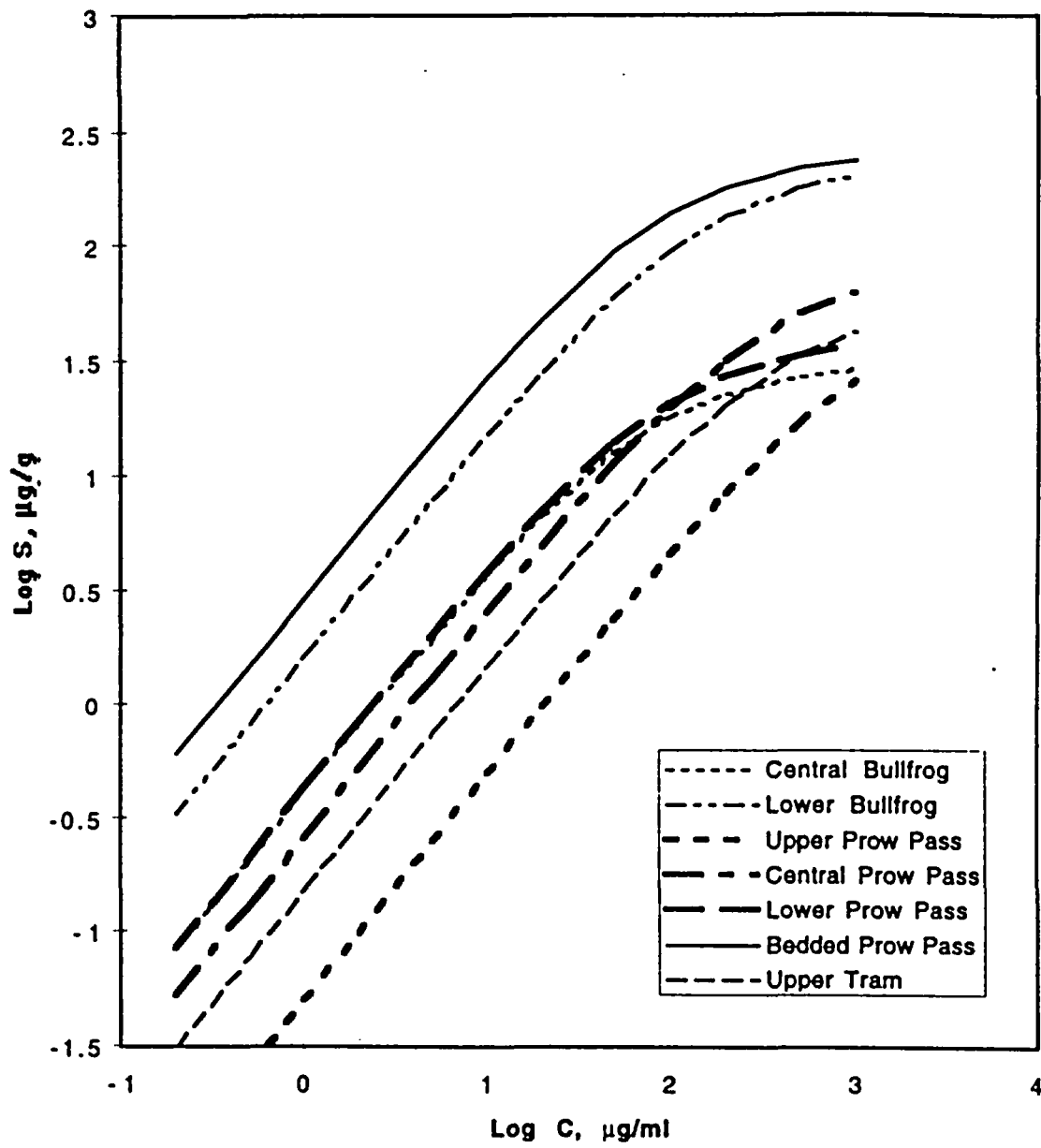


Figure 3-10. Fitted Langmuir isotherms for the seven C-holes tuffs.

4.0 Dynamic Laboratory Transport Experiments

Several dynamic laboratory transport experiments involving lithium ion were conducted to study sorbing tracer transport under flowing conditions in both crushed tuff columns and fractured C-holes cores. The crushed tuff column experiments were conducted to determine lithium sorption rate parameters under flowing conditions, and to study the effects of sorption nonlinearity under dynamic conditions. The fractured core experiments were conducted to study lithium transport under more realistic fracture flow conditions where matrix diffusion and sorption in the matrix should influence transport. The crushed tuff experiments are described in Section 4.1, and the fractured core experiments are described in Section 4.2.

4.1 Crushed Tuff Columns

Experimental Methods

A series of transport experiments was conducted in Plexiglas columns 91.44 cm in length and 0.62 cm in diameter. The columns were packed with crushed central Bullfrog Tuff (the same material that is identified in Section 3.0 as central Bullfrog Tuff from C#2 [location number 2 in Fig. 3-1]) using a wet slurry technique that minimizes layering, but also eliminates particles less than roughly 70 μm in size. With the crushed tuff, approximately 40-50% of the sample was not retained in the column. Column porosity was measured at 57% and dry bulk density was calculated at 1.14 g/mL by assuming a mineral density of 2.65 g/mL typical values for columns prepared in this fashion (e.g. Treher and Raybold, 1982; Thompson, 1989). Three columns were prepared identically. The column apparatus included a constant-rate pump, a valve to switch between a reservoir containing J-13 "background" water and a solution of lithium bromide in J-13 water, and an automatic fraction collector at the downstream end of the column. Each experiment began by pumping approximately 180 mL (roughly 12 pore volumes) of J-13 water through the column at a specified flow rate to equilibrate the tuff with groundwater chemistry. The input was then switched to the lithium bromide solution. Effluent samples were analyzed for lithium and bromide concentration by ion chromatography. In these tests, bromide was assumed to behave as an ideal nonsorbing tracer, in contrast to lithium, a reactive tracer.

Experiments were conducted with two tracer concentrations (approximately 5 mg/L and 20 mg/L) and two flow rates (1.6 and 2.2 mL/h); a 20 mg/L test was also performed at 9.73 mL/h. The different concentrations were intended to quantify effects of sorption nonlinearity, while the different flow rates were intended to reveal kinetically-controlled effects such as sorption nonequilibrium or diffusion-limited sorption. All tests were conducted at 25°C.

Results and Discussion

Results of the columns tests are presented in Table 4-1; breakthrough curves (BTCs) for one of the experiments are shown in Fig. 4-1. The first step in the analysis was the determination of the individual column's transport behavior by fitting a one-dimensional advection-dispersion equation to the bromide BTC, using RELAP, a one-

not RIB data?

dimensional semi-analytic code based on a LaPlace transform inversion method (Appendix A). All five bromide BTCs were fit very well, suggesting near ideal behavior. RELAP can work with a system of dimensionless variables, in which hydrodynamic dispersion is represented by the Peclet number, P_e , defined as L/α , where L is the column length and α the dispersivity. The Peclet numbers shown in Table 4-1 correspond to dispersivities of 0.2 - 0.3 cm, similar in scale to the column radius.

We then analyzed the lithium BTC for each experiment by holding the column's mean residence time and Peclet number fixed at the values determined for bromide, and varying the sorption behavior. RELAP's semi-analytic nature limits its sorption capabilities to a linear isotherm, so its numerical sister-code, RETRAN (Appendix A) was used to simulate Langmuir sorption behavior. Using the Langmuir sorption parameters resulting from the batch sorption studies to the central Bullfrog Tuff from well C#2 (Table 4-2; these represent a subset of the data shown in Fig. 3.2) and assuming local sorption equilibrium, we obtained curve (iv) in Fig. 4-1. Notice that this simulation matches the observed time of breakthrough very closely, but significantly overestimates the slope of the BTC. The observed lower slope (increased apparent dispersion) is symptomatic of kinetic effects (Valocchi, 1985); to explore this possibility, we relaxed the local equilibrium assumption and used RETRAN to better fit the observed BTC. RETRAN includes kinetic effects in terms of the dimensionless Damkohler number, Da , defined as $k\tau$, where k is a first order reaction rate constant and τ is the mean residence time in the column. The observed lithium BTC was well fit by setting Da to 18 [curve (v) in Fig. 4-1], corresponding to a forward rate constant of 2.2 hr^{-1} . This relatively rapid reaction rate is consistent with both ion-exchange theory and measurements of lithium sorption to Prow Pass Tuff (Fuentes et al., 1989), as discussed in Section 3.0.

Note that the rate constants shown in Table 4-1 reflect an effective rate constant for the entire sorption process, including both diffusion from the bulk liquid to the exchange site and the actual exchange process. While the latter should be a function only of the solution and medium, the former may depend on flow geometry, in turn a function of column packing. This sensitivity to column packing may explain why Table 4-1 shows that repeated tests in the same column give similar rate constants, but column 2 yielded consistently lower rate constants than the other two columns.

Isotherm nonlinearity can affect BTCs in two related but different fashions. The first effect of nonlinear sorption on a BTC reflects the fact that in the solute front itself, a distribution of concentrations occurs, ranging from background (in our case, close to 0 mg/L) to the peak influent concentration (here, 5 or 20 mg/L). Changes in retardation as a function of concentration will alter the shape of the breakthrough curve; specifically, decreased sorption and higher transport velocity at high concentration will sharpen the leading edge of the solute front. (Conversely, if the solute is applied as a pulse, with both a leading and trailing edge, this effect will retard the low concentrations at the end of the trailing edge, resulting in increased tailing.) We look for this effect by comparing the shape of the observed BTC to simulations assuming linear and nonlinear sorption.

This sharpening effect will be most pronounced in a high-concentration test, in which the leading edge of the front contains the widest range of concentrations. To determine whether sorption nonlinearity has affected the shape of the BTC, RELAP was used to attempt a linear sorption fit to the lithium BTC in Fig. 4-1. Both equilibrium and

nonequilibrium fits are shown in the figure; the linear sorption simulations yield results virtually indistinguishable from the Langmuir simulations. This implies that for the concentrations and conditions of the column studies, the nonlinearity of the sorption isotherm had no observable effect on the shape of the BTC. This is most likely due to the very low dispersivity of these laboratory columns; the low degree of dispersion keeps the solute front very sharp, and the concentration at any point in the column jumps from background to peak very rapidly. Thus, there is only a very small volume of intermediate concentration liquid in the column. In a higher-dispersion system where a larger portion of the column would contain solutions of varying concentration, nonlinear sorption would be more apparent. Because under the conditions of our tests, nonlinear sorption played no significant role in BTC shape; the rest of the column studies were analyzed assuming linear sorption, leading to the results presented in Table 4-1.

The second effect on nonlinearity arises because behind the solute front, solute concentrations are relatively constant and nonlinearity makes the ratio between dissolved and sorbed concentrations a function of dissolved concentration. This ratio controls the velocity of the solute front through the column, through its influence on the retardation factor (R_F), the ratio of average groundwater velocity to the velocity of the tracer front. This effect changes the position of the BTC as a function of concentration; decreased sorption at higher concentration will move the BTC earlier in time. We look for this effect by comparing measured R_{Fs} for different solution concentrations. Table A-3 shows that R_{Fs} for the 5 mg/L tests ranged from 2.2 to 2.3, with a mean of 2.25; R_{Fs} for the 20 mg/L tests ranged from 1.7 to 2.0, with a mean of 1.87. The observed decreased retardation at higher concentration qualitatively fits our prediction of the effect of nonlinear sorption. We now compare these results to quantitative predictions of nonlinear effects on R_F . For the Langmuir isotherm, the R_F can be shown to be (Fetter, 1993):

$$R_F = 1 + \frac{\rho_B}{\theta} \left(\frac{K_L S_{max}}{(1 + K_L C)^2} \right) \quad (4.1)$$

where ρ_B is the dry bulk density of the medium (g/mL) and θ is the volumetric moisture content, or porosity for a saturated medium.

By solving Eq. (4.1) with our batch Langmuir parameters and column values for ρ_B and θ values, we obtain retardation factor predictions of 2.11 for the 5 mg/L tests and 1.95 for the 20 mg/L tests. Overall these predictions match the observations very well, differing by 7% or less for both concentration levels. However, the observed difference in R_F at the two concentration levels somewhat exceeds that predicted by the model. This may reflect simple experimental variability due to the small number of tests conducted, or may indicate further physical complexities. Additional column studies covering a wider range of concentrations would help settle this question.

We conclude that under our experimental conditions, sorption nonlinearity affects the retardation of lithium, but not the shape of the BTC. This result implies that we can model transport under these conditions using the simple K_D linear sorption model by adjusting the K_D value as a function of solution concentration. Comparison of Eqs. (3.1) and (3.3) shows that at very low concentrations ($C \rightarrow 0$), the Langmuir model approaches the linear model with a K_D value equal to $S_{max} \cdot K_L$, or approximately 0.6 mL/g in the case of the central Bullfrog Tuff from C#2.

4.2 Fractured Core Columns

Laboratory-scale fractured tuff column transport experiments were conducted in two different induced fractures to provide more realistic experimental depictions of field-scale transport in fractured tuffs than can be achieved in crushed rock columns. These experiments also allow more detailed investigations of saturated zone transport processes than can be achieved in field experiments, where testing times, complexities, and costs are all considerably higher than in the laboratory (field tests also involve environmental permitting considerations that are not an issue with laboratory experiments). An additional objective of the fractured tuff column experiments was to obtain laboratory data under fracture flow conditions that would support more refined predictions of tracer transport in the Prow Pass member of the Crater Flat Tuff, where a reactive tracer test will be initiated in FY 1998.

Experimental Methods

Axial fractures were induced in intact C-Holes cores from the upper and central Prow Pass lithologies by striking them with a chisel and hammer. The cores were taken from location numbers 4 and 5 in Fig. 3-1, respectively (C#2, 533 m; and C#2 553 m). Perpendicular cuts were then made on both ends of the fractured cores using a rock saw. After cutting, the cores were approximately 16-cm and 17-cm long, respectively for the upper and central Prow Pass fractures, and both fractures were about 9.5-cm wide (the diameter of the core). Each core was pre-saturated under water and under reduced pressure (vacuum), and then encapsulated within a flow system, as shown in Fig. 4-2 (see also, Ware and Triay, 1995, 1997). The procedure for constructing the flow apparatus was as follows:

- Two end caps, each containing a narrow flow channel that fit exactly over the fracture trace at the ends of the cores, were machined out of Plexiglas stock. Three threaded access ports were drilled from the unmachined side of the end caps into the channel to allow introduction and withdrawal of solutions to/from the channel(s).
- After fixing one cap to an end of the core (using a silastic glue), the fracture trace along the sides of the core was coated with a silastic material, and then the entire side of the core was sealed by pouring a clear epoxy into the annulus formed between the core and a Plexiglas tube surrounding the core.
- The cores were then saturated under water and under strong reduced pressure until air bubbles no longer evolved.
- The remaining open ends of the cores were then fitted with the remaining end cap, and the cores were again saturated under water/reduced pressure.
- The flow apparatus was leak tested by placing several feet of head (of water) on one of the ends with the other end closed off.
- After ensuring there were no leaks, the hydraulic conductivity/aperture of the fractures were estimated by measuring the flow rate through the cores as a function of head difference across them. During these tests, the cores were

visually inspected for flow bypass through the annular region and for leakage of water out of the flow channels under the end caps. The hydraulic apertures were estimated to be 0.0141 cm and 0.0134 cm for the upper and central Prow Pass fractures, respectively.

After determining that the flow systems were satisfactory for further testing, tracer tests were conducted as follows:

- Flow of initially tracer-free J-13 water through the fracture was induced using a precision syringe pump.
- Flow was briefly interrupted, and tracer-bearing J-13 water was introduced in place of the tracer-free solution using a separate syringe pump.
- After a specified period of time (or volume of tracer solution), the inlet solution was switched back over to the tracer-free water, thus creating a finite-duration injection pulse of tracer solution to the fractured core.
- Effluent from the fractured core was collected in test tubes using an automatic fraction collector.
- The fractions were analyzed for tracers to establish tracer breakthrough curves. Iodide was analyzed by ion-selective electrode, PFBA and bromide were analyzed by ion chromatography, and lithium was analyzed by ICP-AES.

why iodide?

To date, five separate tracer experiments have been conducted in the upper Prow Pass Tuff core, and four experiments have been conducted in the central Prow Pass Tuff core. The experimental details in these tests are summarized in Tables 4-3 to 4-7. We first discuss the experiments in the upper Prow Pass core.

Three of the tests in the upper Prow Pass core involved the introduction of a sodium iodide pulse at three different flow rates (2.22 mL/hr, 8.65 mL/hr, and 19.76 mL/hr), with the objectives being to (1) determine tracer residence times so that additional experiments with other tracers could be optimized and (2) determine matrix diffusion parameters by comparing the breakthrough curves at the three different flow rates. The expectation was that iodide peak concentration and recovery would be lower as flow rates decreased because there would be more time for diffusion of iodide out of the fracture and into the stagnant water in the porous matrix at these lower rates. Testing at a single flow rate would not allow unambiguous estimation of matrix diffusion parameters because of the inability to distinguish between the effects of matrix diffusion and flow dispersion in the system. With three flow rates in the same fracture, it can be assumed that the effects of dispersion are approximately the same at each flow rate, and the difference in tracer responses can be attributed to differing amounts of matrix diffusion at the different residence times.

The other two experiments in the upper Prow Pass fracture involved injecting pulses of a solution containing PFBA and LiBr into the core at flow rates of 8.44 mL/hr and 6.33 mL/hr. The second PFBA/LiBr experiment was conducted because (1) an inadvertent flow interruption occurred during the first experiment when tracer concentrations were at their peaks, and (2) it was suspected that the volume of the flow system in the first experiment was different than in all the iodide experiments (see below). The flow volume in the second PFBA/LiBr experiment was more consistent

with those in the iodide experiments, which allowed less ambiguous comparisons between the breakthrough curves in the different experiments.

The PFBA/LiBr experiments also featured intentional flow interruptions during the tails of the breakthrough curves. These flow interruptions provided an additional means of evaluating matrix diffusion in the cores; the concentrations of the solute tracers were expected to rebound during the flow interruptions because tracers should diffuse back into the fracture from the matrix.

There were several objectives of the PFBA/LiBr experiments:

- (1) Determine if the PFBA and bromide breakthrough curves were consistent with the factor of ~3 difference in the matrix diffusion coefficients measured in diffusion cells (see Section 5.0). PFBA was expected to have a higher peak normalized concentration than bromide because of its smaller diffusion coefficient.
- (2) Determine if the lithium breakthrough curve, relative to PFBA and bromide, was consistent with the batch sorption and diffusion cell data.
- (3) Determine if the normalized PFBA and bromide breakthrough curves were consistent with the iodide breakthrough curves from the earlier experiments. The bromide breakthrough curve was expected to be similar to that for iodide at a comparable flow rate because bromide and iodide have similar diffusion coefficients (Newman, 1973).

If consistency were found for items (1) and (2), it would lend credibility to the hypothesis that the diffusion cell and batch sorption experiments provide estimates of transport parameters that can be reliably used to predict and interpret transport behavior in fractured systems. This consistency would further imply that it is valid to use laboratory estimates of transport parameters to refine and reduce uncertainty in the interpretations of field-scale transport tests, and ultimately to predict transport over long time and distance scales in the field.

The experiments conducted in the central Prow Pass Tuff core had the same objectives and followed a very similar sequence to the experiments in the upper Prow Pass core. These experiments included three tests using iodide at three different flow rates (11.48, 19.73, and 49.44 mL/hr), and one test involving the simultaneous injection of PFBA and LiBr. Compared to the tracer responses in the upper Prow Pass fracture, we expected to see less flow rate dependence of iodide transport and smaller differences in the breakthrough curves of bromide and PFBA because the central Prow Pass tuff was considerably less porous than the upper Prow Pass tuff ($\phi = 0.14$ and 0.27 respectively). Also, the diffusion coefficients of bromide and PFBA, as measured in the diffusion cell experiments (Section 5.0), were much lower in the central Prow Pass tuff than in the upper Prow Pass tuff. The results of the tracer tests in both cores are presented in the "Results and Discussion" subsection below.

data so measured values in the Lab

Interpretative Methods

The computer models RELAP and RETRAN (Appendix A) were used to interpret all tracer breakthrough curves obtained in the fractured cores. Briefly, these models simulate sorbing and nonsorbing tracer transport through a dual-porosity

system in which flow is assumed to occur in parallel-plate fractures that are separated by a matrix containing stagnant water in its pores. One-dimensional advective-dispersive transport is assumed to occur within the fractures, and one-dimensional diffusive mass transfer perpendicular to the fracture orientation is assumed to occur in the matrix. RELAP differs from RETRAN in that it is a semi-analytical model that is limited to simulating steady-state flow conditions and linear sorption isotherms. RETRAN is a finite-difference numerical model that can accommodate changing flow rates as well as nonlinear isotherms.

The tracer experiments were initially simulated using the parameter-fitting features of RELAP, which allow specified transport parameters to be systematically varied to obtain a best least-squares fit to one or more data sets (see Appendix A). A simultaneous fit to the iodide breakthrough curves in each core was obtained by adjusting the mean residence time, Peclet number (LV/D , where L = length of column, V = linear flow velocity through column, and D = dispersion coefficient in column), and the lumped parameter $\frac{\phi}{b}\sqrt{D_m}$ (where ϕ = matrix porosity, b = fracture half aperture, cm, and D_m = diffusion coefficient in the matrix, cm^2/sec) to achieve a best fit. After a fit was obtained, average fracture apertures ($2b$) were calculated by (1) dividing the fitted mean fluid residence time by the known volumetric flow rate through the fracture to obtain an estimate of the fracture volume, and then (2) dividing this volume by the product of the length and width of the fracture to obtain an aperture estimate. This aperture estimate assumes that the fracture is a parallel-plate flow channel. Matrix porosities (ϕ) were independently measured as part of the diffusion cell experiments (Section 5.0), so the fitted value of the lumped parameter $\frac{\phi}{b}\sqrt{D_m}$ effectively yielded a direct estimate of the matrix diffusion coefficient, D_m , because independent estimates of b and ϕ were already made. For any given set of iodide simulations, the mean residence times in the fracture were constrained to differ by the inverse of the ratio of the flow rates in the experiments, and the Peclet numbers and matrix diffusion coefficients were constrained to be identical (since the flow system and tracer were the same in each experiment).

This exercise was repeated for the PFBA and bromide data sets, except that in this case, the mean residence times and Peclet numbers were constrained to be identical (since the tracers were introduced simultaneously), and the matrix diffusion coefficients were constrained to differ by a factor of 3 (with bromide being larger, to be consistent with the diffusion cell data). After the column transport parameters were determined from the nonsorbing tracer data, one of two methods were used to fit the lithium breakthrough curve. Either RELAP was used to fit the lithium breakthrough curve by adjusting the fracture and matrix retardation coefficients (as appropriate), or the transport parameters calculated from the simultaneous PFBA and bromide fits were used in RETRAN to fit the lithium curve. The RETRAN code employs sorption parameters such as the sorption partition coefficient, K_D . The K_D used to fit the lithium data was chosen to correspond with batch sorption data. As in the field tracer test interpretations (Section 2.0), the lithium diffusion coefficient was assumed to be two-thirds that of bromide (Newman, 1973).

Because the lithium isotherm was known from batch sorption experiments to be nonlinear (Section 3.0), we also attempted to fit the lithium breakthrough curves by

assuming nonlinear Langmuir sorption behavior and adjusting isotherm parameters using RETRAN. However, the sorption parameters in RETRAN were constrained to be similar to the parameters measured in batch sorption experiments (Section 3.0). All other model parameters in the RETRAN simulations (mean residence time, Peclet number, and matrix diffusion mass transfer coefficients) were set equal to those determined from the RELAP analyses of the nonsorbing tracer responses, except that the lithium diffusion coefficient was adjusted to be two-thirds of the bromide diffusion coefficient, as described above. If the nonlinear isotherm fits to the lithium data offered a significant improvement over the linear isotherm fit provided by RELAP, it was taken to be a strong indication that nonlinear sorption behavior was influencing lithium transport in the fractures. However, measuring the nonlinearity or nonequilibrium of lithium sorption introduces added parameters which introduce ambiguity to the fitting procedure. Thus, for simplicity, lithium sorption was assumed to be linear in the fractured rock column tests.

In all tests featuring flow interruptions, RELAP was used to simulate the tracer breakthrough curves up until the time of the flow interruption (the first interruption if there were more than one). Predictions of tracer responses after flow interruptions were then made using RETRAN. In these cases, the transport parameters determined from RELAP simulations up until the time of the flow interruption were used in RETRAN to effectively extend the simulations to the end of the experiment(s).

Results and Discussion

The three normalized iodide breakthrough curves in the upper Prow Pass Tuff fracture and the best simultaneous fits to the three data sets are shown as a function of volume eluted from the fracture in Figure 4-3. The experimental and model parameters corresponding to the best fits are given in Table 4-3. The quality of the fits was not very sensitive to the value assumed for the iodide matrix diffusion coefficient. That is, changing the iodide matrix diffusion coefficient by as much as a factor of 2 did not significantly hinder the ability to fit the data as long as the mean residence time and Peclet number were allowed to vary.

Figure 4-4 shows the PFBA, bromide, and lithium breakthrough curves in the first PFBA/LiBr experiment in the upper Prow Pass Tuff fracture along with the best simultaneous fits to these data under the modeling constraints discussed in the previous section. The experimental and model parameters corresponding to this experiment are given in Table 4-4. The breakthrough curves from the first PFBA/LiBr experiment in the upper Prow Pass Tuff fracture may have been affected by an increase in the volume of the fracture or in the end caps of the flow system, as there was a significant delay in the arrival of all tracers and greater apparent tracer dispersion in this experiment compared to the iodide experiments in this fracture (Reimus et al. 1997). The apparent increase in volume could have resulted from an expansion of the flow apparatus (due to epoxy shrinkage, for instance), which would have resulted in an increase in fracture aperture (note the calculated mean fracture apertures in Tables 4-3 and 4-4). Another possible explanation is that there was some additional dead volume in the end caps during the first PFBA/LiBr experiment that was not present in the other experiments. This explanation is supported by the observation of a large air bubble (exact volume unknown) under the entrance end cap during all of the experiments except for the first PFBA/LiBr experiment (in which the end cap was almost completely

filled with water). If there were communication between the column inlet and this volume (when filled with water), the effective volume of the flow system could have been significantly increased, thus resulting in longer tracer travel times and greater apparent dispersion. Table 4-4 gives the parameters that resulted in good fits to the data assuming different residence times/dead volumes in the entrance end cap (assumed to be well-mixed and modeled in exactly the same way in RELAP as injection wellbore volumes). Despite the fact that there is considerable variability in the mean residence times for the experiment depending on what end cap dead volume was assumed, the fitted Peclet numbers and matrix diffusion coefficients of bromide and PFBA are in relatively good agreement in all cases. The diffusion coefficients also agree within a factor of two with the matrix diffusion coefficients deduced for these tracers in the other experiments in this fracture, and the bromide diffusion coefficient agrees quite well with that of iodide (Table 4-3), which is expected because these two anions are similar in size (Newman, 1973). The relatively good agreement between the iodide and bromide matrix diffusion coefficients deduced from the different experiments suggests that changes in the flow system did not preclude reasonable estimates of matrix diffusion coefficients.

Figure 4-5 is a plot of the breakthrough curve data for the second PFBA/LiBr test. Table 4-5 lists the experimental and numerical parameters for this experiment. As was seen in the first PFBA/LiBr experiment, numerical fits of the bromide and PFBA data for the second test resulted in a larger fracture aperture than was obtained from the simultaneous iodide fits. However, the difference in apparent aperture was not as great as it was for the first PFBA/LiBr experiment. Because there was an air bubble in the inlet flow manifold for the second PFBA/LiBr experiment, the end cap volume should have been similar to that in the iodide tests. We are currently exploring another hypothesis that might help explain apparent discrepancies in deduced fracture apertures/volumes. This hypothesis involves the sensitivity of the mean fluid residence time parameter to the solute first arrival during each experiment. The first iodide experiment in the upper Prow Pass fractured core resulted in an inordinately early first arrival, which may have caused the numerical solution algorithms to calculate an erroneously short residence time value for the core using the iodide data. There are several ways to check this possibility; the most obvious is to discount the suspect data and use RELAP to recalculate the transport parameters. This analysis are in progress.

Figures 4-6 and 4-7 show the iodide breakthrough curves and the PFBA/LiBr breakthrough curves, respectively, in the central Prow Pass Tuff fracture, along with RELAP/RETRAN fits to these data. Tables 4-6 and 4-7 list the model parameters corresponding to the best fits shown in Figures 4-6 and 4-7, respectively. It is apparent that the agreement between the iodide and PFBA/LiBr experiments is much better in the central Prow Pass Tuff fracture than it was in the upper Prow Pass Tuff fracture. For instance, there is very good agreement between the Peclet numbers and fracture apertures deduced from the two sets of experiments. It is also apparent that there is somewhat less matrix diffusion in the central Prow Pass Tuff fracture than in the upper Prow Pass Tuff fracture, as evidenced by the larger matrix diffusion coefficients in the latter core. This result is consistent with the results of the diffusion cell experiments discussed in Section 5.0.

Figures 4-4, 4-5 and 4-7 show that despite the relatively good agreement between the model and data for the PFBA and LiBr breakthrough curves in each fracture, the

rebound in tracer concentrations following flow interruptions in the tails of the breakthrough curves is underpredicted by the RETRAN simulations for the upper Prow Pass core in both tests. This result is unexplained at this time. For the central Prow Pass PFBA/LiBr experiment, RETRAN accurately predicts the experimental data collected during this planned flow interruption. One possible explanation for the upper Prow Pass core results is that there could be some advective flow out of the matrix and into the fractures during the shut-in period. Unfortunately, we have no direct evidence of such an advective flow. Another possible explanation is that we are seeing the influence of multiple rates of diffusion, as suggested by Haggerty and Gorelick (1995), although it is not immediately clear why the remainder of the tracer breakthrough curves can be adequately explained/predicted without invoking multiple diffusion rates. It is also not clear why one rock type would reflect this possible physical phenomenon and another rock type would not. It may be that such results are related in some way to the porosity or the tortuosity of the rock matrix. We will continue to study this possibility by conducting more flow interruptions in future fractured core experiments and in other rock types.

Of particular interest in the analysis of the fractured core experiments is the comparison of transport parameters deduced from these experiments with parameters deduced from the batch sorption and diffusion cell experiments. The matrix diffusion coefficients of bromide and PFBA in the upper Prow Pass Tuff diffusion cell experiments (see Section 5.0) were estimated to be about twice those deduced in the fractured core tests in this lithology. This discrepancy can be explained by recognizing that flow through the fracture was most likely channelized to some degree, and therefore, the effective aperture in the flow pathways was probably larger than the average aperture obtained by assuming a parallel-plate fracture (as described above). For every twofold increase in the effective half-aperture, b , the diffusion coefficient, D_m , must increase by a factor of four to maintain the same value of the lumped parameter, $\frac{\phi}{b} \sqrt{D_m}$. Thus, the factor of two discrepancy will disappear if it is assumed that the

planar area through which flow occurred in the fracture was a factor of $\sqrt{2}$ less than the entire planar area of the fracture. This amount of channeling is not unexpected; channeling to a greater degree was, in fact, deduced previously in fractured cores from the C-Holes (Reimus, 1995). Qualitative fracture channeling has been visualized at the laboratory-scale by others as well (Brown et al., 1998; Thompson, 1991).

Diffusion coefficients measured in diffusion cell experiments in the central Prow Pass Tuff were considerably smaller than those deduced from the fractured core tests in this lithology. This result may indicate that much of the diffusive mass transfer observed in the fractured core experiments occurred in stagnant zones within the fracture (near the fracture walls or in low flow regions within the fracture) rather than into the matrix proper. In this case, apparent diffusion coefficients would be expected to be much larger than those measured in the matrix.

Although we found that the fits to the lithium breakthrough curves could be slightly improved by assuming nonlinear Langmuir sorption, the fits obtained assuming a linear sorption isotherm were consistently quite satisfactory. We concluded that lithium sorption in the rock cores could be adequately approximated using a linear isotherm. This assumption is more justifiable for the experiments in which the lithium injection concentration was relatively low. The fitted linear distribution coefficient, K_D ,

obtained for lithium in the fractured core experiments was in relatively good agreement with the K_D s deduced in the batch sorption tests (see Section 3.0). The K_D value in the fractured core experiments was obtained by either goodness of fit using RETRAN or by dividing the product of the lithium matrix diffusion coefficient and matrix retardation coefficient (the lumped parameter determined in the RELAP simulations) by a diffusion coefficient that was assumed to be two-thirds of the bromide diffusion coefficient observed in the core experiments. Equation (2.1) was then used to calculate a K_D value from the fitted retardation coefficient.

An important point to note is the lack of agreement for the K_D value obtained for the two PFBA/LiBr tests in the upper Prow Pass core. In the first test, the lithium injection concentration was five times higher than in the second test. Thus, lithium transport in the first test should have been influenced more by nonlinear sorption than in the second. Analysis of this difference shows the opposite effect; that is, a greater difference between the bromide and lithium breakthrough curves was expected in the second test than in the first because of the higher expected degree of lithium sorption. The lower apparent sorption in the second test was perhaps due to some small amount of lithium remaining on sorption sites in the first test due to irreversible sorption, thus decreasing the available sorption sites in the second test (the lithium recovery in the first test was not complete). Chemical analysis of the other major cations (e.g., Na^+ , Ca^{2+} , and K^+) may help elucidate this hypothesis. If the transport behavior of these cations is different for the two experiments, then some amount of lithium may have remained sorbed to the matrix.

In all of the RELAP and RETRAN simulations, sorption was assumed to occur only in the matrix, with no sorption to fracture surfaces. This assumption is consistent with the fact that the fractures were artificially induced in an intact core (so there should have been no sorptive mineral coatings). The relatively good agreement between the lithium K_D values deduced from the batch sorption tests and the fractured core experiments lends validity to the practice of using sorption parameters deduced from simple laboratory experiments to predict sorbing solute transport in fractured media. This is one of the main goals of the Los Alamos C-holes testing effort.

Section 4.0 References

- Brown, S., Caprihan, A., and Hardy, R. Experimental observation of fluid flow channels in a single fracture. *J. Geophys. Res.* 103(B3), 5125-5132 (1998).
- Fetter, C. W. (1993). *Contaminant Hydrogeology*. New York, Macmillan Publishing Company.
- Fuentes, H. R., W. L. Polzer, E. H. Essington and B. D. Newman. Characterization of Reactive Tracers for C-Wells Field Experiment I: Electrostatic Sorption Mechanism, Lithium, Los Alamos National Laboratory, 1989.
- Haggerty, R. and Gorelick, S. M., Multiple-rate mass transfer for modeling diffusion and surface reactions in a media with pore-scale heterogeneity, *Water Resour. Res.*, 31(10), 2383-2400, 1995.

Newman, J. S., *Electrochemical Systems*, Prentice-Hall, Englewood Cliffs, NJ (1973).

Reimus, P. W., T. Callahan, M. Haga, H. J. Turin, D. Frostenson, K. Vought, and D. Counce. Results of Laboratory Characterization of Reactive Tracer Sorption to Prow Pass Tuffs, *YMP Milestone Report SP2379M4*, Los Alamos National Laboratory, 1997.,

Reimus, P. W., The Use of Synthetic Colloids in Tracer Transport Experiments in Saturated Rock Fractures, *Los Alamos National Laboratory Report LA-13004-T (also PhD Dissertation, University of New Mexico)*, Los Alamos National Laboratory, Los Alamos, NM (1995).

Thompson, J. L. Actinide behavior on crushed rock columns. *J. Radioanal. Nucl. Chem.*, 130(2): 353-364, 1989

Thompson, M. E., Numerical Simulation of Solute Transport in Rough Fractures, *J. Geophys. Res.*, 96(B3), 4157-4166, 1991.

Treher, E. N. and N. A. Raybold. The Elution of Radionuclides Through Columns of Crushed Rock from the Nevada Test Site, Los Alamos National Laboratory, 1982.

Valocchi, A. J. Validity of the Local Equilibrium Assumption for Modeling Sorbing Solute Transport Through Homogeneous Soils." *Water Resour. Res.*, 21(6): 808-820, 1985.

Ware, S. D. and Triay, I. R. Transport of Radionuclides through Natural Fractures under Saturated Conditions, *Yucca Mountain Site Characterization Project Milestone Report #3063*, Los Alamos National Laboratory, Los Alamos, NM (1995).

Ware, S. D. and Triay, I. R. Radionuclide Transport through Saturated Fractures, *Yucca Mountain Site Characterization Project Milestone Report SP3426M4*, Los Alamos National Laboratory, Los Alamos, NM (1997).

Section 4.0 Tables

Table 4-1. Results of crushed tuff column studies. Refer to text for notation.

Column	Flow Rate (mL/h)	Li Conc. (mg/L)	τ (hr)	Pe	R_F	k_d (hr ⁻¹)	Da
1	1.6	5	11	400	2.2	14	160
1	2.2	5	8.0	400	2.3	18	140
2	1.6	20	11	300	1.9	3.6	40
2	2.2	20	8.2	300	2.0	2.2	18
3	9.7	20	1.9	400	1.7	14	27

*influenced by
by bulk densities*

Table 4-2. Lithium isotherm parameters derived from batch sorption studies to central Bullfrog Tuff from C#2 (0.5 - 500 $\mu\text{g}/\text{mL}$ concentration range). Note that these data represent a subset of the data shown in Fig. 3-2.

<u>Linear</u>	
K_D	0.21 mL/g
<u>Freundlich</u>	
K_F	0.76 (mL/ μg) ^{0.82}
n	0.82
<u>Langmuir</u>	
K_L	5.3 x 10 ³ mL/ μg
S_{max}	110 $\mu\text{g}/\text{g}$

Table 4-3. Summary of experimental and numerically deduced parameters from the NaI tests in the upper Prow Pass fractured core (16.1 cm long by 9.5 cm diameter).

<i>Parameter</i>	<i>First I Test</i>	<i>Second I Test</i>	<i>Third I Test</i>
Experimental Parameters			
Injection flow rate (mL/hr)	2.22	19.76	8.65
Injection duration (hr)	31.00	2.95	7.03
Injection concentration (mg/L)	1000.	999.3	1000.
Flush flow rate (mL/hr)	2.00	20.16	8.29
Flow interruption, hrs into test (duration, hr)	None	None	None
Modeling Best-fit Parameters			
Mean fluid residence time (hr)	4.10	0.46	1.05
Average fracture aperture (cm)	0.060	0.060	0.060
Peclet number	33.	33.	33.
Dispersivity (cm)	0.49	0.49	0.49
Matrix diffusion coefficient ($\times 10^{-6} \text{ cm}^2 \text{ s}^{-1}$)	3.6	3.6	3.6

Table 4-4. Summary of experimental and numerically deduced parameters from the first PFBA/LiBr test (1997) in the upper Prow Pass fractured core (16.1 cm long by 9.5 cm diameter).

<i>Parameter</i>		Experimental Parameters			
Injection flow rate (mL/hr)		8.44			
Injection duration (hr)		19.2			
Injection concentration (mg/L)		278 (PFBA)			
		11400 (Br ⁻)			
		1010 (Li ⁺)			
Flush flow rate (mL/hr)		8.03			
Flow interruption, hrs into test		19.2 (1.35)			
(duration, hr)		50.4 (14.25)			
		Modeling Best-fit Parameters			
End cap residence time (hr)	0	0.67	1.5	2	
Mean fluid residence time (hr)	4.4	3.8	3.0	2.2	
Average fracture aperture (cm)	0.233	0.202	0.159	0.117	
Peclet number	5.2	4.0	3.5	4.0	
Dispersivity (cm)	3.1	4.0	4.57	4.0	
	1.2	1.1	1.4	1.3	
Matrix diffusion coefficient (x10 ⁻⁶ cm ² s ⁻¹)	(PFBA)	(PFBA)	(PFBA)	(PFBA)	
	3.5 (Br ⁻)	3.3 (Br ⁻)	4.1 (Br ⁻)	3.9 (Br ⁻)	
	2.2 (Li ⁺) ^a	2.1 (Li ⁺) ^a	2.6 (Li ⁺) ^a	2.5 (Li ⁺) ^a	
Lithium matrix retardation coefficient ^b	3	3	3	3	
Lithium matrix K _D (L kg ⁻¹) ^c	0.28	0.28	0.28	0.28	

^aAssumed to be 0.67 times the bromide matrix diffusivity, based on results of diffusion cell test.

^bObtained from RELAP fit to rising portion of breakthrough curve.

^cCalculated from the retardation coefficient using equation (2.1).

Table 4-5. Summary of experimental and numerically deduced parameters from the second PFBA/LiBr test (1998) in the upper Prow Pass fractured core (16.1 cm long by 9.5 cm diameter).

<i>Parameter</i>	<i>PFBA/LiBr Test</i>
Experimental Parameters	
Injection flow rate (mL/hr)	6.33
Injection duration (hr)	11.21
Injection concentration (mg/L)	766 (PFBA)
	2528 (Br ⁻)
	216 (Li ⁺)
Flush flow rate (mL/hr)	6.42
Flow interruption, hrs into test (duration, hr)	43.58 (20.00)
Modeling Best-fit Parameters	
Mean fluid residence time (hr)	3.00
Average fracture aperture (cm)	0.100
Peclet number	6.5
Dispersivity (cm)	2.5
Matrix diffusion coefficient ($\times 10^{-6}$ cm ² s ⁻¹)	1.60 (PFBA)
	4.80 (Br ⁻)
	3.20 (Li ⁺) ^a
Lithium matrix retardation coefficient ^b	0.05
Lithium matrix K _D (L kg ⁻¹) ^c	1.35

^aAssumed to be 0.63 times the bromide matrix diffusivity, based on results of the 1997 diffusion cell test.

^bParameter estimated in RETRAN corresponding to batch sorption data.

^cCalculated from the retardation coefficient using equation (2.1).

Table 4-6. Summary of experimental and numerically deduced parameters from the NaI tests in the central Prow Pass fractured core (17.3 cm long by 9.5 cm diameter).

<i>Parameter</i>	<i>First I Test</i>	<i>Second I Test</i>	<i>Third I Test</i>
Experimental Parameters			
Injection flow rate (mL/hr)	19.73	49.44	11.48
Injection duration (hr)	4.09	1.56	6.37
Injection concentration (mg/L)	1000.	1000.	1000.
Flush flow rate (mL/hr)	20.07	49.60	11.78
Flow interruption, hrs into test (duration, hr)	None	None	None
Modeling Best-fit Parameters			
Mean fluid residence time (hr)	0.55	0.22	0.95
Average fracture aperture (cm)	0.066	0.066	0.066
Peclet number	31.	31.	31.
Dispersivity (cm)	0.56	0.56	0.56
Matrix diffusion coefficient ($\times 10^{-6}$ cm ² s ⁻¹)	2.60	2.60	2.60

Table 4-7. Summary of experimental and numerically deduced parameters from the PFBA/LiBr test in the central Prow Pass fractured core (17.3 cm long by 9.5 cm diameter).

<i>Parameter</i>	<i>PFBA/LiBr Test</i>
	Experimental Parameters
Injection flow rate (mL/hr)	5.92
Injection duration (hr)	11.97
Injection concentration (mg/L)	766 (PFBA)
	2528 (Br ⁻)
	216 (Li ⁺)
Flush flow rate (mL/hr)	5.98
Flow interruption, hrs into test (duration, hr)	42.50 (20.00)
	Modeling Best Fit Parameters
Mean fluid residence time (hr)	1.89
Average fracture aperture (cm)	0.068
Peclet number	28.
Dispersivity (cm)	0.52
Matrix diffusion coefficient ($\times 10^{-6}$ cm ² s ⁻¹)	0.80 (PFBA)
	1.80 (Br ⁻)
	1.07 (Li ⁺) ^a
Lithium matrix retardation coefficient ^b	4.5
Lithium matrix K_p (L kg ⁻¹) ^c	0.25

^aAssumed to be 0.67 times the bromide matrix diffusivity, based on results of the 1997 diffusion cell test.

^bParameter estimated in RETRAN corresponding to batch sorption data.

^cCalculated from the retardation coefficient using equation (2.1).

Section 4.0 Figures

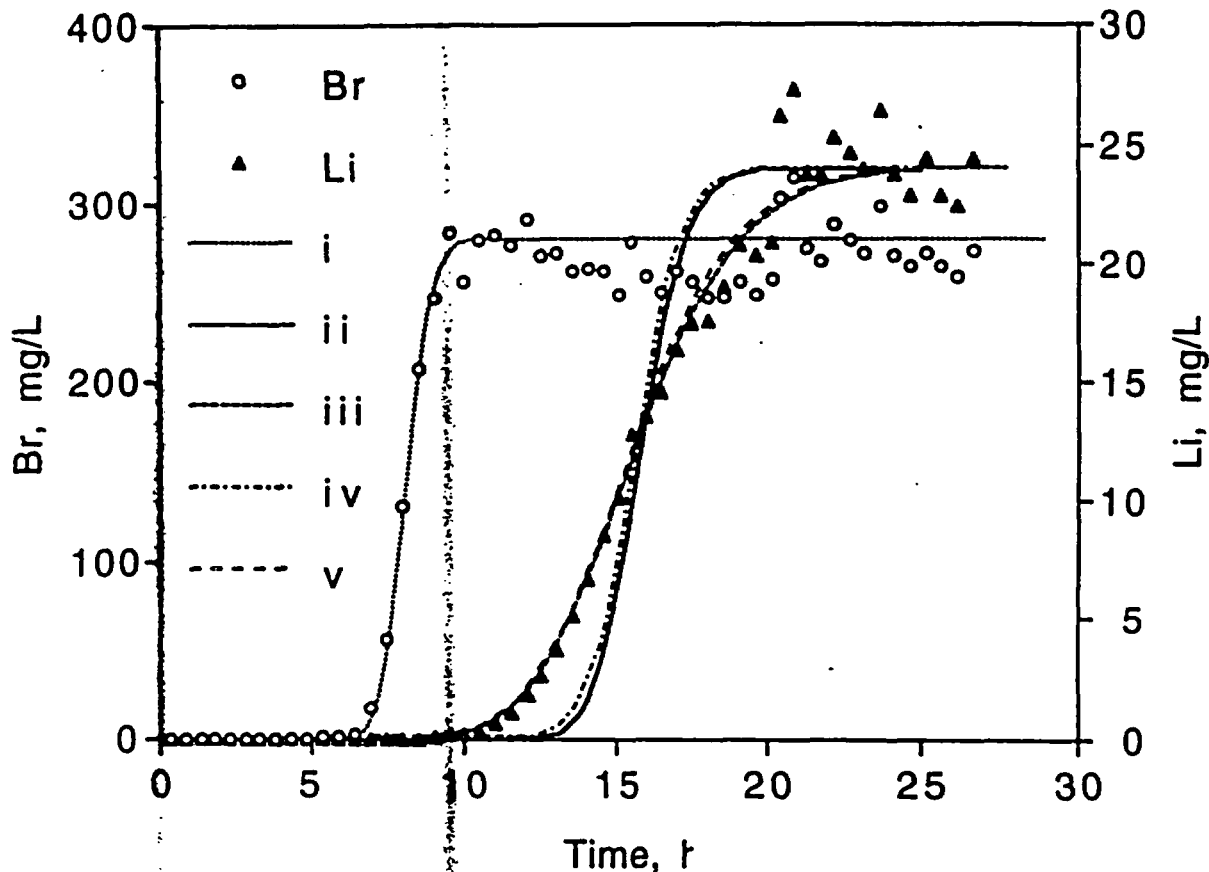
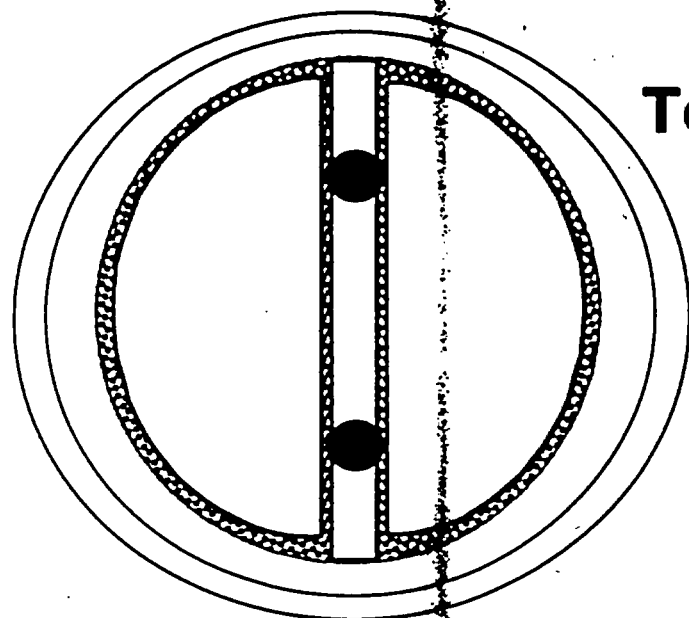
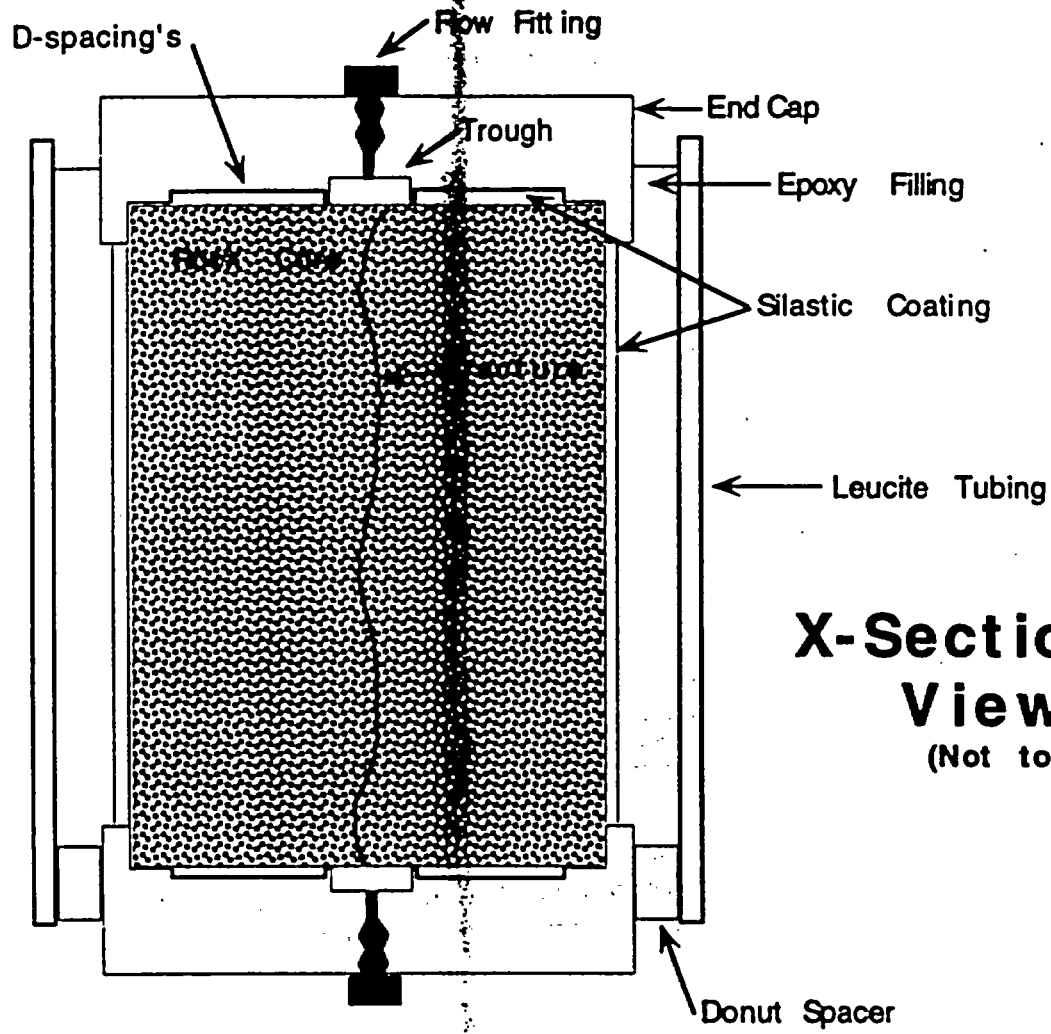


Figure 4-1. Bromide and lithium breakthrough curves in Column 2 at a flow rate of 2.2 mL/h, and corresponding fits to data. (i) Fit to bromide data with a Peclet number of 300, (ii) fit to lithium data assuming linear isotherm ($R_F = 2.0$) with equilibrium sorption, (iii) fit to lithium data assuming linear isotherm with a forward rate constant of 2.2 h^{-1} , (iv) fit to lithium data assuming a Langmuir isotherm with equilibrium sorption, and (v) fit to lithium data assuming a Langmuir isotherm with a forward rate constant of 2.2 h^{-1} . Langmuir isotherm parameters: $K_L = 0.0053 \text{ mL}/\mu\text{g}$ and $S_{\text{max}} = 110 \mu\text{g}/\text{g}$ (batch isotherm values obtained for lithium on central Bullfrog Tuff from C#2).



Top View
(Not to Scale)



X-Sectional View
(Not to Scale)

Figure 4-2. Schematic drawing of fractured core column apparatus.

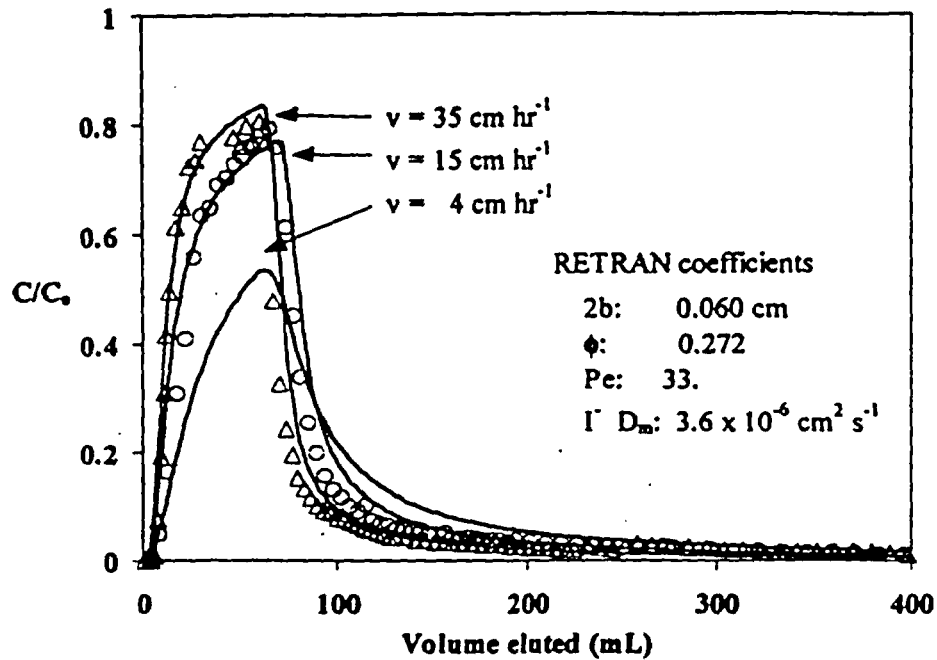


Fig. 4-3. Breakthrough curves and RETRAN fits of the NaI experiments in the upper Prow Pass fractured rock core.

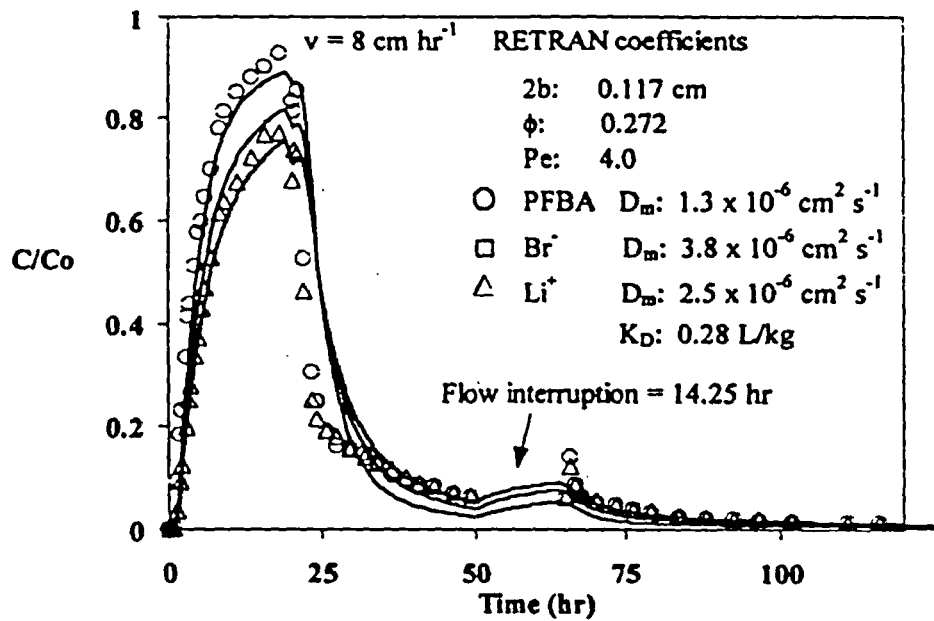


Fig. 4-4. Breakthrough curves and RETRAN fits of the first PFBA/LiBr experiment in the upper Prow Pass fractured rock core.

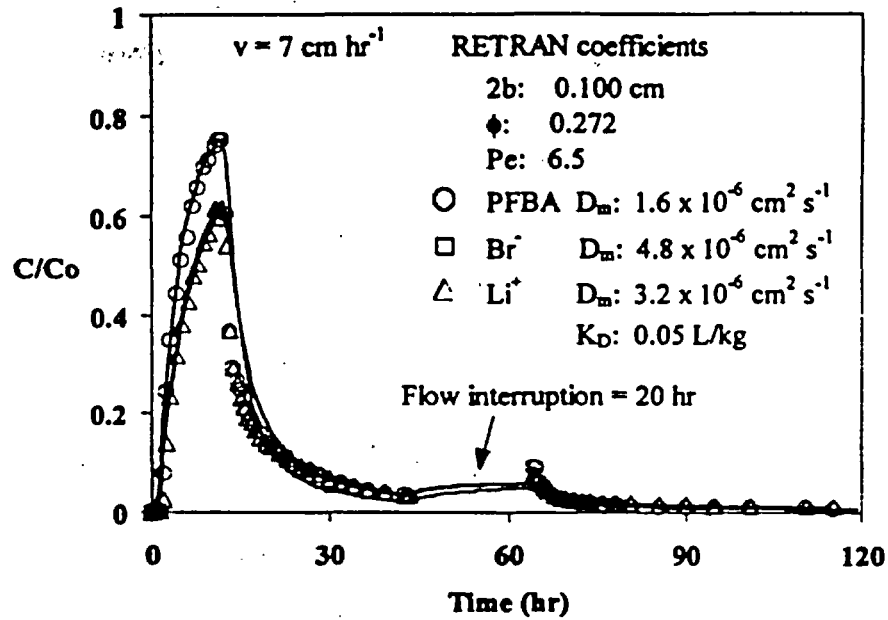


Fig 4-5. Breakthrough curves and RETRAN fits of the second PFBA/LiBr experiment in the upper Prow Pass fractured rock core.

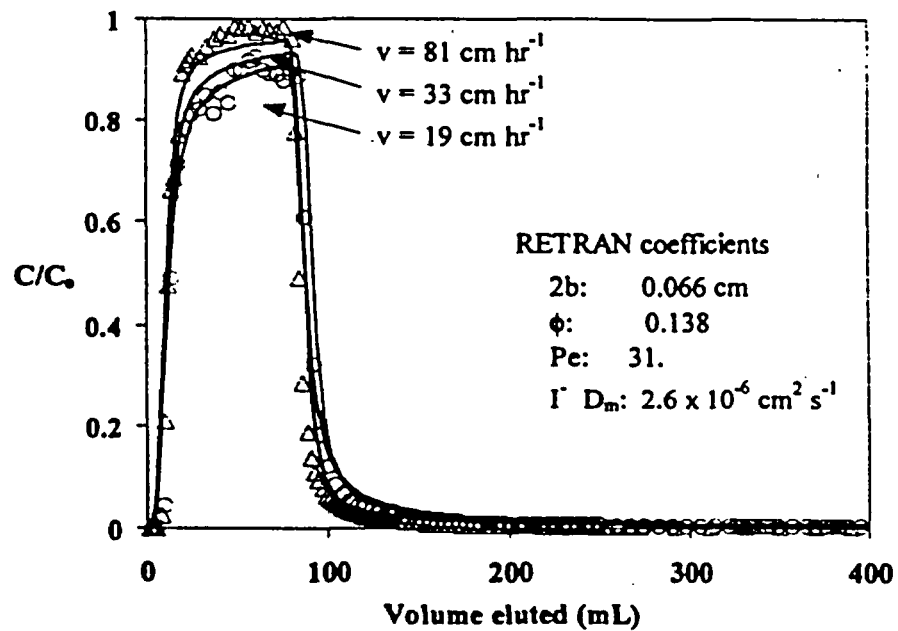


Fig 4-6. Breakthrough curves and RETRAN fits of the iodide experiments in the central Prow Pass fractured rock core.

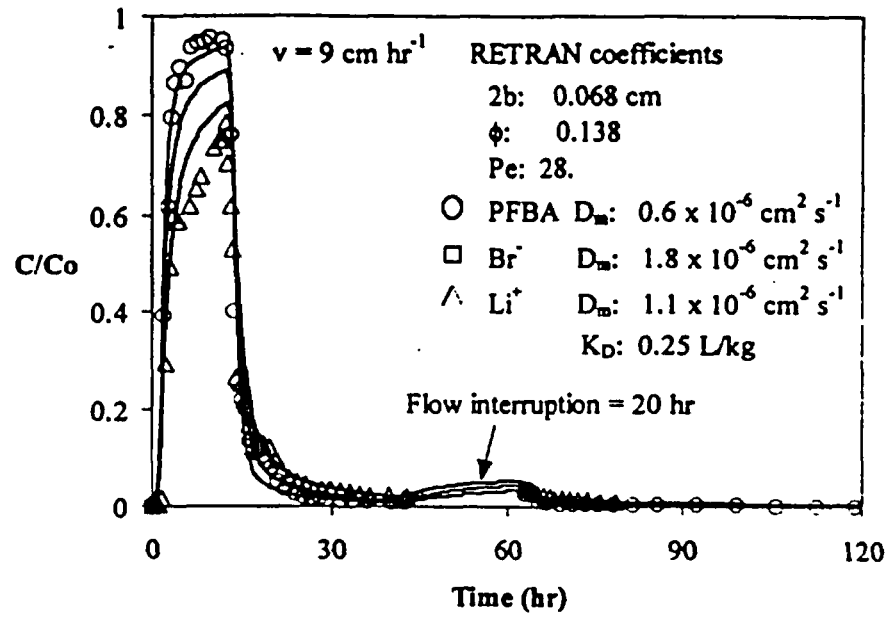


Fig. 4-7. Breakthrough curves and RETRAN fits of the LiBr/PFBA experiment in the central Prow Pass fractured rock core.

5.0 Diffusion Cell Experiments

Methods

Six diffusion cell experiments were conducted to determine diffusion coefficients of PFBA and bromide ion in five different C-holes tuff matrices. Estimates of matrix diffusion coefficients are important because they can greatly reduce uncertainty in interpreting and predicting both field-scale and laboratory-scale tracer experiments. One of the tests was a repeat experiment using a different core from the same interval as another test (the lower Prow Pass Tuff). This test was conducted to determine the reproducibility and variability of the experiments. The five different intervals tested in the diffusion cell experiments represented all of the major lithologies in either the previously-conducted Bullfrog field tracer test or the upcoming Prow Pass reactive tracer test.

A schematic drawing of the experimental diffusion cell apparatus is illustrated in Fig. 5-1. The apparatus consists of two plexiglass reservoirs, one large and one small, separated by a "pellet" of tuff, which is cut/cored from C-holes core and incorporated into either a flat epoxy cast or an RTV silicone cast of the same thickness as the pellet. After saturating the tuff, experiments were initiated by carefully pouring a solution containing PFBA and LiBr into the large reservoir and tracer-free solution into the small reservoir. The pressures in the two reservoirs were kept approximately equal to minimize advective flow through the tuff, thus ensuring that tracer movement through the tuff was by diffusion only. The small reservoir was kept well mixed with a magnetic stir bar and flushed continuously at a relatively low flow rate. The flush water was collected in an automatic fraction collector, and fractions were analyzed for tracers to establish breakthrough curves through the tuff from which diffusion coefficients could be estimated. As in the other laboratory experiments, PFBA and bromide were analyzed by ion chromatography, and lithium was analyzed by inductively-coupled plasma-atomic emission spectrometry (ICP-AES). Filtered J-13 water or synthetic J-13 water (a sodium/calcium bicarbonate solution having the same ionic strength as J-13 water) were used in all experiments.

The porosities of the tuffs were measured by subtracting dry weights from saturated weights of intact tuff samples and dividing by the volumes of the samples (measured by water displacement). Porosity measurements were used to obtain unambiguous estimates of diffusion coefficients in the tuff matrices (see equations below). Hydraulic conductivities/permeabilities of the tuffs were also measured by imposing a known pressure difference across the tuff pellets either before or after a diffusion experiment was conducted. The flow through the pellets at the imposed pressure difference was measured by weighing the water that flowed through the pellet over a specified amount of time. Hydraulic conductivities were then calculated from the following equation:

$$K = \frac{QL}{A \Delta H} \quad (5.1)$$

where, K = hydraulic conductivity, cm/sec
 ΔH = water height (head) difference across pellet, cm
 A = surface area of pellet, cm²
 Q = volumetric flow rate through pellet, ml/sec
 L = thickness of pellet, cm.

Permeabilities (in millidarcys) were calculated from hydraulic conductivities using the following well-known formula (Freeze and Cherry, 1979)

$$k = \left(1.013 \times 10^{12} \frac{\text{mD}}{\text{cm}^2} \right) \frac{K \mu}{\rho g} \quad (5.2)$$

where, k = permeability, millidarcys
 μ = water viscosity, g/cm-sec
 ρ = water density, g/cm³
 g = acceleration due to gravity, cm/sec².

To estimate diffusion coefficients, it was assumed that the tracers moved according to one-dimensional diffusive transport through the tuff pellets. The one-dimensional diffusion equation is:

$$\frac{\partial c}{\partial t} = \frac{D}{R} \frac{\partial^2 c}{\partial x^2} \quad (5.3)$$

where, c = tracer concentration, $\mu\text{g/mL}$
 D = diffusion coefficient, cm²/sec
 R = retardation factor (1 for nonsorbing solutes),
 x = distance, cm
 t = time, sec.

Although analytical solutions to this simple partial differential equation exist for simple boundary conditions (Carslaw and Jaeger, 1959), the time-dependent concentration boundary conditions at the inlet and outlet reservoirs in the diffusion cell experiments demand a numerical solution. Thus, equation (5.3) was solved using an implicit finite-difference technique. The equations describing the tracer concentrations in the inlet and the outlet reservoirs (the first and last finite difference nodes), respectively, were:

$$\frac{\partial c_i}{\partial t} = \frac{\phi \pi r^2 D}{V_i} \left. \frac{\partial c}{\partial x} \right|_{x=0} \quad (5.4)$$

$$\frac{\partial c_o}{\partial t} = -\frac{\phi \pi r^2 D}{V_o} \left. \frac{\partial c}{\partial x} \right|_{x=L} - \frac{Q}{V_o} c_o \quad (5.5)$$

where, c_i = tracer concentration in inlet reservoir, $\mu\text{g/mL}$
 c_o = tracer concentration in outlet reservoir, $\mu\text{g/mL}$
 V_i = volume of inlet reservoir, mL
 V_o = volume of outlet reservoir, mL
 Q = flush rate of outlet reservoir, mL/sec
 ϕ = porosity of tuff
 r = radius of tuff "pellet", cm
 L = thickness of tuff "pellet", cm.

The numerical solution of equations (5.3), (5.4), and (5.5) was obtained using a modified version of the RETRAN computer code called DIFCEL. DIFCEL allows the user to specify changes in the flush rate, Q , with time, which was necessary to simulate the manner in which the experiments were conducted.

Results and Discussion

Figs. 5-2 through 5-7 show the breakthrough curves of the bromide and PFBA in each of the six diffusion cells along with "fits" to the data obtained using DIFCEL. The "fits" are not actual least-squares fits; rather, they were obtained by manual adjustment of the diffusion coefficients until a reasonable match to the data was obtained. The apparent discontinuities in some of the data sets and the corresponding model predictions are a consequence of changes in the flush rate through the outlet reservoirs. A decrease in concentration occurs when the flush rate is increased and vice-versa.

The resulting estimates of tracer diffusion coefficients in each diffusion cell are given in Table 5-1 (measured tuff porosities, pellet thicknesses, and tuff permeabilities are also listed in this table). It is apparent that there is about an order of magnitude range of diffusion coefficients in the various tuff lithologies. Figs. 5-8 and 5-9 show the bromide diffusion coefficients in the tuff matrices as a function of porosity and permeability, respectively, for the five different C-holes tuffs. Although the diffusion coefficients are not well correlated with porosity, they are quite well correlated with permeability (on a log-log scale). This result suggests that permeability may be a good predictor of matrix diffusion coefficients. Such correlations could prove useful for estimating matrix diffusion coefficients; as diffusion coefficients are typically more difficult to measure than matrix properties such as permeabilities.

Table 5-1 shows that excellent agreement was obtained between the two diffusion cell experiments conducted in the same lithology (the lower Prow Pass Tuff). This result suggests that the experiments have reasonably good reproducibility, although certainly more experiments should be conducted in the same lithologies before measurement uncertainty and tuff variability can be properly assessed.

It is interesting that although the PFBA and bromide diffusion coefficients are significantly different in the different tuffs, the ratios of the diffusion coefficients are approximately the same in each tuff. This result suggests that we successfully eliminated advection through the tuff pellets, as any advection would result in

different ratios in different tests. The factor of ~3 difference in the diffusion coefficients of the PFBA and bromide is greater than the factor of 2 difference assumed by Reimus and Turin (1997) in their analyses of the Bullfrog Tuff reactive tracer field test data, which is one of the reasons the Bullfrog test data are reinterpreted in this report.

References for Section 5.0

Carslaw, H. S. and Jaeger, J. C. *Conduction of Heat in Solids*, 2nd ed., Oxford University Press, Oxford (1959).

Freeze, R. A. and Cherry, J. A. *Groundwater*, Prentice Hall, Englewood Cliffs, NJ (1979).

Reimus, P. W. and Turin, H. J. Draft Report of Results of Hydraulic and Tracer Tests at the C-Holes Complex, *Yucca Mountain Site Characterization Project Milestone Report SP23APMD*, Los Alamos National Laboratory, Los Alamos, NM (1997).

Table for Section 5.0

Table 5-1. Measured matrix diffusion coefficients of bromide and PFBA in C-holes tuffs. Measured tuff porosities and permeabilities are also reported. Synthetic J-13 water was used for the experiments involving the first 3 tuffs. Filtered J-13 water was used in the other 3 experiments.

Tuff ⁽¹⁾	Porosity	Matrix Diff. Coef., cm ² /s X 10 ⁶				
		Permeability, mDarcy	L, cm ⁽²⁾	Br	PFBA	Br/PFBA
Central Bullfrog (1)	0.094	0.00107	1.16	0.45	0.13	3.46
Lower Bullfrog (3)	0.298	0.0949	0.84	1.0	0.35	2.86
Upper Prow (4)	0.272	4.72	0.91	6.0	1.9	3.16
Central Prow (5)	0.138	0.000786	1.23	0.4	0.13	3.08
Lower Prow-1 (6)	0.288	0.455	2.27	3.0	1.1	2.73
Lower Prow-2 (6)	0.288	0.455	1.82	3.0	1.0	3.0

⁽¹⁾Numbers in parentheses correspond to numbers in Fig. 3-1 (which shows locations where core was collected from the C-holes) and in Table 3-2 (which lists actual depths associated with the cores).

⁽²⁾L = thickness of tuff wafer.

Figures for Section 5.0

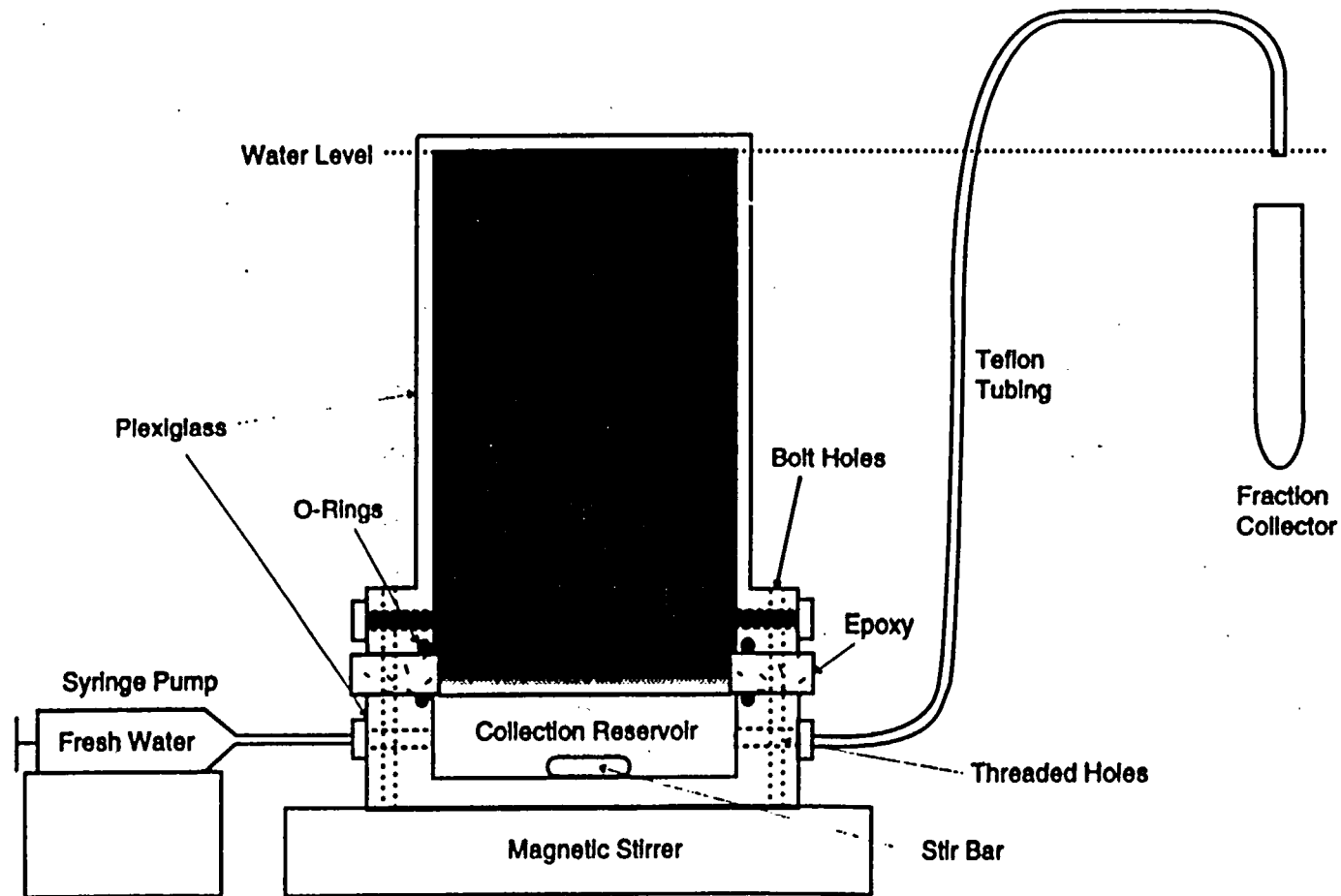


Figure 5-1. Schematic drawing of diffusion cell apparatus. Collection reservoir is continuously flushed by syringe pump, allowing automatic collection of samples.

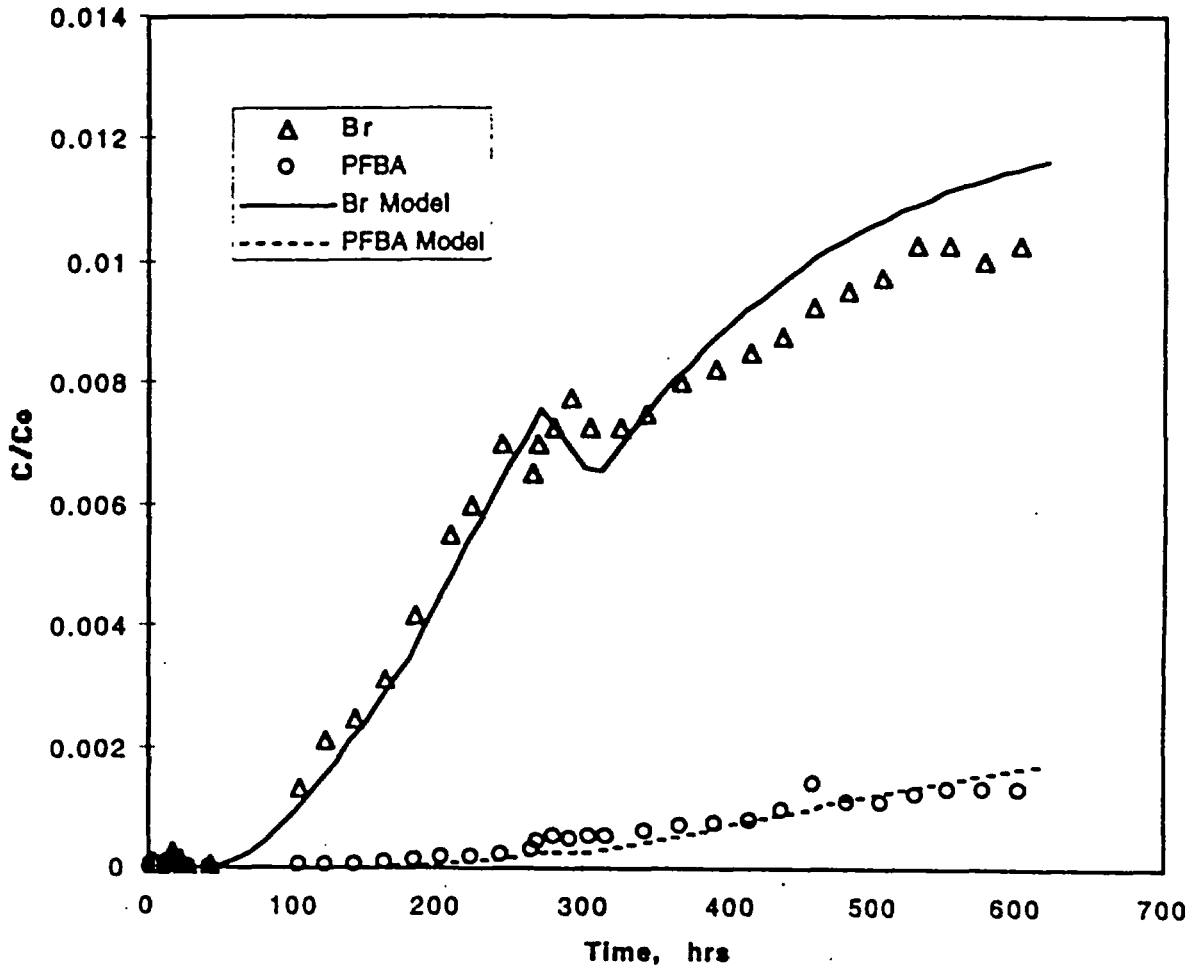


Figure 5-2. Diffusion cell data and DIFCEL model fits for bromide and PFBA in the central Bullfrog Tuff. Diffusion coefficients are given in Table 5-1.

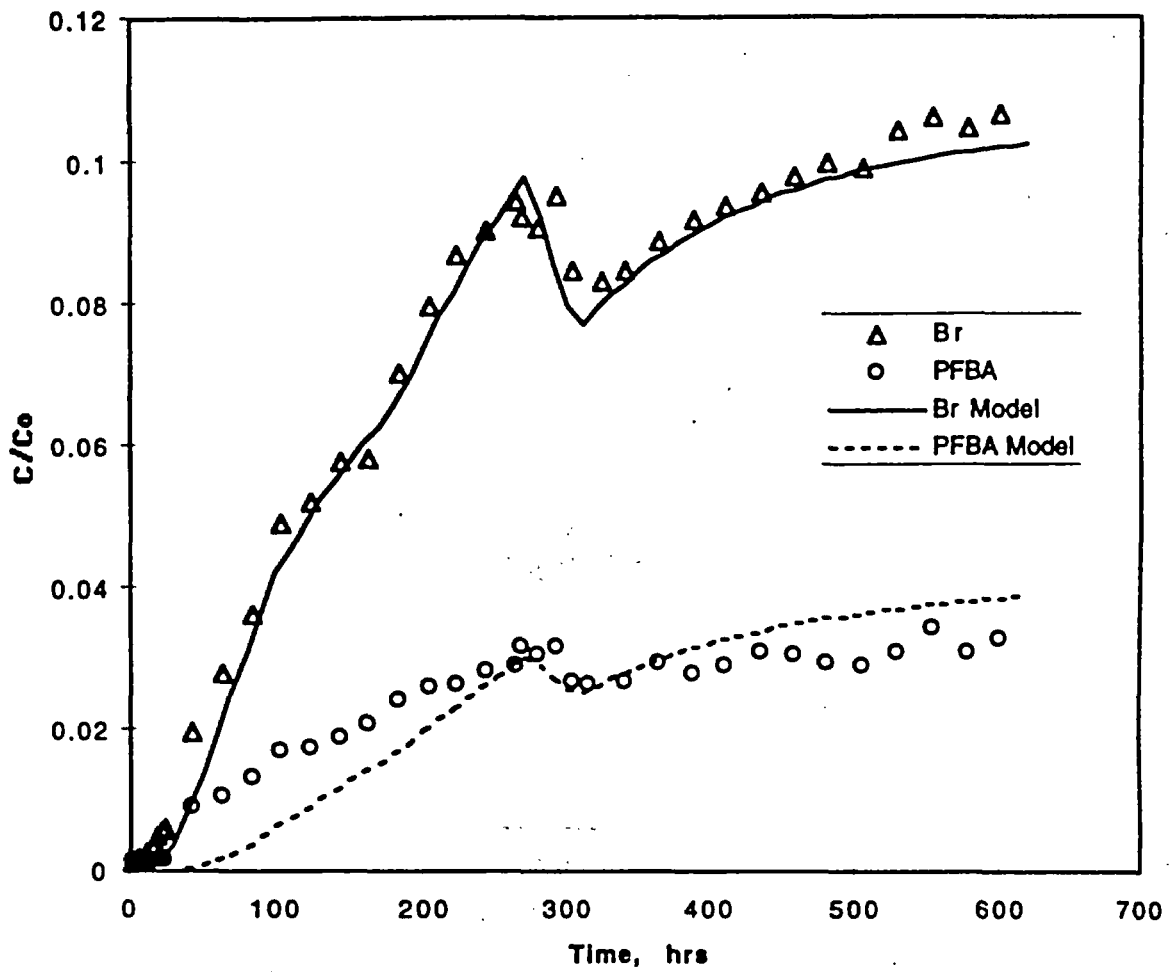


Figure 5-3. Diffusion cell data and DIFCEL model fits for bromide and PFBA in the lower Bullfrog Tuff. Diffusion coefficients are given in Table 5-1.

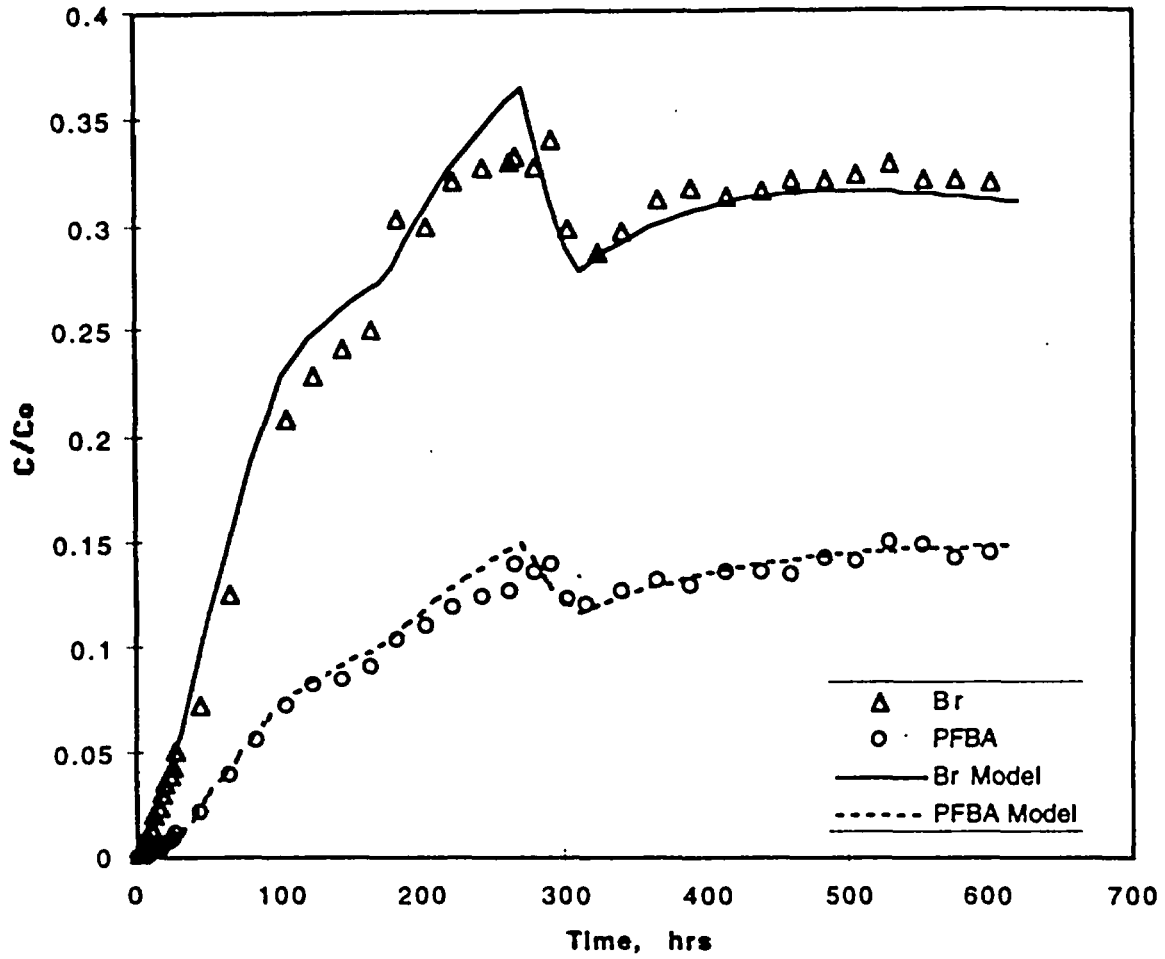


Figure 5-4. Diffusion cell data and DIFCEL model fits for bromide and PFBA in the upper Prow Pass Tuff. Diffusion coefficients are given in Table 5-1.

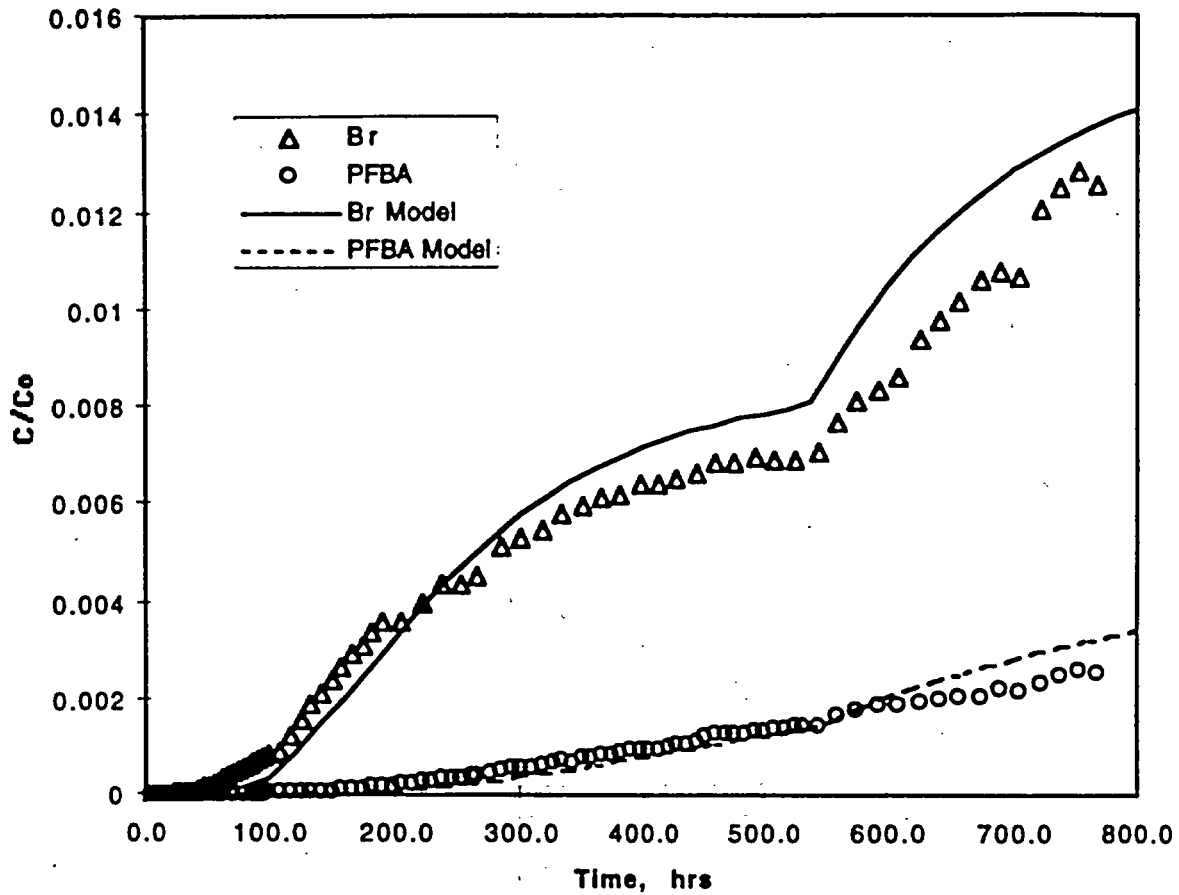


Figure 5-5. Diffusion cell data and DIFCEL model fits for bromide and PFBA in the central Prow Pass Tuff. Diffusion coefficients are given in Table 5-1.

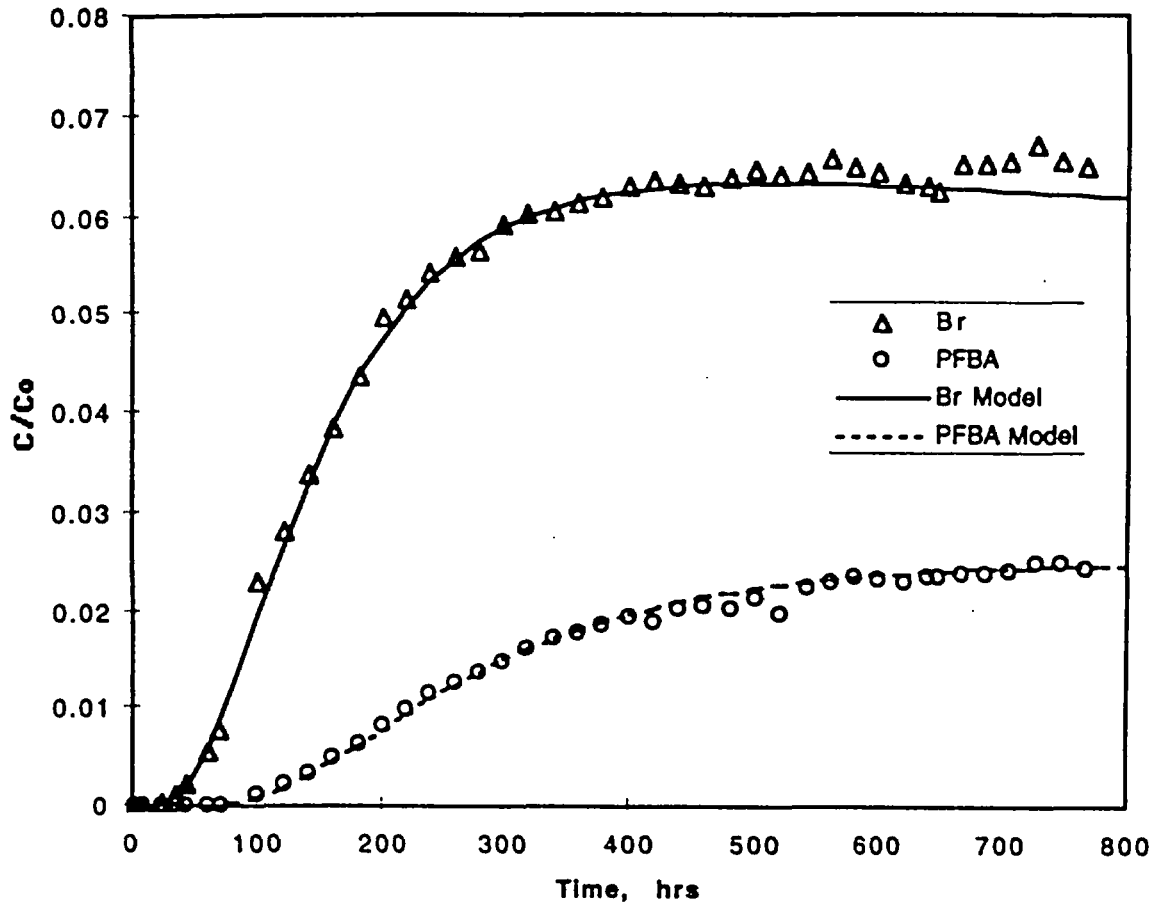


Figure 5-6. Diffusion cell data and DIFCEL model fits for bromide and PFBA in the lower Prow Pass Tuff (first diffusion cell). Diffusion coefficients are given in Table 5-1.

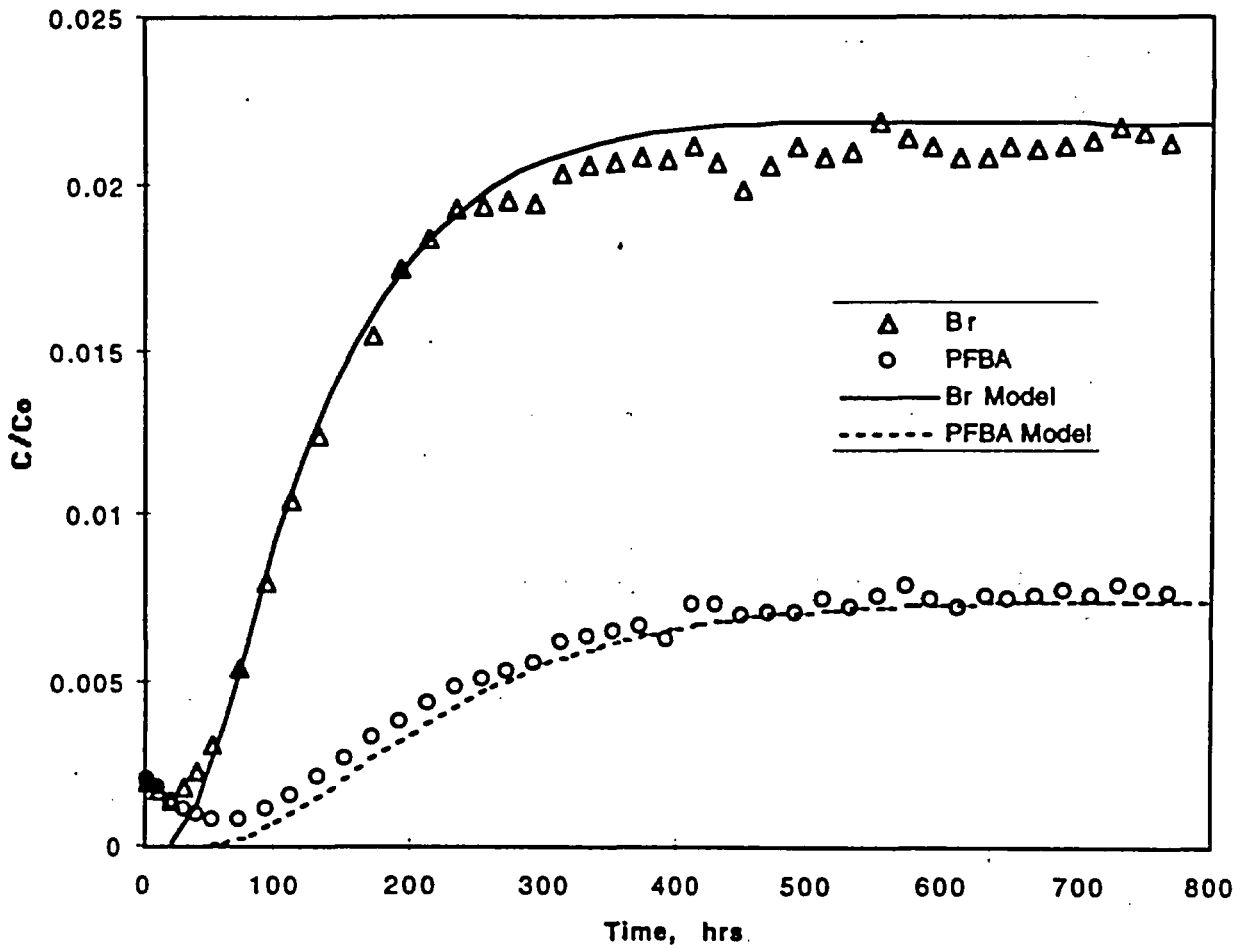


Figure 5-7. Diffusion cell data and DIFCEL model fits for bromide and PFBA in the lower Prow Pass Tuff (second diffusion cell). Diffusion coefficients are given in Table 5-1.

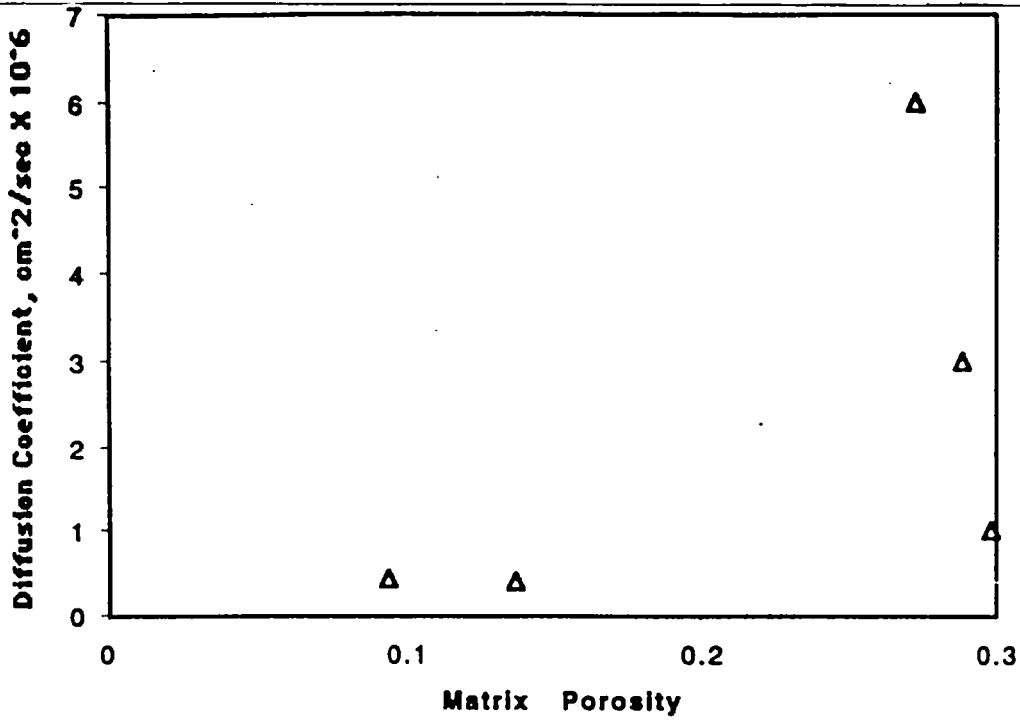


Figure 5-8. Bromide diffusion coefficients vs. tuff porosity for all diffusion cell experiments

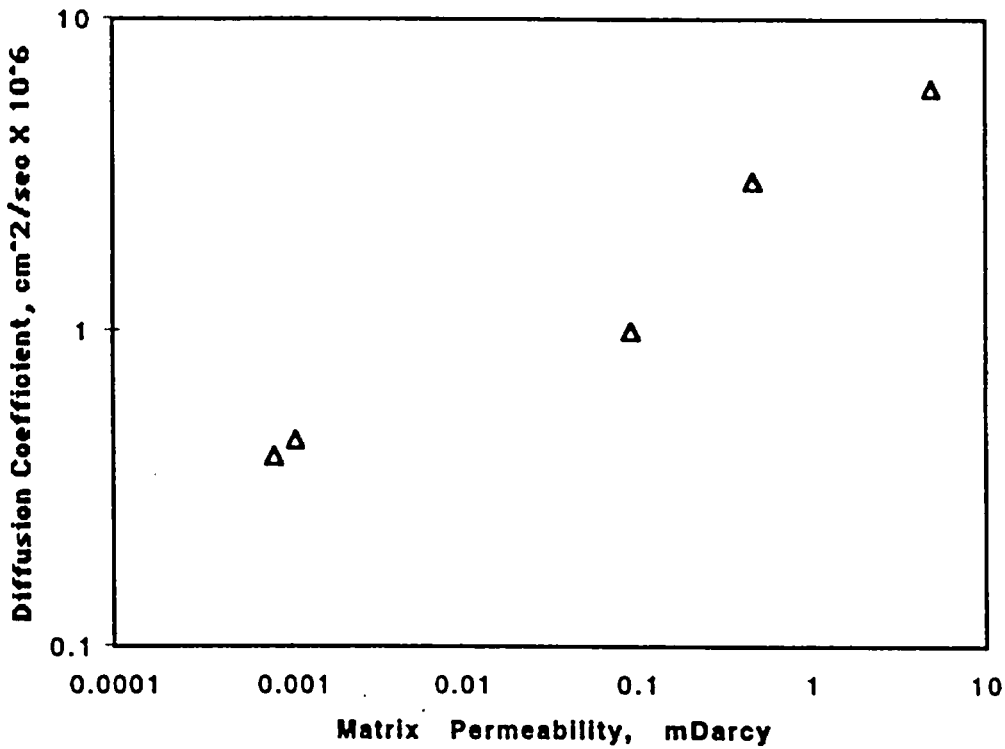


Figure 5-9. Bromide diffusion coefficients vs. tuff permeability for all diffusion cell experiments.

6.0 Predictions of Tracer Transport in the Upcoming Reactive Tracer Test in the Prow Pass Tuff

The RELAP computer model (Appendix A) was used to predict tracer transport in the Prow Pass Tuff at the C-holes based on the preliminary results of a conservative tracer test being conducted by the USGS in the Prow Pass Tuff as well as on the results of laboratory tests described in the preceding 3 sections of this report. This report does not contain any actual data from the USGS tracer test because these data are still considered preliminary; they were provided to Los Alamos as a courtesy to allow predictions of reactive tracer transport in the Prow Pass Tuff. *Why not? what use is it then?*

Fig. 6-1 shows predicted breakthrough curves of PFBA, bromide, and lithium in the upcoming Prow Pass reactive tracer test. This test will be conducted in the same interval and at the same production and recirculation flow rates as the USGS conservative tracer test. The tracers to be used in the test will include PFBA, lithium bromide, and two different sizes of carboxylate-modified latex microspheres. The predicted breakthrough curves for PFBA and bromide in Fig. 6-1 are based on RELAP fits to the preliminary 2,4,5-trifluorobenzoic acid (TFBA) and iodide data from the USGS test (data not shown). These two nonsorbing tracers should have very similar diffusion coefficients to PFBA and bromide, respectively. Lithium breakthrough curves were calculated for the upper, central, and lower Prow Pass Tuff units, as the test interval encompasses all three of these lithologies. The lithium curves were calculated by assuming a matrix diffusion mass transfer coefficient equal to two-thirds that of bromide (iodide) and matrix retardation coefficients calculated from equation (2.1) using laboratory K_D and matrix porosity values for the three different lithologies (Sections 3.0 and 5.0). The lithium sorption parameters used in the predictive calculations are noted in the caption of Fig. 6-1. Lithium sorption in fractures was assumed to be negligible (i.e., a fracture retardation coefficient of 1). Microsphere transport was not predicted. We do not report any of the model parameters used to obtain the fits/predictions because of the preliminary nature of the data and also because the USGS is ultimately responsible for interpreting the conservative tracer test upon which the predictions are based.

Section 6.0 Figure

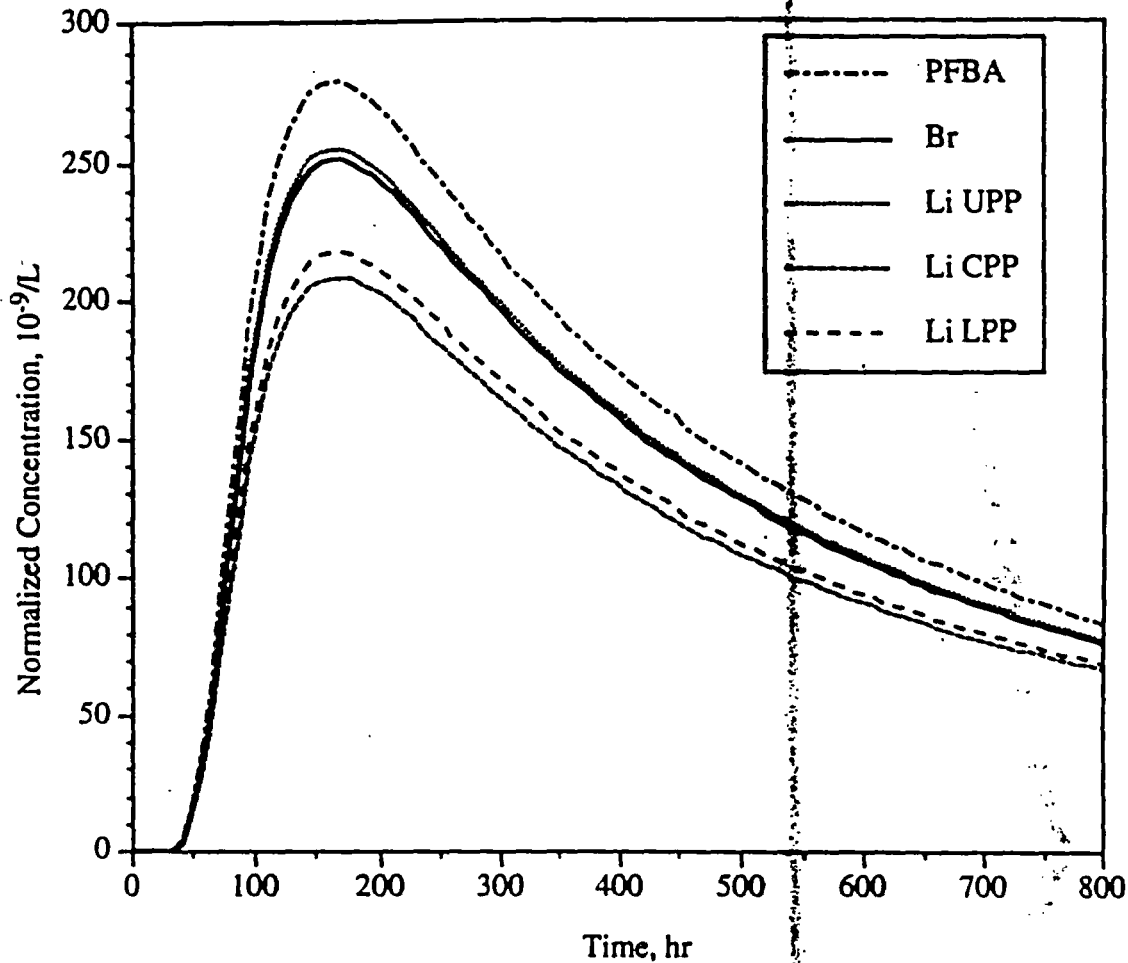


Figure 6-1. Predictions of solute tracer transport in the upcoming reactive tracer test in the Prow Pass Tuff. Predictions are based on the responses of conservative tracers in a USGS tracer test conducted in the same interval that the reactive tracer test will be conducted in. Lithium breakthrough curves were calculated assuming a matrix diffusion mass transfer coefficient equal to two-thirds that of bromide. Lithium matrix retardation coefficients were assumed to be: 1.33 for upper Prow Pass (UPP), 5.5 for central Prow Pass (CPP), and 4.0 for lower Prow Pass (LPP). These retardation coefficients were calculated from equation (2.1) with sorption parameters taken from Table 3-5 ($K_L S_{max}$) and matrix porosities taken from Table 5-1. Fracture retardation was assumed to negligible.

7.0 Acknowledgments

Many people from Los Alamos National Laboratory provided assistance with the field tests, which were conducted over a sixteen-month period. These people are too numerous to mention here by name, but we especially thank Brent Newman for his help in managing site activities, and Alan Noell and Steve Thornton, who spent a great deal of time at the remote site. Matt Becker, formerly Los Alamos, now at the State University of New York-Buffalo, was responsible for much of the preliminary work on what ultimately became the RELAP computer model. We are grateful to staff of the United States Geological Survey, Denver, CO for setting up most of the equipment used in the tracer tests and for collecting samples during the last eight months of testing. We also wish to thank Bruce Robinson, Darlene Bandy, Chuck Cotter, Edward Essington, Armando Furlano, Jason Kitten, Laura Wolfsberg, Brant Wilson, Joshua Adams, Nicole Smythe, and Day Frostenson for their contributions to the laboratory studies described in Sections 3.0, 4.0, and 5.0.

This work was supported by the Yucca Mountain Site Characterization Project Office as part of the Civilian Radioactive Waste Management Program. This Project is managed by the U.S. Department of Energy, Yucca Mountain Site Characterization Project. This report was prepared in accordance with OCRWM-approved quality assurance procedures implementing requirements of the Quality Assurance Requirements Description. All data presented in this report were developed under Project-approved quality assurance procedures. These data have been assigned data tracking number (DTN) LAPR831231AQ98.001, and they are being submitted to the GENISES database in parallel with the submittal of this report. The data package associated with this DTN supercedes all previous data packages that have been submitted to the Project database. The interpretations of the field and laboratory tracer tests (Sections 2.0 and 4.0) were conducted using qualified software, RELAP and RETRAN. The interpretations of the diffusion cell experiments were conducted using software (the DIFCEL code) that has not yet been qualified. As such, these interpretations must be considered non-Q at this time.

Appendix A:

Description of Mathematical Models in Computer Codes RELAP and RETRAN

To model sorbing tracer transport in a dual-porosity system, we start with a conceptual model for conservative tracer transport in fractured systems originally introduced by Maloszewski and Zuber (1983, 1985), and we extend it to include rate-limited, nonlinear sorbing tracer transport. Fig. A-1 shows the assumed model domain, which consists of parallel-plate fractures of aperture $2b$ separated by matrix blocks of thickness L , each of which extend infinitely into the page. Tang et al. (1981) assumed an infinite spacing between fractures, but this is just a special case of a finite matrix with a very large fracture spacing. Others have used similar model conceptualizations but with cylindrical or spherical-shaped matrix blocks (Rasmuson and Neretnieks, 1986). All of these formulations yield similar results when tracer penetration into the matrix is much less than matrix block dimensions; that is, when time scales are short compared to time scales necessary for diffusion to the centerline of the blocks. In Fig. A-1, the fracture apertures, fracture flow velocity, matrix bulk density, matrix porosity, and fracture and matrix sorption parameters are assumed to be the same everywhere in the system (no spatial heterogeneity). This is clearly a simplification, but spatial variation is very difficult to characterize in a field setting, and it also introduces considerable complexity and ambiguity to model interpretations (i.e., more adjustable parameters to fit an observed response). Therefore, we considered it appropriate, as a first approximation, to assume homogeneous properties and use bulk average parameter values.

Referring to Fig. A-1, it is assumed that advective transport occurs only in the x -direction in the fractures and that diffusion into the matrix is important only in the y -direction. It is also assumed that there are no concentration gradients in the y -direction in the fractures. These assumptions allow the equations describing transport in the fractures and the matrix to be decoupled and solved as separate 1-dimensional problems that are linked only through a boundary condition and a single term in the fracture transport equation.

Linear Flow in Fractures

For a constant flow velocity in fractures (i.e., linear flow), the differential equations and boundary conditions describing rate-limited, nonlinear sorbing tracer transport in the fractures and matrix (the most general case) are:

Fractures, Solution Phase:

$$\frac{\partial C_f}{\partial t} + v_f \frac{\partial C_f}{\partial x} - D_f \frac{\partial^2 C_f}{\partial x^2} + \left(\frac{\rho_f}{\eta} \right) \frac{\partial S_f}{\partial t} - \frac{\phi D_m}{b\eta} \frac{\partial C_m}{\partial y} \Big|_{y=b} = 0 \quad (A1)$$

Fractures, Immobile Phase:

$$\left(\frac{\rho_f}{\eta}\right) \frac{\partial S_f}{\partial t} - k_{df} \left(\frac{C_f^{\beta_f}}{1 + \alpha_f C_f} \right) + k_{df} S_f = 0 \quad (A2)$$

Matrix, Solution Phase:

$$\frac{\partial C_m}{\partial t} - D_m \frac{\partial^2 C_m}{\partial y^2} + \left(\frac{\rho_B}{\phi}\right) \frac{\partial S_m}{\partial t} = 0 \quad (A3)$$

Matrix, Immobile Phase:

$$\left(\frac{\rho_B}{\phi}\right) \frac{\partial S_m}{\partial t} - k_{mf} \left(\frac{C_m^{\beta_m}}{1 + \alpha_m C_m} \right) + k_{mf} S_m = 0 \quad (A4)$$

subject to initial and boundary conditions

$$C_f(x, 0) = 0 \quad (A1a)$$

$$C_f(0, t) = \delta(t) \quad (A1b)$$

$$C_f(\infty, t) = 0 \quad (A1c)$$

$$S_f(x, 0) = 0 \quad (A2a)$$

$$C_m(y, x, 0) = 0 \quad (A3a)$$

$$C_m(b, x, t) = C_f(x, t) \quad (A3b)$$

$$\frac{\partial C_m}{\partial y} \left(\frac{L}{2}, x, t \right) = 0 \quad (A3c)$$

$$S_m(y, x, 0) = 0 \quad (A4a)$$

where, C_f = tracer concentration in solution in fractures, M/L³
 C_m = tracer concentration in solution in matrix, M/L³
 S_f = tracer surface concentration on fracture surfaces, M/M solid
 S_m = tracer surface concentration on matrix surfaces, M/M solid
 v_f = fluid velocity in fractures, L/T
 D_f = dispersion coefficient in fractures, L²/T
 D_m = molecular diffusion coefficient in matrix, L²/T
 ρ_f = bulk density of material in fractures, M/L³
 ρ_B = bulk density of matrix, M/L³
 η = porosity within fractures,
 ϕ = matrix porosity,
 b = fracture half aperture, L
 L = distance between parallel fractures in medium, L
 k_{df} = rate constant for sorption to surfaces in fractures, 1/T (if linear)
 k_{df} = rate constant for desorption from surfaces in fractures, M/L³T
 k_{mf} = rate constant for sorption to surfaces in matrix, 1/T (if linear)
 k_{mf} = rate constant for desorption from surfaces in matrix, M/L³T
 α_i, β_i = sorption isotherm parameters defined in equation (A5) (i = f, fractures; i = m, matrix), and
 $\delta(t)$ = dirac delta function.

Coupling between the fractures and matrix is achieved through boundary condition (A3b) and through the last term on the left-hand side of equation (A1). We make use of

the expression $\left(\frac{\rho_f}{\eta}\right)$ to account for surface area available for sorption in fractures. In reality, fractures could be completely open (i.e., $\eta = 1$, $\rho_f = 0$), and sorption might occur only on the walls. In this case, the expression $\left(\frac{\rho_f}{\eta}\right)$ can be considered a proportionality constant that should be adjusted to an appropriate value to describe sorption to the walls. Alternatively, sorption in fractures can be completely ignored by setting this term equal to zero. We use the dirac-delta function as the inlet boundary condition (equation (A1b)) because the solutions obtained using this boundary condition are residence time distributions that can be mathematically convoluted with any generalized input function to obtain a generalized breakthrough curve.

In the above equations, we have used a general expression for the sorption isotherms in both the fractures and the matrix:

$$S = \frac{KC^\beta}{1+\alpha C} \quad (A5)$$

This expression allows a linear, a Freundlich, or a Langmuir isotherm to be defined. A Freundlich isotherm is obtained by setting $\alpha = 0$, a Langmuir isotherm is obtained by setting $\beta = 1$, and a linear isotherm is obtained by setting $\alpha = 0$ and $\beta = 1$. Equations (A2) and (A4) also assume nonlinearity of the adsorption reaction (i.e., not first-order in concentration) while the desorption reaction is assumed to be linear (first-order in surface concentration). Note that $K = k_f/k_m$, where k_f and k_m are the rate constants for sorption and desorption, respectively.

If equilibrium sorption is assumed, the sorption isotherm expression can be substituted directly for S_f and S_m in equations (A1) and (A3), respectively. This eliminates the need for the immobile phase equations (A2) and (A4). Recognizing that $\frac{\partial S}{\partial t} = \frac{\partial S}{\partial C} \cdot \frac{\partial C}{\partial t}$, the fracture and matrix transport equations become

Fractures:

$$\frac{\partial C_f}{\partial t} + v_f \frac{\partial C_f}{\partial x} - D_f \frac{\partial^2 C_f}{\partial x^2} + \left(\frac{\rho_f}{\eta}\right) \left[\frac{K_f \beta_f C_f^{\beta_f - 1}}{1 + \alpha_f C_f} - \frac{\alpha_f K_f C_f^{\beta_f}}{(1 + \alpha_f C_f)^2} \right] \frac{\partial C_f}{\partial t} - \frac{\phi D_m}{b\eta} \frac{\partial C_m}{\partial y} \Big|_{y=b} = 0 \quad (A6)$$

Matrix:

$$\frac{\partial C_m}{\partial t} - D_m \frac{\partial^2 C_m}{\partial y^2} + \left(\frac{\rho_m}{\phi}\right) \left[\frac{K_m \beta_m C_m^{\beta_m - 1}}{1 + \alpha_m C_m} - \frac{\alpha_m K_m C_m^{\beta_m}}{(1 + \alpha_m C_m)^2} \right] \frac{\partial C_m}{\partial t} = 0 \quad (A7)$$

where the terms in brackets, [], are $\frac{\partial S}{\partial C}$ for the fractures and matrix, respectively, and

$$K_m = \frac{k_{mf}}{k_{mr}} \quad \text{and} \quad K_f = \frac{k_{ff}}{k_{fr}}$$

When the sorption isotherm is nonlinear (either rate-limited or equilibrium), the appropriate equations given above are solved numerically using an implicit alternating-direction finite-difference method. By assuming 1-D transport in both the fractures and the matrix and using an explicit time discretization for the adsorption (nonlinear) term, the model equations are reduced to a single tridiagonal linear system for the fractures and a set of independent tridiagonal linear systems for each row of grid points extending into the matrix (perpendicular to the fractures). These tridiagonal systems can be solved very efficiently, and the implicit time discretization provides unconditional stability. The computer code developed to obtain the numerical solution is called RETRAN (REactive TRANsport code).

For linear sorption isotherms (either rate-limited or equilibrium), it is possible to obtain a semi-analytical solution of the transport equations by following the Laplace transform technique of Maloszewski and Zuber (1983). The Laplace transform removes the time derivatives from the governing equations, rendering them ordinary differential equations that can be solved by standard methods. The Laplace transforms of the general rate-limited equations (A1), (A2), (A3), and (A4), assuming linear isotherms, are

Fractures, Solution Phase:

$$s\bar{C}_f + v_f \frac{\partial \bar{C}_f}{\partial x} - D_f \frac{\partial^2 \bar{C}_f}{\partial x^2} + \left(\frac{\rho_f}{\eta} \right) s\bar{S}_f - \frac{\phi D_m}{b\eta} \frac{\partial \bar{C}_m}{\partial y} \Big|_{y=b} = 0 \quad (A8)$$

Fractures, Immobile Phase:

$$\left(\frac{\rho_f}{\eta} \right) s\bar{S}_f - k_{ff} \bar{C}_f + k_{fr} \bar{S}_f = 0 \quad (A9)$$

Matrix, Solution Phase:

$$s\bar{C}_m - D_m \frac{\partial^2 \bar{C}_m}{\partial y^2} + \left(\frac{\rho_B}{\phi} \right) s\bar{S}_m = 0 \quad (A10)$$

Matrix, Immobile Phase:

$$\left(\frac{\rho_B}{\phi} \right) s\bar{S}_m - k_{mf} \bar{C}_m + k_{mr} \bar{S}_m = 0 \quad (A11)$$

where, s = Laplace transform independent variable (replacing time), and
 \bar{X} = Laplace transform of dependent variable.

Equations (A9) and (A11) are now algebraic equations that can be solved for \bar{S} , and the result(s) can be substituted into equations (A8) and (A10) to obtain (see also, Maloszewski and Zuber, 1991):

Fractures:

$$\left[1 + \frac{\left(\frac{\rho_f}{\eta}\right)k_{ff}}{\left(\frac{\rho_f}{\eta}\right)s + k_{fr}} \right] s\bar{C}_f + v_f \frac{\partial \bar{C}_f}{\partial x} - D_f \frac{\partial^2 \bar{C}_f}{\partial x^2} - \frac{\phi D_m}{b\eta} \frac{\partial \bar{C}_m}{\partial y} \Big|_{y=b} = 0 \quad (A12)$$

Matrix:

$$\left[1 + \frac{\left(\frac{\rho_B}{\phi}\right)k_{mf}}{\left(\frac{\rho_B}{\phi}\right)s + k_{mv}} \right] s\bar{C}_m - D_m \frac{\partial^2 \bar{C}_m}{\partial y^2} = 0 \quad (A13)$$

The equilibrium sorption case is readily apparent from equations (A12) and (A13) if we set k_f and k_r to very large values and recognize that $K_d = \frac{k_f}{k_r}$ and

$R = 1 + \left(\frac{\rho_B}{\phi}\right)K_d$. The equilibrium case was also derived by Tang et al. (1981) for an infinite matrix boundary condition.

Equations (A12) and (A13) are in the same form as the equations solved by Maloszewski and Zuber (1983). The only difference is that the sorption expressions in brackets in equations (A12) and (A13) were equal to 1 in Maloszewski and Zuber's equations because they only considered conservative solute transport. Thus, the solution of equations (A12) and (A13) subject to Laplace-transformed boundary conditions (A1a) through (A4a) is identical to the solution presented by Maloszewski and Zuber except that the $s\bar{C}_f$ and $s\bar{C}_m$ terms now have more complicated coefficients. Referring to Maloszewski and Zuber (1983) for details of the derivation, the final result for transport in the fractures coupled with diffusion into the matrix is a single Laplace-domain equation given by

$$\bar{C}_f(x) = \exp\left\{ \frac{v_f x}{2D_f} \left[1 - \sqrt{1 + \frac{4D_f R_f(s)}{v_f^2} s + \frac{4D_f \phi}{v_f^2 b \eta} \sqrt{R_m(s) D_m s} \operatorname{Tanh}\left(\sqrt{\frac{s R_m(s)}{D_m} \left(\frac{L}{2} - b \right)} \right)} \right] \right\} \quad (A14)$$

where,

$$R_f(s) = 1 + \frac{\left(\frac{\rho_f}{\eta}\right)k_{ff}}{\left(\frac{\rho_f}{\eta}\right)s + k_{fr}} \quad (A15)$$

$$R_m(s) = 1 + \frac{\left(\frac{\rho_B}{\phi}\right)k_{mf}}{\left(\frac{\rho_B}{\phi}\right)s + k_{ov}} \quad (A16)$$

If we introduce the mean fluid residence time in fractures, $\tau = \frac{x}{v_f}$, and the dimensionless Peclet number, $Pe = \frac{xv_f}{D_f}$, which are related to the first and second moments of fluid residence time in the system, respectively, equation (A14) can be rewritten as

$$\bar{C}_f(x) = \exp\left\{\frac{Pe}{2}\left[1 - \sqrt{1 + \frac{4\tau}{Pe}\left\{sR_f(s) + \frac{\phi}{b\eta}\sqrt{R_m(s)D_m s} \operatorname{Tanh}\left(\sqrt{\frac{sR_m(s)}{D_m}\left(\frac{L}{2} - b\right)}\right)\right\}}\right]\right\} \quad (A17)$$

Equation (A17) is arguably a more natural expression to work with than equation (A14) when considering field data because actual distances and fluid velocities in a field experiment will be dependent on flow pathways in the system, but the concepts of the first and second moments of fluid residence time are less ambiguous. Equation (A17) also clearly delineates the expression $\frac{\phi}{b\eta}\sqrt{R_m(s)D_m}$ as an effective mass transfer coefficient for matrix diffusion. This expression can be further divided into a flow-system-dependent part, $\frac{\phi}{b\eta}$, and a tracer-dependent part, $\sqrt{R_m(s)D_m}$. In chemical engineering, Laplace-domain expressions such as equations (A14) and (A17) are used extensively in control theory and are referred to as "transfer functions."

We now consider three simplifications to equation (A17). First, by setting $R_f(s)$ and $R_m(s)$ equal to 1, we reproduce the result for a nonsorbing tracer obtained by Maloszewski and Zuber (1983). Second, in the case of an infinite matrix, as was assumed by Tang et al. (1981), the argument of the hyperbolic tangent approaches infinity and hence the hyperbolic tangent itself becomes unity. The resulting expression is identical to that derived by Tang et al. (1981) except that the reaction terms have now been generalized to allow rate-limited as well as equilibrium sorption. Finally, if we set the matrix porosity, ϕ , equal to zero, the entire term accounting for diffusive transport in the matrix (the term containing the hyperbolic tangent) drops out of the equation, and we get an expression describing reactive transport in a single-porosity medium. Thus, the transport expression derived for a dual-porosity medium is consistent in that it reduces to a single-porosity medium when $\phi = 0$.

Radial Convergent Flow in Fractures

The derivations in the preceding section were strictly for a spatially invariant flow rate in fractures (linear flow). In reality, the flow field in a weak recirculation

tracer test in a confined, heterogeneous aquifer is likely to range between linear and radial (National Research Council, 1996), with these two cases representing end members. In a completely unconfined aquifer, spherical flow might be an appropriate end member, but we do not consider that here because of the partially-confined nature of the Bullfrog tuff.

In the case of radial flow, we only have to modify the equations for solution phase transport in the fractures in the preceding section. Specifically, all x-derivatives become r-derivatives and the $D_f \frac{\partial^2 C_f}{\partial x^2}$ terms become $\left(\frac{1}{r}\right) \frac{\partial}{\partial r} \left(r D_f \frac{\partial C_f}{\partial r} \right)$. Equations (A1), (A6), (A8), and (A12) then become, respectively:

$$\frac{\partial C_f}{\partial t} + v_f \frac{\partial C_f}{\partial r} - \left(\frac{1}{r}\right) \frac{\partial}{\partial r} \left(r D_f \frac{\partial C_f}{\partial r} \right) + \left(\frac{\rho_f}{\eta}\right) \frac{\partial S_f}{\partial t} - \frac{\phi D_m}{b\eta} \frac{\partial C_m}{\partial y} \Big|_{y=b} = 0 \quad (A18)$$

$$\frac{\partial C_f}{\partial t} + v_f \frac{\partial C_f}{\partial r} - \left(\frac{1}{r}\right) \frac{\partial}{\partial r} \left(r D_f \frac{\partial C_f}{\partial r} \right) + \left(\frac{\rho_f}{\eta}\right) \left[\frac{K_f \beta_f C_f^{\beta_f - 1}}{1 + \alpha_f C_f} - \frac{\alpha_f K_f C_f^{\beta_f}}{(1 + \alpha_f C_f)^2} \right] \frac{\partial C_f}{\partial t} - \frac{\phi D_m}{b\eta} \frac{\partial C_m}{\partial y} \Big|_{y=b} = 0 \quad (A19)$$

$$s \bar{C}_f + v_f \frac{\partial \bar{C}_f}{\partial r} - \left(\frac{1}{r}\right) \frac{\partial}{\partial r} \left(r D_f \frac{\partial \bar{C}_f}{\partial r} \right) + \left(\frac{\rho_f}{\eta}\right) s \bar{S}_f - \frac{\phi D_m}{b\eta} \frac{\partial \bar{C}_m}{\partial y} \Big|_{y=b} = 0 \quad (A20)$$

$$\left[1 + \frac{\left(\frac{\rho_f}{\eta}\right) k_{fr}}{\left(\frac{\rho_f}{\eta}\right) s + k_{fr}} \right] s \bar{C}_f + v_f \frac{\partial \bar{C}_f}{\partial r} - \left(\frac{1}{r}\right) \frac{\partial}{\partial r} \left(r D_f \frac{\partial \bar{C}_f}{\partial r} \right) - \frac{\phi D_m}{b\eta} \frac{\partial \bar{C}_m}{\partial y} \Big|_{y=b} = 0 \quad (A21)$$

All other equations are the same as for the linear flow case if the model domain is the same as in Fig. A-1.

Becker and Charbeneau (submitted) have solved the radial flow transport problem in the special case of convergent flow with no sorption or matrix diffusion (i.e., a single-porosity system). Their solution differs from other radial convergent transport solutions in the literature (e.g., Moench, 1989, 1995) in that their boundary condition at the production well is an "absorbing" boundary that dictates that any solute mass reaching the production well immediately disappears from the system. This boundary condition is consistent with a transfer function approach to interpreting tracer test responses, discussed below. The resulting Laplace domain solution for the case of no sorption or matrix diffusion in terms of τ and Pe (analogous to equation (A17)) is (Becker and Charbeneau, submitted):

$$\bar{C}_f(r_w) = \exp \left[\frac{Pe}{2} \left(1 - \frac{1}{r_{LW}} \right) \right] \frac{Ai(\sigma^{1/3} y_L)}{Ai(\sigma^{1/3} y_w)} \quad (A22)$$

where, r_w = production well radius,

r_{LW} = production well radius divided by separation between injection and production wells,

$$y_L = Pe + \frac{1}{4\sigma},$$

$$y_w = \frac{Pe}{r_{LW}} + \frac{1}{4\sigma},$$

$$\sigma = \left(\frac{r_{LW}}{Pe} \right)^2 \frac{2\tau s}{(r_{LW}^2 - 1)},$$

$Ai(z)$ = Airy function (Spanier and Oldham, 1987).

Becker (1996) extended this result to a dual-porosity system (with the geometry of Fig. A-1) for a tracer that exhibits equilibrium, linear sorption behavior. We extend it further here to allow for rate-limited, linear sorption. The result, without derivation, is identical to equation (A22) but with σ redefined as

$$\sigma = \left(\frac{r_{LW}}{Pe} \right)^2 \frac{2\tau s \Psi(s)}{(r_{LW}^2 - 1)} \quad (A23)$$

where, $\Psi(s) = R_r(s) + \frac{\phi}{b\eta} \sqrt{\frac{R_m(s)D_m}{s}} \text{Tanh} \left(\sqrt{\frac{sR_m(s)}{D_m}} \left(\frac{L}{2} - b \right) \right)$ and $R_r(s)$ and $R_m(s)$ are as defined in equations (A15) and (A16).

Equation (A22) using σ defined in equation (A23) is the Laplace transform transfer function expression that should be used in lieu of equation (A17) for the case of radial convergent transport of a linearly sorbing tracer in a dual-porosity system. For nonlinear sorption, a numerical formulation of equation (A18) in conjunction with equations (A2), (A3), and (A4) is required for the rate-limited case, and equations (A19) and (A7) are required for the equilibrium case. The numerical model RETRAN can be used to solve these nonlinear, convergent radial flow equations.

Convolution of Transfer Functions to Obtain Tracer Test Responses

Before we can obtain a meaningful field-scale transport prediction, we must convolute equation (A17) or (A22) with a realistic tracer injection function. In the time domain, such a convolution is accomplished by a convolution integral, but in the Laplace domain it becomes a simple multiplication (Churchill, 1958):

$$C(t) = \int_0^t A(\tau) \cdot B(t-\tau) d\tau \Rightarrow \bar{C}(s) = \bar{A}(s) \cdot \bar{B}(s) \quad (A24)$$

where, $X(t)$ = time-domain function,
 $\bar{X}(s)$ = Laplace transform of time-domain function, and
 s = Laplace transform variable.

This process can be extended to more than two transfer functions by taking the product of all applicable functions. Thus, in a field tracer test, transfer functions for tracer injection, pipeline delays, and storage in the injection and production wellbores can all easily be convoluted with the groundwater system transfer function (e.g., equations (A17) or (A22)) to obtain an overall transfer function for the test. We assume the most practical injection function in a field tracer test: a finite-duration, constant concentration pulse, which has a Laplace transform given by

$$\bar{I}(s) = C_o \left(\frac{1 - \exp(-T_p s)}{s} \right) \quad (\text{A25})$$

where, C_o = concentration of injection pulse, M/L³
 T_p = duration of injection pulse, T.

Wellbore storage is accounted for by assuming that the wellbores are well-mixed regions (Moench, 1989, 1995). The Laplace domain transfer function for a well-mixed region is given by

$$\bar{W}(s) = \frac{\gamma}{\gamma + s} \quad (\text{A26})$$

where, γ = time constant, generally assumed to be the volumetric flow rate divided by the volume of well-mixed region, 1/T.

Pipeline delays can be accounted for by a transfer function of the form

$$\bar{P}(s) = \exp(-T_d s) \quad (\text{A27})$$

where, T_d = delay time, T.

Reinjection of produced water (i.e., recirculation of tracers) can be accounted for with transfer functions as follows:

$$\bar{F}_R(s) = \frac{\bar{F}(s)}{1 - \epsilon \bar{F}(s)} \quad (\text{A28})$$

where, $\bar{F}_R(s)$ = transfer function with recirculation,
 $\bar{F}(s)$ = transfer function without recirculation,
 ϵ = recirculation ratio (0 = no recirculation, 1 = full recirculation).

A computer model called RELAP (REactive transport LAPlace transform inversion code) was developed to predict field tracer transport by convoluting (i.e., multiplying) either the linear or radial dual-porosity transfer functions (equations (A17) or (A22), respectively) with the transfer functions described above. RELAP numerically

inverts the resulting Laplace-domain product of transfer functions to obtain a time domain solution. The numerical inversion procedure is described in the next section.

We have given considerable emphasis here to the Laplace transform modeling approach despite the fact that the numerical model RETRAN is more general because it can accommodate nonlinear sorption isotherms and ultimately spatial heterogeneity. The Laplace transform approach, however, has a distinct advantage over the numerical modeling approach in that it is very easy to account for the effects of processes other than transport in the aquifer (by the convolution procedure described above). The transfer function approach is also well suited to estimating model parameters by matching solutions to experimental breakthrough curves. The Laplace transform inversion executes in a fraction of a second on a typical computer workstation, so RELAP can be exercised with different values of transport parameters literally thousands of times per minute. By contrast, a typical RETRAN simulation with comparable numerical accuracy takes 2-3 minutes of compute time on the same workstation. RELAP contains a parameter search algorithm to minimize the sum-of-squares differences between model predictions and a given tracer data set. This feature allows rapid estimation of model parameter values that are consistent with the test data. Because of the fast execution times of the RELAP inversion algorithm and the fact that sum-of-squares response surfaces for the transport problem typically have multiple minima, the search algorithm simply adjusts parameters over a specified range in systematic, brute-force manner to achieve a least-squares fit to the data. The resulting fits can then be used to provide good initial estimates to RETRAN for obtaining estimates of nonlinear sorption parameters.

Another reason for developing the Laplace transform model is to provide semi-analytical solutions against which more general numerical models can be compared and verified. This is important because numerical models will ultimately be used to account for spatial heterogeneity and temporal variations in boundary conditions when making predictions of radionuclide transport over large time and length scales.

The Laplace transform and numerical models were tested by (1) inverting several simple Laplace transforms with known time-domain solution to ensure that the Laplace transform inversion algorithm was working properly, (2) comparing predicted nonsorbing solute breakthrough curves in a single-porosity medium to analytical solutions (Kreft and Zuber, 1978; Levenspiel, 1972), and (3) comparing the semi-analytical (RELAP) and numerical (RETRAN) model predictions for sorbing tracers with linear isotherms (both rate-limited and equilibrium). In all cases, excellent agreement was obtained between model predictions and analytical solutions, or between the two models.

Numerical Inversion of Laplace Transforms

The final step in obtaining a transport prediction from the transfer functions is to invert the solution from the Laplace domain to the time domain. We accomplish this by using a Fourier transform procedure embodied in an algorithm obtained over the World Wide Web (Lindhardt, 1995). We have found this algorithm to be more stable for Laplace transform inversions than any others we have tried (e.g., Stehfest, 1970; de Hoog et al., 1982).

The basic principles of the algorithm used for numerical inversion of Laplace transforms are given below. We thank Sven Lindhardt (unknown affiliation) for

providing the algorithm in the form of a MathCad® worksheet at the World Wide Web address: <http://www.mathsoft.com/appsindex.html>. The worksheet can be found under the program name invsfft.mcd at this web site. Sven also provided much of the following description of the mathematical basis for the algorithm.

The Laplace transform is defined by

$$F(s) = \int_0^{\infty} f(t)e^{-st} dt \quad (A29)$$

where, s = Laplace transform variable,
 t = time,
 $f(t)$ = time domain function,
 $F(s)$ = Laplace domain function.

If we set $s = \sigma + j\omega$, where $j = \sqrt{-1}$, in equation (A29) and change the lower limit of integration to $-\infty$ (which is permissible for any initial-valued problem because $f(t) = 0$ for $t < 0$) we obtain

$$F(s) = \int_{-\infty}^{\infty} f(t)e^{-\sigma t} e^{-j\omega t} dt \quad (A30)$$

If σ is a constant, equation (A29) can be rewritten as

$$F(j\omega) = \int_{-\infty}^{\infty} f_1(t)e^{-j\omega t} dt \quad (A31)$$

where, $f_1(t) = f(t)e^{-\sigma t}$.

Equation (A31) is the Fourier transform of $f_1(t)$, for which very efficient inversion algorithms exist to find $f_1(t)$ given $F(j\omega)$: However, the choice of σ must be such that the integral in equation (A31) converges. This is accomplished by choosing

$$\sigma = \frac{-\ln(0.05)}{1.5 \cdot T_{\max}} \quad (A32)$$

where, T_{\max} = maximum time at which the function $f(t)$ is to be evaluated.

Now, if we have an arbitrary Laplace transform, $F(s)$, we can obtain a spectrum by setting $s = \sigma + j\omega$ and computing $F(s)$ for equally-spaced values of ω ; i.e., for

$$\omega_i = \frac{2\pi i}{T_{\max}} \quad (A33)$$

where, $i = 0, 1, 2, 3 \dots$

The inverse Fourier transform of this spectrum will give the function $f_1(t)$ in equation (A31), from which the desired function $f(t)$ is easily generated from

$$f(t) = f_1(t)e^{\sigma t} \quad (A34)$$

The inversion algorithm has been extensively tested on equations where time-domain solutions are known, and it has proven to be very accurate. Accuracy for the purposes of this work was ensured by using more and more terms in the Fourier transforms until the solutions no longer changed.

Appendix A References

Becker, M. W., Tracer tests in a fractured rock and their first passage time mathematical models, Ph.D. dissertation, University of Texas at Austin, 1996.

Becker, M. W. and Charbeneau, R. J., A first passage time solution for radially convergent tracer tests, submitted to *Water Resour. Res.*, 1996.

Churchill, R. V., *Operational Mathematics*, 2nd ed. McGraw-Hill, New York, 1958.

de Hoog, F. R., Knight, J. H., and Stokes, A. N., An improved method for numerical inversion of Laplace transforms, *SIAM J. Sci. Stat. Comput.*, 3(3), 357-366, 1982.

Kreft, A. and Zuber, A., On the physical meaning of the dispersion equation and its solutions for different initial and boundary conditions, *Chem. Eng. Sci.*, 33, 1471-1480, 1978.

Levenspiel, O. *Chemical Reaction Engineering*, 2nd ed. John Wiley and Sons, New York, 1972.

Lindhardt, S. MathCad® worksheet at the World Wide Web address:
<http://www.mathsoft.com/appsindex.html>, 1995.

Maloszewski, P. and Zuber, A., Interpretation of artificial and environmental tracers in fissured rocks with a porous matrix, in *Isotope Hydrology*, International Atomic Energy Agency (IAEA), Vienna, Austria, pp. 635-651, 1983.

Maloszewski, P. and Zuber, A., On the theory of tracer experiments in fissured rocks with a porous matrix, *J. Hydrology*, 79, 333-358, 1985.

Maloszewski, P. and Zuber, A., Influence of matrix diffusion and exchange reactions on radiocarbon ages in fissured carbonate aquifers, *Water Resour. Res.*, 27(8), 1937-1945, 1991.

Moench, A. F., Convergent radial dispersion: A Laplace transform solution for aquifer tracer testing, *Water Resour. Res.*, 25(3), 439-447, 1989.

Moench, A. F., Convergent radial dispersion in a double-porosity aquifer with fracture skin: Analytical solution and application to a field experiment in fractured chalk, *Water Resour. Res.*, 31(8), 1823-1835, 1995.

National Research Council, *Rock Fractures and Fluid Flow: Contemporary Understanding and Applications*, National Academy Press, Washington, D.C., 1996.

Rasmuson, A. and Neretnieks, I., Radionuclide migration in strongly fissured zones: The sensitivity to some assumptions and parameters, *Water Resour. Res.*, 22(4), 559-569, 1986.

Spanier, J. and Oldham, K. B., *An Atlas of Functions*, Hemisphere Publishing, New York, 1987.

Stehfest, H., Numerical inversion of Laplace transforms, *Commun. ACM*, 13, 47-49, 1970.

Tang, D. H., Frind, E. O., and Sudicky, E. A., Contaminant transport in a fractured porous media: Analytical solution for a single fracture, *Water Resour. Res.*, 17(3), 555-564, 1981.

Appendix A Figure

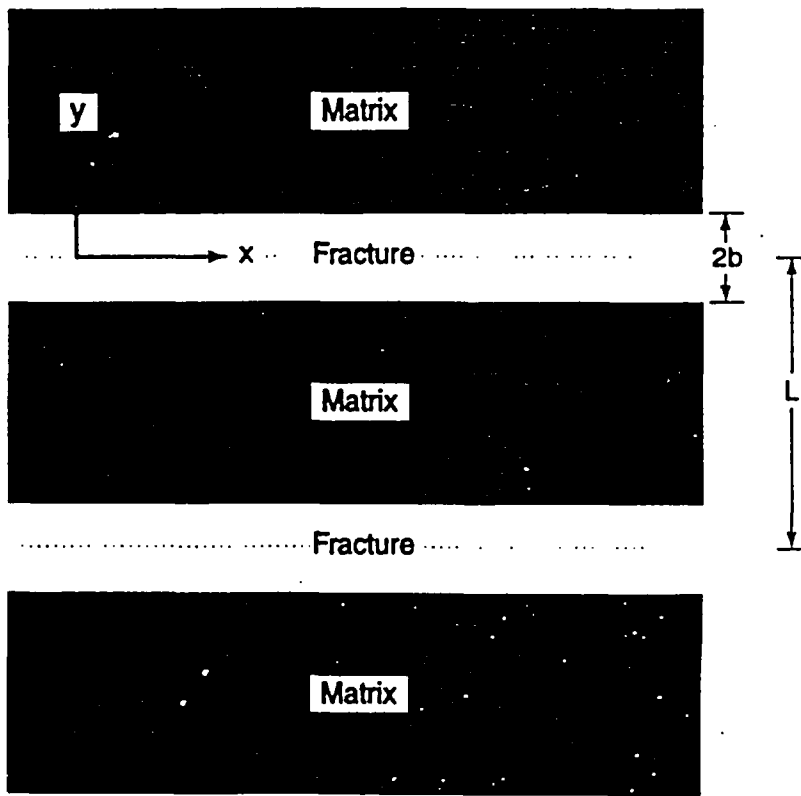


Figure A-1. System geometry assumed in conceptual dual-porosity model.

WBS 1.2.3.3.1.3.1
Deliverable No. SP23APM3
QA: L

**Civilian Radioactive Waste Management System
Management & Operating Contractor**

**Report of Results of Hydraulic and Tracer Tests
at the C-Holes Complex**

August 1, 1997

Prepared for:

**United States Department of Energy
Yucca Mountain Site Characterization Office
Las Vegas, NV**

Prepared by:

Los Alamos National Laboratory

**Civilian Radioactive Waste Management System
Management & Operating Contractor
1180 Town Center Drive
Las Vegas, NV 89134**

**Under Contract Number
DE-AC01-91RW00134**

**This work was supported by the Yucca Mountain Site Characterization Project as part of the
Civilian Radioactive Waste Management Program of the U.S. Department of Energy.**

Report of Results of Hydraulic and Tracer Test at the C-Holes Complex (Milestone SP23APM3)

Paul W. Reimus and H. J. Turin

ABSTRACT

Predicting the future performance of a potential nuclear waste repository at Yucca Mountain requires understanding saturated-zone radionuclide transport processes. Regulatory and environmental concerns currently preclude the field use of radionuclide tracers, so surrogate species must be used in field tests. We conducted a forced-gradient tracer test involving the simultaneous injection of pentafluorobenzoate (PFBA), lithium bromide, and polystyrene microspheres (~0.36- μm diameter) in saturated, fractured tuff near Yucca Mountain, Nevada. Site-specific sorption properties of lithium ion were characterized in laboratory experiments. The breakthrough curves of all tracers were bimodal in nature, indicating multiple flow pathways. Parameters describing dispersion and matrix diffusion in the system were estimated by comparing the responses of the PFBA and bromide, which served as nonsorbing tracers with free diffusion coefficients differing by about a factor of two. Field-scale sorption parameters for lithium were deduced by comparing the lithium response to that of the PFBA and bromide. The polystyrene microspheres provided an indication of the potential for colloid contaminant transport in the system, and they also served as low diffusivity tracers that should have been excluded from the porous matrix. We concluded that (1) a dual-porosity conceptual transport model is valid for the saturated zone in the vicinity of Yucca Mountain, (2) the potential exists for colloid transport over significant distances in the saturated zone, and (3) field-derived lithium sorption parameters are in good agreement with laboratory measurements. The last conclusion lends validity to the practice of using laboratory-derived sorption parameters to predict field-scale transport of ion-exchanging solutes. However, this conclusion should be applied cautiously to sorbing radionuclides, for which there are no field data in the immediate vicinity of Yucca Mountain.

Introduction

Yucca Mountain, Nevada, located about 150 km northwest of Las Vegas, is the site of a potential high-level nuclear waste repository, and it is currently undergoing extensive characterization and assessment to determine its suitability for such a role. Current plans call for wastes emplaced within Yucca Mountain to be isolated from the accessible environment by a system of multiple barriers. These include "engineered barriers," consisting of components within the repository itself, and a two-part "geologic barrier," consisting of (1) the unsaturated tuff between the repository and the regional aquifer below, and (2) the saturated-zone aquifer system

extending from directly below the repository to the down-gradient wells and springs that mark the final groundwater discharge zone. The characterization of radionuclide transport processes within the saturated zone was the subject of this study.

To support this characterization process, we conducted tracer tests at a three-well complex known as the C-wells (UE-25c#1, UE-25c#2, and UE-25c#3), which are located approximately 2 km southeast of the potential repository footprint. Figure 1 shows the layout of the wells and their vertical deviations at depth, including the locations of the intervals in which the tracer tests described in this paper were conducted. Each well penetrates approximately 900 m below surface, with the water table being about 400 m below surface. Regional groundwater flow is believed to be approximately north to south, although local flow at the C-wells has been postulated to be northwest to southeast, in the direction indicated in Figure 1 (Geldon, 1995).

The hydrogeology below the water table at the C-wells is depicted in Figure 2 (derived from Geldon, 1993, 1996). The stratigraphy, consisting of Miocene-age fractured tuff layers, is considered representative of the stratigraphy beneath Yucca Mountain, although the water table occurs in different units at different locations around the mountain because of faulting. Matrix porosities at the C-wells range from about 0.15 to 0.35. A consistent observation in all stratigraphic units below the water table is that bulk permeabilities (determined from hydraulic aquifer tests) exceed matrix permeabilities (determined by laboratory core measurements) by 2 to 6 orders of magnitude (Geldon, 1993). This high bulk-to-matrix permeability contrast is indicative of fracture flow, consistent with flow logs at the C-wells that indicate relatively discrete flow zones. The tracer tests described here were conducted in a packed-off, ~90-m interval of the lower Bullfrog member of the Crater Flat Formation (Figure 2). The lower Bullfrog Tuff exhibits at least a 5 order-of-magnitude bulk-to-matrix permeability contrast (Geldon, 1993), and this interval includes the most transmissive zones in all three wells, accounting for over 60% of the flow during open-hole flow surveys. The interval is not hydrologically isolated, as there are pressure responses both above and below the packed-off zone in c#1 and c#2 when c#3 is pumped. However, vertical conductivity is believed to be only a small fraction of horizontal conductivity, and Geldon (1996) has characterized the Bullfrog Tuff as being a confined, nonleaky "aquifer" based on hydraulic testing.

Although water flow in the Bullfrog Tuff and other stratigraphic units below the water table is expected to occur predominantly in fractures, most of the water volume in the system is contained in the porous tuff matrix, where it is essentially stagnant. Radionuclide and tracer transport is therefore expected to be attenuated by diffusive mass transfer between the flowing water in the fractures and the stagnant water in the matrix, a process known as matrix diffusion. Matrix diffusion in fractured systems has been discussed and modeled at length by others (Neretnieks, 1980; Grisak and Pickens, 1980; Tang et al., 1981; Maloszewski and Zuber, 1983, 1985). A system exhibiting this behavior is frequently called a "dual-porosity" system because of the two distinct porosities corresponding to the fractures and the matrix. We distinguish such a system from a "dual-permeability" or a "dual-porosity, dual-permeability" system because it is assumed that the matrix permeability is negligible relative to fracture permeability and that all flow occurs in fractures. It has been

suggested elsewhere that the saturated zone in the vicinity of Yucca Mountain should behave as a dual-porosity system (Robinson, 1994). This concept has important transport implications, particularly for sorbing radionuclides, because it suggests that solutes will have access to a very large surface area for sorption once they diffuse out of fracture flow pathways and into the matrix.

To study sorbing solute transport at field scales, we used lithium ion as a sorbing tracer. Lithium serves as a reasonable surrogate for ion-exchanging radionuclides (Fuentes et al., 1989); and it has the advantages of being environmentally benign, acceptable to regulators, readily detectable, and affordable. Prior to conducting the field tracer test, we studied the sorption characteristics of lithium onto Bullfrog Tuff in laboratory tests under both static (batch) and dynamic (column) conditions (Appendix A). In the batch experiments, equilibrium sorption of lithium to Bullfrog Tuff was found to be adequately described by a nonlinear Langmuir sorption isotherm,

$$S = K_L S_{max} C / (1 + K_L C) \quad (1)$$

where S = equilibrium mass sorbed per unit mass of tuff ($\mu\text{g/g}$)

C = equilibrium solution concentration ($\mu\text{g/mL}$)

K_L = Langmuir coefficient ($\text{mL}/\mu\text{g}$)

S_{max} = maximum solid sorption capacity ($\mu\text{g/g}$).

The values of K_L and S_{max} that best described the batch sorption data were $0.0053 \text{ mL}/\mu\text{g}$ and $110 \mu\text{g/g}$, respectively (Appendix A). This relatively weak sorption of lithium is actually beneficial in a field test where higher sorption could result in an impractically long test and/or very stringent analytical sensitivity requirements.

The column tests were conducted to (1) verify that the equilibrium sorption parameters determined in the batch tests were also valid under flowing conditions, and (2) estimate rate constants for lithium sorption and desorption. It was found that the equilibrium sorption parameters deduced from the batch and column experiments were in relatively good agreement. Also, although there was considerable variability from column to column, sorption and desorption rates were found to be relatively fast, with forward rate constants ranging from 2.2 to 18 hr^{-1} . A more complete discussion of the methodology and results of these experiments is presented in Appendix A.

Test Strategy

The C-wells tracer tests were conducted with the multiple objectives of (1) testing/validating our conceptual model of radionuclide transport through a dual-porosity system, (2) obtaining estimates of key transport parameters in the Bullfrog Tuff, and (3) assessing the applicability of laboratory-derived sorption parameters to field-scale transport predictions. To accomplish all of the test objectives in a reasonable time, we chose to conduct a forced-gradient, cross-hole tracer test involving the simultaneous injection of four tracers having different physical and

chemical properties. By simultaneously introducing the tracers in one solution, we ensured that they all experienced the same flow field and hence followed identical flow pathways through the system. The test interpretation could then be based on comparing the responses of the different tracers in addition to analyzing the individual responses of the tracers. The tracers used were (1) pentafluorobenzoate (PFBA), (2) bromide ion, (3) lithium ion, and (4) ~360-nm diameter carboxylate-modified-latex polystyrene microspheres (Interfacial Dynamics, Inc.). Lithium bromide salt was used as the source of lithium and bromide. PFBA and bromide were analyzed by high-pressure liquid chromatography with a UV absorbance detector, lithium was analyzed by inductively coupled plasma-atomic emission spectrometry (ICP-AES), and the microspheres were analyzed by flow cytometry (Steinkamp et al. 1991, Reimus et al., in prep).

The bromide and PFBA served as nonsorbing solutes with free diffusion coefficients differing by about a factor of two ($\sim 1.5 \times 10^{-5}$ cm²/sec for bromide and $\sim 0.75 \times 10^{-5}$ cm²/sec for PFBA; Newman, 1973 and Benson and Bowman, 1994, respectively). The nonreactivity of bromide in groundwater systems is generally accepted in the literature, and PFBA has been shown to not react with C-wells tuffs in batch sorption experiments (Stetzenbach and Farnham, 1996). Both tracers are monovalent anions in C-wells groundwater, which has a pH of about 8. A comparison of the responses of these two tracers was expected to yield information about matrix diffusion, as the smaller bromide ion would be expected to diffuse more readily into the matrix than the larger PFBA. Robinson (1994) has shown that in a dual-porosity system, a higher diffusivity tracer is expected to have a breakthrough curve with a lower, slightly delayed peak and a longer tail relative to a lower diffusivity tracer. However, in a single-porosity system (i.e., a classic porous medium) two such tracers should behave identically. Thus, if bromide appeared attenuated relative to PFBA, it would indicate that a dual-porosity system conceptualization was valid. By simultaneously analyzing the breakthrough curves of the two tracers, we planned to obtain quantitative estimates of parameters describing both flow field dispersion and matrix diffusion in the system.

As described in the introduction, lithium ion served as a weakly-sorbing solute tracer. Its response was to be interpreted by comparing with the responses of the PFBA and bromide. The free diffusion coefficient of lithium is intermediate between PFBA and bromide ($\sim 1 \times 10^{-5}$ cm²/sec, Newman 1973), so in the absence of sorption, its response would be expected to fall between that of PFBA and bromide. Therefore, any attenuation of lithium relative to bromide, manifested as either a lower peak, a delayed peak, or both, could be attributed to sorption. In unpublished calculations, we have predicted lithium transport relative to nonsorbing solutes in a field test using the laboratory-derived Bullfrog tuff sorption parameters and assuming both a single- and a dual-porosity medium. These calculations have shown that in a dual-porosity system with no sorption in fractures (i.e., open fractures), the lithium response should have a lower peak relative to nonsorbing solutes, but the peak will not be significantly delayed in time. However, in a single-porosity system or a dual-porosity system with sorption in fractures, the lithium response should have both a much lower peak and a significant time delay relative to the nonsorbing solutes. We planned to deduce lithium sorption parameters in

the system using the models described in Appendix B to fit the lithium breakthrough curve under the constraint that the dispersion and matrix diffusion parameters deduced from the simultaneous analysis of the bromide and PFBA responses must apply to the lithium as well. Thus, the only adjustable parameters in the lithium fitting exercise would be sorption parameters.

The polystyrene microspheres were introduced for two purposes: (1) they served as colloid tracers to provide insights into the potential for colloidal radionuclide transport in the saturated zone near Yucca Mountain, and (2) they served as large, low diffusivity tracers that should be excluded from the matrix and hence provide an indication of true fracture flow in the system without the effects of matrix diffusion. Carboxylate-modified-latex (CML) polystyrene microspheres with fluorescent dye tags were used because these microspheres had previously been shown to have less tendency for attenuation/filtration in fractured systems than other synthetic colloids that we considered (Reimus, 1995). The spheres have a density of 1.055 g/cm^3 , which minimizes their tendency to settle in groundwater. The fluorescent dye tags allowed the spheres to be discriminated from natural colloidal material and to be quantified at concentrations as low as $\sim 100/\text{mL}$ using flow cytometry (Steinkamp et al. 1991, Reimus et al., in prep.). The CML spheres have carboxyl functional groups on their surfaces, which give them a negative surface charge at pHs greater than about 5; and unlike most other polystyrene microspheres, they also have hydrophilic surfaces (Wan and Wilson, 1994). Both of these features tend to minimize attractive interactions with rock surfaces, and they make the spheres very stable against flocculation, even at relatively high ionic strengths, which is important if the spheres are to be injected simultaneously with solutes in a relatively concentrated solution. However, despite these measures, we still expected significant attenuation of the spheres based on previous experience in both laboratory- and field-scale fractured systems (Reimus et al., in prep.). We used 360-nm-diameter spheres because we found in previous work that larger spheres were more attenuated in fractured systems, possibly due to more rapid settling of the larger particles (Reimus et al., in prep.). Also, the flow cytometer that we had access to had a lower size detection limit of about 250-nm diameter, although this does not represent a fundamental limitation of the technique.

Test Procedure

Because of the considerable investment associated with conducting a test involving multiple tracers, we first conducted two single-tracer pilot tests to determine nonsorbing tracer travel times and recoveries from wells c#1 and c#2 to well c#3. Well c#3 was used as the production well in all tests because it has the largest open-hole transmissivity of the three C-wells (Geldon, 1993). The pilot tests allowed us to (1) determine which hole, c#1 or c#2, offered a faster, higher peak concentration response and would therefore be the preferred injection hole for a test involving a reactive tracer, (2) estimate tracer masses required for the multiple tracer test, and (3) plan sampling frequencies for the multiple tracer test. Although c#2 is much closer to c#3 than c#1 ($\sim 30 \text{ m}$ vs. $\sim 80 \text{ m}$ at depth), it was not taken for granted that c#2 would have a better tracer response because (1) local fracture strikes

tend to be oriented more in the direction of c#1-to- c#2, (2) c#1 had approximately the same magnitude pressure response as c#2 when pumping c#3, and (3) the natural gradient is believed to be approximately in the direction from c#3 to c#2 (Geldon 1993). We were particularly concerned that if we didn't inject enough lithium bromide (which is only ~8% lithium by mass) into the system, we would not observe any lithium at the production well. This concern stemmed from the uncertainty in the expected lithium attenuation due to sorption and also because of the relatively high lithium background concentration, ~65 µg/L, in the groundwater. Additionally, environmental permitting dictated that we minimize, within reason, tracer masses injected.

The packed-off zone in c#3 (Fig. 2) was pumped continuously at about 575 L/min in each test. The first pilot tracer test involved the injection of approximately 10 kg of PFBA into well c#2 on May 15, 1996. The PFBA was dissolved in ~1000 L of groundwater. The test was conducted under partial recirculation conditions with about 20 L/min of the water produced from c#3 (~3.5%) being continuously reinjected into c#2. The recirculation was initiated approximately 24 hr before tracer injection to establish a steady flow field, and it was continued for 23 days after injection. The tracer solution was plumbed into the recirculation loop such that there were no flow interruptions during injection.

The second pilot test involved the injection of about 12.7 kg of iodide (~15 kg of sodium iodide dissolved in ~1000 L of groundwater) into c#1. It was conducted in a manner very similar to the PFBA pilot test and was initiated on June 18, 1996. The recirculation rate in this test was about 15 L/min (~2.6% of production rate), and recirculation continued for 16 days after injection.

The results of these two pilot tests clearly indicated that c#2 was the preferred injection hole for the multiple tracer test, as the PFBA recovery from the May injection was about 73% and the iodide recovery from the June injection was estimated between 6 and 10%. The May PFBA response from c#2 was previously reported by Reimus and Turin (1996) (also shown in Figures 5 and 8 of this report), and the iodide response from c#1 is shown in Figure 3. Based on these results, a tracer test involving the simultaneous injection of ~12 kg PFBA, ~180 kg of lithium bromide (14.5 kg lithium, 165.5 kg bromide), and ~7 g of microspheres (~3.5 x 10¹⁴ spheres) into c#2 was initiated on October 9, 1996. Because of the much greater tracer mass in this test than in the pilot tests, and the desire to minimize solute concentrations to prevent microsphere flocculation, the tracers were dissolved in ~12,000 L of groundwater instead of the ~1000 L used in the pilot tests. The greater volume kept the density contrast between tracer solution and the downhole groundwater about the same as in the pilot tests. The microspheres were actually introduced to the tracer mixture after about one-third of the solution had been injected, which corresponded to about one injection interval volume. The test was carried out under partial recirculation conditions with a recirculation rate of about 20 L/min that was continued for 40 days. Steady flow conditions were established by starting recirculation ~36 hr prior to tracer injection.

$$\frac{180 \text{ kg LiBr}}{12000 \text{ L}} = \frac{180,000 \text{ g}}{12,000 \text{ L}} = 15 \text{ g/L}$$

$$= 1.21 \text{ g Li/L}$$

$$= 1.21 \text{ mg/ml}$$

$$= 1210 \text{ µg/ml}$$

7/31/97

Test Results

The breakthrough curves (normalized to mass injected) of the four tracers in the multiple-tracer test are shown on a log-log plot in Figure 4. The tracer recoveries at approximately 5800 hr into the test were ~65% for PFBA, ~65% for bromide, ~35% for lithium, and ~11% for microspheres (at ~4500 hr into the test). It should be noted that the two different late-time PFBA responses in Figure 7 represent uncertainty in the October test data due to uncertainty in how much PFBA was still being recovered from the May injection into c#2. Residual PFBA concentrations in c#3 were about 12 $\mu\text{g/L}$ at the time the October tracer test was initiated. The PFBA curve with the higher response assumes that the residual PFBA concentration from the May injection continued to decay in exponential fashion after the October injection (decay constant determined by fitting a line to the tail of the May breakthrough curve on a log-log plot), while the lower response curve assumes that the residual PFBA concentration from the May test remained constant at 10 $\mu\text{g/L}$ throughout the October test. The latter assumption, while seemingly unrealistic, is supported by the fact that the PFBA concentrations in the May test remained essentially constant at 10-14 $\mu\text{g/L}$ for the last 6-7 weeks prior to the October injection.

The most striking feature of the breakthrough curves in Figure 4 is their bimodal (double-peaked) behavior, discussed below. The PFBA and bromide responses show clear qualitative evidence of matrix diffusion, as the normalized PFBA concentrations are higher than the normalized bromide concentrations at both peaks, and the second bromide peak is somewhat delayed relative to the PFBA with a tail that appears to cross over the PFBA at long times. As discussed above, these are all hallmarks of matrix diffusion in a dual-porosity system. The lithium response shows obvious attenuation relative to the nonsorbing tracers, providing clear evidence of lithium sorption. It is interesting that the attenuation of the first peak is almost exclusively a lowering of the peak with little or no time delay, while the attenuation of the second peak involves a clear time delay along with a dramatic lowering of concentration. Explanations for this behavior are offered in the test interpretation section.

The microsphere breakthrough curve, which is corrected for the ~4-hr delay in their injection time relative to the solutes, is clearly attenuated compared to the solutes. However, it is interesting that their first arrival preceded the solutes (even without the time correction). This behavior has been observed in other field and laboratory tests in fractured systems (Reimus, 1995; Reimus et al., in prep.), and may be attributed to a small fraction of the spheres moving rapidly through high-velocity streamlines in fractures without having the opportunity to diffuse into low-velocity or stagnant water. The majority of the microspheres may have been attenuated by filtration mechanisms, possibly gravitational settling, as proposed by Reimus et al. (in prep.). However, the mass recovery of microspheres relative to the nonsorbing solutes is actually greater in the second peak than the first peak, and also the second microsphere peak is delayed relative to the peaks of the nonsorbing solutes with a tail that appears to be persisting longer (less steeply declining) than the solutes. If simple filtration theory were invoked to explain this behavior, a significantly lower

filtration coefficient would be needed for the second peak than the first peak, and the long tailing behavior could not be explained without assuming some sort of reversible detachment behavior. Interpretation of the microsphere response relative to the solutes is complicated by the fact that the microsphere injection was started later than the solute injection. Thus, the microspheres may not have been distributed into pathways flowing out of the injection borehole in exactly the same proportion as the solutes (i.e., a different source term). Quantitative interpretation of the complex microsphere behavior will be reserved for a future paper. However, the microsphere response clearly indicates that the potential exists for colloid transport over tens of meters in the saturated zone. It also serves to constrain possible interpretations of the solute responses, as discussed in the test interpretation section.

The response to the May PFBA injection into c#2 was significantly different than the response in October. The first 1800 hrs of the normalized PFBA breakthrough curves in the two tests are shown in Figure 5 (with linear axes). The May breakthrough curve is a more conventional single mode response. PFBA concentrations from the May injection were monitored for just over 3000 hr with a total recovery of ~73%, and the total recovery at 3000 hr in the October test was ~58%; i.e., a higher recovery in the May test than in the October test at the same point in time.

We offer the following explanation for the different responses in May and October. Because of the lack of mixing in the injection interval, the tracer solutions, which were injected directly below the top packer and were ~2% more dense than the groundwater in each test, probably sank rapidly to the bottom of the interval in each test. The tests were conducted in an identical manner in every respect except that only ~1000 L of tracer solution was injected in May, while ~12,000 L was injected in October. (The duration of recirculation was also different, 23 vs. 40 days, but all significant differences occurred prior to 23 days.) The injection interval volume was ~4300 L, so in the May test, only one-quarter of an interval volume was injected, and it is very possible that only flow pathways in the lower part of the interval conducted tracers out of the borehole. In contrast, in the October test, approximately three interval volumes of tracer solution were injected, so the volume between the packers should have completely filled with tracer solution and tracers would have accessed flow pathways throughout the entire length of the interval. We suspect that the first peak in October was the result of a small percentage (~13%) of the injected tracer mass entering a flow pathway (or set of pathways) in the upper part of the borehole that was not accessed in May. The flow survey information depicted in Figure 2 certainly suggests that the zone of highest flow in well c#2 occurs in the upper half of the interval, although one cannot necessarily conclude that there is a cross-hole connection originating from these pathways. Much of the remaining mass then presumably followed pathways that were also accessed in May and resulted in the second peak occurring at the same time as the May peak (Fig. 5). However, because the shapes of the May and second October peaks are different, and the total PFBA recovery was actually lower in October despite the early peak, we also suspect that a considerable fraction of the mass injected in October followed other

pathways that were not accessed in May and were slower, in general, than those accessed in May.

Although we have no direct proof to support this hypothesis, we conducted some simple laboratory experiments involving the injection of dyed salt solutions into a ~2-m-long, ~1.5-cm ID, clear plastic tube with a tee about 1 m from the top of the tube to serve as a "pathway" out of the "borehole." The dyed solution had approximately the same density as the solutions injected in the field experiments, and it was injected at the same rate, relative to the diameter of the tube, as in the field. We found that even though the tee was the only exit point for flow out of the tube, most of the dyed solution sank below the tee and remained in the lower part of the tube (unpublished data). However, it must be recognized that the Reynolds number (a measure of turbulence - Bird et al., 1960) was drastically different in the laboratory than in the field; more turbulence would have been expected in the field.

We view the bimodal response in October and the single-peak response in May as serendipitous good fortune. First, the two peaks allow us to objectively conclude that there are at least two separate sets of flow pathways that contributed to the October tracer responses. This allows us to estimate a different set of transport parameters for each set of pathways, meaning that we effectively conducted "two tests in one." It should be noted that if as much as 20% of the tracer mass had followed the faster pathways in October (instead of ~12%), the result probably would have been a single peak instead of two peaks.

Quantitative Test Interpretation

The solute tracer responses were interpreted by simultaneously fitting the breakthrough curves using a semi-analytical, dual-porosity transport model, RELAP, which is described in detail in Appendix B and briefly summarized here. The physical, conceptual, and mathematical models assumed for the field transport system are depicted in Figure 6. The equations shown at the bottom of Figure 6 are Laplace-domain "transfer functions" that describe tracer residence time distributions within each of the system "components." The most important of these is the transfer function for the groundwater system, which is taken from Tang, et. al. (1981). This transfer function assumes 1-dimensional advective-dispersive transport in parallel-plate fractures with 1-dimensional diffusion (perpendicular to fracture flow) into a homogeneous, infinite matrix. It also assumes linear, equilibrium, reversible sorption of a reactive species and a constant flow velocity in the fractures. Model formulations assuming a finite matrix (Maloszewski and Zuber, 1983, 1985), radial flow (Moench, 1995; Becker and Charbenaue, submitted) and rate-limited sorption (Maloszewski and Zuber, 1991) are also embodied in RELAP. These were used to evaluate the sensitivity of the derived transport parameters to radial vs. linear flow, infinite vs. finite matrix, and equilibrium vs. rate-limited sorption. A detailed description of the mathematical development of the models embodied in RELAP is provided in Appendix B.

The transfer functions shown in Figure 6 were multiplied together to describe transport throughout the system; a multiplication in the Laplace domain is equivalent to a convolution integral in the time domain (Churchill, 1958).

Wellbore storage was accounted for by assuming that the boreholes were well-mixed, with the tracers experiencing an exponential-decay residence time distribution with a time constant slightly greater than the volume of the interval divided by the volumetric flow rate into (injection well) or out of (production well) the interval. Note that an equation for wellbore mixing in the production well is not shown in Figure 6 because residence times in this well were very short (less than 10 minutes) due to the high flow rate out of the well (~575 L/m). The Laplace domain solutions were then inverted to the time domain using a Fourier-transform inversion technique (Appendix B). Because the Fourier-transform technique is very efficient (and stable), it could be performed thousands of times per minute on a computer workstation, making it practical to estimate model parameters by systematic, brute-force adjustments of their values to achieve a least-squares fit to the data. The fitting procedure used to quantitatively interpret the October tracer responses is summarized in Table 1 and discussed in detail in the following two subsections.

Nonsorbing Solutes

The first step in the interpretation procedure involved using the transfer function model depicted in Figure 6 to simultaneously fit the PFBA and bromide data assuming that all transport parameters except for diffusion coefficients were identical for the two solutes. Bromide matrix diffusion was assumed to be double that of PFBA. A matrix correction factor, ϵ , of 0.1 (Triay et al., 1993) was used to estimate diffusion coefficients in the matrix from free diffusion coefficients using $D_m = \epsilon D_f$, where D_f is the free diffusion coefficient (given in test strategy section). The matrix and fracture retardation factors for these two nonsorbing tracers were fixed at 1. The procedure involved simultaneously fitting the early tracer peak(s) with a single set of model parameters assuming that only a fraction of the tracer mass accounted for the peak. The parameters adjusted to achieve the fit were (1) the mass fraction, f , (2) the mean fluid residence time, τ , (3) the Peclet number, $Pe = L/\alpha$, where L is the distance between wells and α is the dispersivity, and (4) the lumped parameter, ϕ/b , which is effectively a mass transfer coefficient for diffusion into stagnant water, assumed to be the matrix. All other parameters were fixed according to the manner in which the test was conducted (e.g., the injection concentration, injection duration, and time constants for mixing in the injection and production wellbores).

The best fit to the first peak was subtracted from the entire breakthrough curve of each tracer, leaving only a single second peak. The simultaneous fitting procedure was then repeated for the second peak. All of the parameters describing the second peak were adjusted independently of the parameters that offered the best fit to the first peak (except that the sum of the mass fractions in both fits could not exceed 1). This procedure assumed that each peak could be described by a single advection-dispersion equation to account for flow and dispersion in fractures with a single mass transfer coefficient accounting for matrix diffusion. We recognize that the tracer response in reality was probably the result of flow through many pathways in a fracture network, and that these pathways undoubtedly had a distribution of

residence times, dispersivities, and matrix diffusion mass transfer coefficients. However, without specific data on the geometry and transport properties of individual pathways, it is difficult to justify assuming more pathways than are necessary to achieve a reasonable fit to the data. Thus, we initially limited ourselves to two "pathways," one for each peak.

It is important to recognize that the simultaneous interpretation of the PFBA and bromide breakthrough curves offers a tremendous advantage over interpretation of either tracer breakthrough curve individually. In fact, without this simultaneous interpretation, it is not possible to distinguish between the effects of hydrodynamic dispersion and matrix diffusion in a field tracer test. This dilemma is illustrated in Figure 7, which shows arguably equally good fits to the May PFBA breakthrough curve obtained using the sets of model parameter values given in Table 2. It is apparent that, although there is an upper limit to the matrix diffusion mass transfer coefficient that can be assumed in the system (constrained by the fact that the mass fraction of tracer participating in the test cannot exceed 1), a reasonably good fit to the data can be obtained by assuming no matrix diffusion at all (i.e., a single-porosity system). Note that even though the curve with the largest amount of matrix diffusion appears to offer the best fit to the data in Figure 7, an equally good fit can be obtained by assuming two overlapping single-porosity pathways with different dispersion parameters or by simply assuming a much longer mean residence time for the tracer solution in the injection borehole. We consider fractional mass participation in the tracer tests to be a definite possibility, as the natural gradient is believed to be almost opposite the direction of induced flow from c#2 to c#3 (Fig. 2), and some of the tracer mass could also have "sunk" (due to density effects) out of the zone of influence of induced flow. Thus, while the analysis of a single breakthrough curve can offer an upper bound on matrix diffusion and a range of possible values for the dispersion coefficient and mean fluid residence time in the system, it cannot conclusively establish that matrix diffusion is occurring in the system.

Although the assumption of two sets of pathways was the most logical approach to take in interpreting the October test, we were also interested in determining whether the May and October PFBA responses could be quantitatively reconciled. Because the timing of the May and second October peaks were the same, we renormalized the May PFBA breakthrough curve so that its peak height corresponded almost exactly with the height of the second PFBA peak in October. We then fitted this response using the same matrix diffusion mass transfer coefficient that was obtained from the simultaneous fit to the second PFBA and bromide peaks in October (since the same pathways were presumably accessed in each test). Figure 8 shows that when the renormalized May response is subtracted from the October PFBA response, a third peak results to account for the tail of the October response. This peak was also fitted using the same matrix diffusion mass transfer coefficient that was used to simultaneously fit the second October PFBA and bromide peaks. Figures 9 and 10 show the multiple pathway fits to the October PFBA and bromide data, respectively. The upper plot in each figure shows two-pathway fits, and the lower plot shows three-pathway fits (where the second pathway offers a good fit to the renormalized May PFBA response). The fact that the

bromide data is fitted well in the three-pathway case confirms that the May and October PFBA responses can be consistently interpreted by assuming that a portion of the second peak in October is accounted for by the May peak. However, this result is not terribly surprising because a single large dispersion pathway can always be divided into two or more smaller dispersion pathways that have the same matrix diffusion mass transfer coefficients as the single pathway.

The transport model parameters used to obtain the fits in Figures 9 and 10 are given in Tables 3 and 4; with Table 3 containing the two-pathway parameters, and Table 4 containing the three-pathway parameters. Note that different mean residence times (τ) and Peclet numbers (Pe) were obtained in each pathway depending on whether linear or radial flow was assumed. In a heterogeneous, confined aquifer, the flow velocity to a single production well is expected to vary between linear and radial (National Research Council, 1996). Thus, if we assume that the Bullfrog Tuff is reasonably confined, as suggested by Geldon (1996), presenting the two sets of residence times and Peclet numbers in Tables 3 and 4 is a way of bounding these parameter estimates as a result of flow field uncertainty. The radial mean residence time is always less than the linear residence time, and the radial Peclet number is always greater than the linear Peclet number. This somewhat confusing result can be qualitatively explained by recognizing that the models implicitly assume that the dispersion coefficient is the product of the dispersivity (α) and the fluid velocity. Under this assumption, for a given dispersivity, a solute will tend to experience more dispersion in radial flow than in linear flow because any time the solute disperses ahead of the mean position, it will be subjected to a greater flow rate, and any time it disperses behind the mean position, it will be subjected to a slower flow rate. Thus, leading solute particles will tend to be swept further ahead and lagging solute particles will tend to lag further behind in radial flow than they would be in linear flow. In effect, the radial flow field has an additive effect to the dispersion that would be experienced in a linear flow field. Any breakthrough curve can always be fitted equally well assuming either type of flow field; only the values of the parameters will differ. Figure 11 shows the relationships between τ and Pe in radial and linear flow as a function of linear Peclet number. These relationships were derived using RELAP to fit a linear response with a radial model.

Table 4 also indicates that the assumption of a finite matrix with a fracture spacing of 10 cm in the third pathway offered a better fit to the end of the tracer breakthrough curves than an infinite matrix assumption. This was the only instance where assuming a finite matrix improved a fit. However, we do not consider this result terribly significant because the data at the ends of the breakthrough curves have considerable scatter due to (1) lower analytical precision, (2) approach to background concentrations, and, (3) in the case of PFBA, uncertainty in the contribution from the May injection.

Lithium

We proceeded to fit the lithium data using the same mean residence times, Peclet numbers, and matrix diffusion mass transfer coefficients that offered the best

simultaneous fit(s) to the PFBA and bromide data. Initially, fits were obtained by adjusting the fracture and matrix retardation coefficients in the flow system equation of Figure 6, which assumes equilibrium, linear, and reversible sorption in homogeneous pathways. Sorption in fractures could be the result of the presence of mineral alteration phases (mineral coatings) with a high cation exchange capacity or the presence of crushed tuff within the fractures, or a combination of both. The retardation coefficient, R , is related to the linear distribution coefficient through the well-known expression,

$$R = 1 + \frac{\rho_B}{\phi} K_D \quad (2)$$

where ρ_B = bulk density, g/cm³,
 ϕ = porosity,
 K_D = linear distribution coefficient, cm³/g.

Note that the assumption of a linear sorption isotherm is contrary to the nonlinear Langmuir isotherm behavior observed in the lithium laboratory experiments described in Appendix A. However, the asymptotic, low concentration behavior of a Langmuir isotherm is the same as a linear isotherm with K_D equal to $K_L S_{max}$, so we felt that assuming linear sorption behavior was a reasonable starting point. Also, the relatively fast sorption kinetics observed in the laboratory column experiments suggested that the assumption of equilibrium sorption should be valid for the peak arrival times in the October test.

Our initial attempts to fit the first lithium peak (up to about 120 hr into the test) using the physical model parameters deduced from the PFBA and bromide fits were unsatisfactory. We found that assuming linear, equilibrium sorption in the matrix resulted in a peak that occurred later than the actual data with a tail that was much higher than the data. We also found we had to assume no sorption in fractures (i.e., $R_f = 1$) because any fracture sorption resulted in a peak that occurred much too late to match the data. Note that the absence of fracture sorption does not necessarily mean that lithium wasn't sorbing to fracture surfaces; it simply means that the fractures had very little surface area available for sorption (i.e., without crushed fill or sorptive coatings). Because of the relatively poor fits obtained assuming equilibrium, linear sorption behavior, we proceeded to fit the lithium data assuming (1) rate-limited, linear sorption, (2) equilibrium, nonlinear (Langmuir) sorption, and (3) rate-limited, nonlinear (Langmuir) sorption, respectively. RELAP offers the option of using a transfer function expression for rate-limited, linear sorption in a dual-porosity system; and a numerical model, RETRAN, was used to simulate nonlinear sorptive transport (both equilibrium and rate-limited) through a dual-porosity system (Appendix B).

Figure 12 shows fits to the first lithium peak obtained for each of the cases mentioned above, including the equilibrium, linear case. Sorption parameters corresponding to the fits in Figure 12 are given in Table 5. Although a reasonable fit to the data was obtained assuming rate-limited, linear sorption in both the fractures and matrix, Table 5 shows that the best-fitting rate constants were over an order of

magnitude lower than those observed in the laboratory column experiments. Likewise, the assumption of equilibrium, nonlinear (Langmuir) sorption provided a good fit to the data but resulted in isotherm parameters that were in poor agreement with the laboratory-derived isotherm. The assumption of rate-limited, nonlinear (Langmuir) sorption resulted in good fits with rate constants and isotherm parameters that were in better agreement with the laboratory data than in the cases mentioned above. Figure 13 shows a comparison of the Langmuir isotherms derived from the laboratory data and from the field data assuming both equilibrium and rate-limited sorption. Note that although neither field-derived isotherm is in very good agreement with the laboratory data, the rate-limited isotherm is an improvement over the equilibrium isotherm. It should be emphasized that the fits in Figure 12 and Table 5 are not unique; reasonable fits can be obtained for any isotherm ranging from the equilibrium, field-derived Langmuir isotherm shown in Figure 13 to a linear isotherm, provided that the sorption rate constants are allowed to vary (slower rate constants result in more linear isotherms). The rate-limited, nonlinear fit shown in Figure 12 (with corresponding isotherm in Figure 13) was selected for presentation because it represents a reasonable balance between the extremes of (a) fast sorption rates (equilibrium) with a highly nonlinear isotherm and (b) very slow sorption rates with a linear isotherm. It should be noted that the lithium injection concentration in all RETRAN (nonlinear) simulations was assumed to be 1200 mg/L (the concentration of the injectate), which resulted in the maximum possible effect of isotherm nonlinearity on the resulting fits. The nonlinear "fits" obtained using RETRAN are not true least-squares fits because RETRAN does not currently offer automated minimization of sums of squares of differences. However, after conducting many RETRAN simulations, we were confident that the nonlinear fits in Figure 12 were relatively close to least-squares fits.

We also considered a case in which the first lithium peak was assumed to be the sum of responses from two separate sets of pathways that had different sorption characteristics but which, when sorption was ignored, summed to yield the first PFBA and bromide peaks. Because the difference between the PFBA and bromide responses could be adequately explained using a single set of pathways, which implied a single matrix diffusion mass transfer coefficient, the mass transfer parameter, ϕ/b , in the two sets of pathways were kept the same as in the single pathway PFBA-bromide analysis. We felt that splitting the first peak into two pathways was reasonable because there was undoubtedly some chemical and surface area heterogeneity (and hence sorption heterogeneity) in the flow pathways in the system. In fact, it was clearly a simplification to be assuming that two sorption isotherms (one for fractures and one for the matrix) could effectively represent all of the sorption processes likely to be occurring over a 30-m-long by 90-m-thick section of the saturated zone. By splitting the first peak into two pathways, we found it was possible to obtain a reasonable fit to the lithium data by assuming equilibrium, linear sorption.

The lithium fitting exercise was completed by assuming that additional "sets of pathways" contributed to the late lithium response, just as for the PFBA and bromide. As before, the same physical model parameters that were deduced for the

PFBA and bromide were used for lithium, and only the sorption parameters were adjusted to fit the lithium response. We found that the assumption of equilibrium, linear sorption was adequate to provide good fits to the late lithium response, so rate-limited and nonlinear fits were not attempted. The sorption parameters derived for all pathways in both the split-pathway case and the linear, rate-limited case are presented for comparison in Table 6. Figure 14 shows plots of the fits to the lithium data for these two cases. Composite fits to the lithium data assuming nonlinear sorption (either equilibrium or rate-limited) in the first pathway are not presented, but they were very similar to the linear, rate-limited case shown in the lower plot of Figure 14. The composite fits to all three solute tracers for the split-pathway case are shown in Figure 15.

The sorption parameters in Tables 5 and 6 suggest that, in general, the magnitude of sorption occurring in the field was in reasonably good agreement with that in the laboratory experiments. If anything, sorption in the field was slightly stronger than in the laboratory experiments, but this apparent result could occur if the effective surface-area-to-volume ratio for matrix sorption in the field were greater than that inferred from a bulk density to porosity ratio of 10 g/cm^3 (which was the ratio assumed in calculating the field sorption parameters). Sorption rates in the field were also possibly slower than in the laboratory column experiments. This discrepancy, if real, might be explained by mass-transfer limitations in the field that were not present in the laboratory, rather than by reaction rate limitations, although we have no direct evidence to support either hypothesis. In comparing the laboratory and field data it is important to recognize that we allowed no within-pathway variability of matrix diffusion or sorption parameters in the interpretation of the field experiments (other than "splitting" the first pathway to allow for two sets of sorption parameters within that pathway). Physical and chemical heterogeneity giving rise to such variability certainly exists in the field system, but we had no objective way of building it into our models, and the limited set of laboratory experiments using Bullfrog tuff collected from a single location could not capture this variability. The field-derived Langmuir isotherm parameters suggest that sorption in the field was stronger at lower concentrations and weaker at higher concentrations than in the laboratory. This result suggests that the use of the laboratory data to predict lithium transport over long distances and times, where concentrations should remain low and kinetics will be unimportant, should tend to overestimate transport rates.

Uncertainties and Alternate Interpretations

There are several sources of uncertainty associated with the tracer tests and their interpretation. First, there are data uncertainties, which are related to the accuracy and precision of the tracer chemical analyses, including both random and systematic errors. We believe that random errors were small because the breakthrough curve data are not widely scattered and show well-defined trends. The most significant sources of systematic errors would have been day-to-day differences in analytical instrument operation and in analytical standard preparation. However, careful checks with control samples and cross-checking with

another analytical laboratory (University of Nevada at Las Vegas, unpublished data) indicated that systematic errors were minimal. Incomplete knowledge of the residual concentration of PFBA in the October test due to the May PFBA injection is an additional source of uncertainty in the October PFBA data (see Test Interpretation section and Figs. 4 and 9), but this uncertainty can be bounded and shown to have minimal impact on the interpretative analysis.

Uncertainties in the parameter estimates given in Tables 3 and 4 are related to uncertainties in the data, discussed above, and uncertainties in the uniqueness of the curve fits. Parameter uncertainty due to data scatter can generally be quantified by statistical measures such as "95% confidence intervals" (Draper and Smith, 1981). For a given set of modeling assumptions, we expect this uncertainty to be relatively small given the smoothness of the breakthrough curve data, but we have left its quantification for future work. It is clear that uniqueness-of-fit uncertainties are lower when several tracer responses are analyzed simultaneously (Tables 3 and 4) than when only a single response is analyzed (Table 2) because more constraints are placed on the interpretation. However, a detailed analysis of this uncertainty is also reserved for future work.

We believe that the most important source of uncertainty in the tracer test interpretation is associated with the modeling assumptions made in the curve-fitting procedure. These uncertainties are similar to the uniqueness-of-fit uncertainties mentioned above, but they go beyond a simple examination of various combinations of parameter values that yield good fits to the data. An example of this type of uncertainty is the different values of mean residence times and Peclet numbers obtained depending on whether linear or radial flow is assumed (Tables 3 and 4). Intuitively, we expect that the range of parameter values in Tables 3 and 4 is greater than any 95% confidence interval that would be obtained from standard statistical techniques if only a single assumption were made about the flow field.

Uncertainties also arise from: (1) lack of knowledge of the actual diffusion coefficients of solutes in the matrix, (2) the possibility that bromide and PFBA diffusion coefficients differ by other than a factor of 2, (3) the possibility that tracers may not have entered the fastest pathways out of the injection borehole until late during the injection, and (4) the possibility that the wellbore source function for any of the "pathways" could have been significantly different than an exponential decay with a time constant approximately equal to the borehole volume divided by the injection flow rate. The effect of uncertainty (1) can be deduced by examining the formation transfer function in Figure 6. For instance, if the diffusion coefficients in the matrix are actually an order-of-magnitude lower than we assumed, which is not unrealistic, the matrix diffusion mass transfer coefficient, ϕ/b , in all pathways would have to be increased by a factor of 3.162 ($\sqrt{10}$) to offer the same fits that we obtained. Uncertainty (2) would result in different parameter estimates throughout the model, but even if the difference between bromide and PFBA diffusion coefficients were as much as a factor of 3, which is also not unrealistic, the effect on model parameters would be minimal. For instance, scoping calculations indicated that a factor of 3 difference between bromide and PFBA diffusivity would result in only a 10-20% difference in the model parameter estimates in Tables 3 and 4.

Effects of uncertainties (3) and (4) were also evaluated by conducting scoping calculations, and it was found they had a significant impact on the parameter estimates only for the fastest pathway(s) that explained the first tracer peak. Because there was not an early peak in the May test, it was assumed that the tracer mass resulting in the first October peak exited the injection borehole during the last 2 hours of the injection. When it was assumed that the tracer exited the borehole over the entire 10 hour duration of the injection pulse, the linear τ and Pe were estimated to be 36 hr and 8.0, respectively, compared to 35 hr and 5.5 in Tables 3 and 4. Thus, spreading the injection pulse over a longer time, in effect, reduced the amount of dispersion necessary to fit the early data. Obviously, the actual duration of the injection pulse for the first tracer peak could have varied anywhere from the full 10 hr to ~1.3 hr (to account for the 13% of the tracer mass observed in the first peak). We felt it was reasonable to assume a delayed, short-duration injection because of the lack of an early peak in the May test, where the injection duration was less than an hour. For the later "pathways" accounting for the balance of the October breakthrough curves, we assumed that the injection pulse was 10 hr long. We found that varying the injection duration from 1.3 to 10 hr had virtually no effect on the interpretation of the latter portion of the breakthrough curves.

The source term uncertainty was investigated by varying the exponential decay time constant by about an order of magnitude, from 0.13 to 1 hr⁻¹. For perspective, the value corresponding to the injection borehole volume divided by the injection rate was ~0.26 hr⁻¹. Interestingly enough, both the mean residence times and Peclet numbers decreased as the time constant was decreased (i.e., a slower exponential decay). This result suggested that the model was trying to compensate for a slow release from the injection wellbore by speeding up the movement of tracer through the formation and increasing the amount of mass arriving early as a result of dispersion. Because the fits tended to be better with faster decay constants and also because higher dispersion is actually less conservative in a performance assessment calculation, we decided to use a decay constant of 1 hr⁻¹ to obtain all of the parameter estimates in Tables 3 through 6. This assumption also helped when comparing the nonlinear RETRAN predictions to the RELAP results because RETRAN currently does not explicitly account for an exponentially decaying source term. It should be noted that the value of the decay constant (within the range stated above) had virtually no effect on the interpretation of the latter portion of the breakthrough curves.

We also examined uncertainties associated with various assumptions about lithium sorption in the system. For instance, we found that we could obtain fits that were essentially just as good as the fits shown in Figure 13 by making the following alternative assumptions about lithium behavior.

- (1) The pathways were identical to those in Table 6 for the case with a split first pathway. However, sorption was assumed to occur only in the matrix with no fracture sorption. Matrix sorption in all pathways was assumed to be equilibrium and linear.
- (2) There was a pathway that had no sorption or matrix diffusion at all. This pathway was assumed to account for all of the first lithium peak and a

substantial portion of the first PFBA and bromide peaks. The remainder of the first PFBA and bromide peaks were accounted for by second and third pathways in which there was a large amount of matrix diffusion (and sorption) in both the fractures and the matrix. Sorption was assumed to be equilibrium and linear in all pathways.

The second case actually represents a variation in the interpretation of the PFBA and bromide responses, in addition to the lithium response. This case was included primarily to demonstrate that it is possible, however unlikely, to postulate that matrix diffusion is not necessarily occurring in all flow pathways in the system. Model parameters yielding the best simultaneous fits to the PFBA, bromide, and lithium data for this case are given in Table 7. For the first case listed above, a good fit was obtained with the same three pathways as in the split-pathway case in Table 6, but with matrix retardation factors, R_m , equal to 6.4, 90, and 30 in pathways 1a, 1b, and 2, respectively.

Although this exercise points out considerable ambiguity in the interpretation of the lithium data, we consider the interpretations presented in Tables 3 and 4 (and Figure 14) to be the most reasonable based on our knowledge of lithium sorption derived from the laboratory experiments of Appendix A. The matrix sorption parameters required to obtain good fits in the first alternate case described above (Table 7) seem unreasonably large considering the laboratory sorption data. Given that matrix porosities in the interval tested range from 0.15 to 0.25, and bulk densities correspondingly range from about 2.25 to 2.0 g/cm³, equation (2) suggests that even a K_D as large as 3 would result in a maximum matrix retardation factor, R_m , of about 46. However, local surface-area-to-volume ratios are what really control sorption, and these may be considerably greater than the bulk-density-to-matrix-porosity ratio assumed in equation (2). The second alternate case (Table 6) seems even less plausible than the first given the very large matrix diffusion mass transfer coefficient, $\phi/b = 6 \text{ cm}^{-1}$, required in the second subpathway to compensate for the lack of matrix diffusion in the first subpathway. Such a large mass transfer coefficient implies a relatively small fracture aperture, b , which is at odds with the short residence time (high flow rate) assumed for this subpathway. One would also have to speculate the existence of a single very large aperture fracture pathway in this case that behaved essentially as a "pipe" to transport a fraction of the tracers without any matrix diffusion or sorption. The microsphere data argue against this hypothesis because the microspheres would be expected to move very efficiently through such an open pathway, and this was clearly not the case.

In contrast to the alternate cases, the matrix diffusion and sorption parameters of Tables 3 and 4 have values in all pathways that are reasonably consistent with our current understanding of the saturated zone near Yucca Mountain (Robinson, 1994) and also in better agreement with the laboratory sorption data reported in Appendix A. It is for these reasons that we put more faith in the interpretation of the data represented by Tables 3 and 4 (and Figure 14) than in the other possible interpretations, although we cannot unequivocally rule the others out.

Discussion

We now consider the implications of the test interpretation(s) and the uncertainties discussed in the preceding sections. First, it is apparent that regardless of which uncertainties or alternative explanations are considered, it must be concluded that matrix diffusion and sorption are occurring in most, if not all, flow pathways. Second, the lithium sorption parameters deduced from the fits we associate with the most likely test interpretations (Tables 5 and 6) are in reasonably good agreement with the laboratory sorption data, although they tend to underestimate the sorption rates observed in the lab. The agreement between field and laboratory is considered acceptable given all of the chemical and physical heterogeneity likely in the field and the lack thereof in the interpretive models and the laboratory experiments. Furthermore, a comparison of the laboratory- and field-derived sorption parameters suggests that the use of the laboratory data to predict field-scale lithium transport would tend to slightly overestimate field transport rates over long distances and times. We conclude that a dual-porosity conceptualization of the saturated zone near Yucca Mountain is valid, and that the reasonable agreement between field and laboratory lithium sorption parameters lends validity to the practice of using laboratory-derived sorption data to predict field-scale transport behavior. However, the latter conclusion should be applied cautiously to sorbing radionuclides, for which there are no field data in the immediate vicinity of Yucca Mountain. Finally, although we have not yet quantitatively interpreted the microsphere response in the October tracer test, the breakthrough curve indicates that significant transport of submicron-sized particles can occur over relatively large distances in the saturated zone near Yucca Mountain.

Table 8 provides ranges of physical parameter values derived from the field test interpretations (excluding the two alternative cases discussed in the preceding section). These ranges are intended to provide performance assessment modelers with lower and upper bounds for use in large-scale, abstracted transport models, although it must be recognized that the values strictly apply to only the lower Bullfrog tuff at the C-wells. Lithium sorption parameters are not included in Table 8 because they are not directly relevant to any radionuclides of importance to performance assessment. Although some of the parameter ranges in Table 8 seem large, the use of simultaneously-injected multiple tracers significantly reduced the range that would have been reported in a single tracer test.

The longitudinal dispersivity values in Table 8 were calculated using $\alpha = L/Pe$, where the travel distance, L , was assumed to take on minimum and maximum values of 30 and 100 m, corresponding to interborehole distance and the approximate distance between the bottom of one borehole and the top of the other (the maximum possible linear transport distance), respectively. To put these dispersivities in perspective, Figure 16 shows a box encompassing the entire range of values in Table 8 superimposed on a plot of dispersivity vs. scale taken from Neuman (1990). It is apparent that the C-wells longitudinal dispersivity is reasonably consistent with other data sets and with existing theories on the scale dependence of dispersion.

The values in Table 8 for fracture spacing, fracture apertures, effective flow porosity, and effective fracture porosity are all very uncertain and should be used with caution. The lower bound for fracture spacing is based on fitting the extreme tail of the PFBA and bromide breakthrough curves where there is considerable scatter and uncertainty in the data. Upper and lower bounds for fracture apertures were estimated by dividing the maximum and minimum matrix porosities reported for the interval tested (Fig. 2) by the smallest and largest fitted ϕ/b values, respectively. The flow porosity was calculated from the mean residence times assuming homogeneous, isotropic, radial flow of the entire production flow rate over the entire thickness of the test interval (~100 m). These assumptions can be shown to frequently result in conservatively high estimates of flow porosity when the medium is highly heterogeneous and the test is conducted with weak recirculation and no mixing of the injection interval (unpublished results). Also, the upper bound flow porosity values are derived from the longest residence time pathways, which very likely received much less than 100% of the total production flow rate. The fracture porosity upper bound reported in Table 8 is distinguished from the upper bound flow porosity in that it is estimated by dividing the maximum fracture aperture (0.75 cm) by the minimum fracture spacing (10 cm). The lower bound for fracture porosity is zero because reasonable fits to the tracer data were obtained assuming an infinite matrix.

While we considered the tracer tests to be highly successful, we recognize that much work remains to be done. We tested only one formation at one location near Yucca Mountain, and it would not be prudent to base performance assessments of the entire saturated zone on such a limited data set. Thus, we plan to conduct additional tracer tests, possibly in other test configurations such as single-well injection-withdrawal mode, in other hydrogeologic formations, and at other locations near Yucca Mountain. Issues to be addressed in these tests include, but are not necessarily limited to, (1) the time- and distance-scale dependence of the processes of dispersion, matrix diffusion, and sorption, (2) the spatial variation of transport properties in the vicinity of Yucca Mountain, (3) the variation of transport properties in different stratigraphic zones and in different hydrogeologic settings (e.g., faulted vs. unfaulted rock, high conductivity vs. low conductivity rock, high matrix porosity vs. low matrix porosity rock), and (4) field sorption behavior in different rock types (e.g., mineralogically altered vs. unaltered, high in clays vs. low in clays, welded vs. unwelded). We also plan to conduct additional laboratory experiments to characterize the sorption of lithium and other potential reactive tracers to other tuffs likely to be encountered in the saturated zone near Yucca Mountain. Additionally, we plan to conduct experiments to measure the diffusion coefficients of nonsorbing tracers in tuff matrices so that we can use actual measured values in our interpretive analyses rather than values derived from the literature.

We consider our modeling of the tracer tests to be a relatively simple approach to interpreting the data. This approach involves a minimum number of adjustable parameters, which is consistent with our limited knowledge of flow system geometry and heterogeneity. Although we believe that our conclusions are sound, we recognize that there is much room for revisiting the analyses using more sophisticated modeling tools and introducing more system complexity, particularly

as more site-specific information becomes available. In the future, we plan to incorporate this information into numerical models that can better account for both physical and chemical heterogeneity in two- and three-dimensions. We also plan to examine other semi-analytical modeling approaches, such as the multi-rate diffusion model of Haggerty and Gorelick (1995), which has been used to interpret tracer tests conducted in a fractured dolomite near Carlsbad, NM for the Waste Isolation Pilot Plant project (Meigs et al., in press). The fact that the matrix diffusion mass transfer coefficients in our analyses decreased as pathway residence times increased (Tables 3 and 4) and that a finite fracture spacing offered a better fit to the end of the conservative tracer breakthrough curves suggests that multiple diffusion rates and/or finite fracture spacings may be important at long time scales in the groundwater system. It might also suggest that interconnected porosity, and hence diffusion coefficients in the matrix, decrease with distance into the matrix (away from fractures). It is also possible that some of the apparent matrix diffusion in the field experiments was actually diffusion into stagnant water along the rough fracture walls or within the fractures themselves (occurring as a result of tracers diffusing out of high flow rate channels and into low flow zones), rather than into the matrix proper. These possibilities have important implications for saturated zone performance assessments and merit further study because, if valid, they would suggest that matrix diffusion might be overestimated in short-duration tracer experiments.

Acknowledgments

Many people from Los Alamos National Laboratory provided assistance with the field tests, which were conducted over an eight-month period. These people are too numerous to mention here by name, but we especially thank Marc Haga and Brent Newman for their help in managing site activities, and Tim Callahan, Alan Noell, and Steve Thornton, who spent a great deal of time at the remote site. Dale Counce of Los Alamos National Laboratory conducted all of the solute tracer analyses. Matt Becker, formerly Los Alamos, now USGS, was responsible for much of the preliminary work on what ultimately became the RELAP model. We are grateful to staff of the United States Geological Survey, Denver, CO for setting up most of the equipment used in the tracer tests. We also wish to thank Bruce Robinson, Darlene Bandy, Chuck Cotter, Edward Essington, Armando Furlano, and Jason Kitten for assistance with the laboratory studies described in Appendix A.

This work was supported by the Yucca Mountain Site Characterization Project Office as part of the Civilian Radioactive Waste Management Program. This Project is managed by the U.S. Department of Energy, Yucca Mountain Site Characterization Project. This report was prepared in accordance with OCRWM-approved quality assurance procedures implementing requirements of the Quality Assurance Requirements Description. All data presented in this report were developed under Project-approved quality assurance procedures. These data have been assigned data tracking number (DTN) LAPR831231AQ97.001, and they are being submitted to the GENISES database in parallel with the submittal of this report. The computer

software used for the interpretative analyses discussed in this report are not yet qualified for use in quality-affecting activities on the Project. The interpretations must therefore be considered non-Q at this time.

References

- Becker, M. W. and Charbeneau, R. J., A first passage time solution for radially convergent tracer tests, submitted to *Water Resour. Res.*, 1996.
- Benson, C. F. and Bowman, R. S., Tri- and tetrafluorobenzoates as nonreactive tracers in soil and groundwater, *Soil Sci. Soc. Am. J.*, 58, 1123-1129, 1994.
- Bird, R. B., Stewart, W. E., and Lightfoot, E. N., *Transport Phenomena*, John Wiley and Sons, New York, 1960.
- Churchill, R. V., *Operational Mathematics*, 2nd ed. McGraw-Hill, New York, 1958.
- Draper, N. R. and Smith, H., *Applied Regression Analysis*, 2nd ed. John Wiley and Sons, New York, 1981.
- Fuentes, H. R., Polzer, W. L., Essington, E. H. and Newman, B. D., Characterization of reactive tracers for C-wells field experiment I: Electrostatic sorption mechanism, lithium. *Los Alamos National Laboratory Report LA-11691-MS*, Los Alamos, NM, 1989.
- Geldon, A. L., Preliminary hydrogeologic assessment of boreholes UE-25c#1, UE-25c#2, and UE-25c#3, Yucca Mountain, Nye County, Nevada, *Water-Resources Investigations Report 92-4016*, United States Geological Survey, Denver, CO, 1993.
- Geldon, A. L., Average linear velocity and travel time at the C-hole complex, *Memo to the Record*, March 1, 1995.
- Geldon, A. L., Results and interpretation of preliminary aquifer tests in boreholes UE-25c#1, UE-25c#2, and UE-25c#3, Yucca Mountain, Nye County, Nevada, *Water-Resources Investigations Report 94-W-0412*, United States Geological Survey, Denver, CO, 1996.
- Grisak, G. E. and Pickens, J. F., Solute transport through fractured media, 1: The effect of matrix diffusion, *Water Resour. Res.*, 16(4), 719-730, 1980.
- Haggerty, R. and Gorelick, S. M., Multiple-rate mass transfer for modeling diffusion and surface reactions in a media with pore-scale heterogeneity, *Water Resour. Res.*, 31(10), 2383-2400, 1995.

- Maloszewski, P. and Zuber, A., Interpretation of artificial and environmental tracers in fissured rocks with a porous matrix, in *Isotope Hydrology*, International Atomic Energy Agency (IAEA), Vienna, Austria, pp. 635-651, 1983.
- Maloszewski, P. and Zuber, A., On the theory of tracer experiments in fissured rocks with a porous matrix, *J. Hydrology*, 79, 333-358, 1985.
- Maloszewski, P. and Zuber, A., Influence of matrix diffusion and exchange reactions on radiocarbon ages in fissured carbonate aquifers, *Water Resour. Res.*, 27(8), 1937-1945, 1991.
- Meigs, L. C., Beuheim, R. L., McCord, J. T., Tsang, Y. W., and Haggerty, R., Design, modelling, and current interpretations of the H-19 and H-11 tracer tests at the WIPP Site, for publication in *Field Tracer Transport Experiments*, proceedings of the first GEOTRAP Workshop, Cologne, Germany, August 28-30, 1996.
- Moench, A. F., Convergent radial dispersion in a double-porosity aquifer with fracture skin: Analytical solution and application to a field experiment in fractured chalk, *Water Resour. Res.*, 31(8), 1823-1835, 1995.
- National Research Council, *Rock Fractures and Fluid Flow: Contemporary Understanding and Applications*, National Academy Press, Washington, D.C., 1996.
- Neretnieks, I., Diffusion in the rock matrix: An important factor in radionuclide migration?, *J. Geophys. Res.*, 85(B8), 4379-4397, 1980.
- Neuman, S. P., Universal Scaling of Hydraulic Conductivities and Dispersivities in Geologic Media, *Water Resour. Res.*, 26(8), 1749-1758, 1990.
- Newman, J. S., *Electrochemical Systems*, Prentice-Hall, Englewood Cliffs, NJ, 1973.
- Reimus, P. W., The Use of Synthetic Colloids in Tracer Transport Experiments in Saturated Rock Fractures, *Los Alamos National Laboratory Report LA-13004-T (also PhD Dissertation, University of New Mexico)*, Los Alamos National Laboratory, Los Alamos, NM, 1995.
- Reimus, P. W., Becker, M. W., and Vilks, P., Microspheres detected by flow cytometry and their application as groundwater tracers in fractured rock, in preparation.
- Reimus, P. W. and Turin, H. J., Results of reactive tracer testing at the C-holes, *Yucca Mountain Site Characterization Project Milestone Report 4270M*, Los Alamos National Laboratory, Los Alamos, NM, 1996.

- Robinson, B. A., A strategy for validating a conceptual model for radionuclide migration in the saturated zone beneath Yucca Mountain, *Rad. Waste Mgmt. & Env. Restor.*, 19, 73-96, 1994
- Steinkamp, J. A., Habbersett, R. C., and Hiebert, R. D., Improved multilaser/multiparameter flow cytometer for analysis and sorting of cells and particles, *Rev. Sci. Instrum.*, 62(11), 2751-2764, 1991.
- Stetzenbach, K. and Farnham, I. Identification and characterization of conservative organic tracers for use as hydrologic tracers for the Yucca Mountain site characterization study, *Final Report*, Harry Reid Center for Environmental Studies, University of Nevada-Las Vegas, Las Vegas, NV, 1996.
- Tang, D. H., Frind, E. O., and Sudicky, E. A., Contaminant transport in a fractured porous media: Analytical solution for a single fracture, *Water Resour. Res.*, 17(3), 555-564, 1981.
- Triay, I. R., Birdsell, K. H., Mitchell, A. J., and Ott, M. A., Diffusion of sorbing and non-sorbing radionuclides, in *High-Level Radioactive Waste Management*, proceedings of the 4th Annual International Conference, American Nuclear Society, LaGrange Park, Illinois, pp. 1527-1532, 1993.
- USGS (United States Geological Survey), Postings at the C-wells of packer placements in c#1, c#2, and c#3 (records maintained in USGS files), May, 1996.
- Waddell, R., Printouts of C-holes borehole vertical deviation surveys dated 7/3/84 (c#1), 7/11/84 (c#2), and 7/12/84 (c#3), obtained from A. L. Geldon, USGS, 1995.
- Wan, J. and Wilson, J. L., Colloid transport in unsaturated porous media, *Water Resour. Res.*, 30(4), 857-864, 1994.

Tables

Table 1. Summary of quantitative interpretation procedure for October tracer test.

1. Find the values of τ , Pe , ϕ/b , and f (with R_m and R_f equal to 1) that provide the best simultaneous fit to the first PFBA and bromide peaks.
2. Subtract the fits obtained in step 1 from the PFBA and bromide data sets, and repeat step 1 to fit the resulting second peaks (i.e, second set of pathways).
3. Fit lithium data sequentially as in steps 1 and 2 by adjusting R_m and R_f while using the values of τ , Pe , ϕ/b , and f that gave best fits to PFBA and bromide data.
4. If step 3 results in poor fit to the lithium data for any given peak, attempt to obtain a better fit by allowing rate-limited and/or nonlinear sorption.

Table 2. Parameter values resulting in best fits to May PFBA data as a function of assumed matrix diffusion mass transfer coefficient, ϕ/b .

ϕ/b , cm^{-1}	τ , hr	Pe	Dispersivity, m^*	f
4	150	29	1.1	0.99
2	220	16	1.9	0.8
1	310	9	3.4	0.72
0.4	410	6	5.2	0.65
0 (single-porosity)	470	5	6.2	0.55

*Assumes a 30-m travel distance (borehole separation).

Table 3. Parameters obtained from 2-pathway fits to the October PFBA and bromide responses (R_f and $R_m = 1$).

Parameter	Pathway 1	Pathway 2
f , fraction mass	0.13	0.75
τ , linear flow, hr	35	1010
Pe , linear flow	5.5	1.5
τ , radial flow, hr	29	610
Pe , radial flow	8	2.7
ϕ/b , cm^{-1}	1.5	0.67
fracture spacing, cm	∞	∞

Table 4. Parameters obtained from 3-pathway fits to the October PFBA and bromide responses, where the 2nd pathway provides a good fit to the renormalized May PFBA response.

Parameter	Pathway 1	Pathway 2	Pathway 3
f, fraction mass	0.13	0.33	0.26
τ , linear flow, hr	35	360	940
Pe, linear flow	5.5	6.5	8
τ , radial flow, hr	29	300	810
Pe, radial flow	8.0	9.5	11.5
ϕ/b , cm ⁻¹	1.5	0.67	0.67
fracture spacing, cm	∞	∞	10

Table 5. Sorption parameters derived from fits to the first lithium peak shown in Figure 12. Other parameters used to obtain fits were same as for Pathway 1 in Tables 3 and 4. Laboratory Langmuir isotherm parameters were $K_L = 0.0053$ ml/g and $S_{max} = 110$ μ g/g. Laboratory forward rate constant ranged from 2.2 to 18 hr⁻¹.

Parameter	Linear, Equilibrium	Linear, Kinetic	Langmuir, Equilibrium	Langmuir, Kinetic
R_f	1 (no sorption)	1.3	1 (no sorption)	(see footnote 5)
R_m	7	21	-	-
$k_f^{(1)}$, hr ⁻¹	∞	0.12	∞	0.27
$k_m^{(2)}$, hr ⁻¹	∞	0.18	∞	0.7
$K_D^{(3)}$, ml/g	0.6	2.0	-	-
$K_L^{(4)}$, ml/ μ g	-	-	0.25	0.035
$S_{max}^{(4)}$, μ g/g	-	-	16	67

(1) Forward rate constant in fractures.

(2) Forward rate constant in matrix.

(3) Matrix value, calculated from equation (2) using fitted R_m and assuming $\rho_B = 2.0$ g/cm³ and $\phi = 0.2$. K_D not calculated for fractures because of ambiguity in defining ρ_B and ϕ in fractures. See footnote of Table 6 for laboratory K_D values.

(4) Matrix value, obtained from RETRAN assuming $\rho_B = 2.0$ g/cm³ and $\phi = 0.2$.

(5) Sorption in fractures was assumed to be Langmuirian with same K_L and S_{max} as for matrix, but with $\rho_B/\phi = 0.1$ to simulate a lower surface area to volume ratio.

Table 6. Parameters obtained from fits to October tracer responses assuming (1) equilibrium, linear sorption with split first pathway (pathways 1a and 1b) to account for lithium response, and (2) rate-limited, linear sorption to account for lithium response. Note that pathways 1a and 1b sum to pathway 1 for PFBA and bromide. Rows containing lithium sorption parameters are shaded.

Parameter	Equilibrium Fit with Split 1st Pathway			2-Pathway, Kinetic Fit	
	Pathway 1a	Pathway 1b	Pathway 2	Pathway 1	Pathway 2
f, mass fraction	0.08	0.05	0.75	0.13	0.75
τ , linear flow, hr	25	48	1010	35	1010
Pe, linear flow	8.5	14	1.5	5.5	1.5
τ , radial flow, hr	22	12	610	29	610
Pe, radial flow	44	19	2.7	8	2.7
ϕ/b , cm ⁻¹	1.5	1.5	0.67	1.5	0.67
R_f	1	5	5	13	5
R_m	6.4	43	11	21	11
$K_D^{(1)}$, ml/g	0.54	4.2	1.0	2.0	1.1
k_r , hr ⁻¹	-	-	∞	0.12	∞
k_m , hr ⁻¹	-	-	∞	0.18	∞

⁽¹⁾Matrix value, calculated from equation (2) using fitted R_m and assuming $\rho_B = 2.0$ g/cm³ and $\phi = 0.2$. For comparison, laboratory K_D values were 0.583 ml/g at the low end of the concentration range studied and 0.21 ml/g averaged over the entire concentration range studied (0.5-500 mg/L). See also Appendix A.

Table 7. Parameters obtained from fits to October tracer responses assuming one pathway (pathway 1) that has no matrix diffusion or sorption. Sorption is assumed to be equilibrium and linear in other pathways. τ and Pe for radial flow was not calculated for any of the pathways.

Parameter	Pathway 1	Pathway 2	Pathway 3
f, fraction mass	0.052	0.09	0.75
τ , linear flow, hr	43	22	1010
Pe, linear flow	4.5	7	1.5
ϕ/b , cm ⁻¹	0	6	0.67
R_f	1	10	6
R_m	1	9	11

Table 8. Ranges of physical parameters derived from the interpretation(s) of the October tracer test.

Parameter	lower bound	upper bound
longitudinal dispersivity, m	3.8	67
ϕ/b , cm^{-1}	0.67	1.5
effective fracture aperture, cm	0.2	0.75
effective fracture spacing, cm	10	∞
effective flow porosity ⁽¹⁾	0.004	0.125
effective fracture porosity ⁽²⁾	-0-	0.075

- ⁽¹⁾ Flow porosity estimated from mean residence times assuming homogeneous, isotropic, radial flow field over entire thickness of interval. These assumptions often result in conservative (high) estimates (see text).
- ⁽²⁾ Fracture porosity estimated from fracture half-aperture, b , divided by fracture spacing (Note: Only one finite value of fracture spacing, 10 cm, was obtained in any of the fits -- see Table 4).

Figures

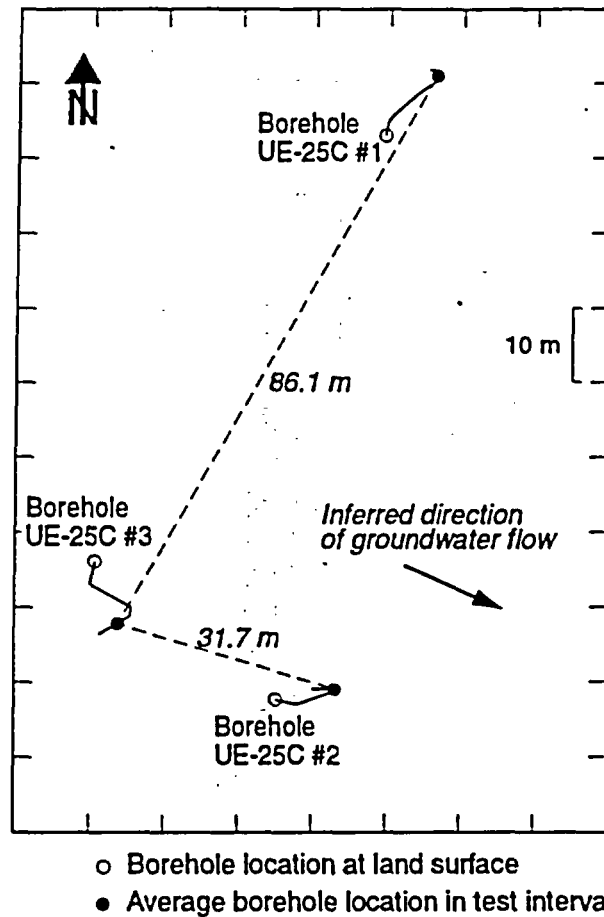


Figure 1. C-wells layout showing interwell distances between tracer test intervals (based on information in Geldon, 1993, and from vertical deviation surveys conducted in July 1984 by R. Waddell, USGS).

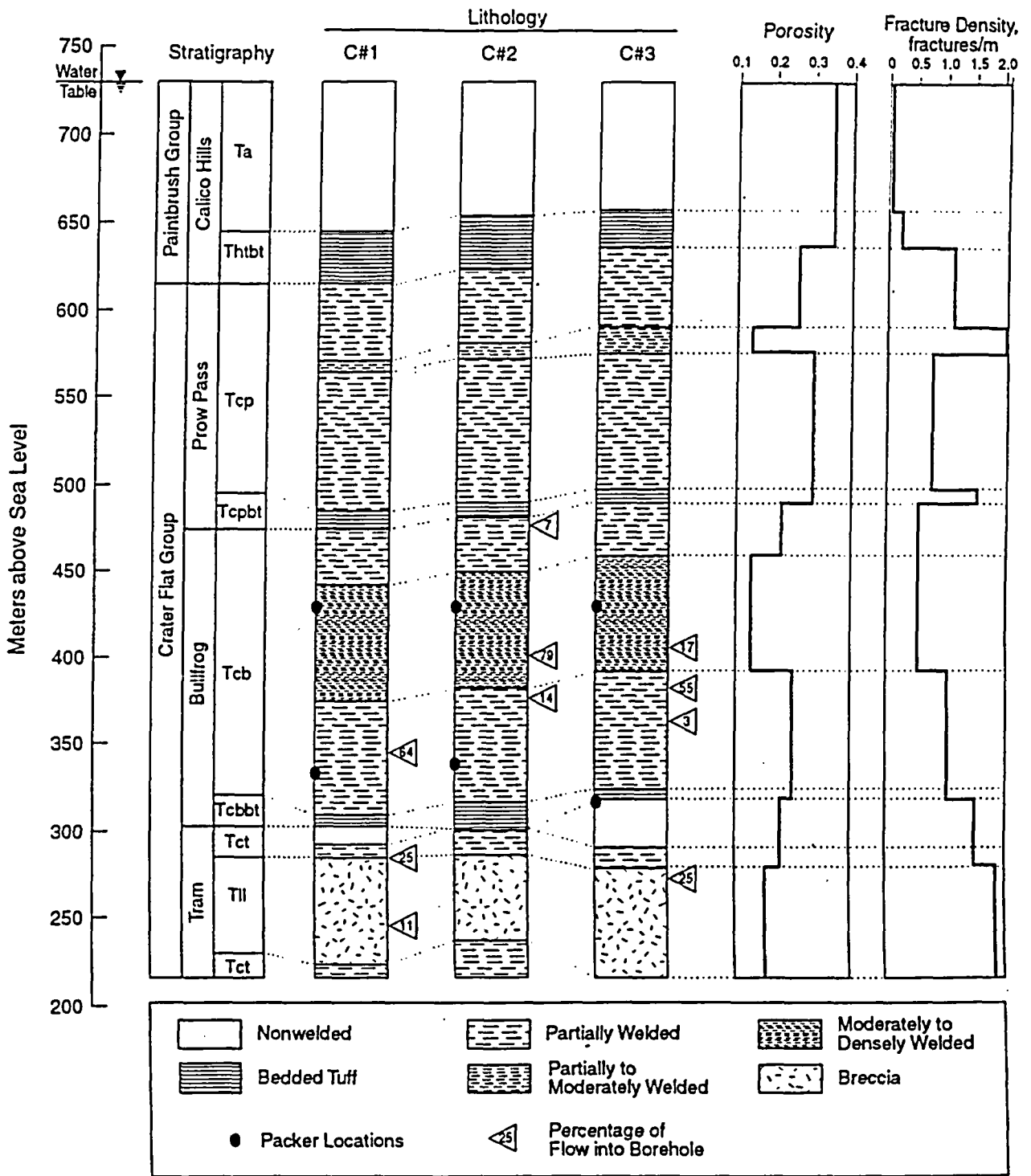


Figure 2. Stratigraphy, lithology, matrix porosity, fracture density, and inflow (from open-hole flow surveys) at the C-wells. Packer locations indicate intervals in which tracer tests were conducted (USGS, 1996). Other information derived from Geldon (1993, 1996).

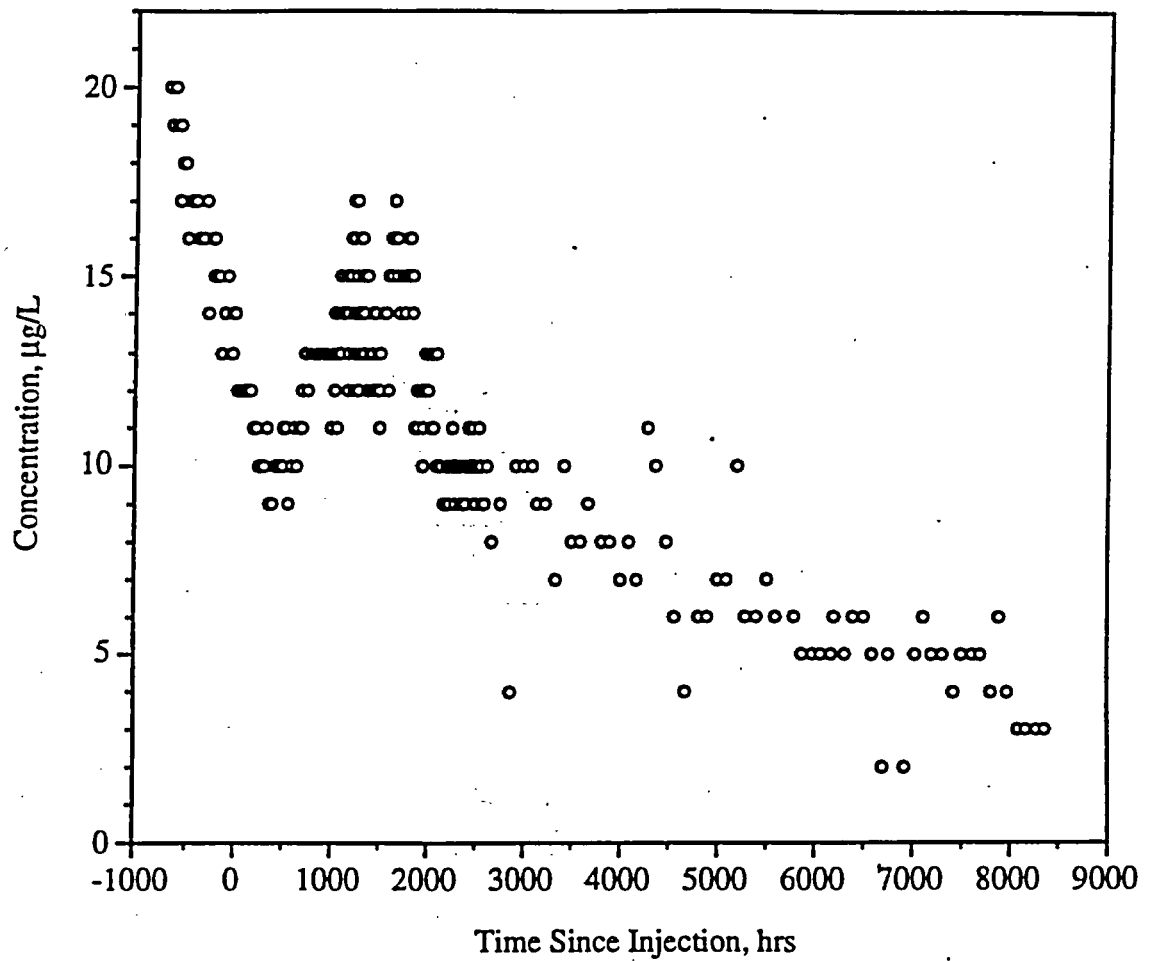


Figure 3. Breakthrough curve of iodide resulting from injection of ~12.7 kg of iodide into c#1 on June 18, 1996. Declining background prior to and immediately after injection is due to recovery of iodide from a February 1996 iodide injection into c#2. Estimated recovery from c#1 accounting for c#2 background was between 6 and 10% through June 1, 1997.

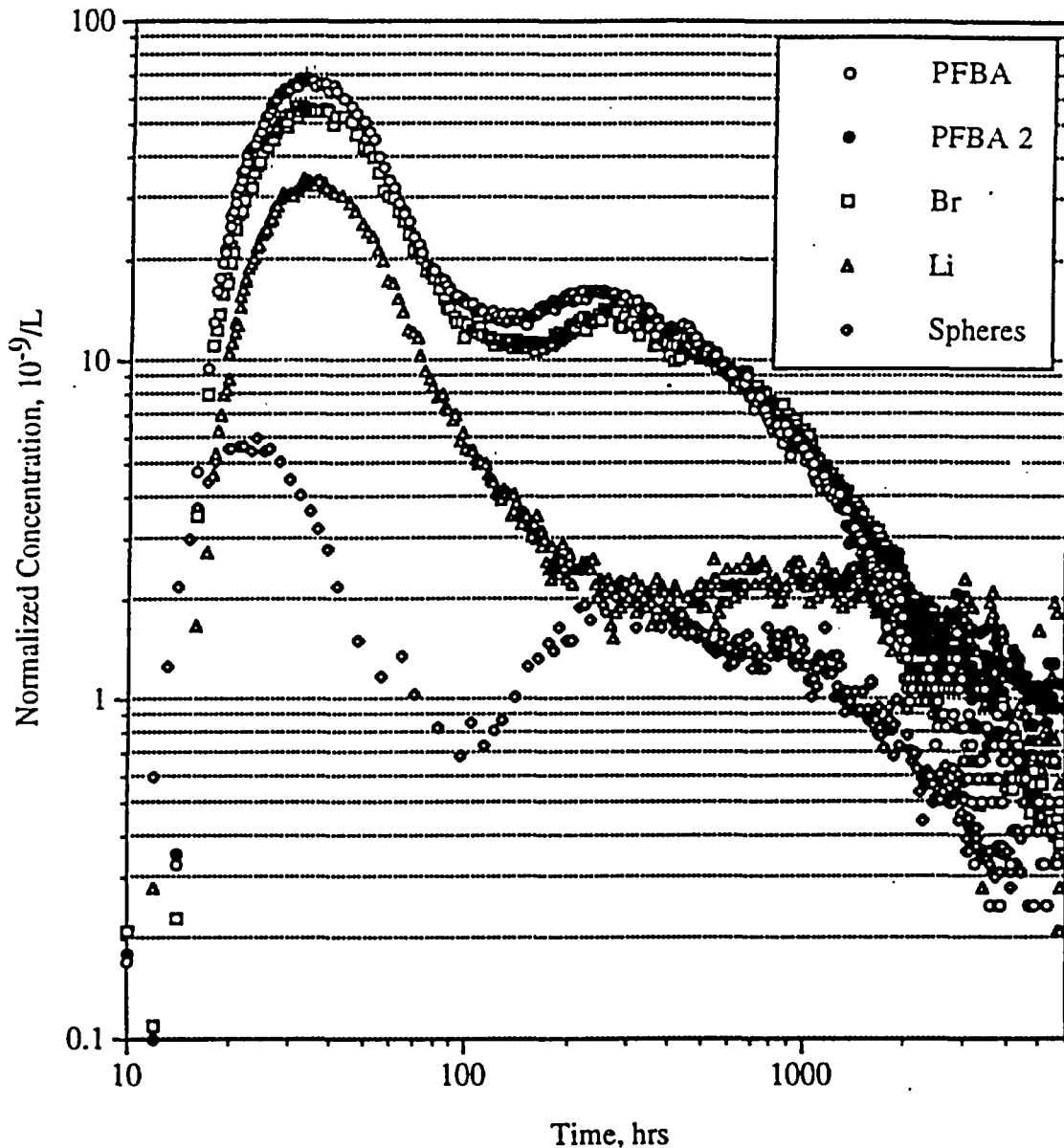


Figure 4. Normalized tracer breakthrough curves from the October 1996 tracer test conducted in the lower Bullfrog Tuff between wells c#2 and c#3. Tracer recoveries as of June 10, 1997 were ~65% for PFBA, ~65% for bromide, ~35% for lithium, and ~11% for microspheres (on April 15, 1997). The curve labelled "PFBA" was obtained by assuming that the PFBA background from the May test remained constant at 10 $\mu\text{g/L}$ throughout the October test, and the curve labelled "PFBA 2" was obtained assuming that the PFBA background from the May test decayed in exponential fashion according to a fit to the tail of the May test data.

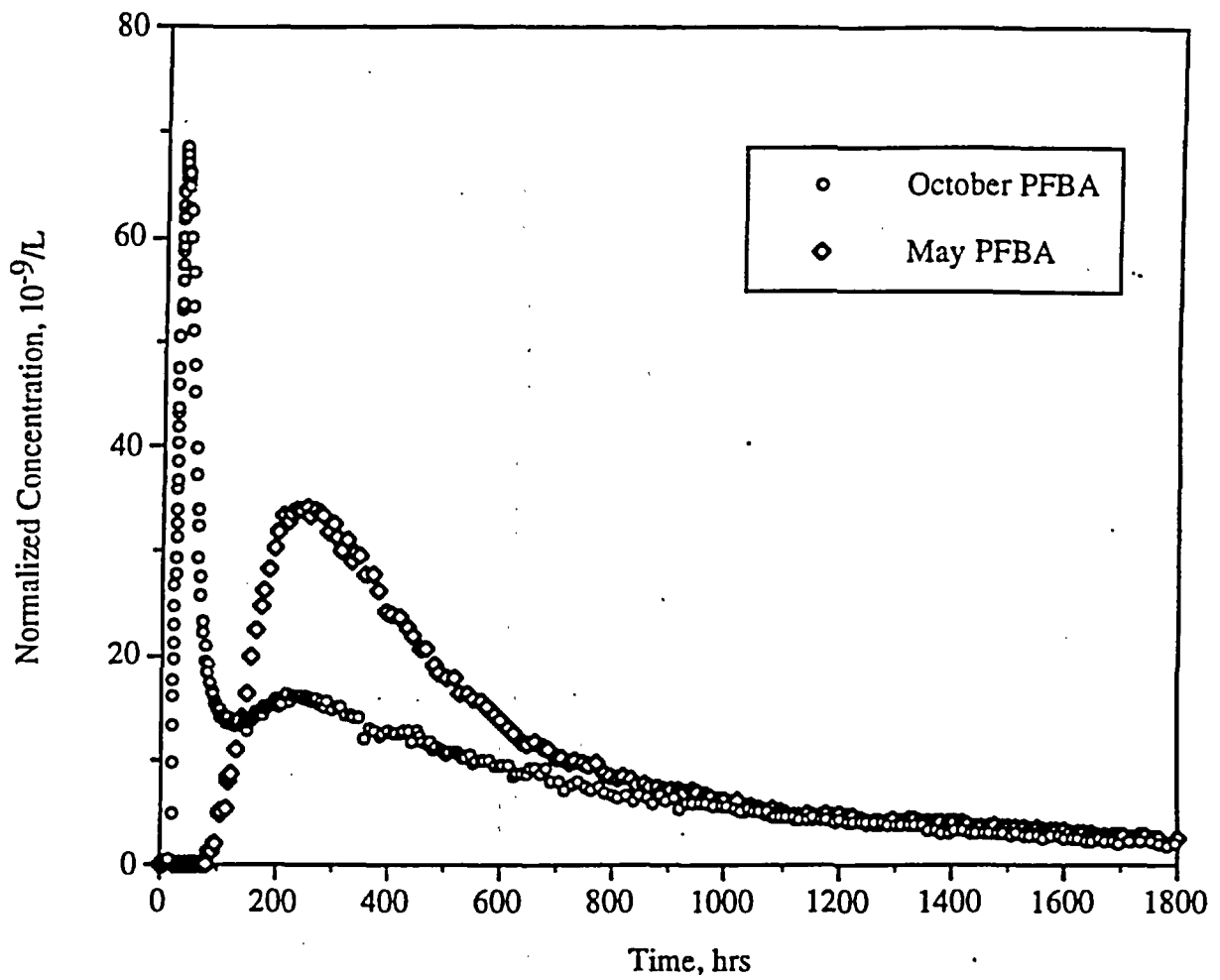


Figure 5. Normalized breakthrough curves of PFBA (through 1800 hrs) in the October and May tests between c#2 and c#3.

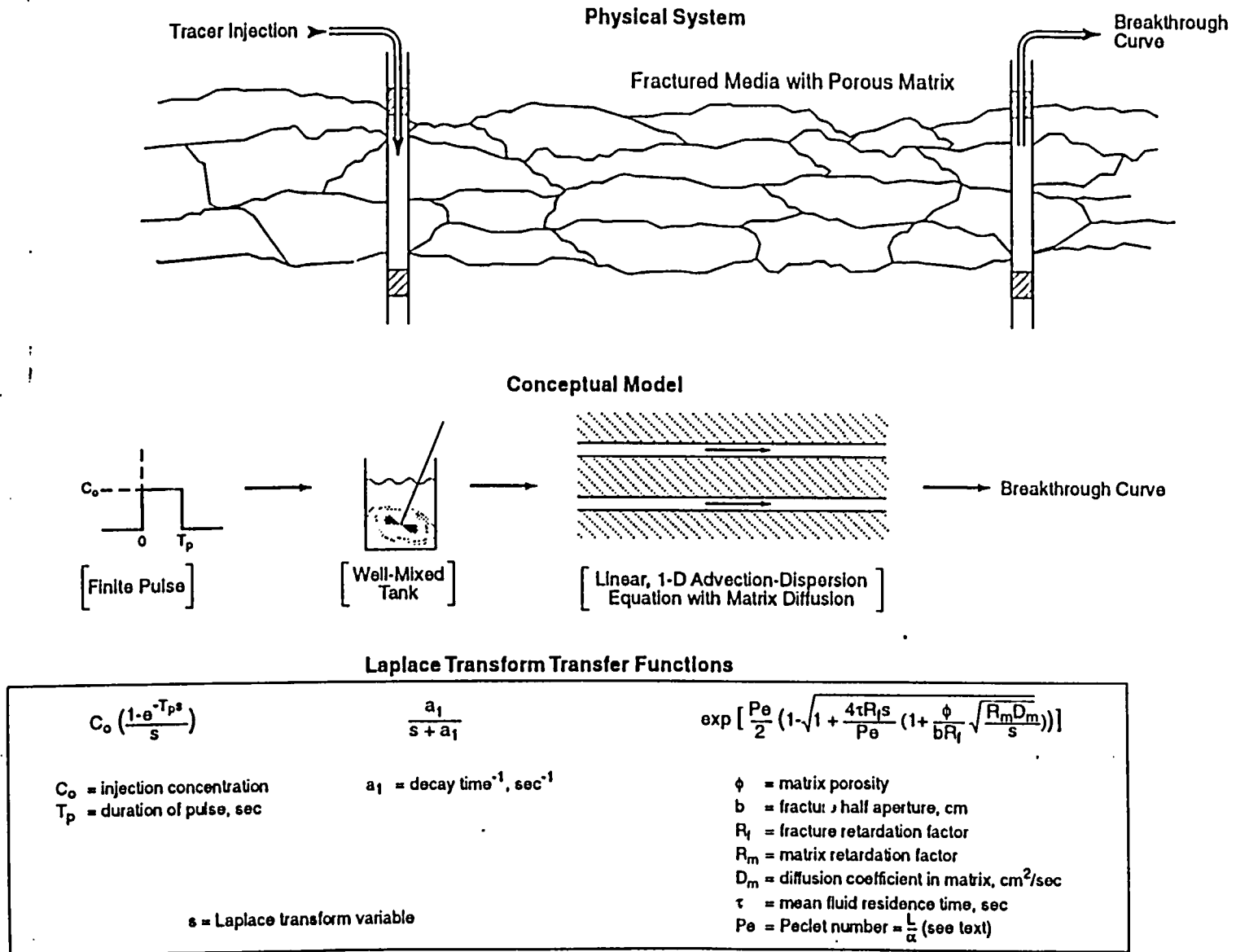


Figure 6. Physical system, conceptual model, and Laplace transform transfer functions used to interpret tracer tests.

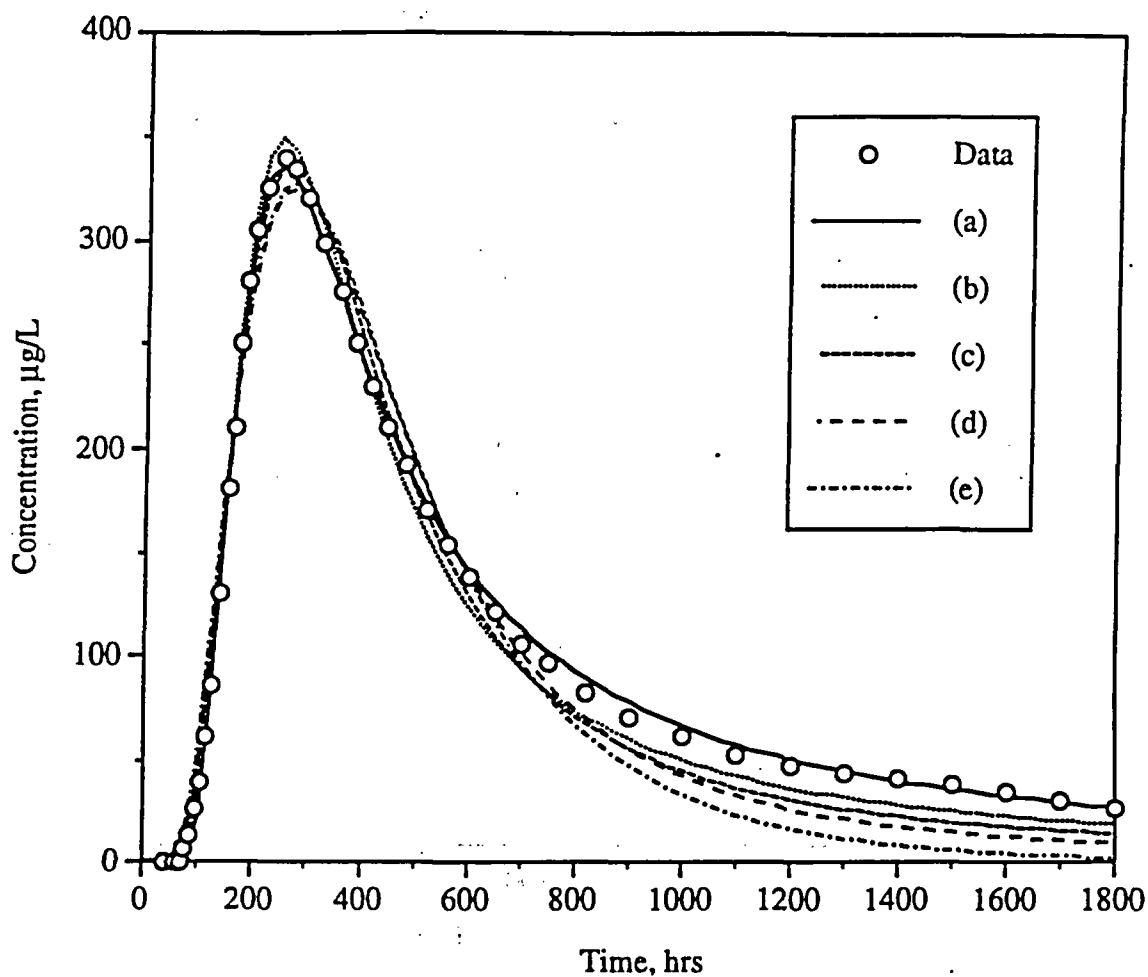


Figure 7. Fits to the May PFBA data assuming different values of the matrix diffusion mass transfer coefficient, ϕ/b : (a) 4 cm^{-1} , (b) 2 cm^{-1} , (c) 1 cm^{-1} , (d) 0.4 cm^{-1} , and (e) 0 cm^{-1} (single-porosity system). Parameter values yielding the fits are given in Table 2. Data points are a subset of the actual data (used for curve-fitting).

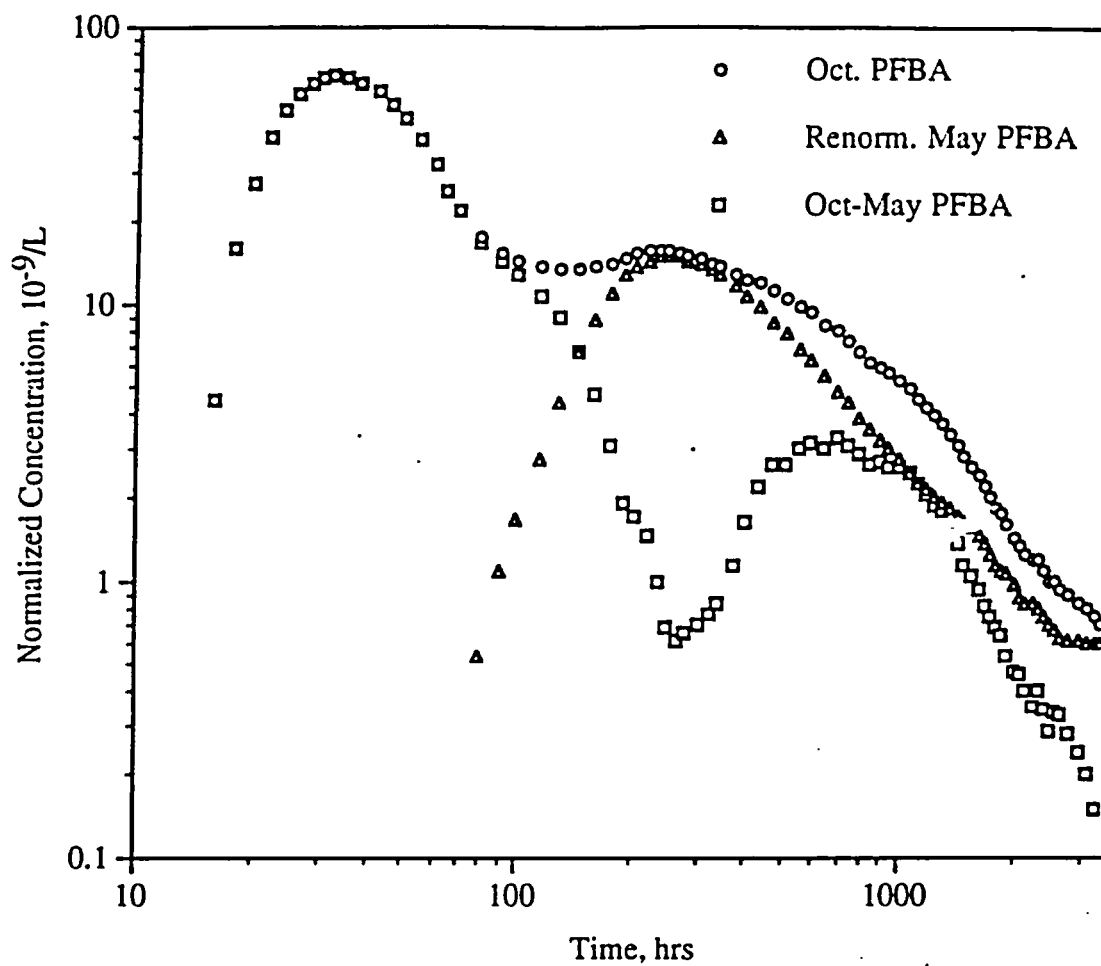


Figure 8. Subtraction of renormalized May PFBA response from October PFBA response to estimate contribution of pathways activated in October that were not activated in May. Data points are a subset of the actual data.

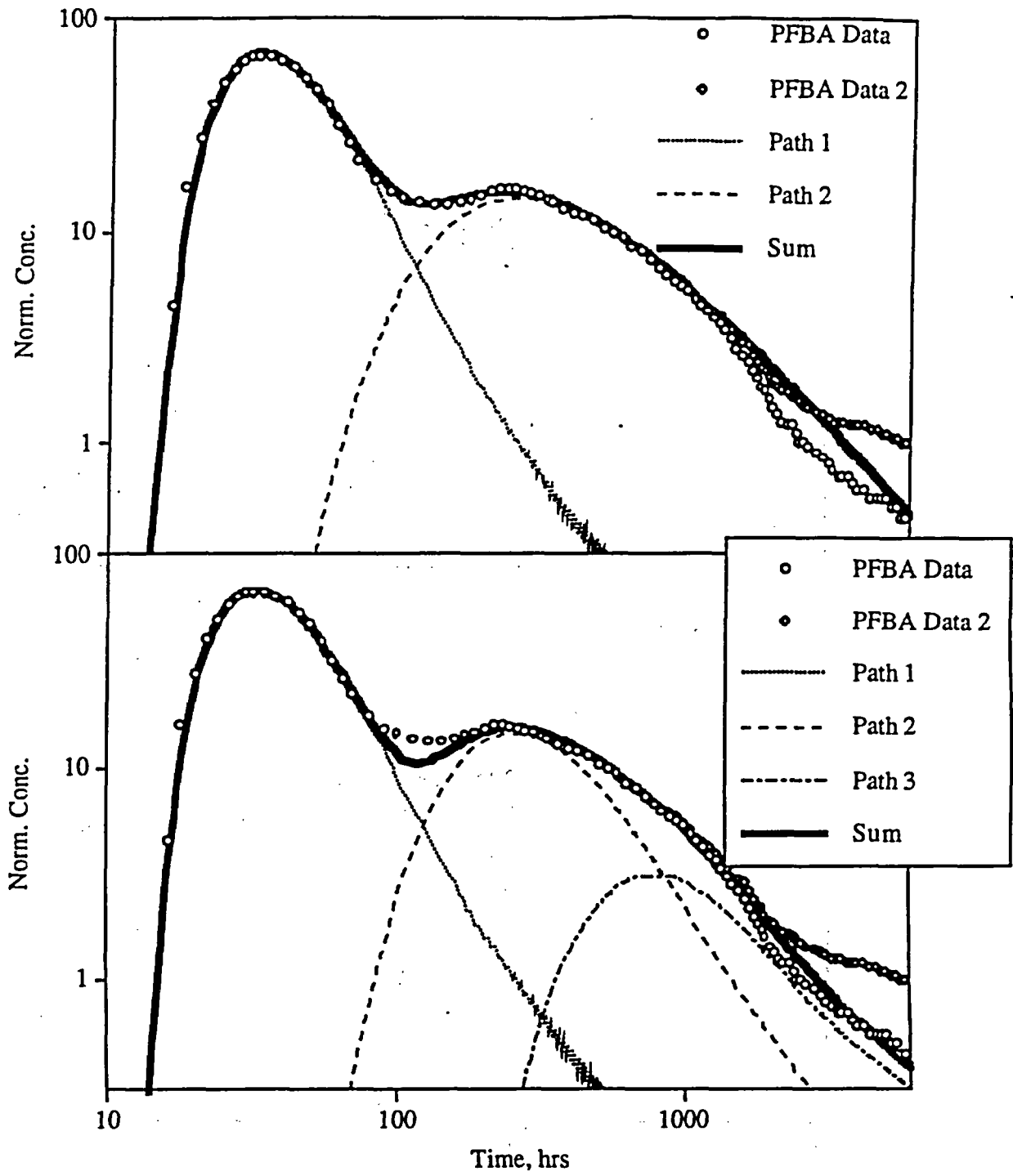


Figure 9. Fits to the October PFBA data assuming two pathways (top), and three pathways (bottom). Path 2 in the bottom figure provides a good fit to the renormalized PFBA data. Model parameters corresponding to the top and bottom fits are given in Tables 3 and 4, respectively. The data points are a subset of the actual data (used for curve-fitting).

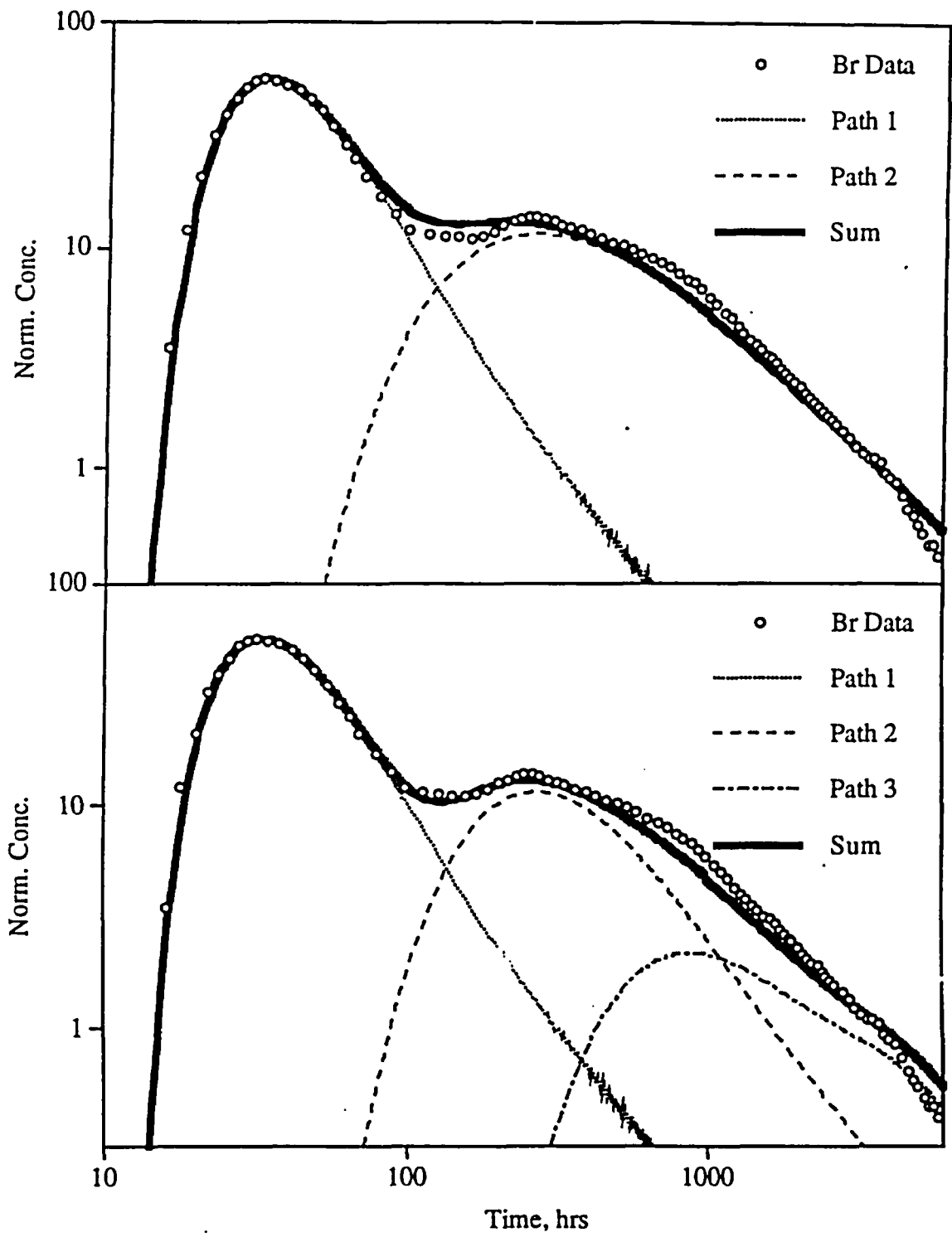


Figure 10. Fits to the October bromide data assuming two pathways (top), and three pathways (bottom). Path 2 in the bottom figure provides a good fit to the renormalized PFBA data. Model parameters corresponding to the top and bottom fits are given in Tables 3 and 4, respectively. The data points are a subset of the actual data (used for curve-fitting).

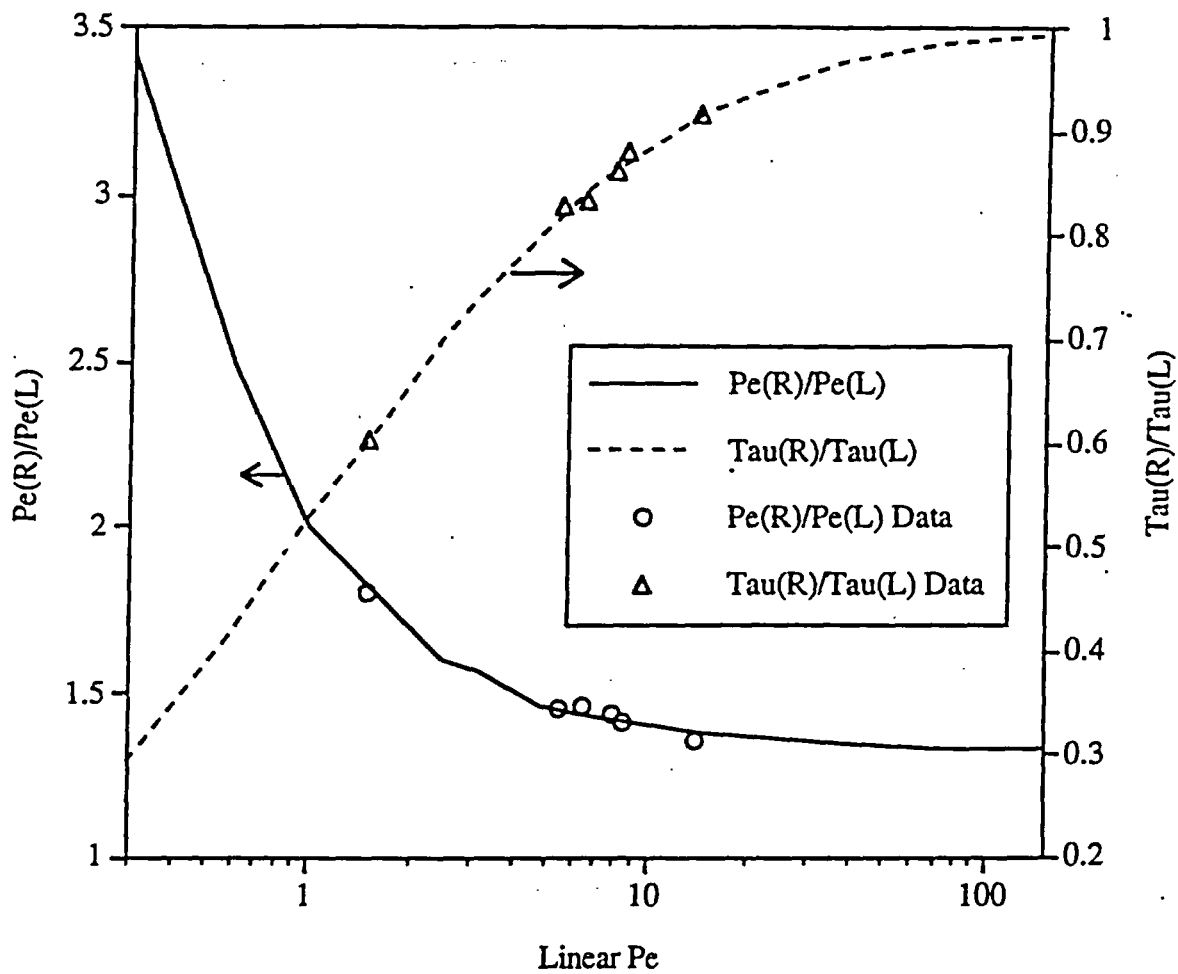


Figure 11. Ratios of radial and linear mean residence times (τ) and Peclet numbers (Pe) as a function of linear Peclet number. Curves were obtained by fitting a linear flow breakthrough curve of known τ and Pe using a radial model in RELAP. Data points correspond to the various fits to the October tracer data (see Tables 3, 4, and 6 for τ and Pe values).

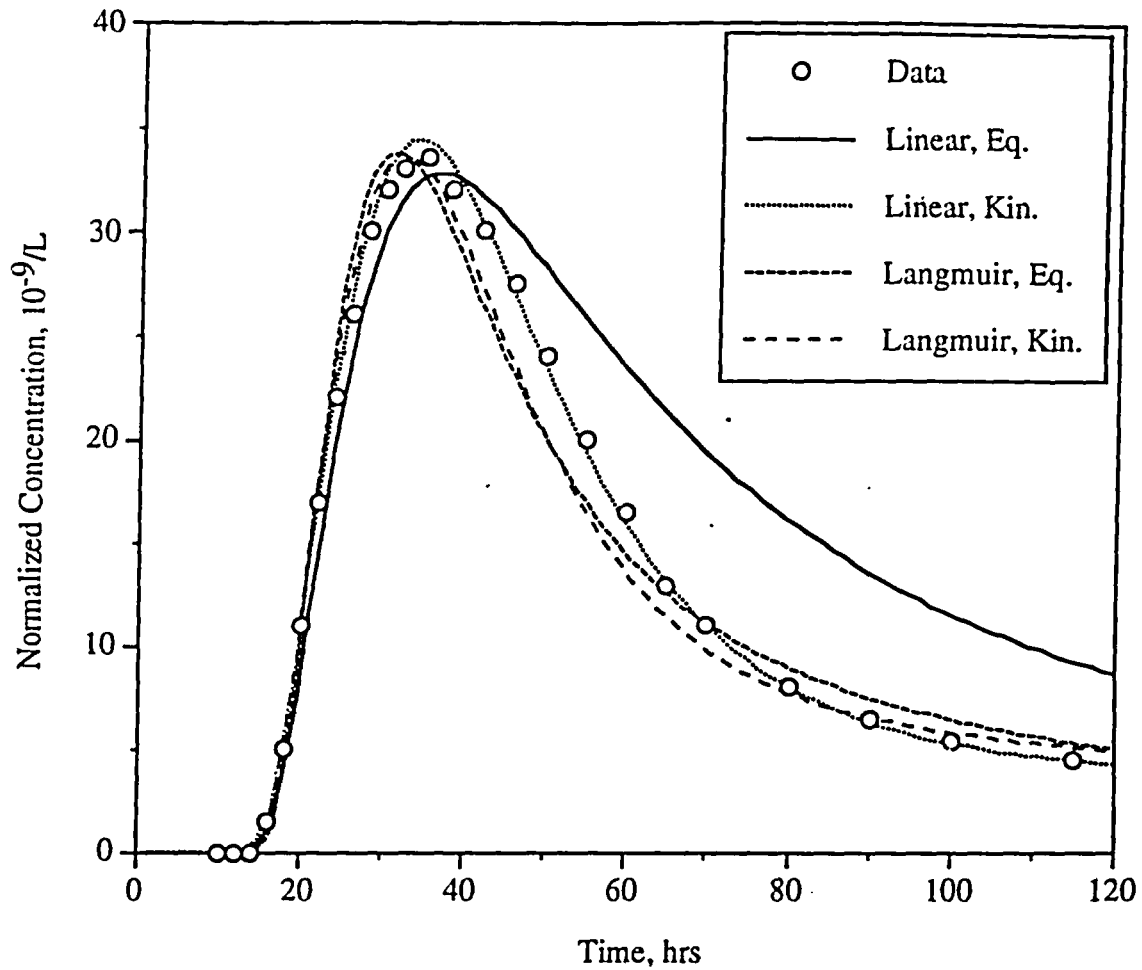


Figure 12. Fits to the first lithium peak in the October tracer test using different isotherms and assuming only a single pathway with the same hydrologic parameters that provided good fits to the PFBA and bromide data. The "Linear" curves were generated using the semi-analytical model, RELAP, while the "Langmuir" curves were generated using the numerical model, RETRAN. "Eq." refers to equilibrium sorption and "Kin." refers to rate-limited (kinetic) sorption. Model parameters corresponding to the fits are given in Table 5. The data points are a subset of the actual data (used for curve-fitting).

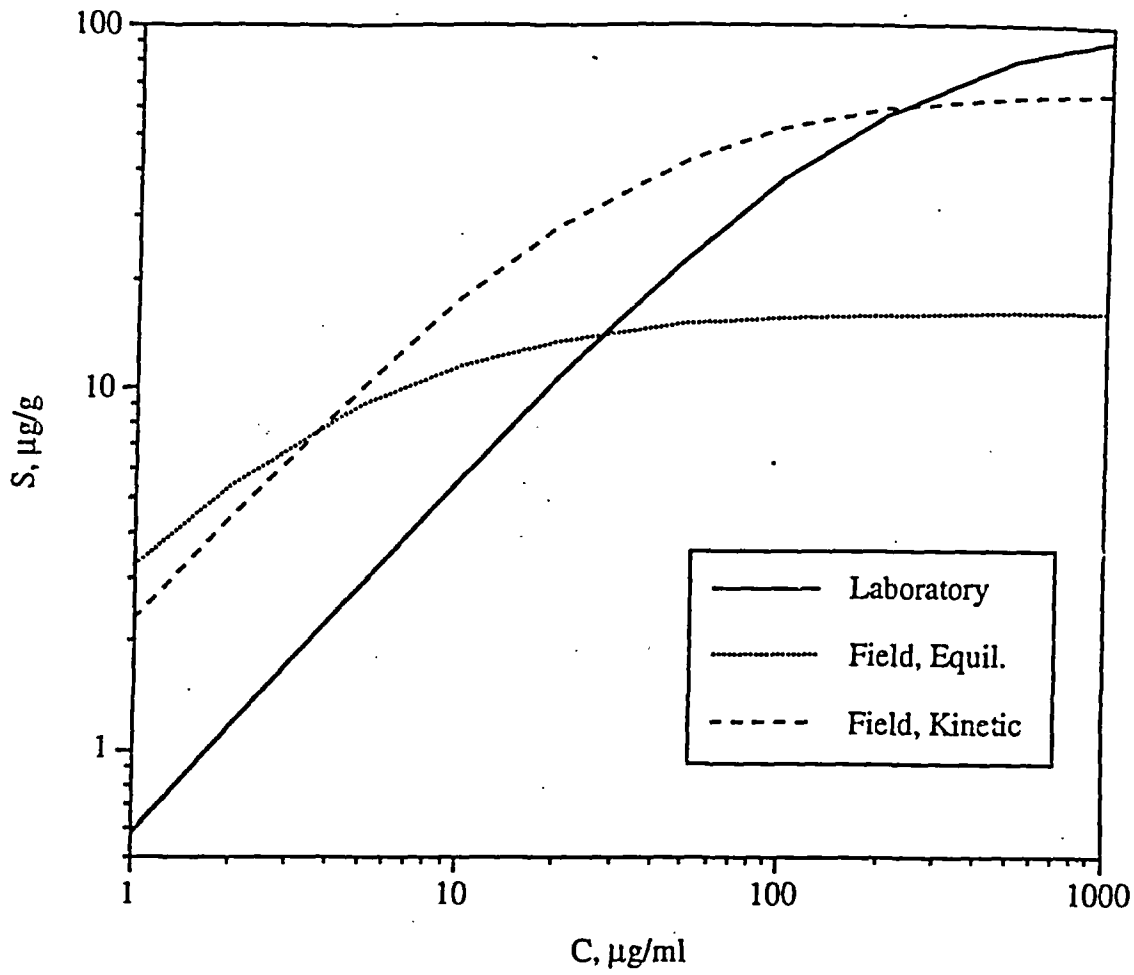


Figure 13. Langmuir isotherms derived for lithium ion from laboratory testing and from interpretations of the first lithium peak in the October tracer test. Table 5 gives Langmuir isotherm parameters used to generate the curves.

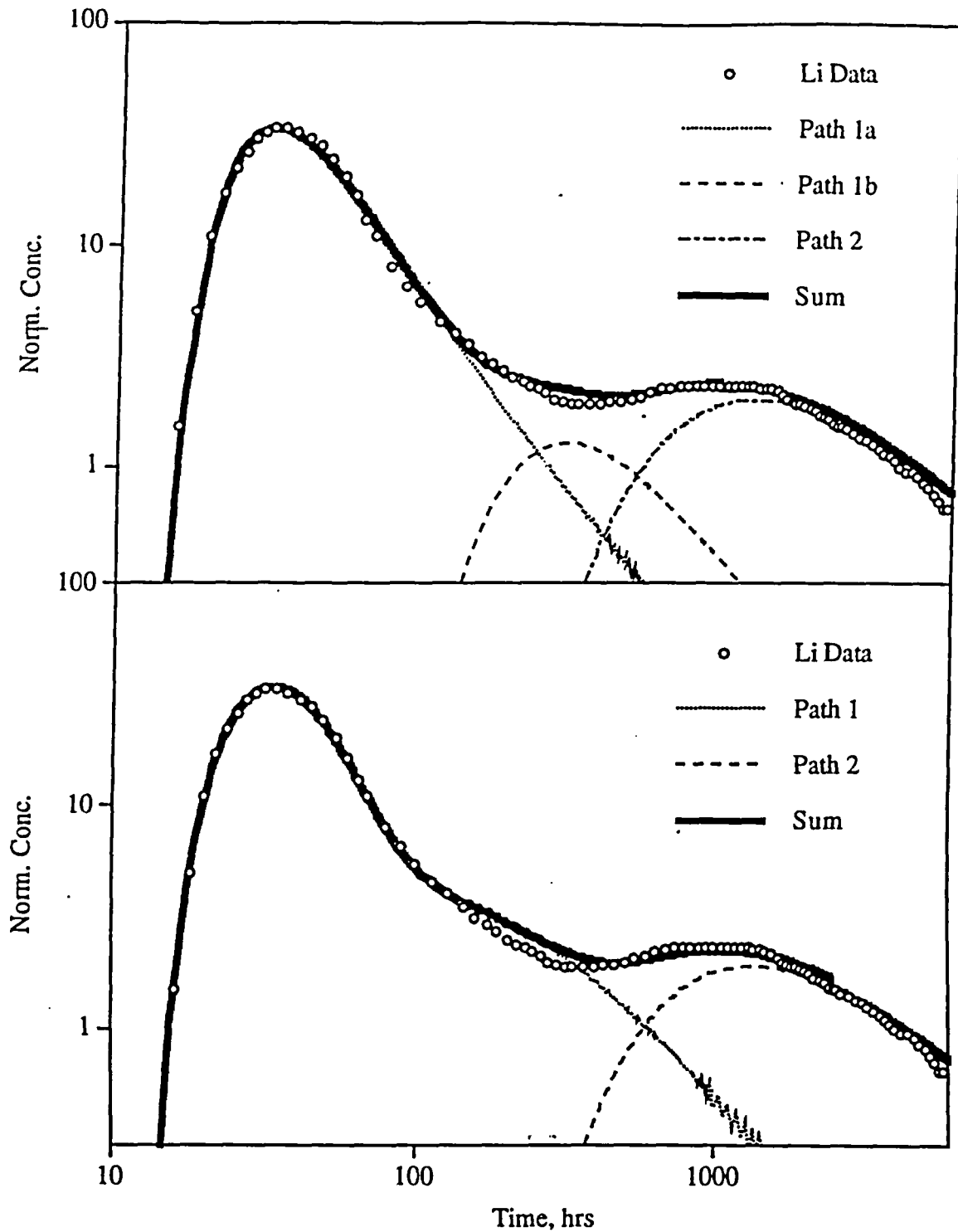


Figure 14. Fits to the October lithium data obtained by splitting the first pathway into two pathways with linear, equilibrium sorption (top), and by assuming linear, rate-limited sorption in just two pathways (bottom). Model parameters corresponding to the top and bottom fits are given in Table 6. The data points are a subset of the actual data (used for curve-fitting).

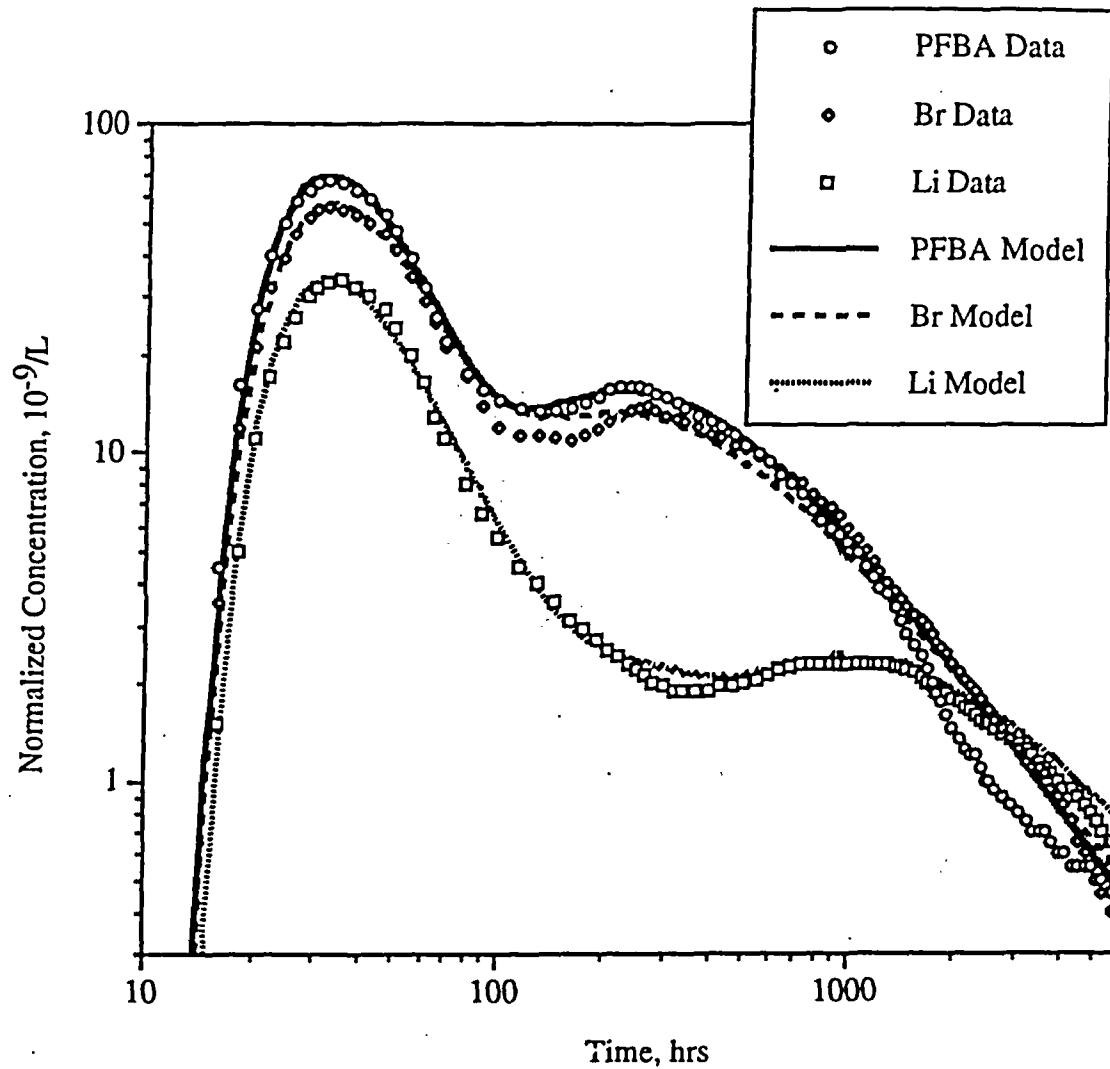


Figure 15. Composite fits to October solute data assuming two sets of pathways, with the first pathway being split to account for lithium response. Parameter estimates corresponding to the fits are given in Tables 3 (PFBA and bromide) and 6 (lithium). The data points are a subset of the actual data (used for curve-fitting).

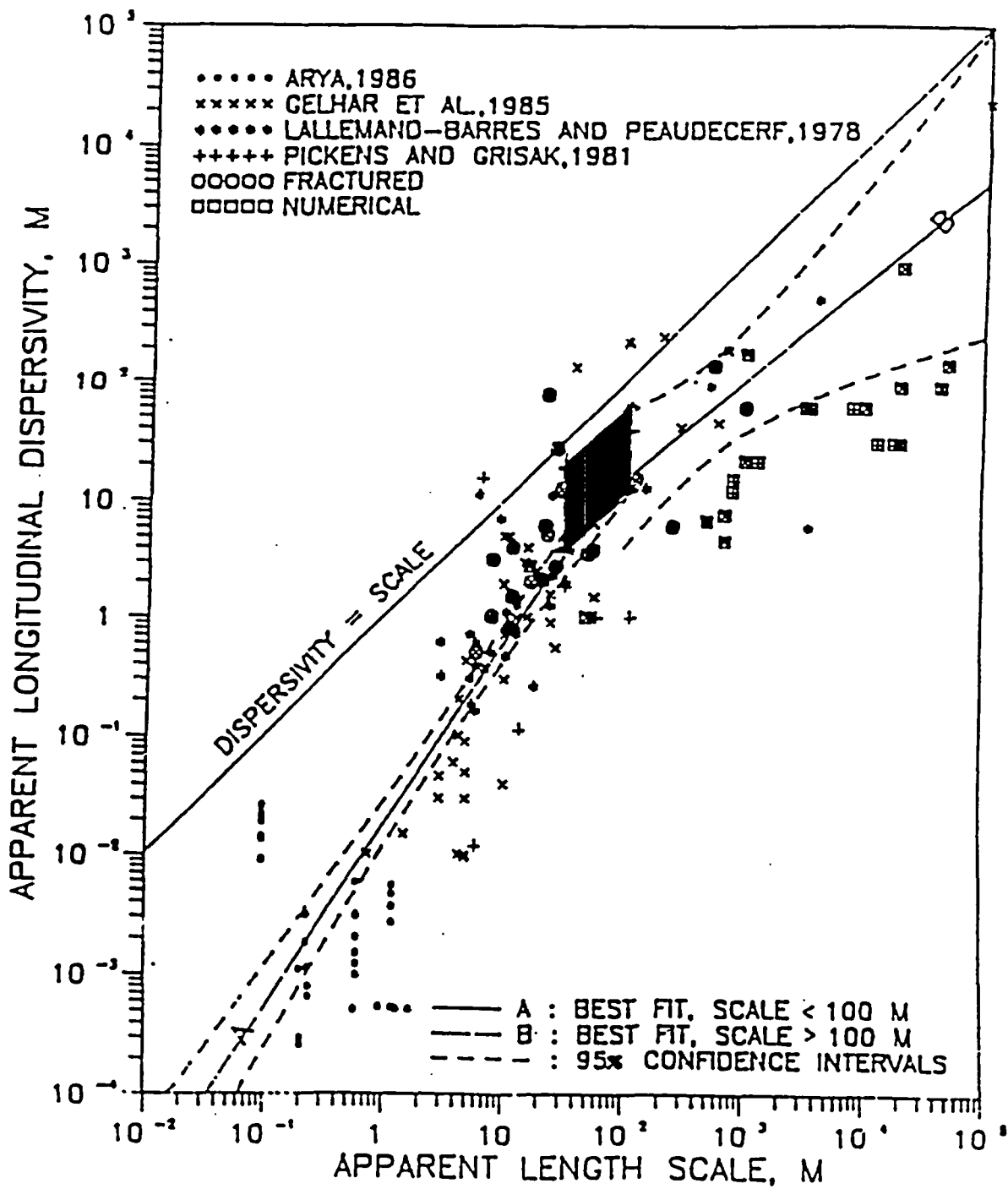


Figure 16. Plot of dispersivity vs. length scale showing range of C-wells values derived from interpretations of the October tracer test (darkened box). Plot taken from Neuman (1990).

Appendix A:

Laboratory Measurements of Lithium Sorption to Bullfrog Tuff

Batch studies

Materials and Methods

Approximately 10 kg of core pieces collected during the drilling of well UE-25c #2 at the Yucca Mountain C-Wells complex was obtained for these laboratory studies. The core was from a depth of approximately 730 m, and consisted of moderately to densely welded tuff from the Bullfrog Member of the Crater Flat Tuff. The core pieces were hand-washed in deionized water, air-dried, crushed to gravel size, and finally pulverized to pass a 500 μm sieve. X-ray diffraction analysis of the crushed tuff indicated a composition of $62\pm 7\%$ feldspar, $32\pm 2\%$ quartz, $5\pm 2\%$ smectite, $1\pm 1\%$ mica, and $1\pm 1\%$ hematite. Subsamples of this batch of crushed tuff were used for all the laboratory studies described in this paper.

In an ion-exchange-dominated system, the ionic composition of the water in which experiments are conducted can have a major impact on observed sorption. At the time of these studies, groundwater from the C-Wells complex was not consistently available, and groundwater from well J-13, located 4 km southeast of the C-Wells complex, was used as a surrogate for some tests. J-13 water is well-characterized and has become the *de facto* standard groundwater for use in Yucca Mountain sorption studies (Harrar et al., 1990; Triay et al., 1993; Triay et al., 1996). A comparison of J-13 and C-Wells groundwater chemistry shows that the two waters are both sodium bicarbonate dominated and in all regards quite similar (Table A-1). Lithium solutions for sorption tests were prepared by dissolving reagent grade lithium bromide in either C-3 or J-13 water. All solutions were filter-sterilized before use.

Drilling disturbances, core storage, and crushing may all have changed the adsorbed ion composition of the tuff. Before sorption studies were initiated, the crushed tuff was re-equilibrated with groundwater by five successive washes with C-3 or J-13 water. For each wash, the tuff and groundwater were mixed for at least 12 h. The crushed tuff and all experimental labware were sterilized by autoclaving before use.

Batch sorption isotherms were determined under three different experimental conditions: 1:1 solution:solid ratio in J-13 water at 25°C (the temperature of the column experiments described below), 1:1 solution:solid ratio in J-13 water at 38°C (the approximate downhole temperature in the Bullfrog Tuff at the C-Wells), and 4:1 solution:solid ratio in C-3 water at 38°C. The 1:1 experiments were conducted at 8 concentrations ranging from 0.5 $\mu\text{g}/\text{mL}$ to 500 $\mu\text{g}/\text{mL}$; sorption at each

concentration was conducted in triplicate. The 4:1 experiment was less extensive, and consisted of duplicate measurements at four concentrations ranging from 1 $\mu\text{g}/\text{mL}$ to 500 $\mu\text{g}/\text{mL}$. Sorption measurements were conducted in 50 mL polyallomer Oak Ridge centrifuge tubes, with either 5 g (4:1 experiment) or 20 g (1:1 experiments) of crushed tuff and 20 mL of lithium solution.

Ion-exchange theory suggests that the actual ion exchange process is rapid and will reach equilibrium quickly; in natural systems apparent equilibration rates are limited by diffusion of ions through the solution to the mineral surface (Bolt et al., 1978). In a well-mixed system such as a shaken centrifuge tube, diffusion is not limiting, and equilibration should be achieved quickly. A previous study of lithium sorption to the Prow Pass Member of the Crater Flat Tuff found that sorption equilibrium was reached within 1 h, confirming this hypothesis (Newman et al., 1991). For consistency with other sorption studies and for scheduling convenience, a minimum equilibration period of 24 h was adopted for these studies. At the conclusion of the equilibration period, during which the centrifuge tubes were shaken at the specified temperature, the samples were centrifuged, the supernatant decanted, and a subsample was filtered through a 0.45 μm membrane. The equilibrium lithium concentration of this subsample was determined by ion chromatography; the equilibrium sorbed concentration was then calculated by mass balance.

Results and Discussion

Results of the three sorption studies (Fig. A-1) showed no significant effects of groundwater source (C-3 or J-13), temperature, or solution:solid ratio; all the data have been combined into a single data set for analysis. Fig. A-1 shows best fits to the data of three common isotherm models, defined as follows:

Linear Isotherm:

$$S = K_D C \quad (1)$$

where S = equilibrium sorbed concentration ($\mu\text{g}/\text{g}$); C = equilibrium solution concentration ($\mu\text{g}/\text{mL}$); and K_D = linear distribution coefficient (mL/g).

Freundlich Isotherm:

$$S = K_F C^n \quad (2)$$

where K_F = Freundlich coefficient ($\text{mL}/\mu\text{g})^n(\mu\text{g}/\text{g})$ and n = Freundlich exponent (dimensionless).

Langmuir Isotherm:

$$S = \frac{K_L S_{\max} C}{(1 + K_L C)} \quad (3)$$

where K_L = Langmuir coefficient (mL/ μ g) and S_{max} = Maximum solid sorption capacity (μ g/g).

Corresponding isotherm coefficients are listed in Table A-2. Figure A-1 suggests that the Langmuir isotherm yields the best fit to the observed data; only the Langmuir isotherm captures the clear curvature of the data when graphed on log-log axes. Furthermore, only the Langmuir isotherm recognizes the finite sorptive capacity of the solid matrix; the other models imply potential infinite sorption. For these reasons, we conclude that the batch sorption data is best represented by a Langmuir isotherm with $K_L = 5.3 \times 10^{-3}$ mL/ μ g and $S_{max} = 110$ μ g/g. A previous study of lithium sorption to the overlying Prow Pass Member of the Crater Flat Tuff also revealed Langmuir behavior (Newman et al., 1991).

Column Studies

Materials and Methods

A series of transport experiments was conducted in Plexiglas columns 91.44 cm in length and 0.62 cm in diameter. The columns were packed with the crushed tuff described above using a wet slurry technique that minimizes layering, but also eliminates particles less than roughly 70 μ m in size. With the crushed Bullfrog Tuff, approximately 40-50% of the sample was not retained in the column. Column porosity was measured at 57% and dry bulk density was calculated at 1.14 g/mL by assuming a mineral density of 2.65 g/mL, typical values for columns prepared in this fashion (e.g. Treher and Raybold, 1982; Thompson, 1989). Three columns were prepared identically. The column apparatus included a constant-rate pump, a valve to switch between a reservoir containing J-13 "background" water and a solution of lithium bromide in J-13 water, and an automatic fraction collector at the downstream end of the column. Each experiment began by pumping approximately 180 mL (roughly 12 pore volumes) of J-13 water through the column at a specified flow rate to equilibrate the tuff with groundwater chemistry. The input was then switched to the lithium bromide solution. Effluent samples were analyzed for lithium and bromide concentration by ion chromatography. In these tests, bromide was assumed to behave as an ideal nonsorbing tracer, in contrast to lithium, a reactive tracer.

Experiments were conducted with two tracer concentrations (approximately 5 mg/L and 20 mg/L) and two flow rates (1.6 and 2.2 mL/h); a 20 mg/L test was also performed at 9.73 mL/h. The different concentrations were intended to quantify effects of sorption nonlinearity, while the different flow rates should reveal kinetically controlled effects such as sorption nonequilibrium or diffusion-limited sorption. All tests were conducted at 25°C.

Results and Discussion

Results of the columns tests are presented in Table A-3; breakthrough curves (BTCs) for one of the experiments are shown in Fig. A-2. The first step in the

analysis was the determination of the individual column's transport behavior by fitting a one-dimensional advection-dispersion equation to the bromide BTC, using RELAP, a one-dimensional semi-analytic code based on a Laplace transform inversion method (Appendix B). All five bromide BTCs were fit very well, suggesting near ideal behavior. RELAP can work with a system of dimensionless variables, in which hydrodynamic dispersion is represented by the Peclet number, P_e , defined as L/α , where L is the column length and α the dispersivity. The Peclet numbers shown in Table A-3 correspond to dispersivities of 0.2 - 0.3 cm, similar in scale to the column radius.

We then analyzed the lithium BTC for each experiment by holding the column's mean residence time and Peclet number fixed at the values determined for bromide, and varying the sorption behavior. RELAP's semi-analytic nature limits its sorption capabilities to a linear isotherm, so its numerical sister-code, RETRAN (Appendix B) was used to simulate Langmuir sorption behavior. Using the Langmuir sorption parameters resulting from the batch studies (Table A-2) and assuming local sorption equilibrium, we obtained curve iv in Fig. A-2. Notice that this simulation matches the observed time of breakthrough very closely, but significantly overestimates the slope of the BTC. The observed lower slope (increased apparent dispersion) is symptomatic of kinetic effects (Valocchi, 1985); to explore this possibility, we relaxed the local equilibrium assumption and used RETRAN to better fit the observed BTC. RETRAN includes kinetic effects in terms of the dimensionless Damkohler number, D_a , defined as $k\tau$, where k is a first order reaction rate constant and τ is the mean residence time in the column. The observed lithium BTC was well fit by setting D_a to 18 (curve v in Fig. A-2), corresponding to a forward rate constant of 2.2 h^{-1} . This rapid reaction rate is consistent with both ion-exchange theory and measurements of lithium sorption to Prow Pass Tuff, mentioned earlier.

Note that the rate constants shown in Table A-3 reflect an effective rate constant for the entire sorption process, including both diffusion from the bulk liquid to the exchange site and the actual exchange process. While the latter should be a function only of the solution and medium, the former may depend on flow geometry, in turn a function of column packing. This sensitivity to column packing may explain why Table A-3 shows that repeated tests in the same column give similar rate constants, but column A-2 shows consistently lower rate constants than the other two columns.

Isotherm nonlinearity can affect BTCs in two related but different fashions. The first effect of nonlinear sorption on a BTC reflects the fact that in the solute front itself, a distribution of concentrations occurs, ranging from background (in our case, close to 0 mg/L) to the peak influent concentration (here, 5 or 20 mg/L). Changes in retardation as a function of concentration will alter the shape of the breakthrough curve; specifically, decreased sorption and higher transport velocity at high concentration will sharpen the leading edge of the solute front. (Conversely, if the solute is applied as a pulse, with both a leading and trailing edge, this effect will retard the low concentrations at the end of the trailing edge, resulting in

increased tailing.) We look for this effect by comparing the shape of the observed BTC to simulations assuming linear and nonlinear sorption.

This sharpening effect will be most pronounced in a high-concentration test, in which the leading edge of the front contains the widest range of concentrations. To determine whether sorption nonlinearity has affected the shape of the BTC, RELAP was used to attempt a linear sorption fit to the lithium BTC in Fig. A-2. Both equilibrium and nonequilibrium fits are shown in the figure; the linear sorption simulations yield results virtually indistinguishable from the Langmuir results. This implies that for the concentrations and conditions of the column studies, the nonlinearity of the sorption isotherm had no observable effect on the shape of the BTC. This is most likely due to the very low dispersivity of these laboratory columns; the low degree of dispersion keeps the solute front very sharp, and the concentration at any point in the column jumps from background to peak very rapidly. Thus, there is only a very small volume of intermediate concentration liquid in the column. In a higher-dispersion system where a larger portion of the column would contain solutions of varying concentration, nonlinear sorption would be more apparent. Because under the conditions of our tests, nonlinear sorption played no significant role in BTC shape; the rest of the column studies were analyzed assuming linear sorption, leading to the results presented in Table A-3.

The second effect on nonlinearity arises because behind the solute front, solute concentrations are relatively constant and nonlinearity makes the ratio between dissolved and sorbed concentrations a function of dissolved concentration. This ratio controls the velocity of the solute front through the column, through its influence on the retardation factor (R_f), the ratio of average groundwater velocity to the velocity of the tracer front. This effect changes the position of the BTC as a function of concentration; decreased sorption at higher concentration will move the BTC earlier in time. We look for this effect by comparing measured R_f s for different solution concentrations.

Table A-3 shows that R_f s for the 5 mg/L tests ranged from 2.2 to 2.3, with a mean of 2.25; R_f s for the 20 mg/L tests ranged from 1.7 to 2.0, with a mean of 1.87. The observed decreased retardation at higher concentration qualitatively fits our prediction of the effect of nonlinear sorption. We now compare these results to quantitative predictions of nonlinear effects on R_f . For the Langmuir isotherm, the R_f can be shown to be (Fetter, 1993):

$$R_f = 1 + \frac{\rho_B}{\theta} \left(\frac{K_L S_{max}}{(1 + K_L C)^2} \right) \quad (4)$$

where ρ_B is the dry bulk density of the medium (g/mL) and θ is the volumetric moisture content, or porosity for a saturated medium.

By solving Eq. 4 with our batch Langmuir parameters column ρ_B and θ values, we obtain retardation factor predictions of 2.11 for the 5 mg/L tests and 1.95 for the 20 mg/L tests. Overall these predictions match the observations very well, differing by 7% or less for both concentration levels. However, the observed difference in R_f at the two concentration levels somewhat exceeds that predicted by the model. This may reflect simple experimental variability due to the small number of tests

conducted, or may indicate further physical complexities. Additional column studies covering a wider range of concentrations would help settle this question.

We conclude that under our experimental conditions, sorption nonlinearity affects the retardation of lithium, but not the shape of the BTC. This result implies that we can model transport under these conditions using the simple K_D linear sorption model by adjusting the K_D value as a function of solution concentration. Comparison of Eqs. 1 and 3 shows that at very low concentrations ($C \rightarrow 0$), the Langmuir model approaches the linear model with a K_D value of $S_{\max} \cdot K_L$, approximately 0.6 mL/g in our case.

Summary and Conclusions

We conducted a series of laboratory batch and column sorption experiments to characterize the reactive transport of lithium through crushed Bullfrog Tuff, the host formation to a field tracer experiment. The batch data indicate that lithium exhibits nonlinear Langmuir sorption. Column studies at different flow rates and concentrations confirmed the nonlinear sorption behavior, and observed retardation factors differed from batch predictions by 7% or less. The column studies also produced clear evidence of sorption nonequilibrium, although the kinetics are relatively fast, with reciprocal forward rate constants on the order of 30 min or less.

Appendix A References

- Bolt, G. H., M. G. M. Bruggenwert and A. Kamphorst (1978). Adsorption of Cations by Soil. Soil Chemistry, A: Basic Elements. G. H. Bolt and M. G. M. Bruggenwert. Amsterdam, Elsevier: 54-90.
- Fetter, C. W. (1993). Contaminant Hydrogeology. New York, Macmillan Publishing Company.
- Fuentes, H. R., W. L. Polzer, E. H. Essington and B. D. Newman (1989). Characterization of Reactive Tracers for C-Wells Field Experiment I: Electrostatic Sorption Mechanism, Lithium, Los Alamos National Laboratory.
- Harrar, J. E., J. F. Carley, W. F. Isherwood and E. Raber (1990). Report of the Committee to Review the Use of J-13 Well Water in Nevada Nuclear Waste Storage Investigations, Lawrence Livermore National Laboratory.
- Newman, B. D., H. R. Fuentes and W. L. Polzer (1991). "An Evaluation of Lithium Sorption Isotherms and Their Application to Ground-Water Transport." Ground Water 29(6): 818-824.
- Thompson, J. L. (1989). "Actinide Behavior on Crushed Rock Columns." I. Radioanal. Nucl. Chem. 130(2): 353-364.
- Treher, E. N. and N. A. Raybold (1982). The Elution of Radionuclides Through Columns of Crushed Rock from the Nevada Test Site, Los Alamos National Laboratory.
- Triay, I. R., A. Meijer, J. L. Conca, K. S. Kung, R. S. Rundberg and E. A. Strietelmeier (1996). Summary and Synthesis Report on Radionuclide Retardation for the Yucca Mountain Site Characterization Project, Los Alamos National Laboratory.
- Triay, I. R., B. A. Robinson, R. M. Lopez, A. J. Mitchell and C. M. Overly (1993). Neptunium Retardation with Tuffs and Groundwaters from Yucca Mountain. Fourth Annual International Conference on High Level Radioactive Waste Management, Las Vegas, NV, American Nuclear Society / American Society of Civil Engineers.
- Valocchi, A. J. (1985). "Validity of the Local Equilibrium Assumption for Modeling Sorbing Solute Transport Through Homogeneous Soils." Water Resour. Res. 21(6): 808-820.

Appendix A Tables

Table A-1. Comparison of J-13 and C-Wells groundwater chemistry. All analyses (except pH) in $\mu\text{g}/\text{mL}$ (Fuentes et al., 1989).

	J-13	C-Wells
Al	<0.03	
B	0.13	
Ba	<0.001	
Ca	11.3	11
Cl	7	7
Fe	0.02	
K	5	2
Li	0.040	0.11
Mg	<0.010	0.38
Mn	0.01	
Na	44	55
Si	30	25
Sr	0.040	0.044
PO ₄	<2.5	
SO ₄	19	22
HCO ₃	124	142
pH	7.2	7.8

Table A-2. Isotherm Parameters Derived from Batch Sorption Studies (0.5 - 500 $\mu\text{g}/\text{mL}$ concentration range)

Linear

K_D 0.21 mL/g

Freundlich

K_F 0.76 (mL/ μg)^{0.82} $\mu\text{g}/\text{g}$

n 0.82

Langmuir

K_L 5.3×10^{-3} mL/ μg

S_{max} 110 $\mu\text{g}/\text{g}$

Table A-3. Results of Column Studies. Refer to text for notation.

Column	Flow Rate (mL/h)	Li Conc. (mg/L)	τ (h)	P_e	R_F	k_p (h ⁻¹)	D_a
1	1.6	5	11	400	2.2	14	160
1	2.2	5	8.0	400	2.3	18	140
2	1.6	20	11	300	1.9	3.6	40
2	2.2	20	8.2	300	2.0	2.2	18
3	9.7	20	1.9	400	1.7	14	27

7/31/97

A-9

Appendix A Figures

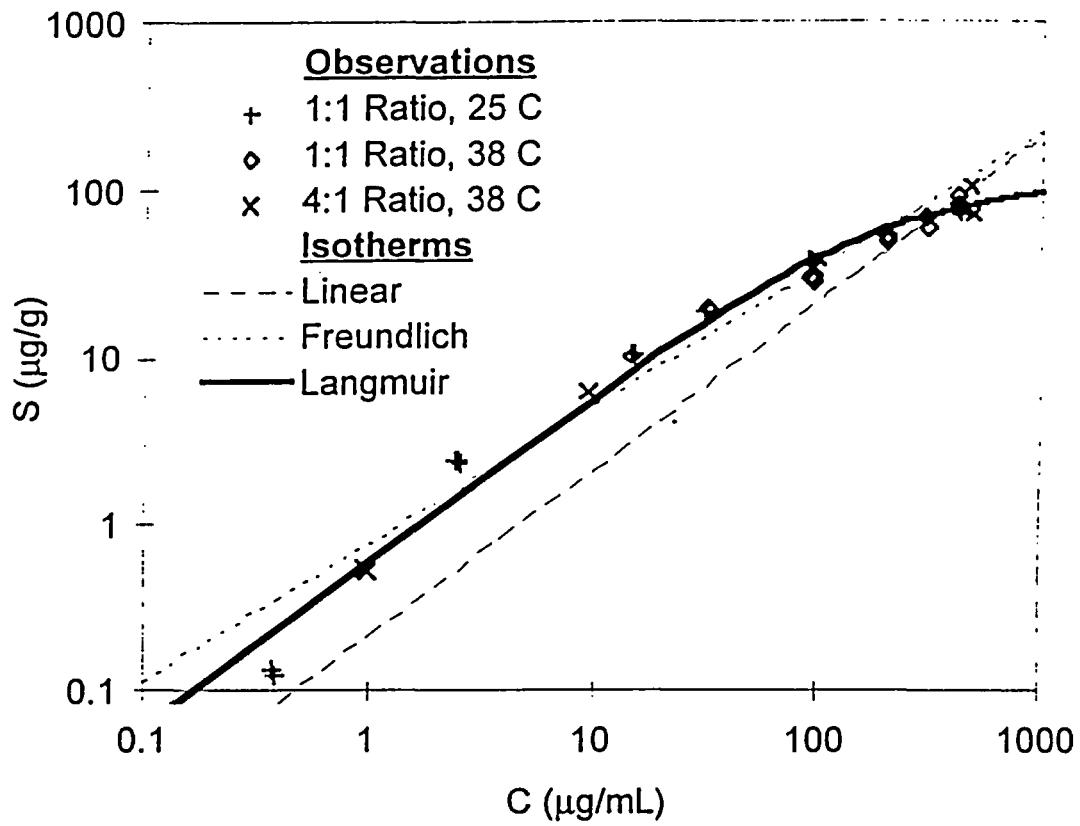


Figure A-1. Batch Sorption Results.

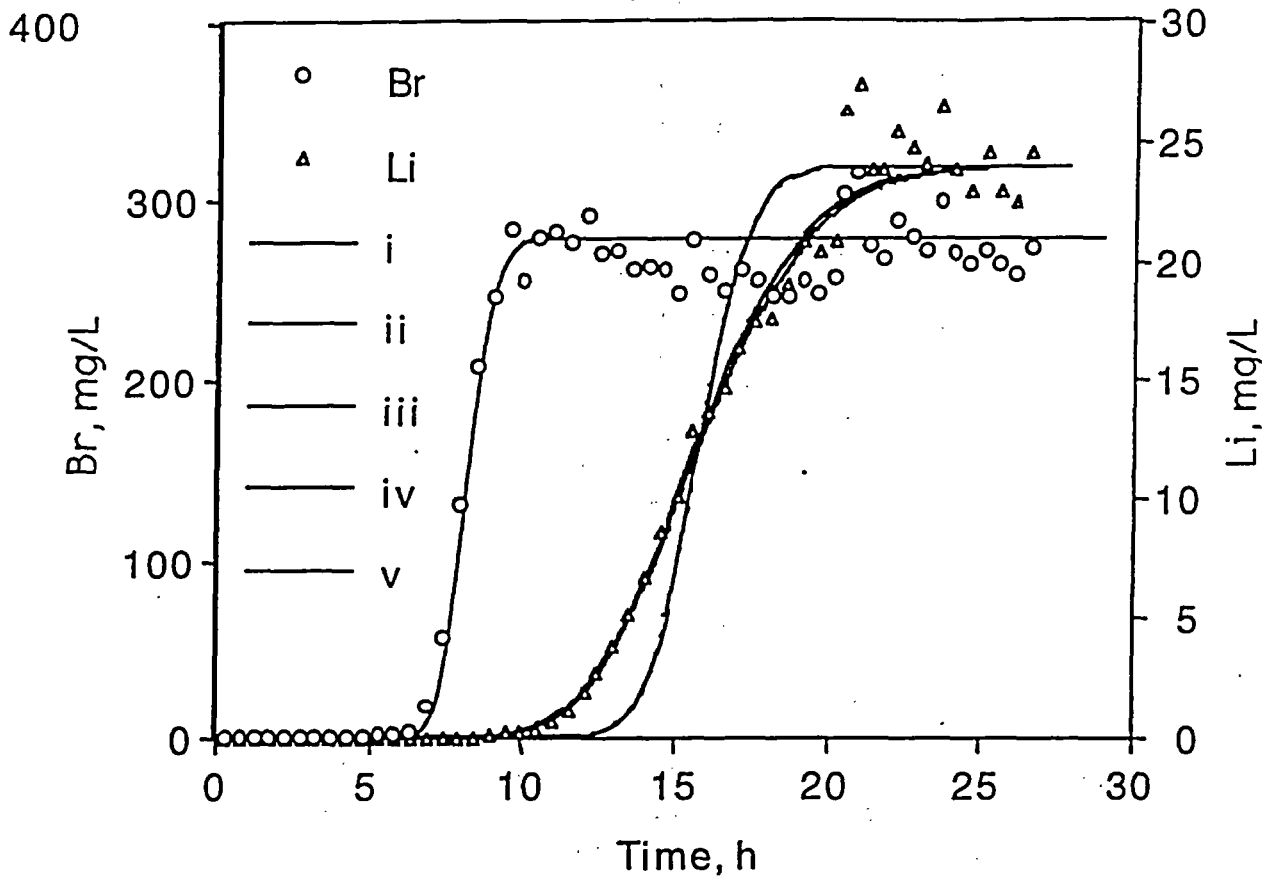


Figure A-2. Bromide and lithium breakthrough curves in Column 2 at a flow rate of 2.2 mL/h, and corresponding fits to data. (i) Fit to bromide data with a Peclet number of 300, (ii) fit to lithium data assuming linear isotherm ($R_F = 2.0$) with equilibrium sorption, (iii) fit to lithium data assuming linear isotherm with a forward rate constant of 2.2 h^{-1} , (iv) fit to lithium data assuming a Langmuir isotherm with equilibrium sorption, and (v) fit to lithium data assuming a Langmuir isotherm with a forward rate constant of 2.2 h^{-1} . Langmuir isotherm parameters: $K_L = 0.0053 \text{ mL}/\mu\text{g}$ and $S_{\text{max}} = 110 \mu\text{g/g}$.

$\frac{300 \text{ mL}}{80}$

$3.75 \times 10^{-3} \text{ mL/g}$

Appendix B:

Description of Mathematical Models in Computer Codes RELAP and RETRAN

To model sorbing tracer transport in a dual-porosity system, we start with a conceptual model for conservative tracer transport in fractured systems originally introduced by Maloszewski and Zuber (1983, 1985), and we extend it to include rate-limited, nonlinear sorbing tracer transport. Figure B-1 shows the assumed model domain, which consists of parallel-plate fractures of aperture $2b$ separated by matrix blocks of thickness L , each of which extend infinitely into the page. Tang et al. (1981) assumed an infinite spacing between fractures, but this is just a special case of a finite matrix with a very large fracture spacing. Others have used similar model conceptualizations but with cylindrical or spherical-shaped matrix blocks (Rasmuson and Neretnieks, 1986). All of these formulations yield similar results when tracer penetration into the matrix is much less than matrix block dimensions; that is, when time scales are short compared to time scales necessary for diffusion to the centerline of the blocks. In Fig. B-1, the fracture apertures, fracture flow velocity, matrix bulk density, matrix porosity, and fracture and matrix sorption parameters are assumed to be the same everywhere in the system (no spatial heterogeneity). This is clearly a simplification, but spatial variation is very difficult to characterize in a field setting, and it also introduces considerable complexity and ambiguity to model interpretations (i.e., more adjustable parameters to fit an observed response). Therefore, we considered it appropriate, as a first approximation, to assume homogeneous properties and use bulk average parameter values.

Referring to Fig. B-1, it is assumed that advective transport occurs only in the x-direction in the fractures and that diffusion into the matrix is important only in the y-direction. It is also assumed that there are no concentration gradients in the y-direction in the fractures. These assumptions allow the equations describing transport in the fractures and the matrix to be decoupled and solved as separate 1-dimensional problems that are linked only through a boundary condition and a single term in the fracture transport equation.

Linear Flow in Fractures

For a constant flow velocity in fractures (i.e., linear flow), the differential equations and boundary conditions describing rate-limited, nonlinear sorbing tracer transport in the fractures and matrix (the most general case) are:

Fractures, Solution Phase:

$$\frac{\partial C_f}{\partial t} + v_f \frac{\partial C_f}{\partial x} - D_f \frac{\partial^2 C_f}{\partial x^2} + \left(\frac{\rho_f}{\eta} \right) \frac{\partial S_f}{\partial t} - \frac{\phi D_m}{b\eta} \frac{\partial C_m}{\partial y} \Big|_{y=b} = 0 \quad (B1)$$

Fractures, Immobile Phase:

$$\left(\frac{\rho_f}{\eta}\right) \frac{\partial S_f}{\partial t} - k_{ff} \left(\frac{C_f^{\beta_f}}{1 + \alpha_f C_f}\right) + k_{fr} S_f = 0 \quad (B2)$$

Matrix, Solution Phase:

$$\frac{\partial C_m}{\partial t} - D_m \frac{\partial^2 C_m}{\partial y^2} + \left(\frac{\rho_B}{\phi}\right) \frac{\partial S_m}{\partial t} = 0 \quad (B3)$$

Matrix, Immobile Phase:

$$\left(\frac{\rho_B}{\phi}\right) \frac{\partial S_m}{\partial t} - k_{mf} \left(\frac{C_m^{\beta_m}}{1 + \alpha_m C_m}\right) + k_{mr} S_m = 0 \quad (B4)$$

subject to initial and boundary conditions

$$C_f(x, 0) = 0 \quad (B1a)$$

$$C_f(0, t) = \delta(t) \quad (B1b)$$

$$C_f(\infty, t) = 0 \quad (B1c)$$

$$S_f(x, 0) = 0 \quad (B2a)$$

$$C_m(y, x, 0) = 0 \quad (B3a)$$

$$C_m(b, x, t) = C_f(x, t) \quad (B3b)$$

$$\frac{\partial C_m}{\partial y} \left(\frac{L}{2}, x, t\right) = 0 \quad (B3c)$$

$$S_m(y, x, 0) = 0 \quad (B4a)$$

where, C_f = tracer concentration in solution in fractures, M/L^3
 C_m = tracer concentration in solution in matrix, M/L^3
 S_f = tracer surface concentration on fracture surfaces, M/M solid
 S_m = tracer surface concentration on matrix surfaces, M/M solid
 v_f = fluid velocity in fractures, L/T
 D_f = dispersion coefficient in fractures, L^2/T
 D_m = molecular diffusion coefficient in matrix, L^2/T
 ρ_f = bulk density of material in fractures, M/L^3
 ρ_B = bulk density of matrix, M/L^3
 η = porosity within fractures,
 ϕ = matrix porosity,
 b = fracture half aperture, L
 L = distance between parallel fractures in medium, L
 k_{ff} = rate constant for sorption to surfaces in fractures, $1/T$ (if linear)
 k_{fr} = rate constant for desorption from surfaces in fractures, M/L^3T
 k_{mf} = rate constant for sorption to surfaces in matrix, $1/T$ (if linear)
 k_{mr} = rate constant for desorption from surfaces in matrix, M/L^3T
 α_i, β_i = sorption isotherm parameters defined in equation (B5) ($i = f$, fractures; $i = m$, matrix), and
 $\delta(t)$ = dirac delta function.

Coupling between the fractures and matrix is achieved through boundary condition (B3b) and through the last term on the left-hand side of equation (B1). We make use of the expression $\left(\frac{\rho_f}{\eta}\right)$ to account for surface area available for sorption in fractures. In reality, fractures could be completely open (i.e., $\eta = 1$, $\rho_f = 0$), and sorption might occur only on the walls. In this case, the expression $\left(\frac{\rho_f}{\eta}\right)$ can be considered a proportionality constant that should be adjusted to an appropriate value to describe sorption to the walls. Alternatively, sorption in fractures can be completely ignored by setting this term equal to zero. We use the dirac-delta function as the inlet boundary condition (equation (B1b)) because the solutions obtained using this boundary condition are residence time distributions that can be mathematically convoluted with any generalized input function to obtain a generalized breakthrough curve.

In the above equations, we have used a general expression for the sorption isotherms in both the fractures and the matrix:

$$S = \frac{KC^\beta}{1+\alpha C} \quad (B5)$$

This expression allows a linear, a Freundlich, or a Langmuir isotherm to be defined. A Freundlich isotherm is obtained by setting $\alpha = 0$, a Langmuir isotherm is obtained by setting $\beta = 1$, and a linear isotherm is obtained by setting $\alpha = 0$ and $\beta = 1$. Equations (B2) and (B4) also assume nonlinearity of the adsorption reaction (i.e., not first-order in concentration) while the desorption reaction is assumed to be linear (first-order in surface concentration). Note that $K = k_f/k_m$, where k_f and k_m are the rate constants for sorption and desorption, respectively.

If equilibrium sorption is assumed, the sorption isotherm expression can be substituted directly for S_f and S_m in equations (B1) and (B3), respectively. This eliminates the need for the immobile phase equations (B2) and (B4). Recognizing that $\frac{\partial S}{\partial t} = \frac{\partial S}{\partial C} \cdot \frac{\partial C}{\partial t}$, the fracture and matrix transport equations become

Fractures:

$$\frac{\partial C_f}{\partial t} + v_f \frac{\partial C_f}{\partial x} - D_f \frac{\partial^2 C_f}{\partial x^2} + \left(\frac{\rho_f}{\eta}\right) \left[\frac{K_f \beta_f C_f^{\beta_f - 1}}{1 + \alpha_f C_f} - \frac{\alpha_f K_f C_f^{\beta_f}}{(1 + \alpha_f C_f)^2} \right] \frac{\partial C_f}{\partial t} - \frac{\phi D_m}{b\eta} \frac{\partial C_m}{\partial y} \Big|_{y=b} = 0 \quad (B6)$$

Matrix:

$$\frac{\partial C_m}{\partial t} - D_m \frac{\partial^2 C_m}{\partial y^2} + \left(\frac{\rho_B}{\phi}\right) \left[\frac{K_m \beta_m C_m^{\beta_m - 1}}{1 + \alpha_m C_m} - \frac{\alpha_m K_m C_m^{\beta_m}}{(1 + \alpha_m C_m)^2} \right] \frac{\partial C_m}{\partial t} = 0 \quad (B7)$$

where the terms in brackets, [], are $\frac{\partial S}{\partial C}$ for the fractures and matrix, respectively, and

$$K_m = \frac{k_{mf}}{k_{mr}} \text{ and } K_f = \frac{k_{ff}}{k_{fr}}$$

When the sorption isotherm is nonlinear (either rate-limited or equilibrium), the appropriate equations given above are solved numerically using an implicit alternating-direction finite-difference method. By assuming 1-D transport in both the fractures and the matrix and using an explicit time discretization for the adsorption (nonlinear) term, the model equations are reduced to a single tridiagonal linear system for the fractures and a set of independent tridiagonal linear systems for each row of grid points extending into the matrix (perpendicular to the fractures). These tridiagonal systems can be solved very efficiently, and the implicit time discretization provides unconditional stability. The computer code developed to obtain the numerical solution is called RETRAN (REactive TRANsport code).

For linear sorption isotherms (either rate-limited or equilibrium), it is possible to obtain a semi-analytical solution of the transport equations by following the Laplace transform technique of Maloszewski and Zuber (1983). The Laplace transform removes the time derivatives from the governing equations, rendering them ordinary differential equations that can be solved by standard methods. The Laplace transforms of the general rate-limited equations (B1), (B2), (B3), and (B4), assuming linear isotherms, are

Fractures, Solution Phase:

$$s\bar{C}_f + v_f \frac{\partial \bar{C}_f}{\partial x} - D_f \frac{\partial^2 \bar{C}_f}{\partial x^2} + \left(\frac{\rho_f}{\eta} \right) s\bar{S}_f - \frac{\phi D_m}{b\eta} \frac{\partial \bar{C}_m}{\partial y} \Big|_{y=b} = 0 \quad (\text{B8})$$

Fractures, Immobile Phase:

$$\left(\frac{\rho_f}{\eta} \right) s\bar{S}_f - k_{ff}\bar{C}_f + k_{fr}\bar{S}_f = 0 \quad (\text{B9})$$

Matrix, Solution Phase:

$$s\bar{C}_m - D_m \frac{\partial^2 \bar{C}_m}{\partial y^2} + \left(\frac{\rho_B}{\phi} \right) s\bar{S}_m = 0 \quad (\text{B10})$$

Matrix, Immobile Phase:

$$\left(\frac{\rho_B}{\phi} \right) s\bar{S}_m - k_{mf}\bar{C}_m + k_{mr}\bar{S}_m = 0 \quad (\text{B11})$$

where, s = Laplace transform independent variable (replacing time), and \bar{X} = Laplace transform of dependent variable.

Equations (B9) and (B11) are now algebraic equations that can be solved for \bar{S} , and the result(s) can be substituted into equations (B8) and (B10) to obtain (see also, Maloszewski and Zuber, 1991):

Fractures:

$$\left[1 + \frac{\left(\frac{\rho_f}{\eta}\right)k_{ff}}{\left(\frac{\rho_f}{\eta}\right)s + k_{fr}} \right] s\bar{C}_f + v_f \frac{\partial \bar{C}_f}{\partial x} - D_f \frac{\partial^2 \bar{C}_f}{\partial x^2} - \frac{\phi D_m}{b\eta} \frac{\partial \bar{C}_m}{\partial y} \Big|_{y=b} = 0 \quad (\text{B12})$$

Matrix:

$$\left[1 + \frac{\left(\frac{\rho_B}{\phi}\right)k_{mf}}{\left(\frac{\rho_B}{\phi}\right)s + k_{mr}} \right] s\bar{C}_m - D_m \frac{\partial^2 \bar{C}_m}{\partial y^2} = 0 \quad (\text{B13})$$

The equilibrium sorption case is readily apparent from equations (B12) and (B13) if we set k_f and k_r to very large values and recognize that $K_d = \frac{k_f}{k_r}$ and

$R = 1 + \left(\frac{\rho_B}{\phi}\right)K_d$. The equilibrium case was also derived by Tang et al. (1981) for an infinite matrix boundary condition.

Equations (B12) and (B13) are in the same form as the equations solved by Maloszewski and Zuber (1983). The only difference is that the sorption expressions in brackets in equations (B12) and (B13) were equal to 1 in Maloszewski and Zuber's equations because they only considered conservative solute transport. Thus, the solution of equations (B12) and (B13) subject to Laplace-transformed boundary conditions (B1a) through (B4a) is identical to the solution presented by Maloszewski and Zuber except that the $s\bar{C}_f$ and $s\bar{C}_m$ terms now have more complicated coefficients. Referring to Maloszewski and Zuber (1983) for details of the derivation, the final result for transport in the fractures coupled with diffusion into the matrix is a single Laplace-domain equation given by

$$\bar{C}_f(x) = \exp \left\{ \frac{v_f x}{2D_f} \left[1 - \sqrt{1 + \frac{4D_f R_f(s)}{v_f^2} s + \frac{4D_f \phi}{v_f^2 b \eta} \sqrt{R_m(s) D_m s} \text{Tanh} \left(\sqrt{\frac{s R_m(s)}{D_m} \left(\frac{L}{2} - b \right)} \right)} \right] \right\} \quad (\text{B14})$$

where,

$$R_f(s) = 1 + \frac{\left(\frac{\rho_f}{\eta}\right)k_{ff}}{\left(\frac{\rho_f}{\eta}\right)s + k_{fr}} \quad (\text{B15})$$

$$R_m(s) = 1 + \frac{\left(\frac{\rho_B}{\phi}\right)k_{mf}}{\left(\frac{\rho_B}{\phi}\right)s + k_{mr}} \quad (\text{B16})$$

If we introduce the mean fluid residence time in fractures, $\tau = \frac{x}{v_f}$, and the dimensionless Peclet number, $Pe = \frac{xv_f}{D_f}$, which are related to the first and second moments of fluid residence time in the system, respectively, equation (B14) can be rewritten as

$$\bar{C}_f(x) = \exp\left\{\frac{Pe}{2}\left[1 - \sqrt{1 + \frac{4\tau}{Pe}\left\{sR_f(s) + \frac{\phi}{b\eta}\sqrt{R_m(s)D_m}s \operatorname{Tanh}\left(\sqrt{\frac{sR_m(s)}{D_m}}\left(\frac{L}{2} - b\right)\right)\right\}}\right]\right\} \quad (\text{B17})$$

Equation (B17) is arguably a more natural expression to work with than equation (B14) when considering field data because actual distances and fluid velocities in a field experiment will be dependent on flow pathways in the system, but the concepts of the first and second moments of fluid residence time are less ambiguous.

Equation (B17) also clearly delineates the expression $\frac{\phi}{b\eta}\sqrt{R_m(s)D_m}$ as an effective mass transfer coefficient for matrix diffusion. This expression can be further divided into a flow-system-dependent part, $\frac{\phi}{b\eta}$, and a tracer-dependent part, $\sqrt{R_m(s)D_m}$. In chemical engineering, Laplace-domain expressions such as equations (B14) and (B17) are used extensively in control theory and are referred to as "transfer functions."

We now consider three simplifications to equation (B17). First, by setting $R_f(s)$ and $R_m(s)$ equal to 1, we reproduce the result for a nonsorbing tracer obtained by Maloszewski and Zuber (1983). Second, in the case of an infinite matrix, as was assumed by Tang et al. (1981), the argument of the hyperbolic tangent approaches infinity and hence the hyperbolic tangent itself becomes unity. The resulting expression is identical to that derived by Tang et al. (1981) except that the reaction terms have now been generalized to allow rate-limited as well as equilibrium sorption. Finally, if we set the matrix porosity, ϕ , equal to zero, the entire term

accounting for diffusive transport in the matrix (the term containing the hyperbolic tangent) drops out of the equation, and we get an expression describing reactive transport in a single-porosity medium. Thus, the transport expression derived for a dual-porosity medium is consistent in that it reduces to a single-porosity medium when $\phi = 0$.

Radial Convergent Flow in Fractures

The derivations in the preceding section were strictly for a spatially invariant flow rate in fractures (linear flow). In reality, the flow field in a weak recirculation tracer test in a confined, heterogeneous aquifer is likely to range between linear and radial (National Research Council, 1996), with these two cases representing end members. In a completely unconfined aquifer, spherical flow might be an appropriate end member, but we do not consider that here because of the partially-confined nature of the Bullfrog tuff.

In the case of radial flow, we only have to modify the equations for solution phase transport in the fractures in the preceding section. Specifically, all x-derivatives become r-derivatives and the $D_f \frac{\partial^2 C_f}{\partial x^2}$ terms become $\left(\frac{1}{r}\right) \frac{\partial}{\partial r} \left(r D_f \frac{\partial C_f}{\partial r} \right)$.

Equations (B1), (B6), (B8), and (B12) then become, respectively:

$$\frac{\partial C_f}{\partial t} + v_f \frac{\partial C_f}{\partial r} - \left(\frac{1}{r}\right) \frac{\partial}{\partial r} \left(r D_f \frac{\partial C_f}{\partial r} \right) + \left(\frac{\rho_f}{\eta}\right) \frac{\partial S_f}{\partial t} - \frac{\phi D_m}{b\eta} \frac{\partial C_m}{\partial y} \Big|_{y=b} = 0 \quad (\text{B18})$$

$$\frac{\partial C_f}{\partial t} + v_f \frac{\partial C_f}{\partial r} - \left(\frac{1}{r}\right) \frac{\partial}{\partial r} \left(r D_f \frac{\partial C_f}{\partial r} \right) + \left(\frac{\rho_f}{\eta}\right) \left[\frac{K_f \beta_f C_f^{\beta_f - 1}}{1 + \alpha_f C_f} - \frac{\alpha_f K_f C_f^{\beta_f}}{(1 + \alpha_f C_f)^2} \right] \frac{\partial C_f}{\partial t} - \frac{\phi D_m}{b\eta} \frac{\partial C_m}{\partial y} \Big|_{y=b} = 0 \quad (\text{B19})$$

$$s \bar{C}_f + v_f \frac{\partial \bar{C}_f}{\partial r} - \left(\frac{1}{r}\right) \frac{\partial}{\partial r} \left(r D_f \frac{\partial \bar{C}_f}{\partial r} \right) + \left(\frac{\rho_f}{\eta}\right) s \bar{S}_f - \frac{\phi D_m}{b\eta} \frac{\partial \bar{C}_m}{\partial y} \Big|_{y=b} = 0 \quad (\text{B20})$$

$$\left[1 + \frac{\left(\frac{\rho_f}{\eta}\right) k_{ff}}{\left(\frac{\rho_f}{\eta}\right) s + k_{fr}} \right] s \bar{C}_f + v_f \frac{\partial \bar{C}_f}{\partial r} - \left(\frac{1}{r}\right) \frac{\partial}{\partial r} \left(r D_f \frac{\partial \bar{C}_f}{\partial r} \right) - \frac{\phi D_m}{b\eta} \frac{\partial \bar{C}_m}{\partial y} \Big|_{y=b} = 0 \quad (\text{B21})$$

All other equations are the same as for the linear flow case if the model domain is the same as in Fig. B-1.

Becker and Charbeneau (submitted) have solved the radial flow transport problem in the special case of convergent flow with no sorption or matrix diffusion (i.e., a single-porosity system). Their solution differs from other radial convergent transport solutions in the literature (e.g., Moench, 1989, 1995) in that their boundary

condition at the production well is an "absorbing" boundary that dictates that any solute mass reaching the production well immediately disappears from the system. This boundary condition is consistent with a transfer function approach to interpreting tracer test responses, discussed below. The resulting Laplace domain solution for the case of no sorption or matrix diffusion in terms of τ and Pe (analogous to equation (B17)) is (Becker and Charbeneau, submitted):

$$\bar{C}_i(r_w) = \exp\left[\frac{Pe}{2}\left(1 - \frac{1}{r_{LW}}\right)\right] \frac{Ai(\sigma^{1/3}y_L)}{Ai(\sigma^{1/3}y_w)} \quad (B22)$$

where, r_w = production well radius,
 r_{LW} = production well radius divided by separation between injection and production wells,

$$y_L = Pe + \frac{1}{4\sigma},$$

$$y_w = \frac{Pe}{r_{LW}} + \frac{1}{4\sigma},$$

$$\sigma = \left(\frac{r_{LW}}{Pe}\right)^2 \frac{2\tau s}{(r_{LW}^2 - 1)},$$

$Ai(z)$ = Airy function (Spanier and Oldham, 1987).

Becker (1996) extended this result to a dual-porosity system (with the geometry of Fig. B-1) for a tracer that exhibits equilibrium, linear sorption behavior. We extend it further here to allow for rate-limited, linear sorption. The result, without derivation, is identical to equation (B22) but with σ redefined as

$$\sigma = \left(\frac{r_{LW}}{Pe}\right)^2 \frac{2\tau s \Psi(s)}{(r_{LW}^2 - 1)} \quad (B23)$$

where, $\Psi(s) = R_f(s) + \frac{\phi}{b\eta} \sqrt{\frac{R_m(s)D_m}{s}} \tanh\left(\sqrt{\frac{sR_m(s)}{D_m}}\left(\frac{L}{2} - b\right)\right)$ and $R_f(s)$ and $R_m(s)$ are as defined in equations (B15) and (B16).

Equation (B22) using σ defined in equation (B23) is the Laplace transform transfer function expression that should be used in lieu of equation (B17) for the case of radial convergent transport of a linearly sorbing tracer in a dual-porosity system. For nonlinear sorption, a numerical formulation of equation (B18) in conjunction with equations (B2), (B3), and (B4) is required for the rate-limited case, and equations (B19) and (B7) are required for the equilibrium case. The numerical model RETRAN can be used to solve these nonlinear, convergent radial flow equations.

Convolution of Transfer Functions to Obtain Tracer Test Responses

Before we can obtain a meaningful field-scale transport prediction, we must convolute equation (B17) or (B22) with a realistic tracer injection function. In the time domain, such a convolution is accomplished by a convolution integral, but in the Laplace domain it becomes a simple multiplication (Churchill, 1958):

$$C(t) = \int_0^t A(\tau) \cdot B(t-\tau) d\tau \Rightarrow \bar{C}(s) = \bar{A}(s) \cdot \bar{B}(s) \quad (\text{B24})$$

where, $X(t)$ = time-domain function,
 $\bar{X}(s)$ = Laplace transform of time-domain function, and
 s = Laplace transform variable.

This process can be extended to more than two transfer functions by taking the product of all applicable functions. Thus, in a field tracer test, transfer functions for tracer injection, pipeline delays, and storage in the injection and production wellbores can all easily be convoluted with the groundwater system transfer function (e.g., equations (B17) or (B22)) to obtain an overall transfer function for the test. We assume the most practical injection function in a field tracer test: a finite-duration, constant concentration pulse, which has a Laplace transform given by

$$\bar{I}(s) = C_o \left(\frac{1 - \exp(-T_p s)}{s} \right) \quad (\text{B25})$$

where, C_o = concentration of injection pulse, M/L^3
 T_p = duration of injection pulse, T .

Wellbore storage is accounted for by assuming that the wellbores are well-mixed regions (Moench, 1989, 1995). The Laplace domain transfer function for a well-mixed region is given by

$$\bar{W}(s) = \frac{\gamma}{\gamma + s} \quad (\text{B26})$$

where, γ = time constant, generally assumed to be the volumetric flow rate divided by the volume of well-mixed region, $1/T$.

Pipeline delays can be accounted for by a transfer function of the form

$$\bar{P}(s) = \exp(-T_d s) \quad (\text{B27})$$

where, T_d = delay time, T .

Reinjection of tracers can also be accounted for with transfer functions, but that is not considered here because scoping calculations indicated that the effects of recirculation in the October tracer test should have been insignificant because of the amount of dilution occurring in the test and the fact that only 3.5% of the produced water was recirculated.

A computer model called RELAP (REactive transport LAPlace transform inversion code) was developed to predict field tracer transport by convoluting (i.e., multiplying) either the linear or radial dual-porosity transfer functions (equations (B17) or (B22), respectively) with the transfer functions described above. RELAP numerically inverts the resulting Laplace-domain product of transfer functions to obtain a time domain solution. The numerical inversion procedure is described in the next section.

We have given considerable emphasis here to the Laplace transform modeling approach despite the fact that the numerical model RETRAN is more general because it can accommodate nonlinear sorption isotherms and ultimately spatial heterogeneity. The Laplace transform approach, however, has a distinct advantage over the numerical modeling approach in that it is very easy to account for the effects of processes other than transport in the aquifer (by the convolution procedure described above). The transfer function approach is also well suited to estimating model parameters by matching solutions to experimental breakthrough curves. The Laplace transform inversion executes in a fraction of a second on a typical computer workstation, so RELAP can be exercised with different values of transport parameters literally thousands of times per minute. By contrast, a typical RETRAN simulation with comparable numerical accuracy takes 2-3 minutes of compute time on the same workstation. RELAP contains a parameter search algorithm to minimize the sum-of-squares differences between model predictions and a given tracer data set. This feature allows rapid estimation of model parameter values that are consistent with the test data. Because of the fast execution times of the RELAP inversion algorithm and the fact that sum-of-squares response surfaces for the transport problem typically have multiple minima, the search algorithm simply adjusts parameters over a specified range in systematic, brute-force manner to achieve a least-squares fit to the data. The resulting fits can then be used to provide good initial estimates to RETRAN for obtaining estimates of nonlinear sorption parameters.

Another reason for developing the Laplace transform model is to provide semi-analytical solutions against which more general numerical models can be compared and verified. This is important because numerical models will ultimately be used to account for spatial heterogeneity and temporal variations in boundary conditions when making predictions of radionuclide transport over large time and length scales.

The Laplace transform and numerical models were tested by (1) inverting several simple Laplace transforms with known time-domain solution to ensure that the Laplace transform inversion algorithm was working properly, (2) comparing predicted nonsorbing solute breakthrough curves in a single-porosity medium to analytical solutions (Kreft and Zuber, 1978; Levenspiel, 1972), and (3) comparing the semi-analytical (RELAP) and numerical (RETRAN) model predictions for sorbing

tracers with linear isotherms (both rate-limited and equilibrium). In all cases, excellent agreement was obtained between model predictions and analytical solutions, or between the two models.

Numerical Inversion of Laplace Transforms

The final step in obtaining a transport prediction from the transfer functions is to invert the solution from the Laplace domain to the time domain. We accomplish this by using a Fourier transform procedure embodied in an algorithm obtained over the World Wide Web (Lindhardt, 1995). We have found this algorithm to be more stable for Laplace transform inversions than any others we have tried (e.g., Stehfest, 1970; de Hoog et al., 1982).

The basic principles of the algorithm used for numerical inversion of Laplace transforms are given below. We thank Sven Lindhardt (unknown affiliation) for providing the algorithm in the form of a MathCad[®] worksheet at the World Wide Web address: <http://www.mathsoft.com/appsindex.html>. The worksheet can be found under the program name invsfft.mcd at this web site. Sven also provided much of the following description of the mathematical basis for the algorithm.

The Laplace transform is defined by

$$F(s) = \int_0^{\infty} f(t)e^{-st} dt \quad (B28)$$

where, s = Laplace transform variable,
 t = time,
 $f(t)$ = time domain function,
 $F(s)$ = Laplace domain function.

If we set $s = \sigma + j\omega$, where $j = \sqrt{-1}$, in equation (B28) and change the lower limit of integration to $-\infty$ (which is permissible for any initial-valued problem because $f(t) = 0$ for $t < 0$) we obtain

$$F(s) = \int_{-\infty}^{\infty} f(t)e^{-\sigma t} e^{-j\omega t} dt \quad (B29)$$

If σ is a constant, equation (B29) can be rewritten as

$$F(j\omega) = \int_{-\infty}^{\infty} f_1(t)e^{-j\omega t} dt \quad (B30)$$

where, $f_1(t) = f(t)e^{-\sigma t}$.

Equation (B30) is the Fourier transform of $f_1(t)$, for which very efficient inversion algorithms exist to find $f_1(t)$ given $F(j\omega)$. However, the choice of σ must be such that the integral in equation (B30) converges. This is accomplished by choosing

$$\sigma = \frac{-\ln(0.05)}{1.5 \cdot T_{\max}} \quad (\text{B31})$$

where, T_{\max} = maximum time at which the function $f(t)$ is to be evaluated.

Now, if we have an arbitrary Laplace transform, $F(s)$, we can obtain a spectrum by setting $s = \sigma + j\omega$ and computing $F(s)$ for equally-spaced values of ω ; i.e., for

$$\omega_i = \frac{2\pi i}{T_{\max}} \quad (\text{B32})$$

where, $i = 0, 1, 2, 3 \dots$

The inverse Fourier transform of this spectrum will give the function $f_1(t)$ in equation (B30), from which the desired function $f(t)$ is easily generated from

$$f(t) = f_1(t)e^{\sigma t} \quad (\text{B33})$$

The inversion algorithm has been extensively tested on equations where time-domain solutions are known, and it has proven to be very accurate. Accuracy for the purposes of this work was ensured by using more and more terms in the Fourier transforms until the solutions no longer changed.

Appendix B References

- Becker, M. W., Tracer tests in a fractured rock and their first passage time mathematical models, Ph.D. dissertation, University of Texas at Austin, 1996.
- Becker, M. W. and Charbeneau, R. J., A first passage time solution for radially convergent tracer tests, submitted to *Water Resour. Res.*, 1996.
- Churchill, R. V., *Operational Mathematics*, 2nd ed. McGraw-Hill, New York, 1958.
- de Hoog, F. R., Knight, J. H., and Stokes, A. N., An improved method for numerical inversion of Laplace transforms, *SIAM J. Sci. Stat. Comput.*, 3(3), 357-366, 1982.
- Kreft, A. and Zuber, A., On the physical meaning of the dispersion equation and its solutions for different initial and boundary conditions, *Chem. Eng. Sci.*, 33, 1471-1480, 1978.

- Levenspiel, O. *Chemical Reaction Engineering*, 2nd ed. John Wiley and Sons, New York, 1972.
- Lindhardt, S. MathCad® worksheet at the World Wide Web address:
<http://www.mathsoft.com/appsindex.html>, 1995.
- Maloszewski, P. and Zuber, A., Interpretation of artificial and environmental tracers in fissured rocks with a porous matrix, in *Isotope Hydrology*, International Atomic Energy Agency (IAEA), Vienna, Austria, pp. 635-651, 1983.
- Maloszewski, P. and Zuber, A., On the theory of tracer experiments in fissured rocks with a porous matrix, *J. Hydrology*, 79, 333-358, 1985.
- Maloszewski, P. and Zuber, A., Influence of matrix diffusion and exchange reactions on radiocarbon ages in fissured carbonate aquifers, *Water Resour. Res.*, 27(8), 1937-1945, 1991.
- Moench, A. F., Convergent radial dispersion: A Laplace transform solution for aquifer tracer testing, *Water Resour. Res.*, 25(3), 439-447, 1989.
- Moench, A. F., Convergent radial dispersion in a double-porosity aquifer with fracture skin: Analytical solution and application to a field experiment in fractured chalk, *Water Resour. Res.*, 31(8), 1823-1835, 1995.
- National Research Council, *Rock Fractures and Fluid Flow: Contemporary Understanding and Applications*, National Academy Press, Washington, D.C., 1996.
- Rasmuson, A. and Neretnieks, I., Radionuclide migration in strongly fissured zones: The sensitivity to some assumptions and parameters, *Water Resour. Res.*, 22(4), 559-569, 1986.
- Spanier, J. and Oldham, K. B., *An Atlas of Functions*, Hemisphere Publishing, New York, 1987.
- Stehfest, H., Numerical inversion of Laplace transforms, *Commun. ACM*, 13, 47-49, 1970.
- Tang, D. H., Frind, E. O., and Sudicky, E. A., Contaminant transport in a fractured porous media: Analytical solution for a single fracture, *Water Resour. Res.*, 17(3), 555-564, 1981.

Appendix B Figure

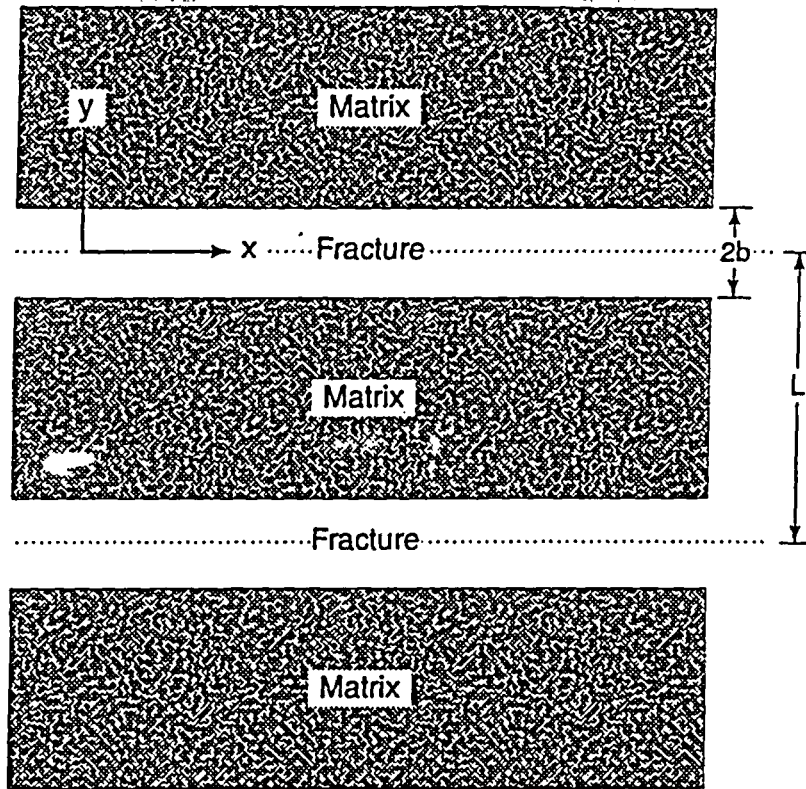


Figure B-1. System geometry assumed in conceptual dual-porosity model.



UNITED STATES
NUCLEAR REGULATORY COMMISSION
ADVISORY COMMITTEE ON NUCLEAR WASTE
WASHINGTON, D.C. 20555

Bradberry Ciocco

October 7, 1997

MEMORANDUM TO: ACNW Members

FROM: Andy Campbell, Senior Staff Scientist *AC*

SUBJECT: "Report of Results of Hydraulic and Tracer Tests at the C-Hole Complex"

ACTION: None, Additional Information from ESF Tour

I requested more information on the tracer tests during the site visit to the C-Well complex, and recently received the subject paper, dated 8/1/97, by P.W. Reimus and H.J. Turin, LANL. The three main conclusions of the study are: (1) the dual-porosity transport model is valid for the saturated zone at Yucca Mountain; (2) there is a potential for colloid transport over significant distances in the saturated zone; and (3) there is good agreement between laboratory and field measurements of Li sorption parameters. In addition, dispersion coefficients derived from the data set are consistent with other field and laboratory work (e.g., Gelhar, 1985, Neuman, 1990).

The first conclusion is important to the DOE Waste Containment and Isolation Strategy, which takes significant credit for diffusion into the matrix and concomitant sorption during transport of radionuclides in the fractured tuff. However, there are alternative interpretations to the dual break through of tracers in the C-Well data. The authors say that it is possible that some of the apparent matrix diffusion seen in the field data may actually be due to diffusion into low flow portions of the interconnected fracture network rather than diffusion into the matrix itself. If this is the case then the short term tracer tests in the field overestimate matrix diffusion.

The second conclusion concerning colloid transport is an issue that ACNW raised in last year's Working Group and subsequent letter on Radionuclide Transport at Yucca Mountain. The importance of the conclusion is heightened by the recent announcement of Pu transport as a colloid more than one mile from a below ground nuclear test site.

The third conclusion is important because it provides a link between laboratory derived sorption parameters for Li and application to its field-scale transport. The authors caution that the absence of field data near Yucca Mountain for other radionuclides of interest limits the applicability of this result.

The authors propose a series of other tracer tests to confirm and extend the C-well test results.

ATTACHMENT: As stated

cc w/att: ACNW Staff
J.T. Larkins
R.P. Savio

September 29, 1997

Andrew C. Campbell, Ph.D.
Senior Staff Scientist
Advisory Committee on Nuclear Waste
U.S. Nuclear Regulatory Commission
Washington, DC 20555

Dear Dr. Campbell:

It was a pleasure meeting you on the ACNW field trip to Yucca Mountain last week, and I trust you and the other field trip participants found the excursion worthwhile and informative regarding ongoing site characterization activities.

Following the short presentation made at the C-Holes saturated zone testing complex, you expressed an interest in additional information concerning the reactive tracer testing and hydrochemical studies conducted at the site. Enclosed is an August 1997 deliverable prepared by Los Alamos National Laboratory entitled, "Report of Results of Hydraulic and Tracer Tests at the C-Holes Complex" which summarizes recent progress in this area.

If you have any questions or require additional information concerning this or other topics of interest, please feel free to contact me at (702) 794-1404, or (702) 794-1323 (FAX).

Regards,



Ronald M. Linden, Ph.D.
Senior Geoscientist
Golder Federal Services
Management and Technical Support Services
Yucca Mountain Project

cc: Russ Patterson, DOE
Carol Hanlon, DOE